Applications of Laser- and Phase-Doppler Velocimetry

Cheng-Hsin Liu
B.Sc., M.Sc.

Thesis submitted for the degree of
Doctor of Philosophy in the University of London
and for the Diploma of Imperial College

Department of Mechanical Engineering
Imperial College of Science, Technology and Medicine

September 1992

BIBL. LONDIN. UNIV.

To Ling-Ling

and above all my parents

ABSTRACT

The thesis describes experimental investigations in a centrifugal pump and in burner c nfigurations and a theoretical study of the phase-Doppler velocimetry. The pump comprised a radial-flow impeller with four back-swept blades and a single volute; the configurations with burners involved a liquid flow simulation of a furnace with a quarl burner and a liquid-fuelled flame stabilised by a disk and a quarl. The velocities in the pump and of the isothermal single- and two-phase flows in the furnace geometry were measured by laser-Doppler velocimetry, and the refraction at the walls was eliminated by using plexiglas for the models with the working fluid a temperature controlled mixture of hydrocarbons. The velocity and size of burning fuel droplets in the liquid-fuelled flames were measured by phase-Doppler velocimetry with the results complemented by measurements of temperature and flammability limit and flow visualisation. An analysis of phase-Doppler velocimetry was carried out to determine the effects of optical geometry and refractive index of the discrete phase.

The analysis showed that the effects of the refractive index of the particles and of a Gaussian intensity profile have larger consequences for the performance of the phase-Doppler velocimetry with back- and side-scattered light than with forward-scattered light. Sizing with back- and side-scattered light requires that the receiving optics be placed close to the bisector plane of the laser beams, with the linear response curve limited by a critical value of phase difference for a particular optical arrangement. It was found that kerosene droplets can be sized in combustion with uncertainties smaller than 7 o at a scattering angle of 30 and of the order of 100° at an angle of 160°. Sizing errors caused by the Gaussian intensity profile can be reduced to around 5 with forward-scattered light and can not be neglected with back- and side-scattered light.

The flows in the impeller passages departed from blade curvatures at off-design conditi ns with separation from the suction surface of the blades and from the shroud surface. There were secondary flows from suction to pressure surfaces, dominated

by the influences of the relative motion between the shroud and impeller surfaces and leakage flow. Geometric differences of around 0.5 mm and one degree in spacing of the four blades cause differences in passage velocity of up to 6% of the impeller tip velocity close to the design flowrate and up to 16% near shutdown, and the discharge flowrate of the impeller passage varied with volute circumferential angle up to 25% at an off-design flowrate. Poor matching of the impeller and volute at off-design conditions caused swirl and separation in the inlet and exit pipes.

The toroidal vortex caused by swirl in the isothermal furnace arrangement decreased in size with increasing flowrate of the central jet, and the effect of the swirl tended to centrifuge particles to larger radii in the two-phase flow resulting in distortion of velocity profiles and suppression of turbulence at high concentrations, which were measured up to a value of particle of 0.113. In the liquid-fuelled flame, kerosene droplets smaller than 10 μm followed the recirculation of the gas phase with those larger than 50 μm being centrifuged from the axis by the vortex induced by the disk. Consideration of burning time and transit time of the droplets confirmed that sizes larger than around 50 μm are responsible for the contribution of unburned liquid fuel in the downstream and for the wall wetting of the quarl. The quarl improved the combustion so that, for a disk blockage ratio of 0.74, the liquid fuel was reduced by 40% at 1.2 diameters from the plane of the disk. The flammability limit depended on the size of the disk and on the presence of the quarl, and the length of the flame scaled with the velocity ratio of the fuel spray to air and the overall equivalence ratio.

Additional investigations with the coolant flow of an internal combustion engine and with the vaporiser of a gas-turbine combustor confirmed that the distributions of coolant flow were affected strongly by the irregular geometry of the internal passages and that the performance of the vaporiser depended on the configurations and operating conditions, with important consequences for combustor performance.

ACKNOWLEDGEMENTS

I would like to express my most sincere gratitude to my supervisor, Prof. J.H. Whitelaw, who provided me with sound guidance, suggestions and criticism throughout the course of this work, and without his continuous interest and support the thesis would not have been possible.

I am especially grateful to Drs. Y. Hardalupas, J.M. Nouri, D.G.N. Tse and C. Vafidis from whom I obtained valuable advice and practical experiences.

I would like to thank all my colleagues in the Thermofluids Section, particularly Drs. A.M.K.P. Taylor, S. Sivasegaram, R. Hockey, S. Yu, S.K. Chow, B. Ozdemir and Z.Y. Hu, Mr. V. Milosavljevic and Miss R. Perez-Ortiz, for their assistance and many useful discussions.

The research programs benefited from technical support by the staffs of the Thermofluids Section, and particularly by Messrs. W. Crew, I. Wright, P. Trowell, D. Symon and J. Laker who helped in design and constructed the experiment apparatus.

The support of research scholarship from Chung Shan Institute of Science and Technology, Taiwan, Republic of China and the financial supports from Commission of the European Communities, Scientific Research Associates Inc., U.S.A., Rolls-Royce Ltd., U.K. and Fiat Research Centre, Italy are acknowledged.

Finally, I would like to thank my wife Ling-Ling who gave me continuous encouragement and shared my disappointments and successes over the years. My deepest gratitude goes to my parents who have born pain to have their son away from home for a long time with full understanding.

CONTENTS

	page
Abstract	1
Acknowledgement	3
Contents	4
List of Tables	6
List of Figures	7
Nomenclature	16
1 Introduction	**21**
2 Phase-Doppler Velocimetry for Transparent Non-absorbing Spheres with Gaussian Laser Beams	**24**
2.1 Introduction	24
2.2 Theoretical background	26
2.2.1 Geometrical optics approximation	26
2.2.2 Scattering angle dependence of the scattered light	31
2.3 Results and discussion	35
2.3.1 Forward-scattered light	37
2.3.2 Back-scattered light	42
2.3.3 Side-scattered light	51
2.4 Conclusions	54
References	57
3 Flow Characteristics of a Centrifugal Pump	**88**
3.1 Introduction	88
3.2 Flow configuration and instrumentation	90
3.3 Results and discussion	94
3.3.1 Flows in the inlet and exit pipes	95
3.3.2 Flows in the impeller passages	97
3.3.3 Variation of relative flow of impeller	103
3.3.4 Flow in the volute passage	104
3.3.5 Slip factor	107
3.4 Conclusions	108
References	111

4 Particle Velocities in a Confined Swirling Flow **154**
4.1 Introduction 154
4.2 Flow configuration and instrumentation 156
4.3 Results and discussion 158
4.3.1 Single-phase flow 158
4.3.2 Beads suspended in the central jet 160
4.3.3 Beads suspended in the annulus 161
4.4 Conclusions 163
References 165

5 Experiment with Disk Stabilised Kerosene-Fuelled Flames **178**
5.1 Introduction 178
5.2 Flow configuration and instrumentation 180
5.3 Results and discussion 182
5.3.1 Characteristics of droplets in isothermal flow 183
5.3.1.1 Spray droplet characteristics without co-flowing annular air 184
5.3.1.2 The effect of air flow in the annulus on the spray characteristics 186
5.3.2 Velocity, droplet size and liquid fuel flux in the flame stabilised by a bluff-body 187
5.3.3 Effect of a quarl and of the size of bluff-body 196
5.4 Conclusions 201
References 206

6 Summary Conclusions and Recommendation **230**
6.1 Summary conclusions 230
6.2 Recommendation 233

Appendix A Flow in the coolant passages of an internal combustion engine cylinder head **235**
Appendix B Vaporiser performance **241**

LIST OF TABLES

page

Chapter 3

3.1 Investigations of flows in centrifugal pumps and rotating passages made by non-laser based techniques 115

3.2 Investigations of flows in centrifugal pumps made by laser velocimetry 122

3.3 Experimental conditions 125

3.4 Characteristics of the laser-Doppler velocimeter 125

Chapter 4

4.1 Flow and fluid properties of two-phase flow 167

4.2 Bead characteristics 167

4.3 Optical characteristics of laser-Doppler velocimetry 168

Chapter 5

5.1 Properties of kerosene 209

5.2 Characteristics of the phase-Doppler velocimeter 209

5.3 Characteristics of kerosene droplets 210

LIST OF FIGURES

page

Chapter 2

2.1 Ray tracing through a spherical particle showing the surface reflected, refracted and the first and second internal reflected rays. 59

2.2 (a) Geometry and coordinate system of the phase-Doppler anemometer. (b) Arrangement of the collection apertures. (c) Particle in probe volume with Gaussian intensity profile. 60

2.3 Scattering angles of the forward-, side- and back-scattered light as a function of refractive index of the particle. 61

2.4 Intensity of the forward-, side- and back-scattered light for particle refractive index of 1.33. 62

2.5 Intensity of the forward-, side- and back-scattered light for particle refractive index of 1.4. 63

2.6 Intensity of the forward-, side- and back-scattered light for particle refractive index of 1.5. 64

2.7 Diagram of the incident and emerging rays of (a) forward-scattered light at $\theta = 30°$, (b) side-scattered light at $\theta = 125°$ and (c) back-scattered light at $\theta = 150°$, for particle refractive index of 1.33. 65

2.8 Diagram of the incident and emerging rays of the back-scattered light for particle refractive index of 1.5 at $\theta = 170°$. 66

2.9 (a) Normalised response curves with refracted light. (b) Intensity distributions of the forward-scattered light, considering refraction only. 67

2.10 Variations of (a) amplitude of the modulation signal and (b) phase difference with particle trajectory at the off-axis light collection angle $\Omega = 30°$. 68

2.11 Amplitude profiles of the 60 μm particle of Figure 2.10, considering separately the intensities of refraction and reflection. 68

page

2.12 Intensity distributions of the forward-scattered light for a 60 μm particle illuminated by (a) uniform intensity and Gaussian intensity profiles at the trajectories of $2Y/D_b$ = (b) -0.5 and (c) 0.9, considering refraction and reflection. 69

2.13 Variations of amplitude of the modulation signal and phase difference of a 140 μm particle along a trajectory inclined 45° to the fringes of the velocimeter, at the light collection angle $\Omega = 30°$. 70

2.14 Response curves calculated between two points of (α, β) of (150°, 0°) and (150°, 2.5°), considering: (a) surface reflection and both parts of FIR; (b) the first part and the second part and both parts of FIR and that after integration of light intensity over the apertures, centred at the same points. 71

2.15 Intensity distributions of the back-scattered light of a 47 μm particle, considering surface reflection and both parts of FIR. 72

2.16 Intensity distributions of the back-scattered light of a 47 μm particle, considering the interference of (a) the first and (b) the second parts of FIR from both beams, (c) the first part of FIR from beam 1 and the second part from beam 2 and (d) the first part of FIR from beam 2 and the second part from beam 1. 73

2.17 Intensity distributions of the back-scattered light considering both parts of FIR, for particle diameters of (a) 16, (b) 26, (c) 36 and (d) 47 μm. 75

2.18 (a) Effect of size of collection aperture on the response curve with the back scattered light. (b) Effect of optical geometry on the response curve with the back scattered light. (c) Intensity distributions of the back-scattered light of a 120 μm particle, considering both parts of FIR. 76

2.19 (a) Normalised response curves of Figure 2.18b. (b) Intensity distributions of the back-scattered light of a 94 μm particle, considering both parts of the FIR. 77

2.20 (a) Response curves for apertures 1 and 2 centred at (α, β) of (150°, 10°) and (150°, 12.5°) with the dimension of the apertures $\Delta\alpha \times \Delta\beta$ of 9.5° x 1.1° and 9.5° x 2.2°. (b) Intensity distributions of the back-scattered light of a 47 μm particle, considering both parts of FIR. 78

page

2.21 Response curves for a three photomultipliers phase-Doppler system calculated for particle refractive index of 1.33 and off-axis collection angle of 150°, with the three collection apertures centred at β_1=-3.75°, β_2=-1.25° and β_3=3.75° and α=150°. 79

2.22 (a) Response curves for particle refractive index m = 1.4 and off-axis angle Ω = 160° and 155°, and for m = 1.33 and Ω = 160°. (b) Intensity distributions of the back-scattered light of a 47 μm particle, considering both parts of FIR. 80

2.23 (a) Intensity distributions of the central fringes of the back-scattered light as a function of particle diameter. (b) Number of intensity maxima of the central fringes of the back-scattered light over a range of scattering angle of 20°. 81

2.24 Variations of (a) amplitude of the modulation signal and (b) phase difference with particle trajectory at the off-axis light collection angle Ω = 160°. 82

2.25 Amplitude profiles of the 140 μm particle of Figure 2.24a, considering separately the intensities of FIR and surface reflection. 82

2.26 Intensity distributions of the back-scattered light of a 140 μm particle illuminated by (a) uniform intensity and Gaussian intensity profiles at the trajectories of $2Y/D_b$ = (b) -1.6, (c) -0.5 and (d) 0.5, considering FIR and surface reflection. 83

2.27 Response curves calculated between two points of (α, β) of (120°, 0°) and (120°, 2.5°), considering: (a) surface reflection and SIR; (b) surface reflection and SIR and that after integration of intensity over the apertures centred at the same points. 84

2.28 Intensity distributions of the side-scattered light of a 200 μm particle, considering surface reflection and SIR. Particle was aligned with (a) a bright fringe and (b) a dark fringe in the probe volume. 85

2.29 Variations of (a) amplitude of the modulation signals and (b) phase difference with particle trajectory at the off-axis light collection angle Ω = 104°. 86

2.30 Amplitude profiles of the 140 μm particle in Figure 2.29a, considering separately the intensity of SIR and surface reflection. 86

page

2.31 Intensity distributions of the side-scattered light of a 140 μm particle illuminated by (a) uniform intensity and Gaussian intensity profiles at the trajectories of $2Y/D_b$ = (b) 0.2 and (c) 2.2. 87

Chapter 3

3.1 Flow configuration and instrumentation. 126

3.2 Dimensions of the centrifugal pump and coordinate systems. 127

3.3 Head coefficient of the pump running at 2910 rpm. 128

3.4 Radial profiles of x-component and y-component of mean velocity at the axial station z/D_i of 0.7 in the inlet pipe and flowrates of $0.93Q_n$, $0.57Q_n$, $0.29Q_n$ and $0.15Q_n$. 129

3.5 Radial profiles of x-component and y-component of rms velocity at the axial station z/D_i of 0.7 in the inlet pipe and flowrates of $0.93Q_n$, $0.57Q_n$, $0.29Q_n$ and $0.15Q_n$. 130

3.6 Radial profiles of x-component and y-component of mean velocity at the axial station x/D_e of 1.8 in the exit pipe and flowrates of $0.93Q_n$, $0.57Q_n$, $0.29Q_n$ and $0.15Q_n$. 131

3.7 Radial profiles of x-component and y-component of mean velocity at the axial station x/D_e of 3.2 in the exit pipe and flowrates of $0.93Q_n$, $0.57Q_n$, $0.29Q_n$ and $0.15Q_n$. 132

3.8 Radial profiles of x-component and y-component of rms velocity at the axial station x/D_e of 3.2 in the exit pipe and flowrates of $0.93Q_n$, $0.57Q_n$, $0.29Q_n$ and $0.15Q_n$. 133

3.9 Blade-to-blade distributions of angle-resolved axial, radial and tangential components of mean velocity on the mid-plane of the impeller passage at discharge, measured at Ψ=330 degrees and the flowrates of $0.93Q_n$, $0.57Q_n$, $0.29Q_n$ and $0.15Q_n$. 134

3.10 Blade-to-blade distributions of angle-resolved axial, radial and tangential components of mean and rms velocities on the mid-plane of the impeller passage at the discharge, measured at Ψ=330 degrees and the flowrates of $0.93Q_n$, $0.57Q_n$, $0.29Q_n$ and $0.15Q_n$. 135

page

3.11 Mean velocity vectors of the absolute flow in an impeller passage at the flowrate of $0.93Q_n$ measured at Ψ=330 degrees. 136

3.12 Mean velocity vectors of the relative flow in an impeller passage at the flowrates of $0.93Q_n$, $0.57Q_n$, $0.29Q_n$ and $0.15Q_n$ measured at Ψ=330 degrees. 137

3.13 Blade-to-blade distributions of mean flow angle on the mid-plane of the impeller passage, at the flowrate of $0.93Q_n$ measured at Ψ=330 degrees with the radial locations r/R_t=0.7, 0.8, 0.9 and 1. 139

3.14 Blade-to-blade distributions of mean flow angle on the mid-plane of the impeller passage at discharge, measured at Ψ=330 degrees. 139

3.15 Blade-to-blade distributions of angle-resolved radial component of mean velocity at the flowrates of $0.93Q_n$, $0.57Q_n$, $0.29Q_n$ and $0.15Q_n$ measured at Ψ=330 degrees. 140

3.16 Blade-to-blade distributions of angle-resolved streamwise component of mean velocity at the flowrates of $0.93Q_n$, $0.57Q_n$, $0.29Q_n$ and $0.15Q_n$ measured at Ψ=330 degrees. 141

3.17 Angle-resolved cross-stream mean velocity in an impeller passage measured at Ψ=330 degrees with the radial planes of r/R_t of 0.71, 0.9 and 1 and the flowrates of $0.93Q_n$, $0.57Q_n$, $0.29Q_n$ and $0.15Q_n$. 142

3.18 Mean velocity vectors of the relative flow in an impeller passage at the flowrate of $0.57Q_n$ measured at Ψ=60 and 240 degrees. 143

3.19 Blade-to-blade distributions of angle-resolved radial and tangential components of mean and rms velocities on the mid-plane of the impeller passage at discharge, at the flowrate of $0.57Q_n$ measured at Ψ=60, 240 and 330 degrees. 145

3.20 Blade-to-blade distributions of flow angle on the mid-plane of the impeller passage at discharge, at the flowrate of $0.57Q_n$ measured at Ψ=60, 24 and 330 degrees. 145

page

3.21 Angle-resolved tangential component of mean velocity in the volute passage at the flowrate of $0.57Q_n$. 146

3.22 Angle-resolved tangential component of rms velocity in the volute passage at the flowrate of $0.57Q_n$. 147

3.23 Mean flow vectors on the plane of z=0 close to the cutwater at the flowrate of $0.57Q_n$. 148

3.24 Angle-resolved tangential component of mean velocity in the volute passage measured at Ψ of 330 degrees with the flowrates of $0.93Q_n$, $0.29Q_n$ and $0.15Q_n$. 149

3.25 Cross-stream mean flow in the volute on the plane of Ψ=330 degrees at the flowrates of $0.93Q_n$ and $0.57Q_n$. 150

3.26 Angle-resolved axial and radial components of mean velocity traces on the centreline of the exit pipe at axial stations x/D_e=0, 1, 1.8 and 3.2. 151

3.27 Radial distributions of angular momentum at the flowrates of $0.93Q_n$ and $0.29Q_n$. 152

3.28 Radial distributions of slip factor at the flowrates of $0.93Q_n$ and $0.29Q_n$. 152

3.29 Variations of slip factor with flowrate and volute circumferential angle at impeller discharge. 153

Chapter 4

4.1 Flow circuit and model. 169

4.2 Symmetry of mean velocities at different axial locations. 170

4.3 Streamline of single-phase flow with different mass-flow ratio of central jet and annulus flow. (a) near field; (b) overall flow. 171

4.4 Bead mean and rms velocities on centreline. 172

4.5 Radial distribution of bead mean and rms velocities of central jet on plane of z/D=-0.26 and R=7.45mm. 173

4.6 Radial distribution of bead mean velocities; beads suspended in the central jet. 173

4.7 Bead mean and rms velocities on centreline. 174

page

4.8 (a) Data rate of 700μm beads suspended in the annulus on plane of z/D=-0.26 at C_v =8.5%. 175

4.8 (b) Radial distribution of bead mean and rms velocities in the annulus on plane of z/D=-0.26 and R=19.5mm. 176

4.9 Radial distribution of bead mean velocities; bead suspended in the annulus. 177

Chapter 5

5.1 Schematic of the experimental system. 211

5.2 Dimensions and coordinates of the kerosene burner. 211

5.3 Kerosene flame stabilised by a 43.8 mm disk bluff-body. (a) sheet-lighted non-combusting spray; (b) sheet-lighted non-combusting flow; (c) combusting flow. 212

5.4 Axial component of mean and rms velocities of fuel droplets in the non-combusting spray. (a) along the centreline; (b) radial profile at z/R=0.4. 213

5.5 Sauter-mean diameter and size distributions of fuel droplets in the non-combusting spray. (a) along the centreline; (b) radial distribution at z/R=0.4. 214

5.6 Volume flux of fuel droplets in the non-combusting spray. (a) along the centreline; (b) radial distribution at z/R=0.4. 215

5.7 Axial component of mean and rms velocities of fuel droplets along the centreline in the non-combusting flow downstream of a 43.8 mm disk bluff-body. 216

5.8 Velocity probability density function of fuel droplets at z/R=1.2 on the centreline of Figure 5.7. 216

5.9 Volume flux of fuel droplets along the centreline in the non-combusting flow downstream of a 43.8 mm disk bluff-body. 216

5.10 Flammability limit of the kerosene flames stabilised by flat disk bluff-bodies. Shaded area represents the region with stable flame. (a) without quarl; (b) with quarl. 217

5.11 Axial and radial components of mean and rms velocities of fuel droplets along the centreline in the flame stabilised by a 43.8 mm disk bluff-body. 218

page

5.12 Mean velocity vectors of fuel droplets on a radial cross-section in the flame stabilised by a 43.8 mm disk bluff-body, with the radial profiles at the axial stations z/R of 0.1, 0.4, 0.8, 1.2 and 2.4. (a) 10 μm, (b) 30 μm and (c) 50 μm droplets. 219

5.13 Radial profiles of axial and radial components of mean velocity of fuel droplets in the flame stabilised by a 43.8 mm disk bluff-body. 220

5.14 Radial profiles of axial and radial components of rms velocity of fuel droplets in the flame stabilised by a 43.8 mm disk bluff-body. 221

5.15 Sauter-mean diameter and size distributions of fuel droplets in the flame stabilised by a 43.8 mm disk bluff-body. (a) along the centreline;
(b) radial distributions in combusting flow 222

5.16 Volume flux of fuel droplets along the centreline in the flame stabilised by a 43.8 mm disk bluff-body. 223

5.17 Radial distributions of volume flux of fuel droplets in the flame stabilised by a 43.8 mm disk bluff-body.
(a) forward flux; (b) reverse flux. 223

5.18 Isoflowrate lines of liquid fuel in the flames stabilised by a 43.8 mm disk bluff-body. (a) 10 μm, (b) 30 μm and (c) 50 μm droplets; (d) all sizes of droplets. 224

5.19 Kerosene flames stabilised by bluff-body with a quarl. (a) 43.8 mm, (b) 38.2 mm and (c) 31.6 mm disks. 225

5.20 Temperature isotherms in the flames stabilised by bluff-body with a quarl. (a) 43.8 mm and (b) 31.6 mm disks. 226

5.21 Axial component of mean and rms velocities of fuel droplets along the centreline in the flame stabilised by a 43.8 mm disk bluff-body with a quarl. 227

5.22 Radial profiles of axial component of mean velocity of fuel droplets in the flames stabilised by bluff-body with a quarl. (a) 43.8 mm and (b) 31.6 mm disk. 227

5.23 Radial profiles of radial component of mean velocity of fuel droplets at the exit of the quarl in the flame stabilised by a 43.8 mm disk bluff-body with a quarl. 228

5.24 Radial distributions of Sauter-mean diameter of fuel droplets in the flame stabilised by a 43.8 mm disk bluff-body with a quarl. 228

page

5.25 Flowrate of fuel droplets in the flames stabilised by a 43.8 mm disk bluff-body at different radial planes along the axis of the burner. 229

5.26 Variation of flame length with spray-to-air velocity ratio in the flames stabilised by bluff-body with a quarl. 229

5.27 Variation of flame length with equivalence ratio in the flames stabilised by bluff-body with a quarl. 229

NOMENCLATURE

Chapter 2

Roman letter

A	amplitude of the pedestal signal
B	amplitude of the modulation signal
D	divergence of the emerging ray
D_b	diameter of the probe volume
d	particle diameter
d_f	fringe spacing of the anemometer ($= \frac{\lambda}{2 \sin\frac{\Phi}{2}}$)
E	scattering light wave
I	intensity of the scatter light
i	$\sqrt{-1}$
i_b	intensity distribution in the probe volume
m	real part refractive index of the particle
p	integer for component of scatter light, (= 0 surface reflection; 1 refraction; 2 first internal reflection; 3 second internal reflection)
r	Fresnel reflection coefficient
S	amplitude function of scatter light wave
t	time
Δw	angular spacing between the apertures
X-Y-Z	Cartesian co-ordinate
x	Mie size parameter ($= \frac{\pi d}{\lambda}$)

Greek letter

α	elevation angle
$\Delta\alpha$	angular height of the aperture
β	rotation angle
$\Delta\beta$	angular width of the aperture
χ	angle between scattering plane and plane of the beams
ε	parameter for the fraction of energy contained in the emerging ray
Φ	phase difference between two Doppler signals
λ	wavelength of the laser light

$\emptyset$	intersection angle of the two beams
θ	scattering angle (between 0 and π)
θ'	angle between incident and emerging rays
$\theta_{2,diff}$	scattering angle of the second dark ring of the diffraction pattern
σ	phase of the scatter light
τ	angle of incidence
τ'	angle of refraction
Ω	off-axis angle of light collection
ω_D	angular frequency of the Doppler signal
ξ	optical path length difference

Subscript

diff	diffraction
j	polarisation perpendicular(=1) or parallel (=2) to the scattering plane
n	index of the two laser beams (= 1 or 2)
r	rainbow
T	total contribution

Chapter 3

Roman letters

A	area
C_n	relative cross-stream mean velocity
C_s	relative streamwise mean velocity
D_e	exit pipe diameter (= 28.5 mm)
D_i	inlet pipe diameter (= 36 mm)
Ek	Ekman number (= $\frac{\mu}{4\rho R_t^2 \omega}$)
H	head
M	normalised angular momentum (= $\frac{r \tilde{w}}{R_t^2 \omega}$)
n	number of blade (= 4)
N	impeller rotation speed (= 2910 rpm)
N_s	specific speed (= $\frac{\sqrt{\Phi}}{\Gamma^{0.75}}$)
N_{sUS}	specific speed (= $\frac{N\sqrt{Q}}{H^{0.75}}$; Q: GPM; H: feet, N: rpm)
Q	flowrate
Q_n	design flowrate (= 2.72×10^{-3} m^3/s)

r, θ, z	cylindrical coordinates (see Figure 3.2)
Re	Reynolds number (= $\frac{U\,D}{\nu}$)
Ro	Rossby number (= $\frac{W_t}{2R_t\,\omega}$)
R_t	impeller outer diameter (= 62.7 mm)
S	slip factor (= $\frac{\tilde{w}}{r\omega - \hat{v}\tan\beta}$)
t	impeller blade thickness (= 2.5 mm)
U, V, W	absolute mean velocities (see Figure 3.2)
u', v', w'	absolute rms velocities (see Figure 3.2)
U_e	bulk mean velocity in exit pipe
U_i	bulk mean velocity in inlet pipe
V_R	theoretical radial velocity at R_t, (= $\frac{Q}{(2\pi R_t - n\frac{t}{\cos\beta})(Z_t + \delta)}$)
$\hat{v}$	area averaged radial velocity, (= $\frac{1}{A}\int_A V\,dA$)
W_R	theoretical absolute tangential velocity at R_t, (= $W_t - V_R \tan\beta$)
W_t	impeller peripheral velocity at R_t (= 19.1 m/s)
$\tilde{w}$	mass averaged tangential velocity, (= $\frac{\int_A V\,W\,da}{\int_A V\,da}$)
x, y, z	Cartesian coordinates (see Figure 3.2)
Z_b	passage width (≈ 6.7 mm at R_t)
Z_t	impeller blade height at R_t (= 6.2 mm)

Greek letters

β	impeller blade angle (= 58° for R ≥ 40 mm)
δ	blade tip clearance (≈ 0.5 mm)
Φ	flow coefficient (= $\frac{Q}{2\pi R_t Z_t W_t}$)
Ø	impeller shaft angle
Γ	head coefficient (= $\frac{g\,H}{W_t^2}$)
μ	Stodola slip factor (= $1 - \frac{\pi\cos\beta}{n}$)
ν	kinematic viscosity of the liquid (= 1.74×10^{-6} m^2/s)
ρ	density of the liquid (= 0.893 kg/m^3)

Ω	relative angular position on the impeller
σ	Busemann slip factor $(= \dfrac{A_1 - A_2 \frac{V_R}{W_t} \tan\beta}{1 - \frac{V_R}{W_t} \tan\beta})$
ω	impeller angular velocity
Ψ	volute circumferential angle

Chapter 4

Roman letters

C_v	volume concentration of beads
D	inner diameter of the annulus
d_p	mean diameter of the beads
m_a	mass flowrate in the annulus
m_c	mass flowrate in the central pipe
R	radius
Re	Reynolds number
r	radial coordinate
St_t	turbulent Stokes number
St_ω	centrifugal Stokes number
U	streamwise mean velocity
u'	rms of streamwise velocity fluctuation
u_f^2	variance of streamwise velocity of fluid
U_a	bulk mean velocity of the annular flow
V	radial mean velocity
v'	rms of radial velocity fluctuation
V_t	terminal velocity of the beads
W	tangential mean velocity
w'	rms of tangential velocity fluctuation
z	longitudinal coordinate

Greek letters

μ	dynamic viscosity
ν	kinematic viscosity
$\nu_{eff,f}$	effective kinematic viscosity
ρ_p	density of the beads
τ_p	characteristic response time of beads
τ_f	turbulent time scale of fluid
ω	rotational speed

Chapter 5

Roman letters

D_a	Damkoekler number
D_c	diameter of the disk bluff-body
D_i	inner diameter of the annulus (= 18 mm)
d_o	initial diameter of the droplet
D_o	outer diameter of the annulus (= 50.8 mm)
N	total number of data
r	radial coordinate
R	outer radius of the annulus (= 25.4 mm)
SMD	Sauter-mean diameter
St_m	mean Stokes number
St_{tr}	transit time Stokes number
St_ω	centrifuge Stokes number
T	temperature
t_b	burning time of the droplet
t_f	mean time scale of the flow
t_r	radial transit time
t_t	time scale of the turbulence
t_{tr}	transit time of the droplet
t_u	axial transit time
U	mean value of the axial velocity
u'	rms value of the axial velocity
U_a	bulk mean velocity in the annulus
U_c	bulk mean velocity at the exit of the bluff-body
U_{jet}	typical gas-phase velocity of the spray (see text)
V	mean value of the radial velocity
v'	rms value of the radial velocity
z	axial coordinate

Greek letters

λ_b	burning constant of kerosene (= 10^{-6} m^2/s)
τ	relaxation time of the droplet
ω	angular velocity of the vortex

CHAPTER 1
Introduction

It is well known that laser-Doppler velocimetry can lead to detailed measurements of velocity characteristics in a wide range of flows and that it can be limited by problems of optical access. The closely related technique of phase-Doppler velocimetry has been shown to allow measurements of the diameters of spherical droplets and particles but is less well established. The research described here makes use of both techniques to provide information of flows where little previously existed and made use of fluids of refractive index identical to those of walls where it was necessary to overcome access difficulties. In addition, analysis of phase-Doppler velocimetry has led to improved knowledge of the manner in which its principles should be used, and detailed measurements of droplet velocity, size and flux have been obtained in quarl stabilised flames similar to those used in furnaces.

The emphasis of the thesis is on the improvement of understanding of flows of engineering importance, and the flows considered include those in a centrifugal pump and in burner configurations, with additional investigations of the flow in coolant passages of an internal-combustion engine and of the droplets characteristics produced by the vaporiser of a gas-turbine combustor reported in appendices. The pump had a casing made of acrylic material and this, together with a working fluid comprising a temperature controlled mixture of hydrocarbons, allowed detailed measurements of three components of velocity and the corresponding normal stresses in the intake, within the blade passages and in the volute and outlet pipe. The investigation of burner flows was conducted in two parts: the first with isothermal flow of the same hydrocarbon mixture and acrylic particles in order to examine the two phase flow characteristics in the absence of combustion, and the second with burning kerosene droplets and with the size-resolved velocity and liquid

flux measurements complemented by flow visualisation, examination of flammability limits and the measurement of temperature.

The following chapter is concerned with the phase-Doppler technique and with analysis based on geometric optics and performed in order to provide better understanding of the technique and particularly of the practical consequences of different angles of light collection, the Gaussian intensity distribution of laser light and the possible uncertainties which stem from variations in refractive indices. The measurements of two-phase flows, Chapter 5 and Appendix B, were obtained with light collected in forward scatter at angles known to allow the separation of the contributions of diffraction, refraction and reflection but the consequence of using side- and back-scattered light are less well understood and are examined here. As will be shown, the use of light of non-uniform intensity has greater consequences with side- and back-scattered light. Also, since the measurements of Chapter 5 involve droplets whose temperature varied over a wide range with related variations in refractive index, the implications for accuracy are examined. In this chapter, as in all others, the presentation is made in the context of previous work to which full reference is made.

The behaviour of centrifugal pumps has been examined previously in terms of overall performance and measurements, sometimes performed with laser-Doppler velocimetry, but without consideration of the flows within the blade passages and usually with insufficient data to allow detailed conclusions. The investigation of Chapter 3 was carried out in considerable detail with inter-blade measurements made possible by the method of refractive-index matching. The investigation includes consideration of the entire flow from intake to outflow, with comparison of results in the four blade passages as a function of load and for a single rotation speed of 2910 rpm.

The method of refractive-index matching was also used in the investigation of the two-phase flow in Chapter 4 in a liquid-flow simulation of a furnace geometry with a single burner, with a quarl diffuser, located on the axis. The main purpose was to determine

the behaviour of the particles added to the liquid flow, particularly in terms of their ability to follow the flow and their influence on the liquid phase. The results show, for example, that large particles were centrifuged by the swirler, and this is important to the combusting flow of Chapter 5.

The burner arrangement of Chapter 5 is one of several investigated at Imperial College and was used to burn kerosene so that it was desirable to measure the velocity of the droplets as a function of size and to determine the unburned liquid flux at various locations. A phase-Doppler velocimeter was used for this purpose, and the velocity and size results were complemented by measurements of flammability limits and local temperature. The kerosene was added on the axis, and the flame stability depended upon a disk-shaped bluff body, so that the centrifuging process revealed in Chapter 4 was less important but nevertheless was observed and quantified. The importance of a quarl diffuser was also examined together with the effects of confinement and the recirculation caused by the bluff body.

Each of the following chapters has been prepared as an independent contribution so that previous work is cited in the text and referenced at the end of the chapter. Similarly the flow configuration, instrumentation and consideration of uncertainties is included in each chapter in which measurements are presented. The thesis ends with summary conclusions and a brief statement of recommendations for future work.

CHAPTER 2

Phase-Doppler Velocimetry for Transparent Non-Absorbing Spheres with Gaussian Laser Beams

2.1 INTRODUCTION

Phase-Doppler velocimetry measures the size and velocity of spherical particles simultaneously, and is based on a spatial fringe pattern of light scattered by a particle which generates two Doppler signals of the same frequency proportional to particle velocity with a phase shift proportional to particle diameter, see Durst and Zaré (1975), Bachalo and Houser (1984), Saffman *et al.* (1984), Bauckhage *et al.* (1988) and Hardalupas (1989). Extensive analysis of the technique by Hardalupas and Taylor (1988), Al-Chalabi *et al.* (1988) and Sankar and Bachalo (1991) has shown that collection of light at certain scattering angles results in a linear relationship between the phase difference and particle diameter for transparent particles. This linear relationship can be modified by the Gaussian intensity profile of the laser light, and Sankar and Bachalo (1991) and Gréhan *et al.* (1991 and 1992) have shown that the response curve can become non-monotonic for certain particle trajectories through the fringe pattern of the velocimeter. However, the previous work did not examine in detail the implications of the Gaussian intensity profile on the sizing accuracy of the technique, and this is one purpose of the present chapter.

Although sizing with forward-scattered light has the advantages of higher intensity and larger signal-to-noise ratio, it may be necessary to collect light at other angles in confined flows such as in internal combustion engines or gas turbines, see for example Saffman *et al.* (1989) and Levy (1989). Al-Chalabi *et al.* (1988) have shown that for back-scattered light the interference between the first internal reflected and the external reflected light can

cause low and high frequency oscillations of the phase-diameter relationship, which can be damped using large rectangular shaped apertures to integrate light intensity, and the response curve is linear over a range of particle size. However, Sankar and Bachalo (1991) have suggested a difference up to 15% between the measured Sauter-mean diameter of a spray with forward- and back-scattered light, while no effort was made to explain the cause for these differences. Also, there is no information on the use of the technique with side scattered light. The second purpose of this work is, therefore, to examine the operation of the phase-Doppler velocimetry with back- and side-scattered light.

In general, the response curve of the technique is affected by the refractive index of the particle, and different approaches have been used in the forward-scatter direction, either to minimise the effect (Pitcher *et al.*, 1990) or to measure the refractive index (Naqwi *et al.*, 1991). In particular, in combusting flows the refractive index of liquid fuel may vary with temperature, and some indication of the associated sizing uncertainties for the forward-scattered light is provided by Pitcher *et al.* (1990), while no related information exists for back- and side-scattered light. The third purpose of the work is to quantify the influence of the refractive index on the sizing uncertainties with forward-, back- and side-scattered light.

The accuracy of the measurements of size of transparent non-absorbing spherical particles with phase-Doppler technique is examined in this chapter theoretically using the geometrical optics approximation. The analysis has quantified the uncertainties due to particle trajectory and refractive index of combusting liquid fuel and allowed analysis of the uncertainties of the measurements of Chapter 5 and Appendix B. Section 2.2 describes the theoretical background of the calculations and quantifies the scattering angle dependence of the scattered light. Section 2.3 presents results for forward-, back- and side-scattered light, each treated in a sub-section in which particles are considered to be illuminated by uniform or Gaussian intensity profiles. The last section summarises the more important conclusions.

2.2 THEORETICAL BACKGROUND

Calculations of the phase difference of the Doppler signals at two detectors separated in space can be made by geometrical optics or Mie theory. Calculations by Mie theory imply the assumptions of spherical particles and uniform illumination and require the evaluation of infinite series, with the number of terms required for convergence increasing with particle diameter, see for example Saffman *et al.* (1984) and Al-Chalabi *et al.* (1988). Although Gouesbet *et al.* (1988) has shown that a generalised Mie theory can allow non-uniform illumination of the particle, still the infinite series of Mie calculation are more complicated to further increase the time of calculation.

For most practical applications of phase-Doppler velocimetry, particles are much larger than the wave length of visible laser light and have refractive indices different from the surroundings, i.e. $x = \frac{\pi\, d}{\lambda} >> 1$ and $2\, x\, (m-1) > 1$, so that calculations by geometrical optics provide good approximations to the exact solution of Mie theory, Van de Hulst (1957). The approach of geometrical optics is preferred here due to its computational speed and easy adaptation to allow the Gaussian intensity profile. However, one disadvantage is that it can not represent the intensity and phase at certain angles, e.g. the angles of rainbows and glory.

The following sub-section describes the procedure for calculations by geometrical optics, and sub-section 2.2.2 presents the dependence of the scattering intensity with the scattering angles. More details of the method are provided by Van de Hulst (1957) and Hardalupas (1989).

2.2.1 Geometrical Optics Approximation

The light scattered by a spherical particle in a plane wave front has contributions from reflection at the external surface of the particle, refraction through the particle, those refracted after one and two reflections at the inner surface of the particle and diffraction. Contributions from more than two internal reflections

are negligible and will not be considered. The amplitude and phase of the light for a specific ray path through the particle is described by the amplitude function

$$S_{jp}(x,m,\tau_p) = x\ |\varepsilon_{jp}|\ \sqrt{D_p}\ e^{i\,\sigma_p}. \qquad (2.1)$$

The index j identifies the polarisation of the light and is equal to 1 or 2 for polarisation perpendicular or parallel to the plane of scattering (the plane of the incident and emerging rays), respectively. The index p identifies the interface of scattering where p = 0, 1, 2 and 3 for surface reflection, refraction and first and second internal reflections respectively, Figure 2.1. The value of ε is determined by the Fresnel reflection coefficient and is equal to

$$\begin{aligned} \varepsilon_{jp} &= r_j && \text{for } p = 0 \text{ and} \\ &= (1-r_j^2)(-r_j)^{p-1} && \text{for } p = 1, 2 \text{ and } 3. \end{aligned} \qquad (2.2)$$

The Fresnel reflection coefficients for perpendicular and parallel polarisation are given by

$$\begin{aligned} r_j &= \frac{\sin\tau - m\sin\tau'}{\sin\tau + m\sin\tau'} && \text{for } j=1 \text{ and} \\ &= \frac{m\sin\tau - \sin\tau'}{m\sin\tau + \sin\tau'} && \text{for } j=2, \end{aligned} \qquad (2.3)$$

where τ and τ' are the angles of incidence and refraction respectively, Figure 2.1. Snell's law of refraction is written as

$$\cos\tau = m\cos\tau'. \qquad (2.4)$$

The ray divergence D due to the curvature of the sphere is given by

$$D = \frac{\sin\tau\cos\tau}{\sin\theta\ \left|\frac{d\theta'}{d\tau}\right|}, \qquad (2.5)$$

where θ' is the angle between the incident and emerging rays and is written as

$$\theta' = 2\,\tau - 2\,p\,\tau', \tag{2.6}$$

and its derivative is

$$\frac{d\theta'}{d\tau} = 2 - 2\,p\,\frac{\tan\tau}{\tan\tau'}. \tag{2.7}$$

For convenience, the scattering angle of the emerging ray, θ, is defined in the interval between 0 and π, Figure 2.1, by

$$\theta' = k\,2\pi + q\,\theta \tag{2.8}$$

with k and q the integers. The angle of incidence τ_p for each light contribution at the scattering angle θ can be determined from equations 2.4, 2.6 and 2.8. Glantschnig and Chen (1981) have shown that a closed form solution for τ as a function of θ and m can be obtained for p = 1, and the amplitude function can also be given in closed form, i.e. $S_{j1n}(x,m,\theta)$. However, no closed form solution for τ is available for p = 2 and 3, and a Newton-Raphson iteration method was used to solve τ at each θ. It is noted that for $p \geq 2$, there is a maximum or minimum of θ, and a certain value of θ gives rise to two values of τ. Details of the implications are discussed in sub-section 2.2.2.

The phase of the scattered light, σ_p, is calculated in terms of the phase lag through the optical path length and the phase changes at reflection interface and focal lines, Van de Hulst (1957), and is given by

$$\sigma_p = \frac{\pi}{2} + (\text{phase of } \varepsilon_{jp}) + \xi_p + \frac{\pi}{2}(p - 2k + \frac{s}{2} - \frac{q}{2}). \tag{2.9}$$

The second term on the right hand side is the phase change due to reflection at the surface of particle which has already been taken into account by the definition of ε_{jp} in equation 2. The term ξ_p is the difference of optical path length between the emerging ray and the reference ray passing through the centre of the sphere, and is given by

$$\xi_p = 2\,x\,(\sin\tau_p - p\,m\,\sin\tau'_p). \tag{2.10}$$

The last term on the right hand side is due to the phase change at the focal lines where the phase advances by $\frac{\pi}{2}$, according to the integers of p, k and q and the integer s = 1 or -1 determined by the sign of $\frac{d\theta'}{d\tau}$. The values of the integers p, k, q and s are provided in the following table, Van de Hulst (1957):

Light contributions	Parts	p	k	q	s
Surface reflection	—	0	0	1	1
Refraction	—	1	0	-1	1
First internal reflection	first	2	0	-1	-1
	second	2	0	-1	1
	third	2	1	1	1
Second internal reflection	first	3	-1	1	-1
	second	3	-1	1	1

The amplitude and phase of the scatter light $S_{jp}(x,m,\tau_p(\theta))$ is calculated by equation 2.1 for each contribution to the scattered light after estimating the corresponding incident angle τ_p at the scattering angle θ. The total contribution at a particular scattering angle is the summation of the amplitude functions of the individual contributions at that angle. For a particle in the crossing region of two laser beams, the light is scattered by two incident waves, and the total light contribution requires the evaluation of the amplitude functions for each beam.

Figure 2.2a shows the geometry of the optical system, and that two laser beams propagate on the X-O-Z plane (beam plane) intersecting at an angle of Ø at point O and with the polarisation normal to the plane. The scattered light is collected at an off-axis angle Ω by three rectangular apertures, each corresponding to the signal for a photodetector, in front of a lens and arranged around the Y-O-Z plane (bisector plane). The emerging rays of the scattered light are identified by the spherical coordinate of the elevation angles α and rotation angle β. For each laser beam, the scattering angle θ corresponding to a point (α, β) in space is given by

$$\theta_n = \cos^{-1}\{\cos(\beta \pm \frac{\emptyset}{2}) \cos \alpha\}, \quad \text{'+' for n=1; '-' for n=2} \quad (2.11)$$

So, the total amplitude function for each beam is

$$S_{Tjn}(x,m,\theta_n) = \sum_{p=0}^{3} \sqrt{i_b(X,Y)}\, S_{jpn}(x,m,\theta_n), \quad (2.12)$$

and the scattering wave at a point in space is

$$E_{jn}(x,m,\theta_n,t) = S_{Tjn}(x,m,\theta_n) \frac{-i}{k\,r} e^{i(\omega_n t - k\,r)}, \quad (2.13)$$

where i_b is the intensity profile at the beam waist. For polarisation normal to the beam plane, the resulting scattering wave function is the summation of the components from polarisation perpendicular and parallel to the scattering plane, which is given by

$$E_{Tn}(x,m,\theta_n,t) = E_{1n}(x,m,\theta_n,t) \cos \chi_n + E_{2n}(x,m,\theta_n,t) \sin \chi_n \quad (2.14)$$

where χ_n is the angle between the scattering plane and the beam plane defined by

$$\sin \chi_n = \frac{\sin \alpha}{\sin \theta_n}. \quad (2.15)$$

The scattering contribution from each beam interferes at a point on the surface of light detection where the intensity of the light is obtained by

$$I(x,m,\theta_n,t) = |E_{T1}(x,m,\theta_n,t) + E_{T2}(x,m,\theta_n,t)|^2 \quad (2.16)$$

and can be written as

$$I(x,m,\theta_n,t) = A(x,m,\theta_n,t) + B(x,m,\theta_n,t) \cos(\omega_D t - \Phi(x,m,\theta_n,t)) \quad (2.17)$$

where A and B correspond to the amplitudes of the pedestal and modulation signals, respectively, and Φ is the phase of the interference pattern at the point of detection. The information of particle size is provided by the phase Φ and, when the light

detection occurs at two points in space, the phase difference of the modulation signal between the two detections is given by

$$\Phi_{12} = \Phi_1 - \Phi_2 \, . \tag{2.18}$$

Equation 2.16, can be evaluated at an instant of time over a range of elevation and rotation angles to provide the intensity distribution of the scattered light.

The above analysis does not consider diffraction which, though it provides no size information, can interfere with the reflected and refracted light. The amplitude function of diffraction is given by

$$S_{diff,n}(x,\theta_n) = x^2 \frac{J_1(x \sin \theta_n)}{x \sin \theta_n}, \tag{2.19}$$

where $J_1(x \sin \theta)$ is the first order Bessel function of the first kind, and equation 2.19 can be added to equation 2.12.

2.2.2 Scattering Angle Dependence of Scattered Light

The major contributions to the intensity of forward scattered light are caused by refraction, external surface reflection and diffraction. The intensity of diffraction dominates around direct forward scatter, $\theta \approx 0°$, with up to 91% of the energy concentrated within the boundary of the second dark ring of the diffraction pattern defined by the angle

$$\theta_{2,diff} = \sin^{-1}(2.23 \frac{\lambda}{d}) \tag{2.20}$$

which decreases rapidly with particle diameter. For example, for λ = 632.8 nm, $\theta_{2,diff}$ is 16.4° for a 5 μm particle and 8.1° for a 10 μm particle, and a 10 μm particle leads to diffracted-light intensity at least one order of magnitude weaker than that of refraction for scattering angles larger than around 20°. Since diffracted-light intensity is to be avoided to prevent sizing errors, the receiving optics of a phase-Doppler velocimeter is arranged at off-axis angles greater than 20°.

Figure 2.3 presents the scattering angles of the light contributions of p = 0 to 3 for refractive indices from 1.2 to 1.5, corresponding

to a range of liquid fuels commonly used in engineering applications and including that of the subsequent chapters. Light is reflected at the external surface of the particle at all scattering angles, and refracted through the particle between the angles of $\theta = 0°$ and

$$\theta_{\tau=0,p=1} = 2\cos^{-1}\left(\frac{1}{m}\right) \tag{2.21}$$

which increases from 67° to 96° with refractive indices from 1.2 to 1.5. The intensity of refraction, shown in Figures 2.4 to 2.6 for particle refractive indices of 1.33, 1.4 and 1.5, dominates for scattering angle larger than 20° and decreases with scattering angle with small variation with refractive index. For scattering angles from 30° to 60°, refracted-light intensity is at least 40 times stronger than that of the coexisting reflected light. The intensity was calculated for one particle diameter with the incident wave linearly polarised parallel to the scattering plane and is presented in arbitrary units.

For scattering angles larger than around 90°, the intensity of the scattered light stems mainly from external-surface reflection and the first and second internal reflections. The minimum value of θ for $p = 2$ and the maximum for $p = 3$ define the main and second rainbow angles, respectively, of the first and second internal reflections. The angle of incidence for the rainbow angle, τ_r, is given by (Van de Hulst, 1957)

$$\sin^2 \tau_r = \frac{m^2 - 1}{p^2 - 1} \tag{2.22}$$

Using Snell's law and equations 2.6 and 2.8, the expressions for the main ($p = 2$) and second ($p = 3$) rainbows angles are

$$\theta_{r,p=2} = 4\cos^{-1}\left\{\frac{\cos\left[\sin^{-1}\sqrt{\frac{m^2 - 1}{3}}\right]}{m}\right\} - 2\sin^{-1}\sqrt{\frac{m^2 - 1}{3}} \quad \text{and} \tag{2.23}$$

$$\theta_{r,p=3} = 2\pi - 6\cos^{-1}\left\{\frac{\cos\left[\sin^{-1}\sqrt{\frac{m^2 - 1}{8}}\right]}{m}\right\} + 2\sin^{-1}\sqrt{\frac{m^2 - 1}{8}} \tag{2.24}$$

Equations 2.23 and 2.24, plotted in Figure 2.3, identify the limiting scattering angles for the first and second internal reflections, and vary with refractive index. It is noted that the first internal reflection exists between the main rainbow and $\theta = 180°$, and the second internal reflection between the second rainbow and $\theta = 0°$.

Also, for certain scattering angles of the first and second internal reflections, there are two incident angles which gives rise to two emerging rays scattering at the same scattering angle. One set of emerging rays exists for $90° \geq \tau \geq \tau_r$ and the other for $\tau_r \geq \tau \geq 0°$, and they identify the first and second parts, respectively, of the first and second internal reflected light. For example, for a particle refractive index of 1.33, the main rainbow scatters at 137.5° ($\theta_{r,p=2}$) with the incident angle of 30.4° ($\tau_{r,p=2}$); at a scattering angle $\theta = 150°$, two rays emerge with angles of incidence of 57.9° and 0.9° and each corresponds to the first and second parts of the first internal reflection. The existence of two parts of the first and second internal reflections is indicated by Figures 2.7c and 2.7b, respectively, suggesting the paths of the two sets of incident and emerging rays for the scattering angles of 125° and 150° together with the rays of the main and second rainbows scattering at 137.5° and 128.7°.

The first and second internal reflections are identified in Figure 2.3. The first part exists throughout the scattering angles for each internal reflection while the second part is limited by the scattering angle for the incident angle $\tau = 0$. The scattering angles where the second part of the first and second internal reflections end are given by

$$\theta_{\tau=0,p=2} = 4 \cos^{-1}\left(\frac{1}{m}\right) \quad \text{and} \tag{2.25}$$

$$\theta_{\tau=0,p=3} = 2\pi - 6 \cos^{-1}\left(\frac{1}{m}\right), \tag{2.26}$$

as also identified in Figure 2.3.

For refractive indices larger than around 1.414, $\theta_{\tau=0,p=2}$ is larger than 180°. Since the scattering angle varies between 0° and 180°, a third part of the first internal reflection can be defined for

$m > 1.414$ and corresponds to the incident rays close to the edge of the particle on the side towards the scattering direction, in contrast to the incident rays corresponding to the first and second parts. Figure 2.8 shows the incident and emerging rays of the three parts of the first internal reflection for a refractive index of 1.5, and the presence of the third part of the light is identified in Figure 2.3.

Figures 2.4 to 2.6 identify the intensity of the first and second internal reflections and show that the intensity of the first internal reflection is the largest for back scatter, and the total intensity of its two parts is around two orders of magnitude larger than that of the co-existing surface reflection. The intensity of the second internal reflection is dominated by its second part which exists within around 20° of scattering angle with the intensity of the same order of magnitude as the co-existing surface reflection. The relative intensities of the two parts of the first internal reflection and that of the second internal reflection and surface reflection vary with scattering angle and particle refractive index. It is noted that the intensity scattered at the rainbow angles cannot be accurately calculated by geometrical optics, and the maxima or minima of the intensity suggest only the location of the rainbows.

For scattering angles larger than around 170°, the intensity of the scattered light is dominated by glory, caused mainly by the edge rays, i.e. $\tau \approx 0°$, Van de Hulst, (1957) and Drain (1985), with the scattered intensity patterns similar to that of diffraction. For refractive indices larger than 1.5, the intensity of the second and third part of the first internal reflection increase rapidly from 170° to 180°, Figure 2.6. The application of phase-Doppler velocimetry is not recommended in this region since, as in direct forward scatter, the increased size of measuring volume observed by the collection optics may limit the maximum number density of particles, before the existence of multiple particles in the measuring volume.

In summary, the following comments can be made concerning sizing transparent particles by the phase-Doppler velocimetry:

i) Sizing is better with forward-scattered light because of the higher intensity of the dominating refraction light. The receiving optics needs to be arranged at an off-axis scattering angle between 20° and 70° to ensure this domination.

ii) Sizing with back- and side-scattered light is recommended only for particle refractive indices between 1.3 to 1.41. In this region, the back scattered light is dominated by two parts of the first internal reflection and the side-scattered light by the second internal reflection and surface reflection, with lower intensities than forward scattered light.

iii) For refractive indices of 1.33 and 1.4, the receiving optics needs to be arranged between 145°-160° and 155°-160°, respectively, to collect back scattered light, and at around 120° and 104° for side-scattered light.

iv) Sizing with the light between the first and second internal reflections is questionable due to its lower intensity and the presence of other light contributions to interfere with the surface reflected light, Al-Chalabi *et al.* (1988).

2.3 RESULTS AND DISCUSSION

The results in this section are presented in three sub-sections, each concerned with particle sizing with forward-, back- and side-scattered components of the refraction, the first and second internal reflections and the external surface reflection. In each sub-section, the phase-Doppler technique is examined by assuming incident light with uniform and with Gaussian intensity. The use the back-scattered light is examined in greater detail to consider the effects of collection apertures, collection angles, beam intersection angles, and refractive index on the linearity of the relationship between size and phase.

The geometry of the optics is presented in Figure 2.2a, and parameters used in the calculations are summarised in the following table, with that for the Gaussian intensity related to arrangements of the instrument used in Chapter 5.

	Uniform Intensity	Gaussian Intensity
Laser wavelength, λ	632.8 nm	514.5 nm
Beam intersection angle, $\emptyset$	10°	4.85°
Fringe spacing, d_f	3.63 μm	6.07 μm
Refractive index, m	1.33	1.4
Off-axis angle, Ω		
Forward scattered light	30°-70°	30°
Back scattered light	145°-160°	160°
Side scattered light	120°	104°
Collection apertures		
Size, ($\Delta\alpha$ x $\Delta\beta$)	9.5° x 1.1°	9.5° x 1.1°
Spacing, Δw	2.5°	1.2°
Phase difference, Φ	aperture 1-2	aperture 1-2
Probe diameter, D_b	——	84 μm

The axis of the collection lens was positioned at off-axis angles Ω between 30° and 160° on the bisector plane, $\beta = 0°$, with aperture 2 centred with the lens, $\beta_2 = 0°$ and apertures 1 and 3 centred at the rotation angles $\beta_1 = \Delta w$ and $\beta_3 = -\Delta w$ respectively, Figure 2.2b. The rectangular shape of the collection apertures was arranged with the large dimension ($\Delta\alpha$) normal to the beam plane, with the dimensions ($\Delta\alpha = 9.5°$ and $\Delta\beta = 1.1°$) corresponding to a 50 mm-by-6 mm rectangle in front of a collection lens of 300 mm focal length. In most cases, the response curves were calculated between apertures 1 and 2, with the intensity of the scattered light integrated over the area of the apertures using a grid of 20-by-4 points and diameter steps of 2 μm.

With uniform intensity, i_b in equation 2.12 was assumed unity, and the particle was centred with the measurement volume at point O. With Gaussian intensity, the intensity profile is described by

$$i_b(X,Y) = i_0 \, e^{-2\frac{X^2+Y^2}{D_b^2}} \qquad (2.27)$$

with i_0 the intensity at the centre (= 1) and D_b (= 84 μm) the probe diameter at the beam waist, defined by the intensity of

$1/e^2$. The effect of particle trajectory was examined by moving the particle centre along the Y-axis in steps of $0.05D_b$, Figure 2.2c, and the phase difference and associated amplitude of the modulation signal were calculated at each particle location.

2.3.1 Forward-Scattered Light

Uniform intensity

Figure 2.9a shows the linear phase-diameter relationship at off-axis angles Ω of 30°, 50° and 70° for three particle refractive indices, based mainly on the intensity of the refracted light. It is known that the weaker contributions of the diffracted and reflected light can interfere with the refracted light to cause oscillations in phase which can be damped using finite size collection apertures to integrate the intensity of the scattered light, Hardalupas and Taylor (1988) and Al-Chalabi *et al.* (1988), and the response curves with forward-scatter light are linear for diameters larger than around 10 μm with small phase oscillations at smaller diameters due to diffracted light. The slope of the curve scales linearly with the fringe spacing of the velocimeter d_f and the angular spacing of the collection apertures Δw, parameters related to the geometry of the transmission and the collection optics respectively, Hardalupas (1989). If the response curves are plotted with the phase difference Φ normalised by Δw and the particle diameter d normalised by d_f, there is a universal curve, depending only on particle refractive index and scattering angle, to characterise the operation of the technique with forward off-axis light collection as shown in Figure 2.9a.

The normalised curves of Figure 2.9a show the decrease of slope with increase of off-axis angle and refractive index which are related to the characteristics of the scattered intensity distributions of refracted light of Figure 2.9b for refractive indices of 1.33 and 1.5 and a normalised particle diameter d/d_f of 11.02 since the pattern scales with the parameter of d/d_f. The intensity distribution is presented as iso-intensity lines as well as ten levels of grey with the lighter tone suggesting higher intensity, as for the rest of the chapter. It is evident that the horizontal spacing of the vertical fringe pattern increases with elevation angle, α, and

refractive index, and this can be used to identify the refractive index with a pair of collection optics arranged at two off-axis angles, as suggested by Naqwi *et al.* (1991).

The sensitivity of measured size to refractive index is quantified by Figure 2.9a, which shows that a change of refractive index from 1.5 to 1.33 causes a decrease of phase difference of 15%, 7% and 2.5% for off-axis angles Ω of 30°, 50° and 70° respectively, in accord with Pitcher *et al.* (1990). Although, light collection at 70° is least sensitive to refractive index, there is loss of scattered light intensity by a factor of around 20 compared to the angle of 30° for a refractive index of 1.4, Figure 2.5. These results imply that kerosene droplets with a nominal refractive index of 1.4 at 298°K and a value of 1.33 at its middle boiling temperature of 495°K can be measured at the off-axis angle of 30°, as of the experiments of Chapter 5 and Appendix B, with an uncertainty of less than 7%.

The above response curves are for light collected around the bisector plane. Since the intensity pattern of refracted light remains regular over a wide range of elevation and rotation angles, it is possible that size can be measured away from the bisector plane, keeping the linearity of the response curve. The technique allows a one-component system to measure more than one vector and to obtain the information of size-resolved cross-correlations of velocity by rotation of the beam plane and without re-adjusting the receiving optics. The response curve after rotation of the beam plane needs to be recalculated, and the details of the technique are provided by Hardalupas and Liu (1992).

Gaussian intensity

Figure 2.10a shows the variations of amplitude of the modulation signal with particle trajectory for diameters of 20, 60, 100 and 140 μm, i.e. particle-to-probe diameter ratios of 0.24, 0.71, 1.2 and 1.67. The non-dimensional parameter $2Y/D_b$ identifies the locations of particle centres along the Y-axis, and the values of 1 and -1 identify the probe diameter. The negative value of Y is towards the location of light collection. The amplitude was calculated based on the term $B(x,m,\theta_n,t)$ of equation 2.17 after integration of the intensity over the aperture 2 and indicates the

maximum amplitude for particle trajectory normal to the fringes. The figure shows that the amplitude and the width of the profiles increase with particle diameter, as expected, and for diameters larger than 60 μm the profiles show two maxima. Figure 2.11 confirms that the maxima with $Y < 0$ corresponds to refracted light and that with $Y > 0$ to reflected light.

For particles much smaller than the probe diameter, e.g. 20 μm, particles are near-uniformly illuminated, therefore, refraction remains dominant. For particle sizes comparable with that of the probe diameter, e.g. 60 μm and larger, refraction and reflection may contribute in different ranges of trajectory, as suggested by the twin peaks of the amplitude profiles, and reflection may dominate in others. This is due to the difference in ray paths of refraction and reflection so that the incident rays are separated by a distance proportional to diameter, Figure 2.7a. The incident intensity for each contribution becomes unequal when the distance between the incident rays is comparable with the diameter of the probe.

The intensity distributions of the scattered light for trajectories dominated by refraction and reflection are presented for a 60 μm particle in Figures 2.12b and 2.12c for a particle located at $2Y/D_b$ of -0.5 and 0.9, respectively, and both fringes are in contrast to the intensity distribution of Figure 2.12a calculated with the assumption of uniform incident intensity. The fringes dominated by refraction are similar to those of Figure 2.9b which considers only refraction, while that of Figure 2.12c is characterised by interference between reflection and refraction showing lower contrast and corresponding to an intensity lower by a factor of 50 than that of Figure 2.12b, as inferred by Figure 2.11.

Since in most prosessors the Doppler signals are detected by an amplitude threshold, the phase difference of the signals needs to be examined by assuming a threshold level, equal to the amplitude of a 10 μm particle in Figure 2.10a. The range of effective trajectory, i.e. amplitude > threshold, is identified in terms of $2Y/D_b$ for each size as {-0.8 to 0.5}, {-1.5 to 0.4}, {-2 to 0.2; 0.7 to 1.4} and {-2.4 to 0; 1 to 2.2}, for 20, 60, 100 and 140 μm

particles, respectively. The associated values of phase difference for these ranges are presented in Figure 2.10b and show near constant positive or negative values. The positive values caused by refraction provide information of size, while the negative values caused by reflection are recognised by the instrument as positive due to the 360° ambiguity in phase. For example the -106° of the 100 μm particle is measured as a phase difference of 360°-106°=254° which corresponds to a 329 μm particle, while the -148° of the 140 μm particle is interpreted as a 247 μm particle, and hence sizes are reported incorrectly when the phase difference is caused by reflected light. The amplitude between the range of $2Y/D_b$ of {0.2 to 0.7} and {0 to 1} of the 100 and 140 μm particles, respectively, is lower than the threshold, and in these regions the phase differences vary rapidly between positive and negative values from $2Y/D_b$ of 0.4 to 0.6 where the local intensities of refraction and reflection are nearly equal.

The signals caused by reflected light may be eliminated by limiting the dynamic range of sizing to ensure that phase differences caused by reflected light are always larger than those by refracted light, Hardalupas and Taylor (1992), manipulating the polarisation of the illuminating and scattered light to minimise the intensity of reflected light, Saffman (1986), and using a pair of receiving optics arranged symmetrically around the axis of the velocimeter to identify only signals caused by refracted light, Gréhan *et al.* (1992). For systems with three photodetectors, e.g. Sankar and Bachalo (1991) and as used in the subsequent chapters, the phase ratio between two detector pairs, e.g. Φ_{13}/Φ_{12}, allows discrimination between the signals from reflected and refracted light and rejection of signals from non-spherical particles or of low signal-to-noise ratio, see Hardalupas and Taylor (1992).

The mixing of signals from reflected and refracted light occurs within a small range of trajectory which, for the collection angle of 30°, is between $2Y/D_b$ of 0.4 to 0.6, corresponding to around 10% of the probe diameter, D_b. Sizing ambiguity in this region occurs in the form of rapid variations in phase between positive and negative values, related to the opposite motions of the refracted and reflected fringe patterns. Figure 2.10a confirms that signals

in this region are of low amplitude, and can be eliminated by amplitude validation. For the present optical arrangement, a threshold level corresponding to the amplitude of a 10 μm particle avoids the signals in this region.

For a 140 μm particle with an oblique trajectory, Figure 2.13 presents the variations of amplitude and phase difference with a 45° trajectory passing the centre of the probe volume, i.e. ($2X/D_b$, $2Y/D_b$) from (-2, -2) to (2, 2). The profiles of amplitude and phase difference show similar trends to that of Figure 2.10, and the rapid variation of phase difference between positive and negative values remains in the region of $2Y/D_b$ of 0.4 to 0.6. The result confirms that the influence of trajectory on phase difference depends mainly on the Y-coordinate of particle locations. Hence, the results of Figure 2.10 made by varying the Y-coordinate of particle locations are justified.

The above results confirm that sizing ambiguity occurs for about 30% of the trajectories inside the probe diameter, i.e. $0.4 \leq 2Y/D_b \leq 1$, in agreement with the observations by Sankar and Bachalo (1991) and Gréhan *et al.* (1991) based on non-monotonic response curves calculated for particle locations inside the probe. Regions of ambiguous and non-ambiguous trajectories outside the probe diameter are also observed, i.e. $2Y/D_b > 1$ and $2Y/D_b < -1$ respectively, and were not suggested by previous work. It was found that the signals giving erroneous size information can be suppressed by validation schemes, e.g. amplitude and phase ratio validation. By eliminating the signal of the ambiguous trajectories, i.e. $2Y/D_b > 0.4$, the variations of the positive values of phase difference within the effective trajectory, i.e. amplitude > threshold, were found to be around 10% for a 20 μm particle and less than 5% for particles larger than 60 μm, influenced by the weak reflected light. By applying validation schemes to improve sizing accuracy, the size-dependent area of the probe volume could be affected, and the possible consequences require further investigation.

In summary, collection of the forward scattered light between angles of 20° to 70° results in linear response curves which scale with the fringe spacing of the velocimeter and the spacing

between the collection apertures. The response curves after normalisation by the above scaling parameters depend on the refractive index of the particle and scattering angle. For a range of particle refractive indices from 1.33 to 1.5, sizing sensitivity can vary by 15% at the scattering angle of 30° and is minimised at the angle of 70°. This result implies that kerosene droplets can be sized in combusting flows at 30° angle with uncertainties of less than 7%, after considering the variation of refractive index by ar ound 5% due to variation of temperature. Sizing ambiguity due to a Gaussian intensity distribution occurs mainly in trajectories of around 30% of the probe diameter in the far side of the location of light collection and further, i.e. $2Y/D_b > 0.4$, for a scattering angle of 30°. Signal validation schemes based on amplitude and phase ratio can eliminate these uncertainties, and those due to the light distribution can be reduced to around 5% for particle diameters up to 1.67 times the diameter of the probe.

2.3.2 Back-Scattered Light

The results in this sub-section are concerned with back-scattered light and with light collected between angles of 145° and 160° and of 155° and 160° for particle refractive indices of 1.33 and 1.4, respectively, as suggested in sub-section 2.2.2. The intensities in these regions are caused mainly by two parts of the first internal reflection and surface reflection, and they are responsible for the sizing response curves. The parameters of optical arrangements used in the following analysis were given at the beginning of section 2.3.

Uniform intensity

The technique of sizing with back-scattered light is examined in the following three parts: the first is concerned with the influence of each light contribution and the effect of integration of light intensity by the collection apertures, the second with the characteristics of the response curve and the effects of the parameters of optical arrangement, and the third with the effect of particle refractive index.

(i) Integration of light intensity over the collection apertures

Figure 2.14a shows the response curve calculated on the basis of the centre of the two apertures, (α, β) of (150°, 0°) and (150°, 2.5°), for a particle refractive index of 1.33 and an off-axis angle of 150°. The high frequency oscillations of the curve were observed also by Al-Chalabi *et al.* (1988) and Sankar and Bachalo (1991) and were caused by the interference of surface reflection with the first internal reflection. The complexity of the scattering intensity distribution which, for example for a diameter of 47 μm, is identified in Figure 2.15a, justifies the high frequency oscillations of the response curve calculated at distinct points. Figure 2.14b shows that the high frequency oscillations in Figure 2.14a do not exist on the response curve based on the intensity of both parts of the first internal reflection, and confirms that they are caused by surface reflection. Although the interference between only the first or second parts of first internal reflection from each beam results in linear curves, the interference between both parts causes departures from linearity for certain size ranges, e.g. 20 to 30 μm, in agreement with Al-Chalabi *et al.* (1988). However, the curve of Figure 2.14a becomes linear after integration of the intensity of the scattered light over the collection apertures and both the high and low frequency oscillations are reduced for particle diameters up to 60 μm, in agreement with Sankar and Bachalo (1991). Although it is known that the high frequency oscillations are reduced by integration of the light over the collection apertures (Saffman, 1986; Al-Chalabi *et al.*, 1988), it is not clear why the low frequency oscillations are reduced and this observation will be examined in the next paragraphs.

The intensity distributions of the scattered light corresponding to the interference between the first or second parts of the first internal reflection is shown in Figures 2.16a and 2.16b, respectively, for a diameter of 47 μm. The following three characteristics can be observed on the two fringe patterns. First, the maximum intensity of the first part is towards direct back scatter, α = 180°, while that of the second part is towards the main rainbow, see also Figure 2.4; second, the fringes around the bisector plane, β = 0°, of both patterns are normal to the plane of

the beams with that of the first part wider; third, the horizontal spacing of the vertical fringes of the second part decreases with elevation angle α in contrast to a more uniform horizontal spacing of the first part. The intensity distributions corresponding to the interference of the cross terms, between the first part from beam 1 and the second part from beam 2 and *vice versa*, show anti-symmetry with respect to $\beta = 0°$, Figures 2.16c and 2.16d, with both fringes inclined and the concave side of the curved fringes towards the beam contributing the second part.

The interference of all the contributions of the first internal reflection, i.e. the fringes of Figures 2.16a to 2.16d, results in one fringe around the bisector plane, as shown in Figure 2.17d, which is broken into regions of local intensity maxima. A less regular intensity pattern exists outside the bisector plane dominated by the influence of the second part and caused by the different spacing of the fringes of the two individual patterns of Figures 2.16a and 2.16b in this region. The local intensity maxima of the fringes around the bisector plane are related to the interference of the cross terms, i.e. Figures 2.16c and 2.16d, and are responsible for the low frequency oscillations of the response curve of Figure 2.14b. This observation is made clear by the intensity distributions of particle diameters of 16, 26, 36 and 47 μm, Figure 2.17, corresponding to the regions of local maxima and minima of the response curve. The rectangle on the figures shows the position of aperture 1 while the circle indicates its centre, $(\alpha\ ,\ \beta)$ of (150°, 2.5°), at which the curve of Figure 2.14b were made. Aperture 2 (not shown in the figure) is identical and centred at (150°, 0°). The phase difference calculated at the centre of the apertures departs from linearity for the 26 and 47 μm particles because these points correspond to a region between two local intensity maxima of the interference fringe patterns, Figures 2.17b and 2.17d, while those of the 16 and 36 μm particles, Figures 2.17a and 2.17c, correspond to the positions on the central fringe with local intensity maxima. The integration of the scattered light intensity by apertures removes the minimum intensity regions along the central fringe provided that the height of the apertures, $\Delta\alpha$, is sufficient to integrate over at least one of the local intensity maxima of the central fringes.

It should be noted that the local intensity maxima of the fringes on the bisector plane disappear when the particle is artificially moved by a half fringe spacing, $d_f/2$, away from the centre of the probe volume and a continuous dark fringe exists around the bisector plane, as shown in Figure 2.15b. This confirms that the local intensity maxima are caused by the time dependent terms of the interference pattern and shows that they do not move in the vertical direction, so the phase variation of the intensity along the central fringe cannot be used for particle sizing. Comparison of Figures 2.17d and 2.15a shows that surface reflection reduces the contrast of the local intensity maxima regions of the central fringe, so the integration of the light over the apertures also removes the high frequency oscillations of the response curve.

The effects of the size and shape of the apertures on the linearity of the response curve are examined in Figure 2.18a which shows a decrease of the height of the aperture from 9.5° to 4.5° resulting in sizing uncertainties of the order of 20%, and for an aperture height of 2.5° large low frequency departures from linearity cause increase of sizing uncertainties to around 50%. Increase of the aperture width from 1.1° to 2.2° (not shown in figure) has negligible effect.

The above results confirm that the combination of a rectangular shaped aperture, its height and position on the intensity pattern of the scattered light filters the low frequency oscillations of the response curve caused by the interference of the two parts of the first internal reflection, and also removes the high frequency oscillations caused by surface reflected light. The height of the aperture, $\Delta\alpha$, is found to be important for the linearity of the phase-diameter relationship, and a value of 9.5° is sufficient to cause linear curves.

(ii) Effects of position and spacing of the collection apertures and of beam intersection angle

Figure 2.18b shows the response curve of Figure 2.14b extended to larger diameters and reveals that, even after the integration of intensity over the apertures, the response curve becomes non-monotonic for diameters larger than 110 μm and phase

differences larger than around 330° (curve a). Figure 2.18c shows the intensity distributions for a 120 μm diameter, corresponding to the phase maximum of the curve a, and confirms that the departure from linearity of the response curve is caused by aperture integration of the intensity of the less regular fringes outside the central fringe. The result suggests that the linear relationship between the phase difference and particle diameter exists only for a limited size range, in contrast to that with forward-scattered light for which the collection apertures integrate the intensity within the region of the central fringe around the bisector plane. The influence of the optical arrangement on the non-monotonic behaviour of the response curve is examined in the following paragraphs.

Figure 2.18b shows the effects of changing the off-axis angle of light collection (curve b), the angular spacing of the apertures (curve c) and the beam intersection angle (curve d) on the extent of the non-monotonic behaviour of the response curve. In each case, the response curves are linear up to a critical value of phase difference from around 220° to 280°, and that the curve is non-linear or non-monotonic outside this range. The linear part of the curve is extended when the integration of light intensity occurs in the region of the central fringe. The variations of the slope of the linear part of the curves suggest scaling of this part of the curve with the optical parameters of the transmitting and collection optics. If the response curves of Figure 2.18b are plotted with the phase difference Φ normalised by the aperture spacing Δw and the diameter d normalised by the fringe spacing of the velocimeter d_f, similar to Figure 2.9a, Figure 2.19a shows that the linear part of the curve scales with the normalisation factors but not the critical value of $\Phi/\Delta w$ for which the curves become non-monotonic. It should be noted that the apertures should not integrate the intensity of the light at angles less than around 2° from the rainbow angle due to the intensity maxima and irregular interference close to the main rainbow. For the present optical arrangement and refractive index, m = 1.33, the angular dimension of the aperture limits the off-axis angle, Ω, to a minimum of around 145°.

Since the scaling parameter for particle diameter is d_f, the effect of beam intersection angle is identified by comparing the intensity distributions of Figures 2.15a and 2.19b, both corresponding to the same value of $d/d_f = 12.9$ with the former corresponding to $\emptyset = 10°$ and $d = 47$ μm and the later $\emptyset = 5°$ and $d = 94$ μm. The figures suggest that the horizontal period of the central fringe scales with d_f but not the vertical period which is inversely proportional to particle diameter. The fringes away from the centre are less correlated between the two fringe patterns which explains why the critical value of phase difference of Figure 2.19a (curve a and d) does not scale with d_f. The number of maxima of the central fringe is proportional to particle diameter and can provide size information as discussed in (iii).

If the collection lens is not located around the bisector plane, the collection angle can be modified by changing the rotation angle while keeping the elevation angle constant as in Figure 2.10a and, as shown in Figure 2.20a for collection apertures located at (α, β) of (150°, 10°) and (150°, 12.5°), the response curve is non-monotonic and cannot be used for sizing. This is caused mainly by the irregular shape of the scattered intensity patterns, as shown in Figure 2.20b for a 47 μm diameter, which does not consist of distinct fringes lying in a direction normal to the plane of the beams. An increase of the width of the apertures by a factor of two shows little effect on the non-linear curve.

The above results show that the phase-diameter relationship with the back scattered light is only linear up to a critical value of phase difference for each optical arrangement and for light collection around the bisector plane. Within the present optical arrangements, the critical values vary between 220° to 330°. This characteristic of the response curve limits the size range of the instrument using two photodetectors up to that corresponding to the critical value of phase difference. Since the critical value of phase difference does not scale with the usual optical parameters, i.e. d_f and Δw, the response curve must be evaluated for each optical arrangement. The value of the critical phase may be increased to larger than 360° by locating the two collection apertures evenly around the bisector plane, but this alignment is

critical, and small misalignment can cause a discrepancy between the actual and theoretical values. Collection of light away from the bisector plane results in a non-linear phase-diameter relationship.

For a system based on three photodetectors, e.g. Sankar and Bachalo (1991), the response curves were calculated for one optical arrangement in Figure 2.21, plotted for phase differences between 0° to 360° according to the range recognised by the instrument. The sizing sensitivity of Φ_{13} is three times that of Φ_{12}; hence the curve of Φ_{13} can reach three times the value of 360° for Φ_{12} to reach once. However, Figure 2.21 shows that only the first part of the high size-sensitivity curve Φ_{13} is linear and reaches 360° and can be used for sizing, while it becomes non-monotonic in the second part at around 150°. The low size-sensitivity curve Φ_{12} also becomes non-monotonic above a phase difference of around 180° and then the curves of Φ_{12} and Φ_{13} exhibit large oscillations of the phase shift where no size information can be obtained. These curves are similar to that of Sankar and Bachalo (1991) who calculated up to a 50 μm diameter and did not identify the non-montonic characteristics of the response curve which, in contrast to forward scatter, limits the otherwise wider possible size range with three detectors.

(iii) Effect of particle refractive index

Figure 2.22a presents the response curves for a refractive index of 1.4 with light collection at the off-axis angle Ω = 160° which corresponds to the same angular distance from the main rainbow for light collection at Ω = 150° and the refractive index of 1.33. The response curve at Ω = 160° is linear up to a phase difference of around 280°, lower than the 330° in Figure 18b (curve a) for m = 1.33. Comparison between the intensity distributions of Figure 2.22b for m = 1.4 and Figure 2.17d for m = 1.33 indicates that the central fringe is narrower and has a larger number of intensity maxima for the larger refractive index which causes the integration of the intensity pattern by the apertures at a region outside the central fringe to occur at a smaller particle size, resulting a lower critical phase value. A decrease of off-axis angle Ω to 155°, Figure 2.22a, reduces the slope of the curve while the value of the critical phase shift remains at around 280°.

If light collection is at the off-axis angle Ω of 160°, Figure 2.22a shows also the effect of a change of particle refractive index from 1.4 to 1.33, corresponding to the range of combusting kerosene droplets, and suggesting that sizing uncertainties of the order of around 100% could arise for some 5% variation of refractive index, stemmed mainly from the sensitivity of scattering angle and intensity of the back-scattered light. This result is in contrast to that with forward-scattered light for which a similar refractive index variation leads to a sizing uncertainty of less than 7% at an off-axis angle of 30° and almost negligible at 70°. Therefore, sizing of combusting liquid fuel sprays is not recommended with back scattered light.

An alternative method to size transparent particles using back-scattered light is to detect the local intensity maxima of the fringes around the bisector plane, since its number over a certain range of scattering angle is proportional to particle size. Figure 2.23a shows the variation of intensity distribution on the bisector plane as a function of particle diameter over a range of elevation angle of 20°. The number of intensity maxima is a linear function with diameter, Figure 2.23b, and a variation of refractive index between 1.4 and 1.33 results in a variation of the sensitivity of the sizing curve of around 25%, smaller than with the phase-Doppler technique with back-scattered light.

Gaussian intensity

Figure 2.24a shows the variations of amplitude of the modulation signal with particle trajectory for a particle refractive index of 1.4 and an off-axis collection angle of 160°. The amplitude profiles increase in value and width and are moving towards the negative Y-coordinate with increasing diameter. Again, a threshold level corresponding to the amplitude of a 10 μm particle is assumed to identify the range of effective trajectory which, as inferred from the figure, is between $2Y/D_b$ of {-0.8 to 0.2}, {-1.6 to 0.6}, {-2.2 to 0.6} and {-2.7 to 0.5} for the 20, 60, 100 and 140 μm particles respectively.

The associated values of phase difference within these ranges, Figure 2.24b, vary with trajectory in a manner different from that

B 3
LON N
UNIV

with forward-scattered light, Figure 2.10b. For smaller diameters, e.g. 20 μm, the phase difference varies gradually with trajectory but varies in steps for larger diameters, e.g. 140 μm. Within the effective trajectories, the phase differences vary between 29°-20°, 98°-21° and 165°-7° for 20, 60 and 100 μm, and from 224° to 100° to -58° for 140 μm. It is noted that the phase of -58° is recognised by the instrument as 360°-58° = 302°. Compared with the values of phase difference calculated with the assumption of uniform intensity of 24°, 71°, 93° and 206°, the sizing errors were quantified as +20%/-16%, +38%/-70%, +77%/-92% and +46%/-100% for the 20, 60, 100 and 140 μm particles respectively, i.e. for particle-to-probe diameter ratios of 0.24, 0.71, 1.2, 1.67. These results suggest that sizing ambiguity exists for a wide range of trajectories, in agreement with Sankar and Bachalo (1991) who calculated the response curves at 150° scattering angle for water droplets and observed that up to 75% of particle trajectories inside the probe diameter resulted in non-linear curves up to a 50 μm particle in a 80 μm probe, which is related to the present result of continuous decrease in phase difference from $2Y/D_b$ of -1 to 1 for the 60 μm particle.

The variations of phase difference are caused by the variation of the relative intensity of the scattered light contributions, which are indicated in Figure 2.25 for example for a 140 μm particle. It is evident that the intensities of the second and first parts of the first internal reflection dominate in the range of $2Y/D_b$ of {-2.7 to -1.1} and {-1.1 to 0} and that of surface reflection in {0 to 0.5}, and they correspond to the plateaus of the phase difference profile in Figure 2.24b. The intensity distributions of the scattered light corresponding to the three trajectory ranges are identified in Figure 2.26. The fringes for $2Y/D_b$ of {-2.7 to -1.1} (Figure 2.26b) are narrower and more regular than that of {-1.1 to 0} (Figure 2.26c) and correspond to the positive values of phase difference of 224° and 100°, respectively, calculated between the apertures centred at (α, β) of (160°, 0°) and (160°, 1.2°). The fringes for $2Y/D_b$ of {0 to 0.5} are dominated by surface reflection (Figure 2.26d) and move in direction opposite to that of the first internal reflection to give a negative value of phase difference of -58°. The fringes calculated by assuming a uniform intensity

profile, Figure 2.26a, are in contrast to the other three and correspond to a phase difference of 206° for the same apertures.

The above results confirm that a Gaussian intensity profile can cause significant sizing errors with the back-scattered light. The errors stem mainly from variations of the relative intensity between the light contributions responsible for sizing caused by uneven illuminations. The errors caused by surface reflection may be minimised by the methods suggested in sub-section 2.3.2 for the forward scattered light, while that caused by the two parts of the first internal reflection cannot be removed since they determine the sizing response curves. Therefore, a large particle-to-probe diameter ratio should be used to minimise the sizing uncertainties.

In summary, collection of back-scattered light at angles between 145° to 160° and 155° to 160° for particle refractive indices of 1.33 and 1.4, respectively, result in linear response curves, based on the intensity of two parts of the first internal reflection. The linearity of the response curve requires the rectangular-shaped collection apertures to integrate the intensity of the central fringe around the bisector plane of the scattered fringe pattern, with the angular height of the aperture no less than 9.5°. The linearity of the response curve extends up to a value of critical phase difference for a particular optical arrangement, which varies from 220° up to 360°. Sizing with back-scattered light is sensitive to the variations in the refractive index of the particle, and a range from 1.4 to 1.33 can cause sizing uncertainties of the order of 100%. The effect of a Gaussian intensity profile can cause large ambiguity in size with particle trajectory. Sizing errors are of the order of 100% for particles larger than the probe diameter and up to 20% for particles up to a quarter of the probe diameter.

2.3.3 Side-Scattered Light

The results in this sub-section are concerned with side-scattered light and with light collected at angles of 120° and 104° for particle refractive indices of 1.33 and 1.4, respectively, sub-section 2.2.2. The light intensities in these regions are caused mainly by surface reflection and the second parts of the second

internal reflection. The parameters of the optical arrangements for the results were given at the beginning of section 2.3.

Uniform intensity

The response curve for the side-scattered light, calculated at two points in space of (α, β) of (120°, 0°) and (120°, 2 5°) for a particle refractive index of 1.33, is presented in Figure 2.27a and shows high frequency oscillations caused by the interference of surface reflection with the second internal reflection. The response curves are linear for each of the light contributions, Figure 2.27b, with that of the second internal reflected light showing nearly twice the sensitivity to size as that for the surface reflected light. The high frequency oscillations of the response curve are removed by calculating the curve with integration of the intensity over the area of the collection apertures centred at the same points, Figure 2.27b, and the phase-diameter relationship is linear up to a diameter of around 250 μm with the phase difference of around 230°. The response curve becomes non-monotonic after the diameter of 250 μm. It is noted that the sensitivity to size of the response curve after integration of intensity is between those of surface reflection and second internal reflection, suggesting that the sizing curve is based on the interference of the two light contributions.

The intensity distribution of the side-scattered light, shown in Figure 2.28a for a 200 μm particle, is characterised by vertical fringes broken into local intensity maxima and inclined towards the second rainbow, $\theta_{r,p=3}$ = 128.7°. The figure corresponds to the particle aligned with a bright fringe of the probe volume, and the vertical fringes away from the bisector plane show less contrast and smaller horizontal spacing than the central fringes around the bisector plane, which is further evidenced by the patterns with the particle aligned with a dark fringe of the probe volume of Figure 2.28b. The rectangle shown in the figure identifies the position of aperture 1 centred at the point of (α, β) of (120°, 2.5°) with aperture 2 (not shown in the figure) centred at (120°, 0°). The phase difference calculated after integration of the intensity between the two apertures is 187°, and aperture 1 is seen to integrate the intensity at the edge of the central fringe

around the bisector plane. For larger diameters, the horizontal spacing of the vertical fringes decreases, and aperture 1 begins to integrate the less regular intensity pattern outside the central fringe where the phase-diameter relationship becomes non-monotonic after 250 μm.

Gaussian intensity

The variation of amplitude of the modulation signal with particle trajectory for particle refractive index of 1.4 and off-axis collection angle of 104°, Figure 2.29a, shows a trend similar that of Figure 2.24a for back-scattered light, except that the profiles are towards the positive Y-coordinate with increasing diameter due to the positions of the incident rays relative to the centre of the particle, as shown by Figure 2.7b. The range of effective trajectory is identified in the figure by assuming a threshold level equal to the amplitude of a 10 μm particle and is for $2Y/D_b$ of {-0.5 to 1}, {-0.5 to 1.7}, {-0.3 to 2.3} and {-0.1 to 2.6} for the 20, 60, 100 and 140 μm particles respectively. Figure 2.29b shows the associated values of phase difference in the ranges which vary with trajectory in a manner similar to that in Figure 2.24b for the back-scattered light. The phase differences vary within the effective trajectories between 2.75°-3.05°, 6.4°-9.6°, 10.2°-16.2° and 14.1°-22.6° for 20, 60, 100 and 140 μm particles respectively. The values of the phase difference calculated with the assumption of uniform intensity are of 2.9°, 8.4°, 14.2° and 19°, and the sizing errors are quantified to be ±5%, +24%/-26%, +14%/-28% and +19%/-26% for the 20, 60, 100 and 140 μm particles, respectively, i.e. for particle-to-probe diameter ratios of 0.24, 0.71, 1.2, 1.67.

Figure 2.30 confirms that the variations of phase difference are caused by the relative intensities of the light contributions responsible for the sizing relationship, where surface reflection dominates for $2Y/D_b$ of {-0.2 to 0.8}, the second internal reflection dominates for {1.6 to 3}, and both light contributions have similar intensity for {0.8 to 1.6} for a 140 μm particle; these results correspond to the plateaus and transition of the profile of phase difference of Figure 2.29b. The scattered fringe patterns dominated by surface reflection are shown in Figure 2.31b for the trajectories of $2Y/D_b$ of 0.2 and that dominated by the second

internal reflection in Figure 2.31c for $2Y/D_b$ of 2.2. The former shows wider fringes and corresponds to a phase difference of 14.1°, calculated for the apertures centred at (α, β) of (104°, 0°) and (104°, 1.2°), while the latter corresponds to a phase difference of 22.6°. The fringes of Figure 2.31a, calculated based on uniform illumination, show interference of the two light contributions and correspond to a phase difference of 19°.

In summary, collection of side-scattered light at angles of 120° and 104° for particle refractive indices of 1.33 and 1.4, respectively, result in linear response curves based on the intensity of the second internal reflection and surface reflection. The linearity of the response curves depends on the integration of the intensity by the rectangular-shaped collection apertures over the central fringes around the bisector plane, similar to that with back-scattered light, and is limited by a critical phase difference for a particular optical arrangement. Since the range of scattering angle of the second internal reflection is around 20°, as determined by the refractive index of the particle, the technique is recommended only for flows with little uncertainty in refractive index. The effect of a Gaussian intensity profile is smaller than that with the back scattered light but larger than with forward scattered light. Sizing errors are up to 26% for particles larger than the probe diameter, and up to 5% for particles smaller than a quarter of the probe diameter.

2.4 CONCLUSIONS

The performance of the phase-Doppler technique has been investigated using geometrical optics approximations. The results have considered the use of forward-, back- and side-scattered light to size transparent non-absorbing spherical particles in the range of relative refractive indices between 1.33 and 1.5 and with the influence of the Gaussian light intensity profile. The following summarises the more important findings:

1. To size transparent particles, the light can be collected at forward-, back- and side-scattered angles. The light refracted in the forward direction is preferred with the two parts of the first

internal reflected light for back scattering and the second internal reflected light and external reflected light for side scattering. The relationship between the particle diameter and phase difference of two Doppler signals detected at two locations adjacent in space is almost linear over a limited range of light collection angle and refractive index, provided the intensity of the scattered light is integrated over a sufficiently large area of the rectangular shaped apertures with the long axis mainly perpendicular to the beam plane.

2. For refractive indices of 1.33 and 1.4, back-scattered light should be collected between scattering angles of 145° and 160° and of 155° and 160°, respectively, and that for side-scattered light at around 104° and 120°, and for both arrangements the collection optics needs to be within a small range of angles around the bisector plane of the beams. The linearity of the response curve is limited by a critical value of phase difference which varies between from 220° to larger than 360°.

3. The Gaussian intensity profile of the laser beams was shown to cause variations of phase difference and associated amplitude of the signal with particle trajectory. It was found that the related uncertainties of sizing are around 5% for forward-scattered light if phase-ratio validation is assumed. For back-scattered light the sizing uncertainties were found to be +46%/-100% and +20%/-16% for particle-to-probe diameter ratios of 1.67 and 0.24, respectively, for the side-scattered light the uncertainties become +19%/-26% and ±5%, respectively.

4. For refractive indices between 1.4 and 1.33, corresponding to the combusting kerosene droplets of chapter 5, the uncertainty in size measurement was calculated to be less than 7% with forward-scattered light at the off-axis angle of 30° and this can be reduced at an angle of 70°. The associated uncertainties are larger for back- and side-scattered light with a value of the order of 100% for this range of refractive indices and an off-axis angle of 160°.

5. It is recommended that sizing with back- and side-scattered light should be used only where there is little uncertainty in particle refractive index, with the diameter of the probe much

larger than the maximum size of particle and the maximum phase difference smaller than that of the critical value.

REFERENCES

Al-Chalabi, S.A.M., Hardalupas, Y., Jones, A.R. and Taylor, A.M.K.P. (1988) Calculation of calibration curves for the phase-Doppler technique: comparison between Mie theory and geometrical optics. In Optical Particle Sizing: Theory and Practice, editors: G. Gouesbet and G. Gréhan, Plenum Press, New York, 107.

Bachalo, W.D. and Houser, M.J. (1984) Phase-Doppler spray analyser for simultaneous measurements of drop size and velocity distributions. *Optical Engineering*, **23**, 583.

Bauckhage, K., Floegel, H.H., Fritsching, U. and Hiller, R. (1988) The phase-Doppler-difference-method, a new laser-Doppler technique for simultaneous size and velocity measurements. Part 2: Optical particle characteristics as a base for the new diagnostic technique. *Part. Part. Syst. Charact.*, **5**, 66.

Drain, L.E. (1985) Laser anemometry and particle sizing. In Proc. Int'l Conf. on Laser Anemometry Advances and Applications. Manchester, U.K., 17.

Durst, F. and Zaré, M. (1975) Laser Doppler measurements in two phase flows. In The Accuracy of Flow Measurements by Laser-Doppler Methods, Proc. of LDA Symposium, Copenhagen, Denmark, 403.

Glatschnig, W.J. and Chen, S.H. (1981) Light scattering from water droplets in the geometric optics approximation. *Applied Optics*, **20**, 2499.

Gouesbet, G., Maheu, B. and Gréhan, G. (1988) Scattering of a Gaussian beam by a sphere using a Bromwich formulation : case of an arbitrary location. In Optical Particle Sizing: Theory and Practice, editors: G. Gouesbet and G. Gréhan, Plenum Press, New York, 27.

Gréhan, G., Gouesbet, G., Naqwi, A. and Durst, F. (1991) Evaluation of phase Doppler system using generalised Lorenz-Mie theory. Proc. Int'l Conf. on Multiphase Flows '91-Tsukuba, Tsukuba, Japan, 24-27 Sept. 1991.

Gréhan, G., Gouesbet, G., Naqwi, A. and Durst, F. (1992) On elimination of the trajectory effects in phase Doppler systems. European Symp. on Particle Characterisation, Nürnberg, Germany, 24-26 Mar. 1992.

Hardalupas, Y. (1989) Experiments with isothermal two phase flows. Ph.D. thesis, University of London.

Hardalupas, Y. and Liu, C.H. (1992) Size-discriminated velocity cross-correlation measured by a single channel phase-Doppler velocimeter. in Proc. 6th Int'l Symp. on Appl. of Laser Anemometry in Fluid Mechanics, Lisbon, Portugal.

Hardalupas, Y. and Taylor, A.M.K.P. (1988) The identification of LDA seeding particles by the phase-Doppler technique. *Exp. in Fluids*, **6**, 137.

Hardalupas, Y. and Taylor, A.M.K.P. (1992) Phase validation criteria of size measurements for the phase-Doppler technique. Imperial College, Thermofluids Section Report TF/92/07, submitted to *Exp. in Fluids*.

Levy, Y. (1989) Back scattered phase-Doppler anemometry (PDA) for spray diagnostics. in Applications of Laser Anemometry to Fluid Mechanics, editors: R.J. Adrian, T. Asanuma, D.F.G. Durão, F. Durst and J.H. Whitelaw, Springer-Verlag, 240.

Naqwi, A., Durst, F. and Liu, X (1991) Two optical methods for simultaneous measurement of particle size, velocity and refractive index. *Applied Optics*, **30**, 4949.

Pitcher G., Wigley G. and Saffman M. (1990) Sensitivity of drop-size measurements by phase-Doppler anemometry to refractive index changes in combusting fuel sprays. In Proc. 5th Int'l Symp. on Appl. of Laser Techniques to Fluid Mechanics, Lisbon, Portugal, paper 14.4.

Saffman, M. (1986) The use of polarised light for optical particle sizing. In Laser Anemometry in Fluid Mechanics 3 (editors: R.J. Adrian, T. Asanuma, D.F.G. Durão, F. Durst and J.H. Whitelaw), Ladoan, 387.

Saffman, M., Buchhave, P. and Tanger, H. (1984) Simultaneous measurements of size, concentration and velocity of spherical particles by a laser Doppler method. In Proc. 2nd Int'l Symp. on Appl. of Laser Anemometry in Fluid Mechanics, Lisbon, Portugal, paper 8.1.

Saffman, M., Fraidl, G. and Wigley, G. (1989) Application of phase and laser Doppler anemometry to the measurement of droplet size and velocity in gasoline and Diesel fuel injection systems. in Applications of Laser Anemometry to Fluid Mechanics, editors: R.J. Adrian, T. Asanuma, D.F.G. Durão, F. Durst and J.H. Whitelaw, Springer-Verlag, 260.

Sankar, S.V. and Bachalo W.D. (1991) Response characteristics of the phase-Doppler particle analyser for sizing spherical particles larger than the light wavelength. *Appl. Optics*, **30**, 1487.

Van de Hulst, H.C. (1957) Light Scattering by Small Particles. Dover, New York.

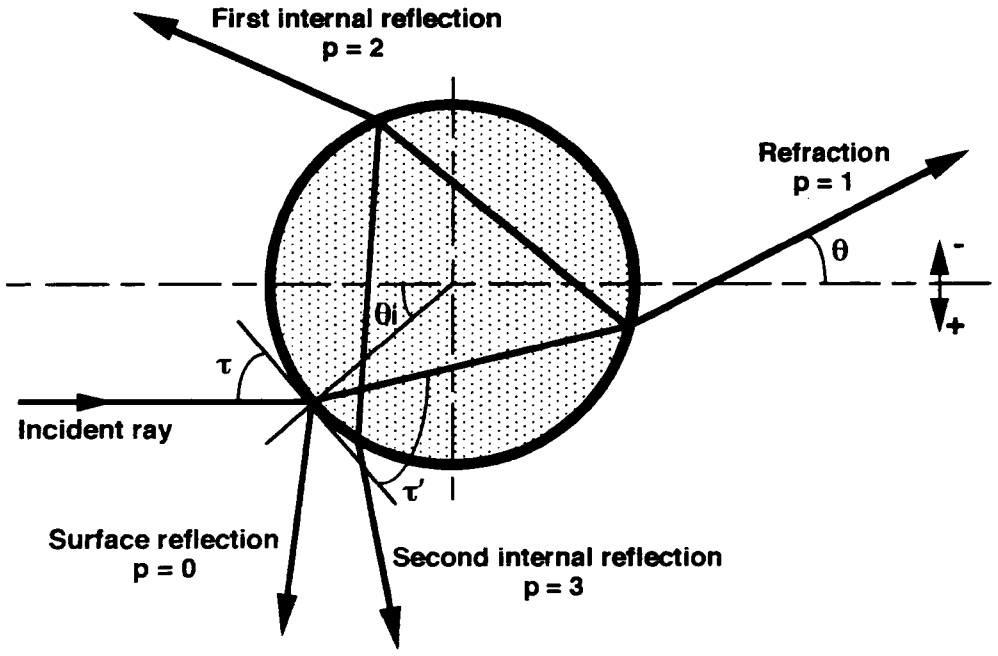


FIGURE 2.1 Ray tracing through a spherical particle showing the surface reflected, refracted, the first and second internal reflected rays.

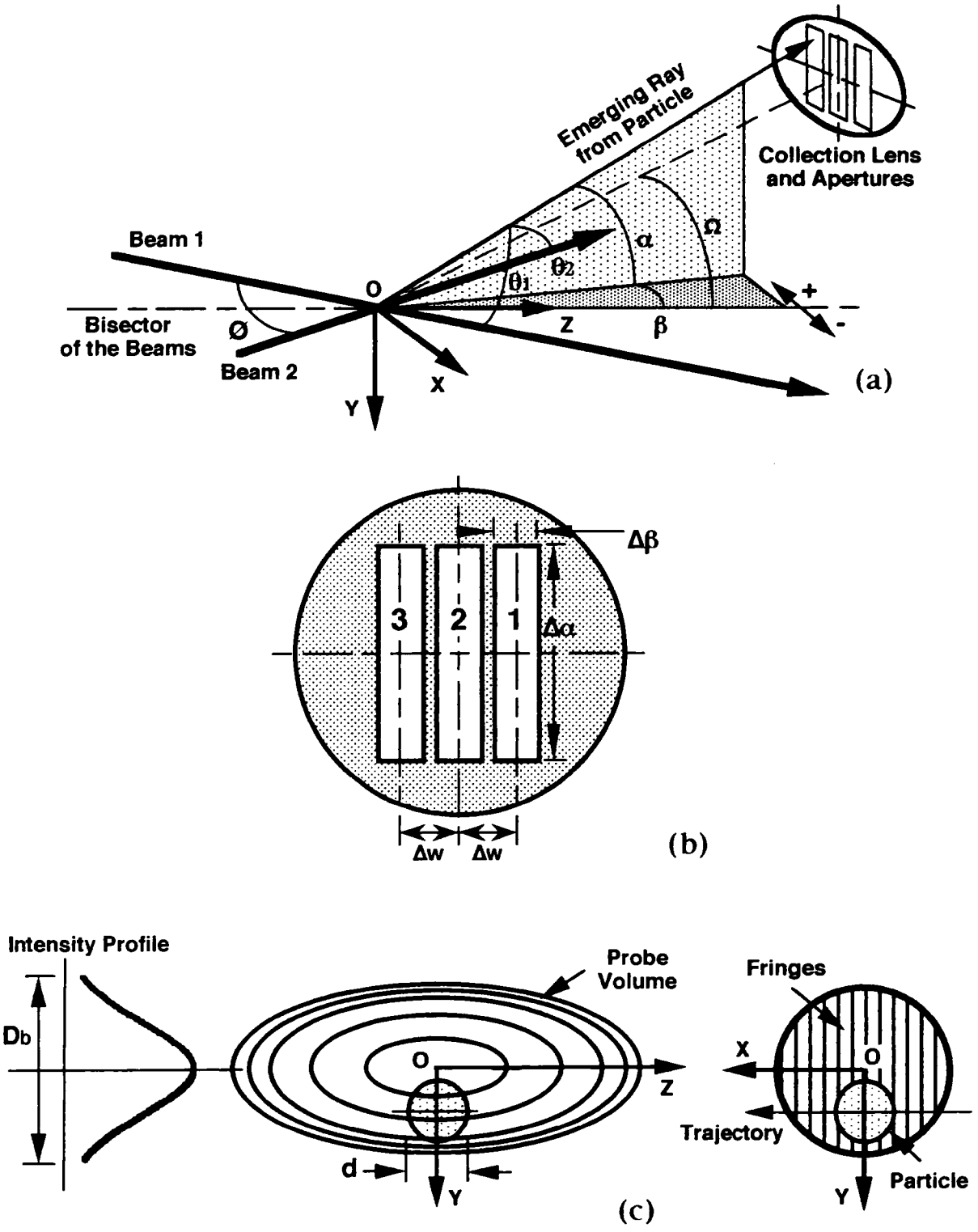


FIGURE 2.2 (a) Geometry and co-ordinate system of the phase-Doppler anemometer. (b) Arrangement of the collection apertures. (c) Particle in the probe volume with Gaussian intensity profile.

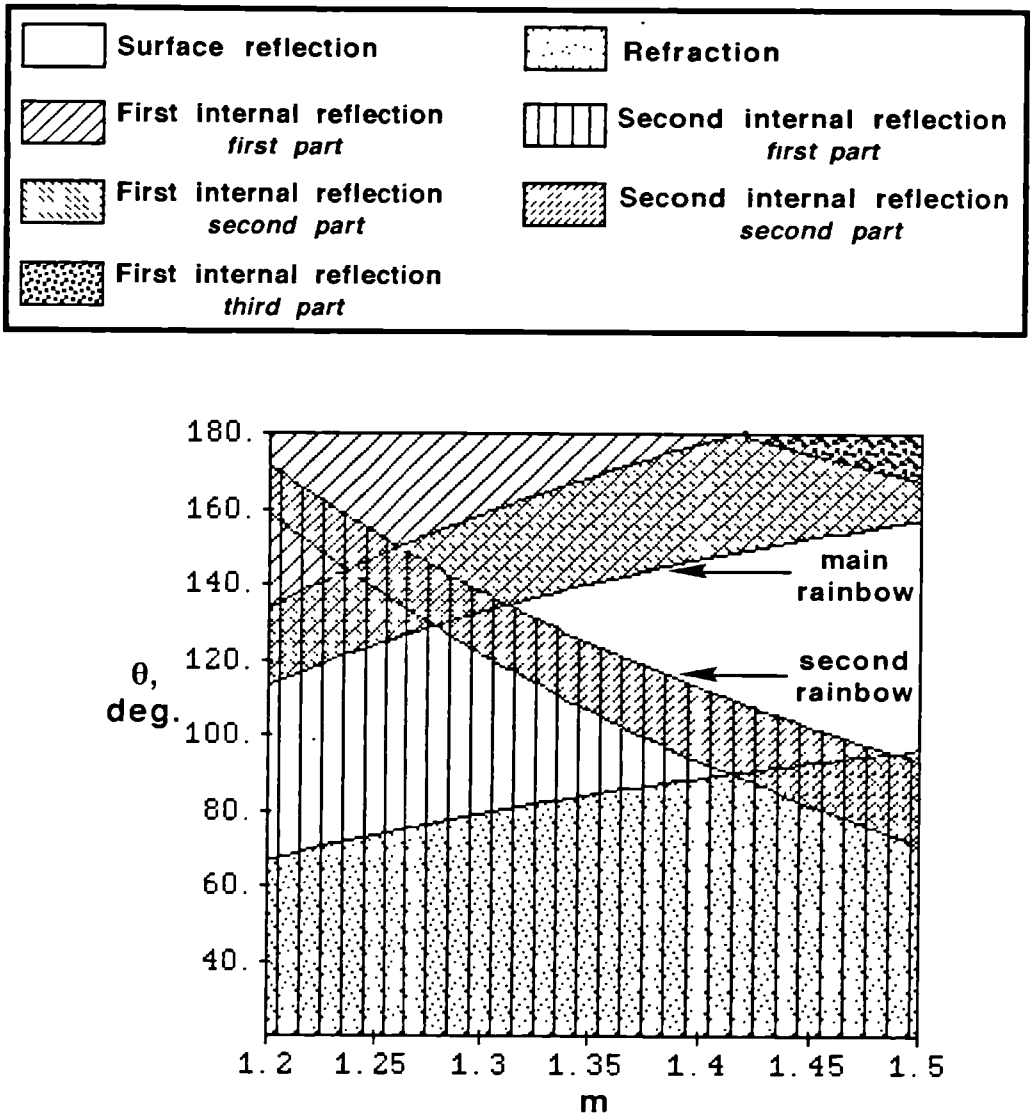


FIGURE 2.3 Scattering angles of the forward-, side- and back-scattered light as a function of refractive index of the particle.

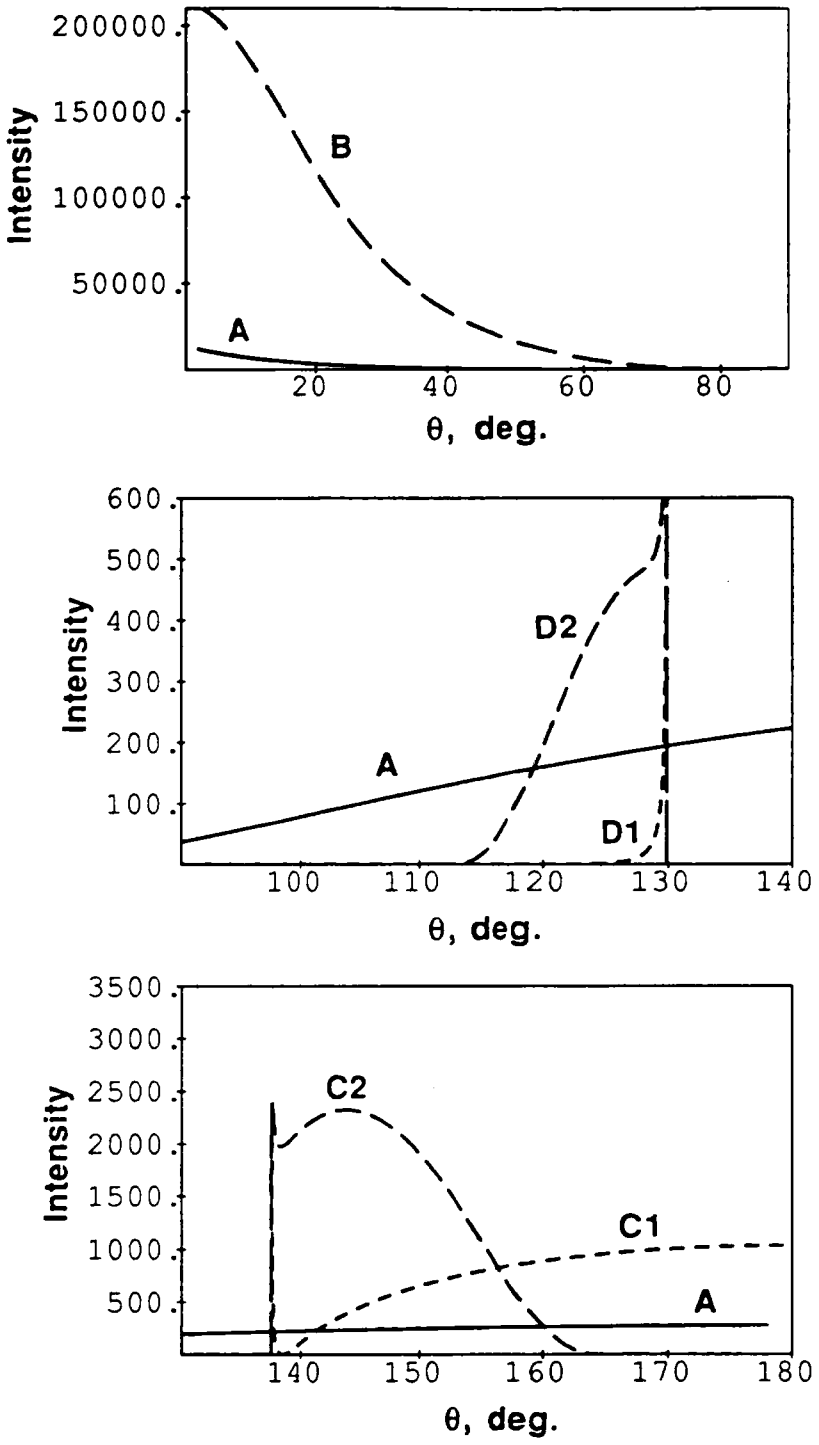


FIGURE 2.4 Intensity of the forward-, side- and back-scattered light for particle refractive index of 1.33. (A) surface reflection; (B) refraction; (C1) the first, (C2) second and (C3) third parts of the first internal reflection, in short FIR; (D1) the first and (D2) second parts of the second internal reflection, in short SIR.

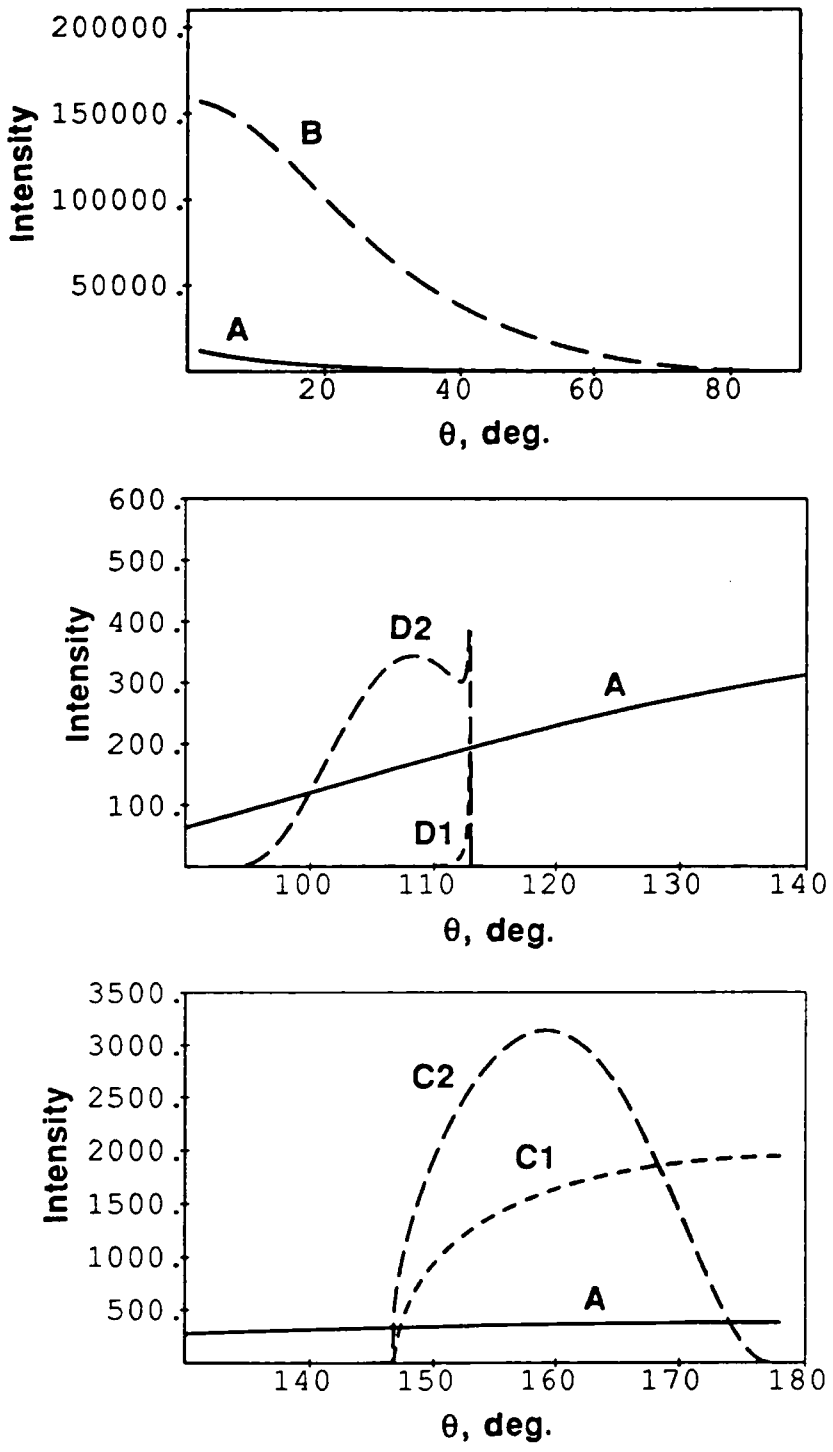


FIGURE 2.5 Intensity of the forward-, side- and back-scattered light for particle refractive index of 1.4.
(see Figure 2.4 for legend)

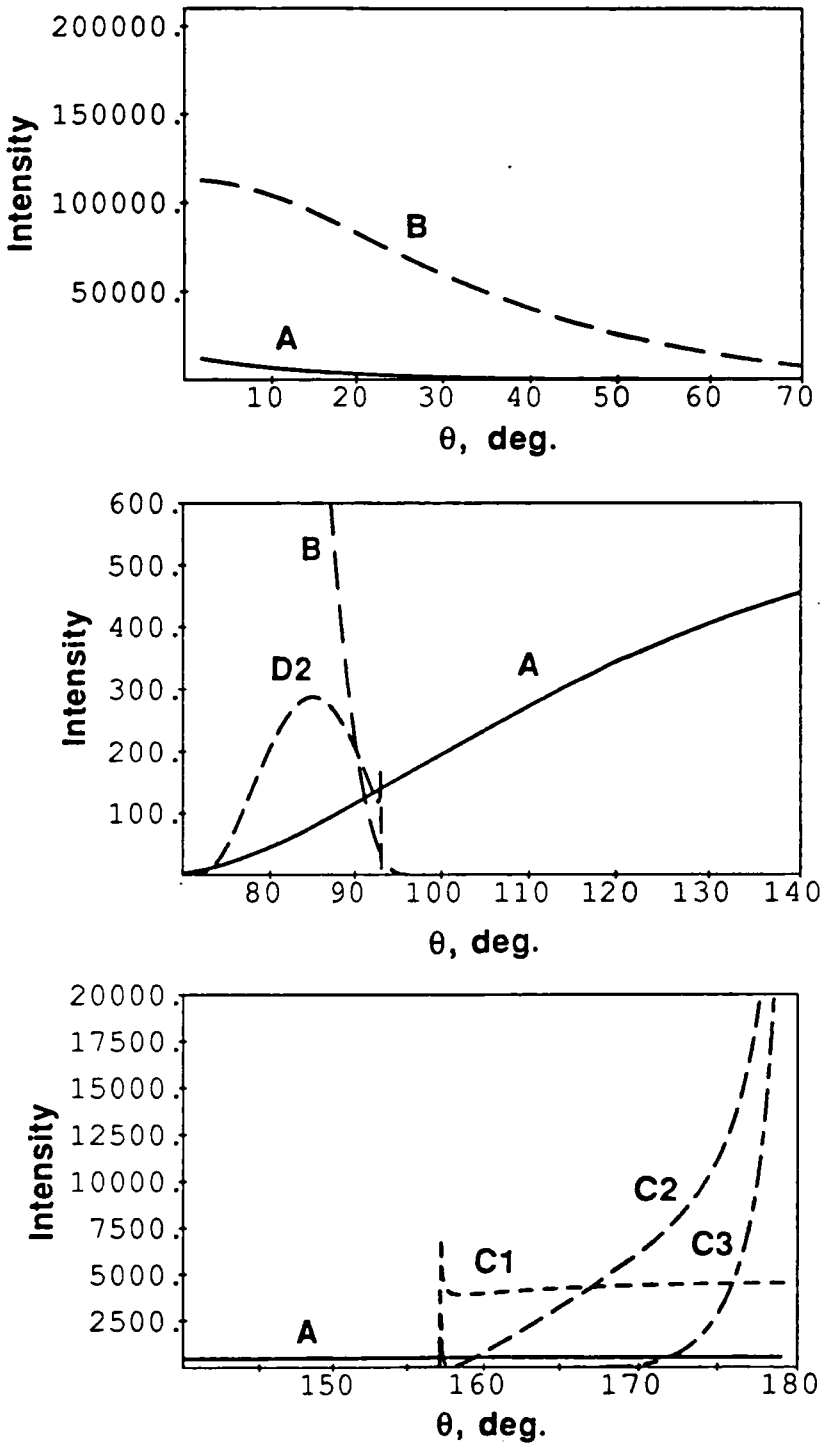
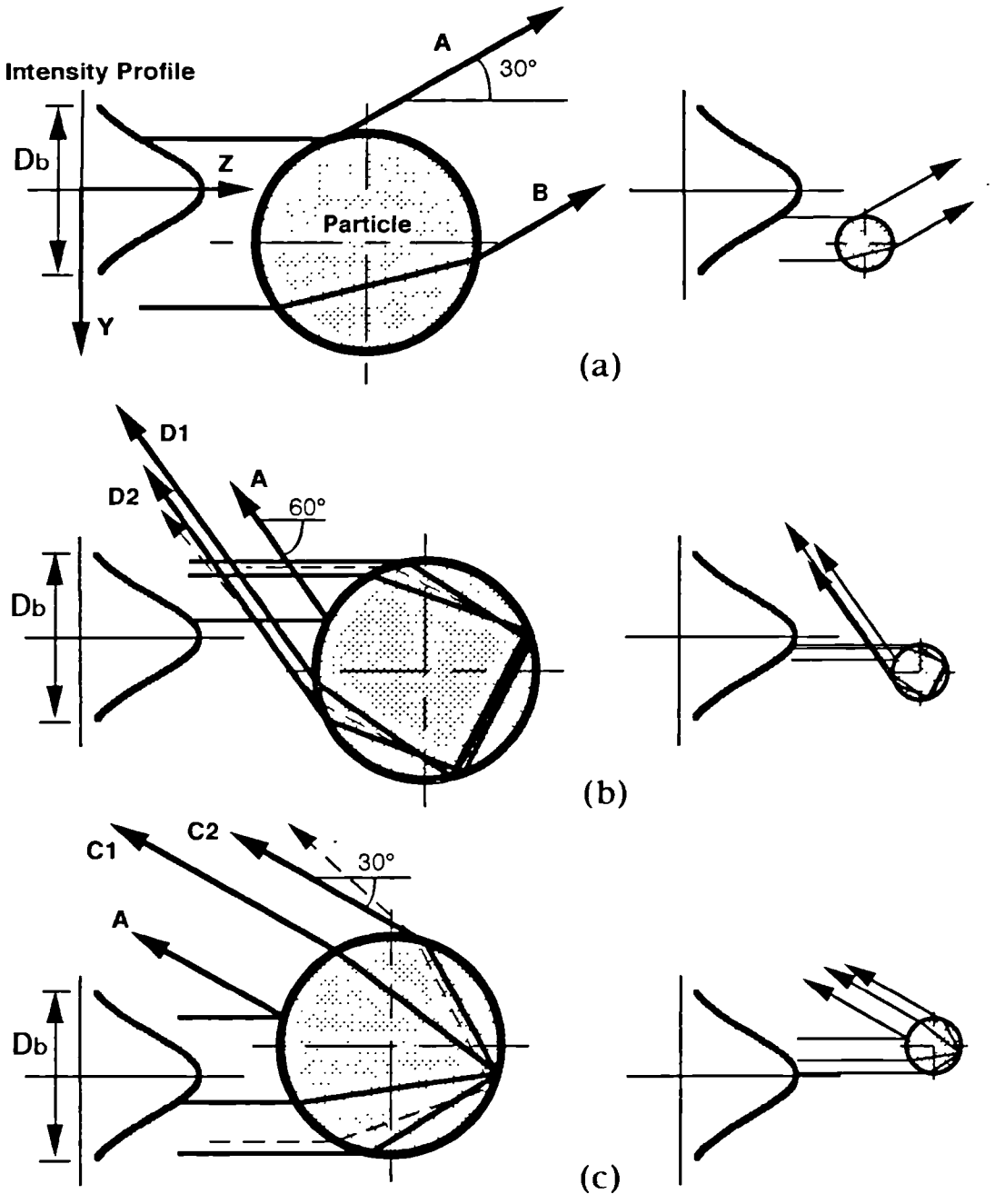


FIGURE 2.6 Intensity of the forward-, side- and back-scattered light for particle refractive index of 1.5.
(see Figure 2.4 for legend)



A: Surface reflection
C1: First internal reflection, *first part*
C2: First internal reflection, *second part*
— — — Ray of the rainbow

B: Refraction
D1: Second internal reflection, *first part*
D2: Second internal reflection, *second part*

FIGURE 2.7 Diagram of the incident and emerging rays of (a) forward-scattered light at $\theta = 30°$, (b) side-scattered light at $\theta = 120°$ and (c) back-scattered light at $\theta = 150°$, for particle refractive index of 1.33.

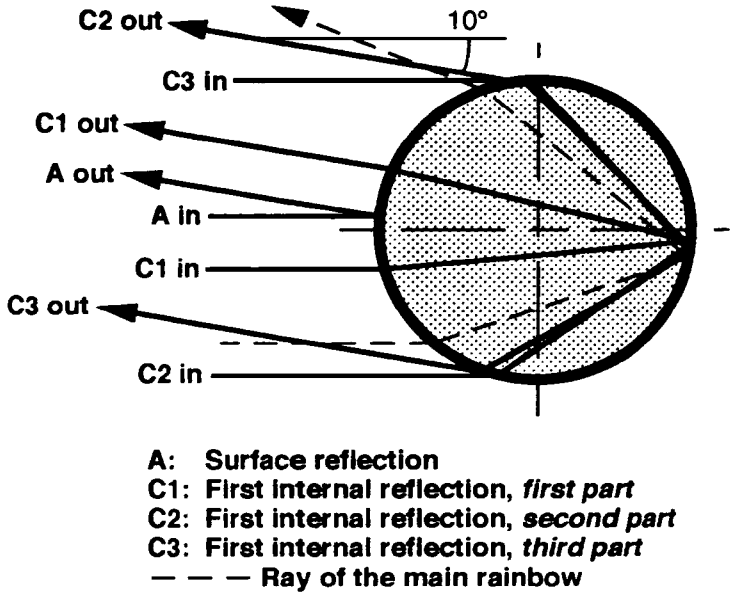


FIGURE 2.8 Diagram of the incident and emerging rays of the back-scattered light for particle refractive index of 1.5 at $\theta = 170°$.

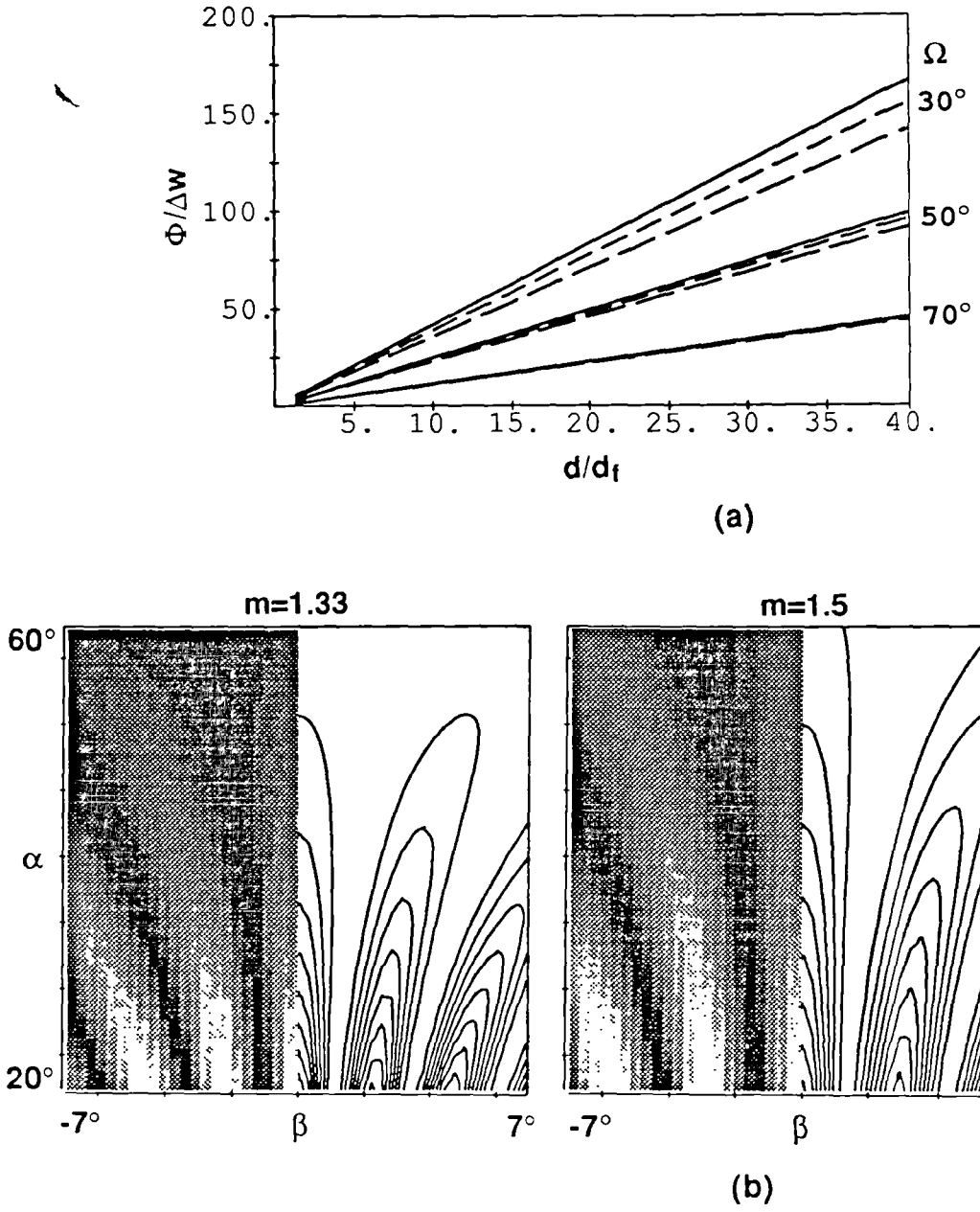


FIGURE 2.9 (a) Normalised response curves with refracted light. (m = 1.33 ———, 1.4 — — — and 1.5 — — —)
(b) Intensity distributions of the forward-scattered light, considering refraction only. (d/d_f = 11.02)

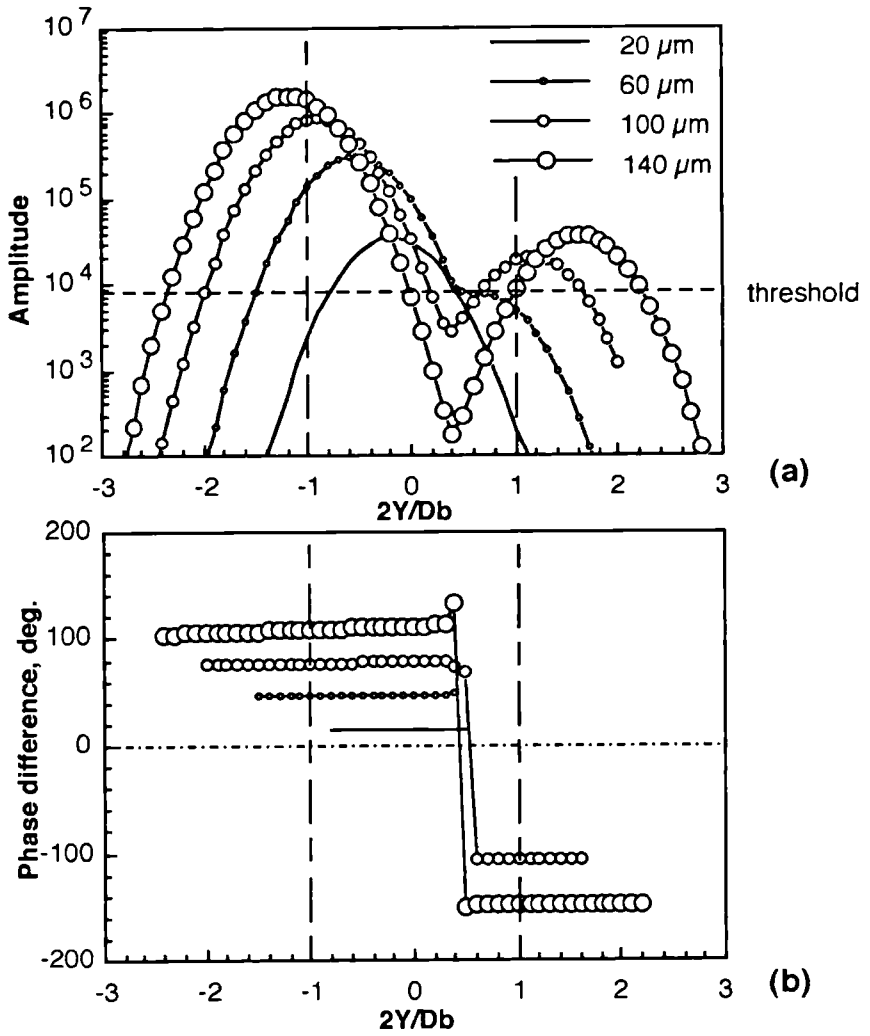


FIGURE 2.10 Variations of (a) amplitude of the modulation signal and (b) phase difference with particle trajectory at the off-axis light collection angle Ω = 30°. (threshold: the amplitude of a 10 μm particle)

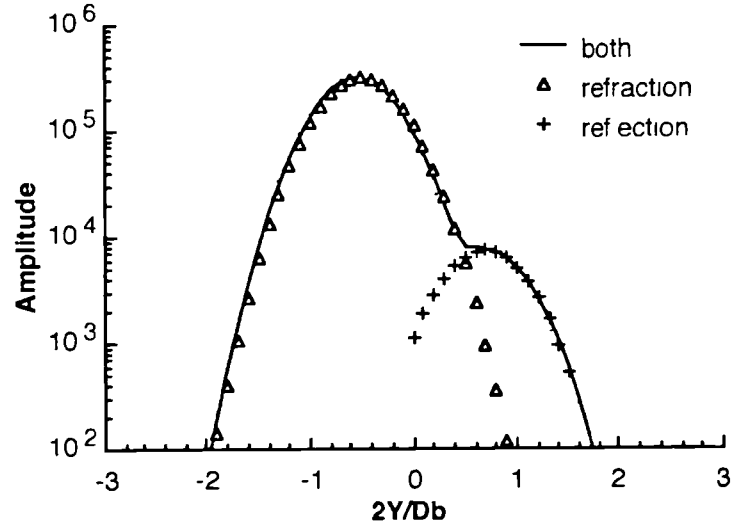
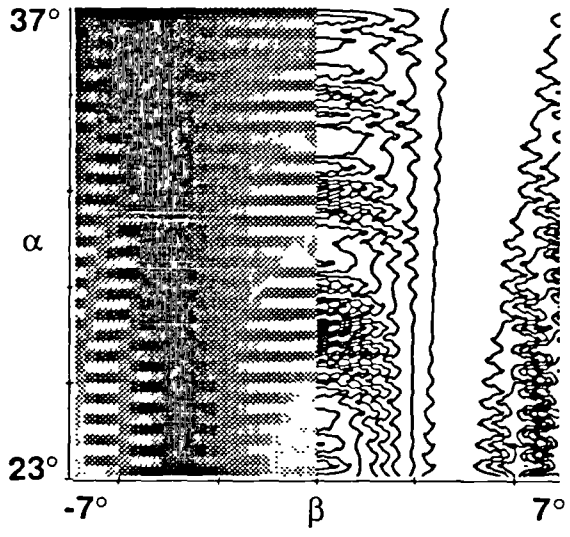
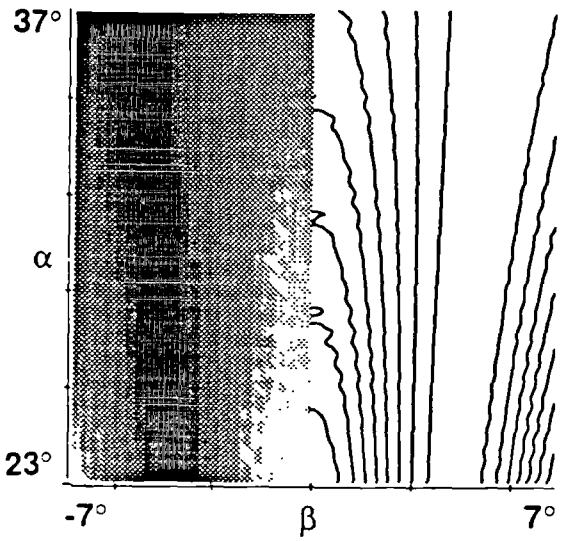


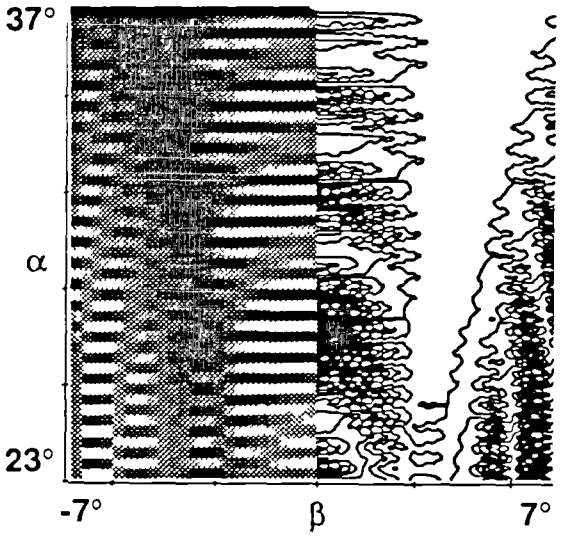
FIGURE 2.11 Amplitude profiles of the 60 μm particle of Figure 2.10, considering separately the intensities of refraction and reflection.



(a)



(b)



(c)

FIGURE 2.12 Intensity distributions of the forward-scattered light for a 60 μm particle illuminated by (a) uniform intensity and Gaussian intensity profiles at the trajectories of $2Y/D_b$ = (b) -0.5 and (c) 0.9, considering refraction and reflection.

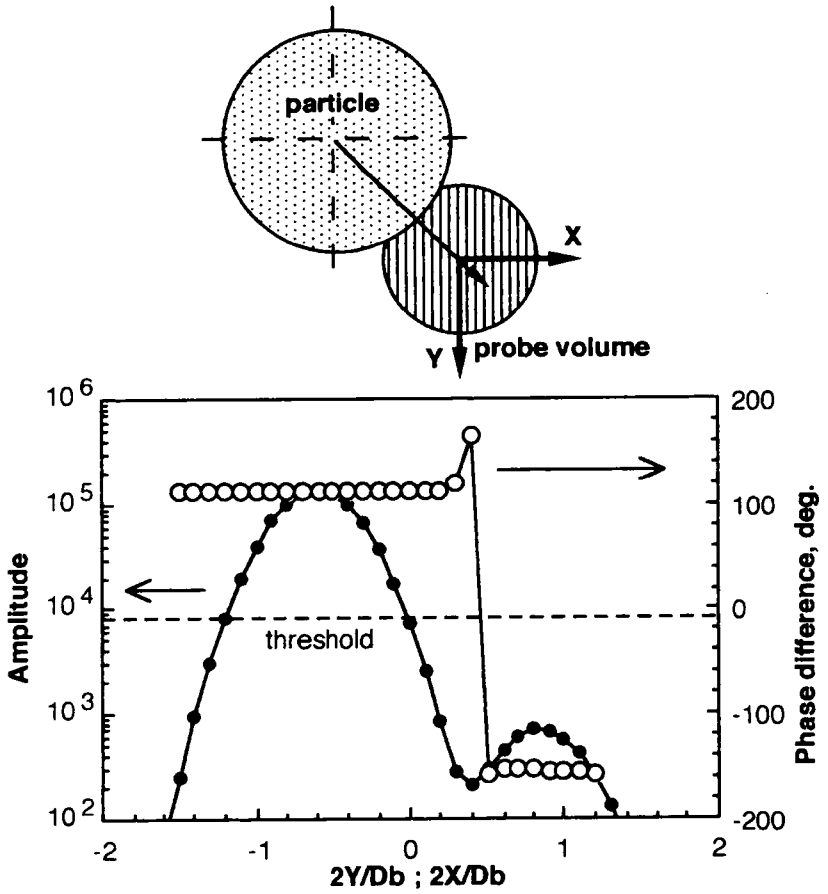


FIGURE 2.13 Variations of amplitude of the modulation signal and phase difference of a 140 μm particle along a trajectory inclined 45° to the fringes of the velocimeter, at the light collection angle Ω = 30°. (threshold: the amplitude of a 10 μm particle)

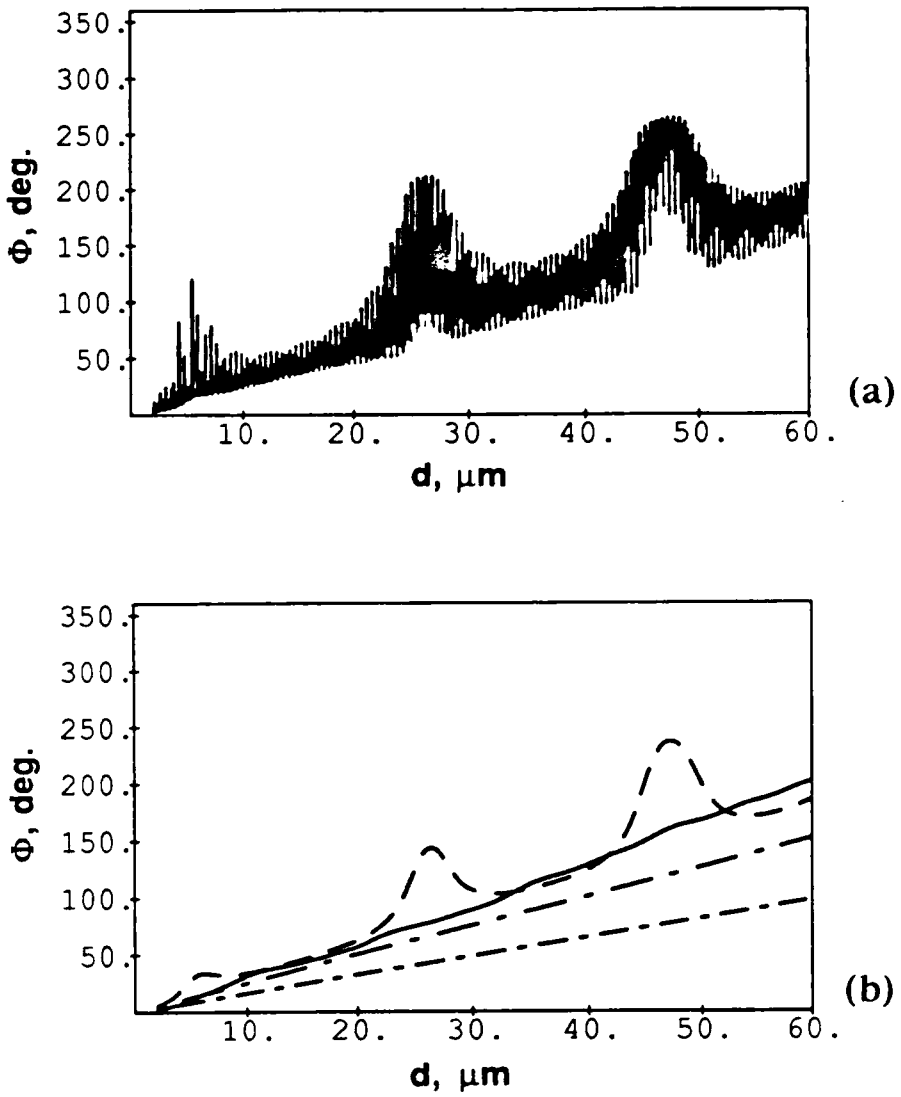


FIGURE 2.14 Response curves calculated between two points of (α, β) of (150°, 0°) and (150°, 2.5°), considering: (a) surface reflection and both parts of FIR; (b) the first part(— - —) and the second part(—— - ——) and both parts(— — —) of FIR and that after integration of light intensity over the apertures, centred at the same points(———).

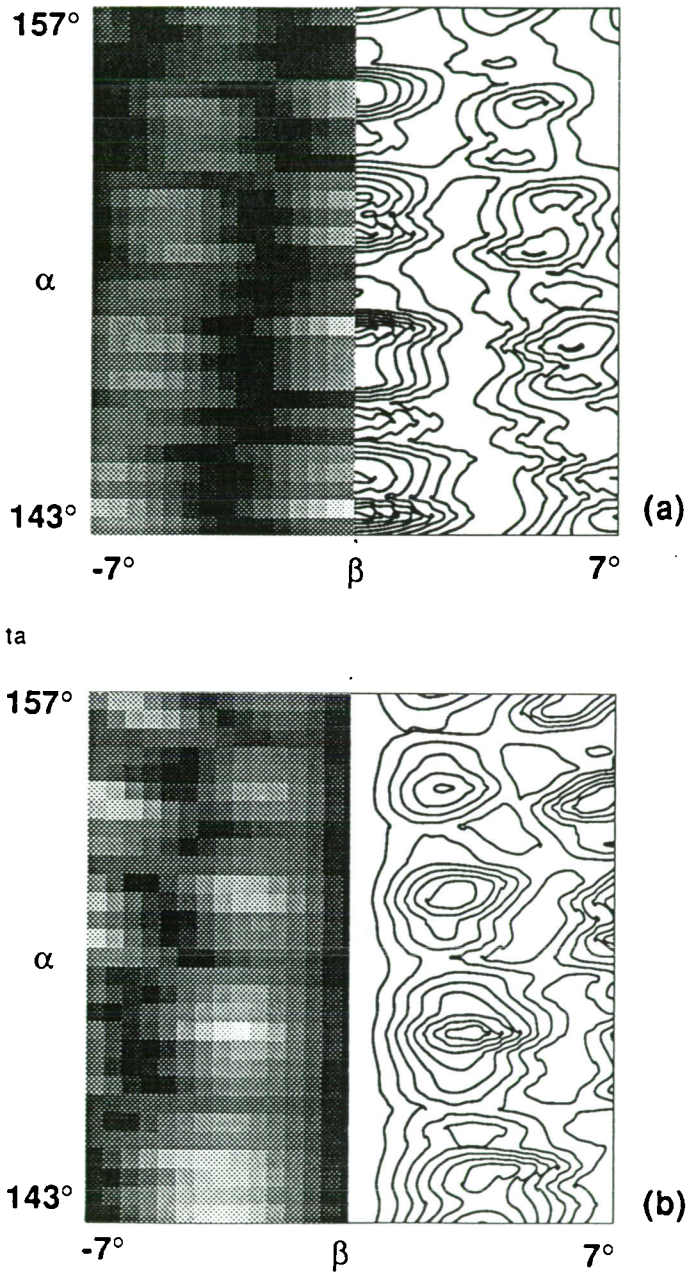


FIGURE 2.15 Intensity distributions of the back-scattered light of a 47 μm particle, considering surface reflection and both parts of FIR. Particle was aligned with (a) a bright fringe and (b) a dark fringe in the probe volume. (m = 1.33; Ø = 10°)

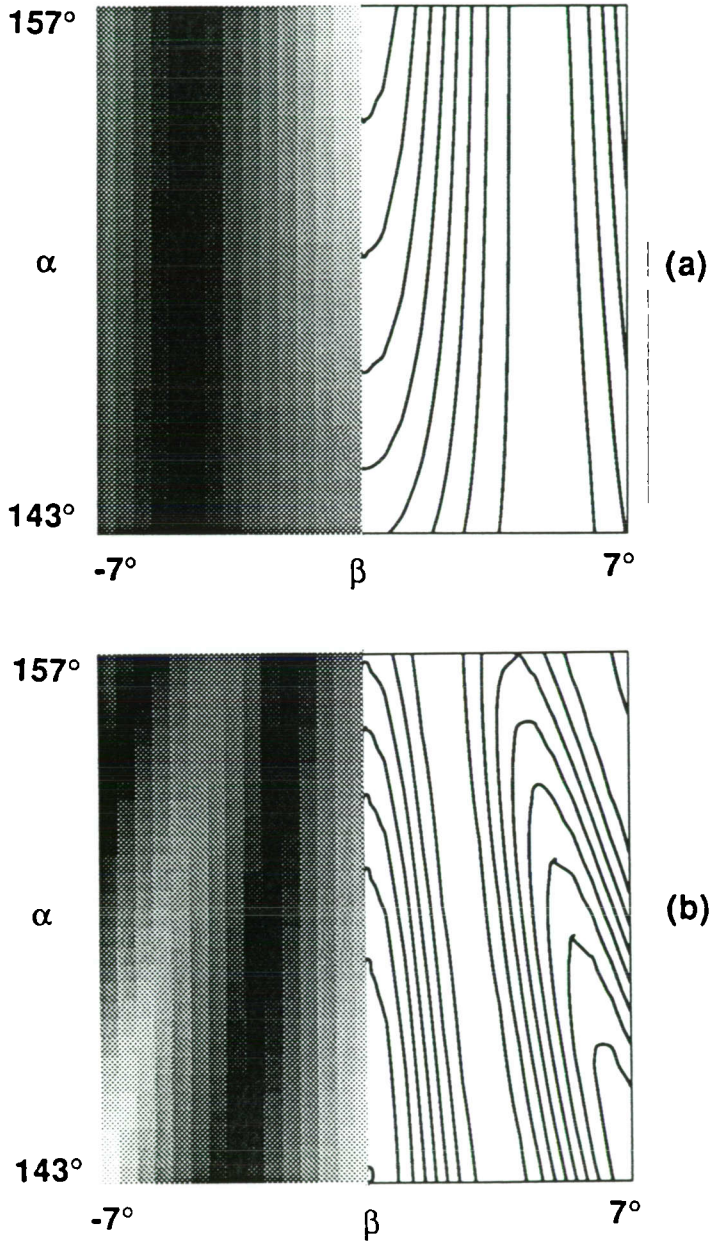
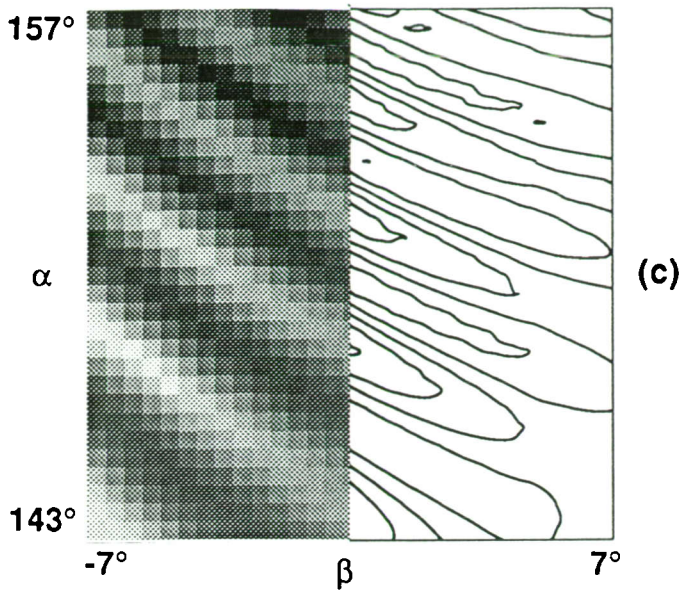


FIGURE 2.16 Intensity distributions of the back-scattered light of a 47 μm particle, considering the interference of (a) the first and (b) the second parts of FIR from both beams, (c) the first part of FIR from beam 1 and the second part from beam 2 and (d) the first part of FIR from beam 2 and the second part from beam 1.



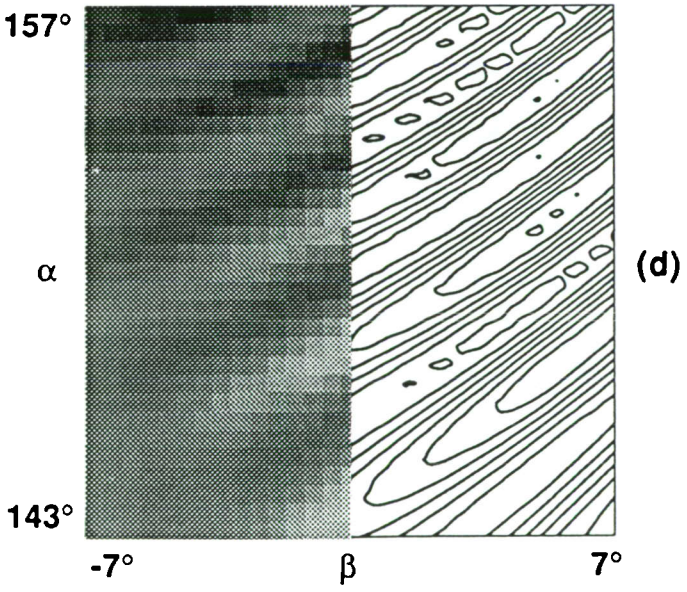


FIGURE 2.16 Continued.

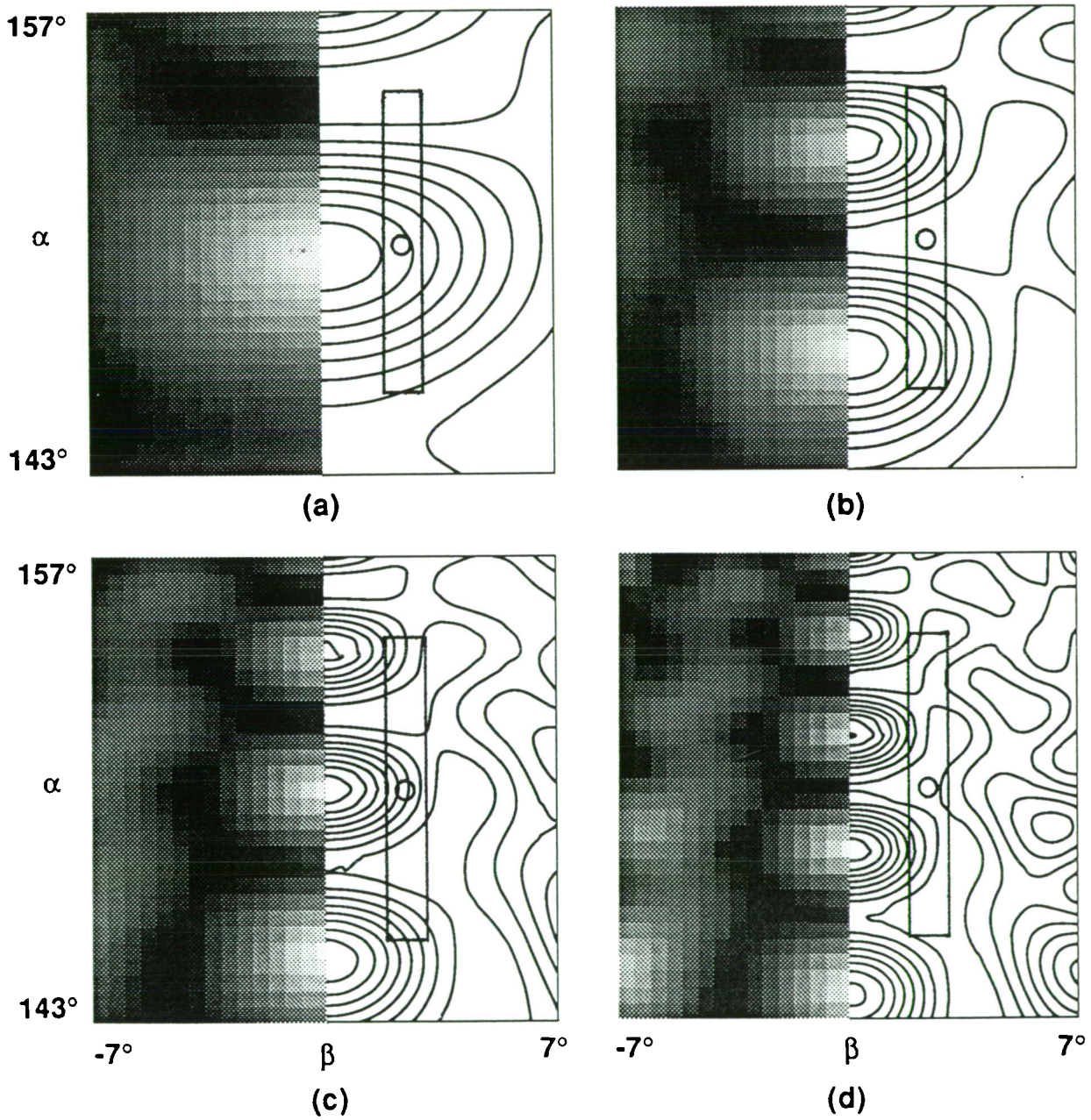


FIGURE 2.17 Intensity distributions of the back-scattered light considering both parts of FIR, for particle diameters of (a) 16, (b) 26, (c) 36 and (d) 47 μm. The rectangle shows the aperture, and the circle is its centre where the point calculation in Figure 2.14 was performed.

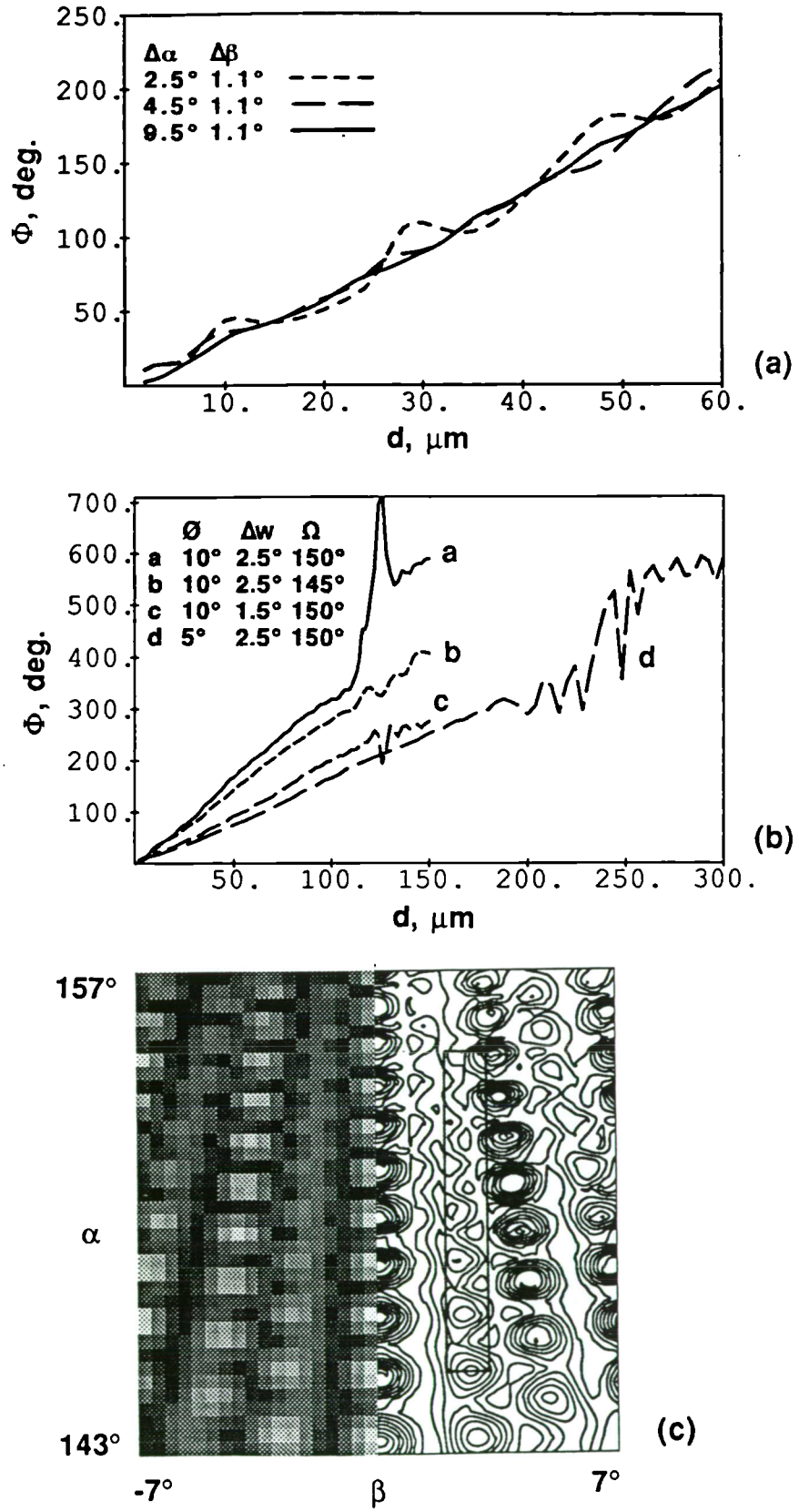


FIGURE 2.18 (a) Effect of size of collection aperture on the response curve with the back scattered light. (Ω = 150°; Δw = 2.5°; Ø = 10°) (b) Effect of optical geometry on the response curve with the back scattered light. ($\Delta\alpha$ = 9.5°; $\Delta\beta$ = 1.1°) (c) Intensity distributions of the back-scattered light of a 120 μm particle, considering both parts of FIR.

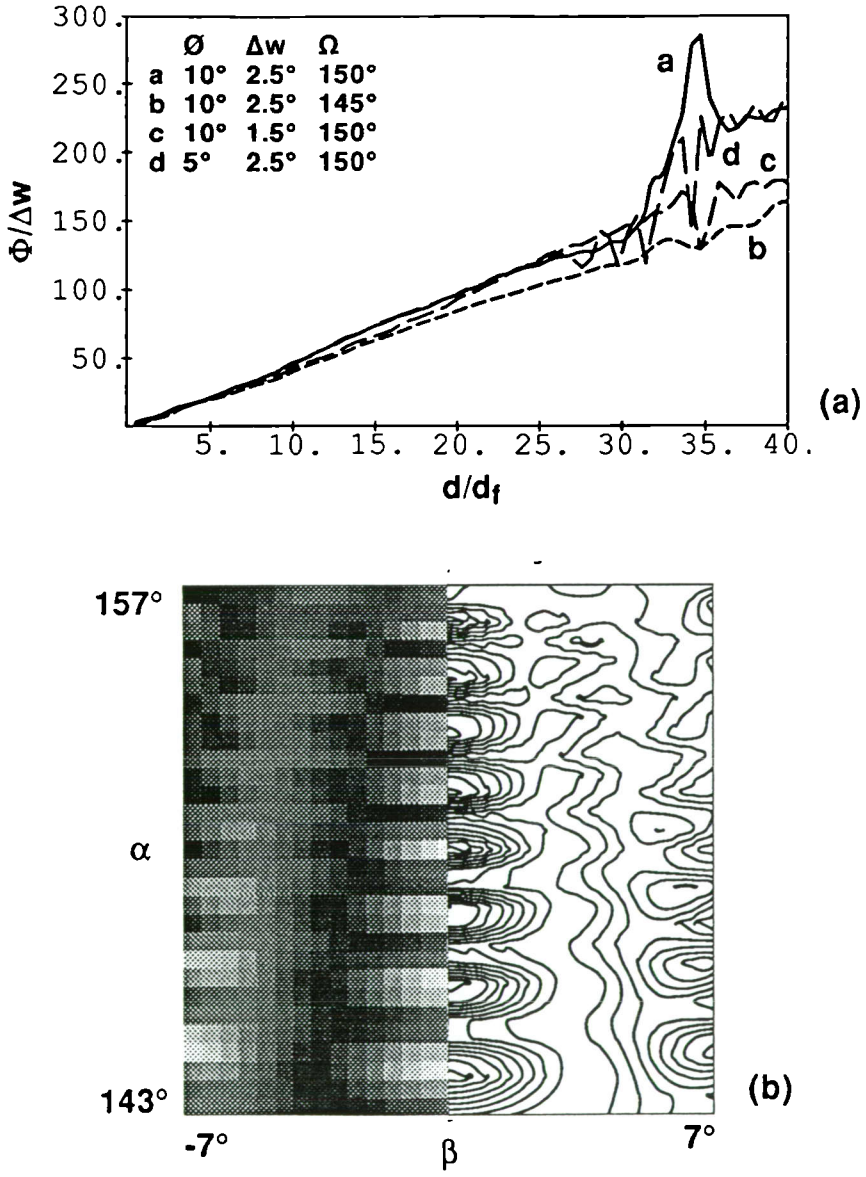


FIGURE 2.19 (a) Normalised response curves of Figure 2.18b.
(b) Intensity distributions of the back-scattered light of a 94 μm particle, considering both parts of the FIR. (m = 1.33; Ø = 5°)

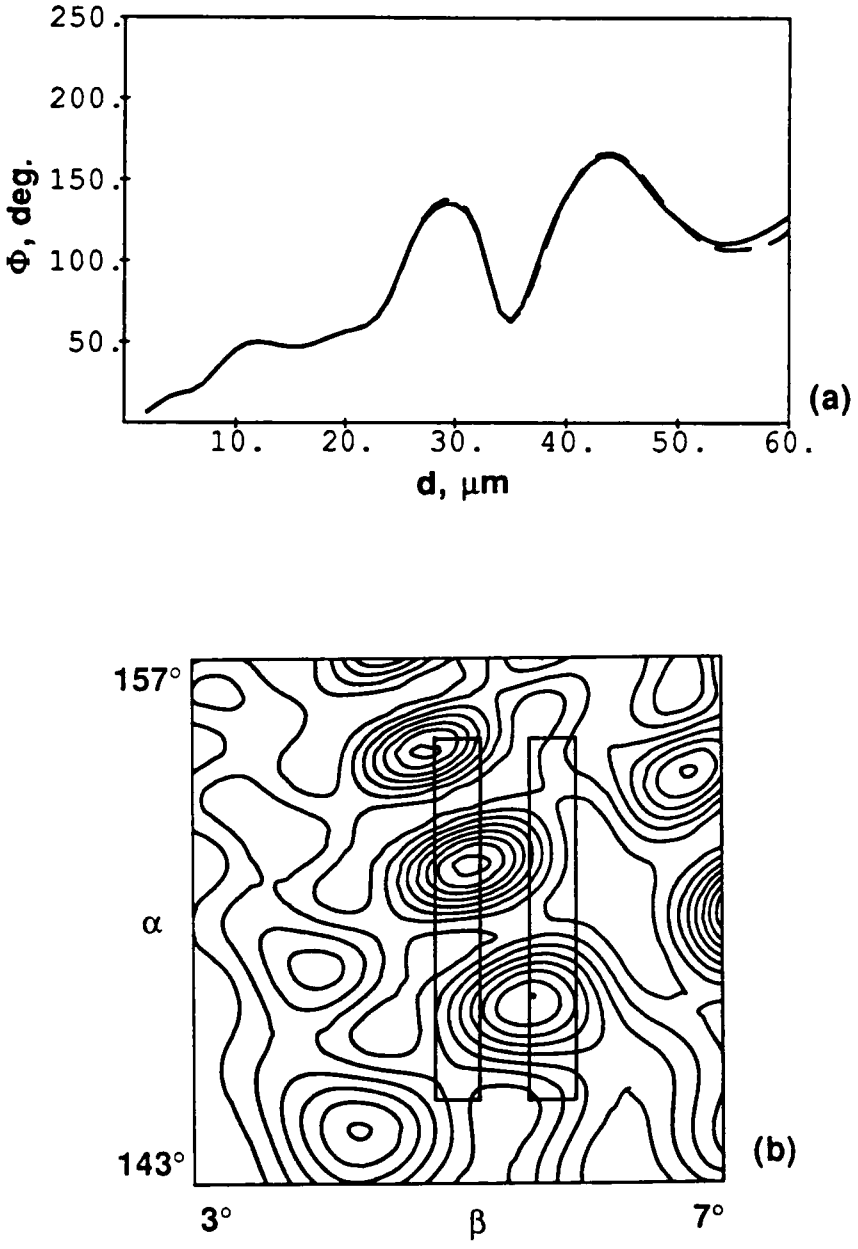


FIGURE 2.20 (a) Response curves for apertures 1 and 2 centred at (α, β) of (150°, 10°) and (150°, 12.5°) with the dimension of the apertures Δα x Δβ of 9.5° x 1.1°(———) and 9.5° x 2.2°(— — —). (b) Intensity distributions of the back-scattered light of a 47 μm particle, considering both parts of FIR.

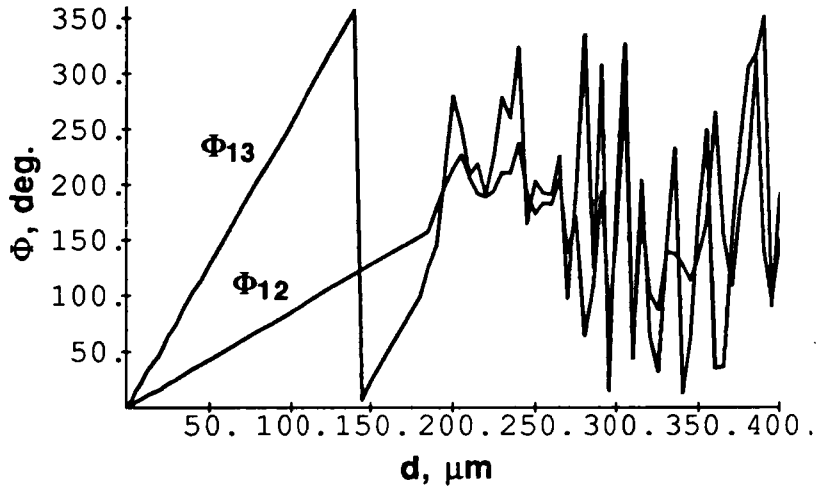


FIGURE 2.21 Response curves for a three-photomultiplier phase-Doppler system calculated for particle refractive index of 1.33 and off-axis collection angle of 150°, with the three collection apertures (dimension 9.5°x2.2°) centred at β_1=-3.75°, β_2=-1.25° and β_3=3.75° and α=150°. Calculation was based on beam intersection angle Ø=2.92° and wavelength of λ=632.8 nm.

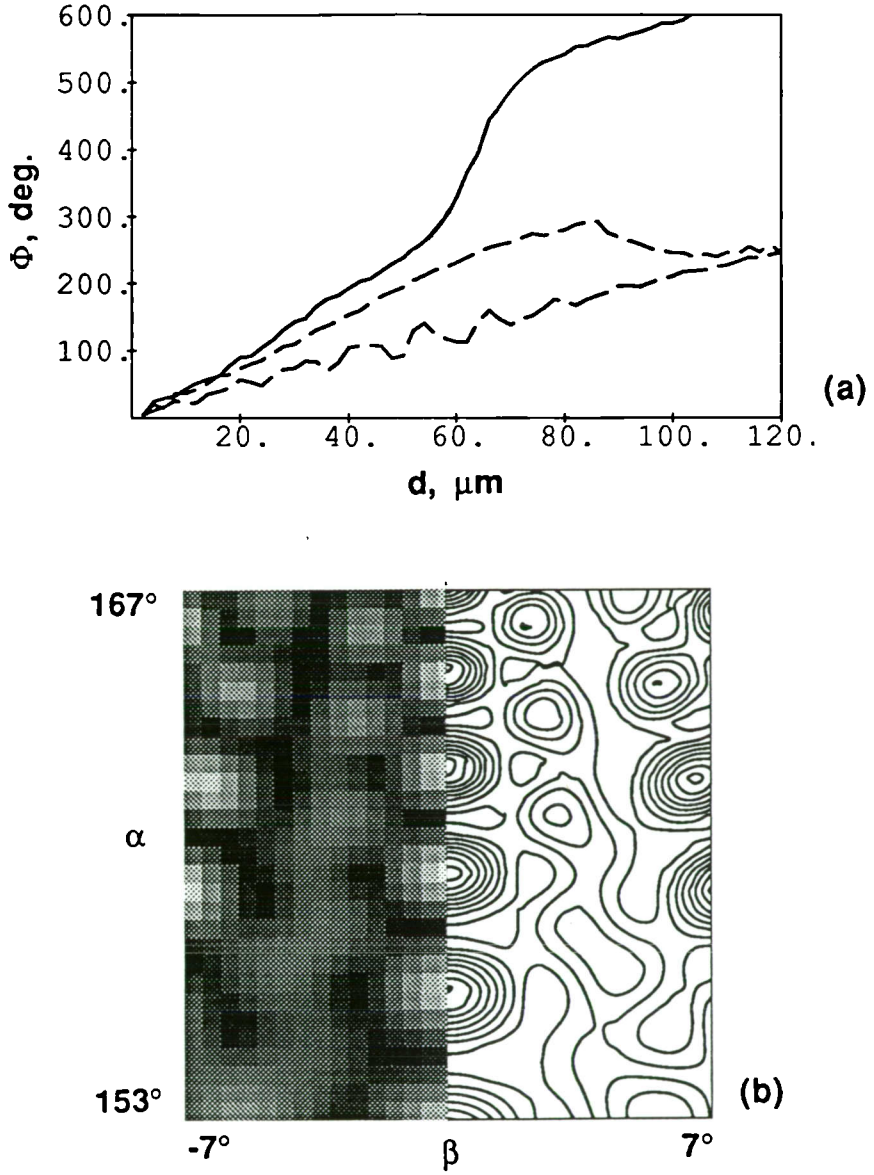


FIGURE 2.22 (a) Response curves for particle refractive index m = 1.4 and off-axis angle Ω = 160°(———) and 155°(— — —), and for m = 1.33 and Ω = 160°(—— ——).
(b) Intensity distributions of the back-scattered light of a 47 μm particle, considering both parts of FIR. (m = 1.4; Ø = 10°)

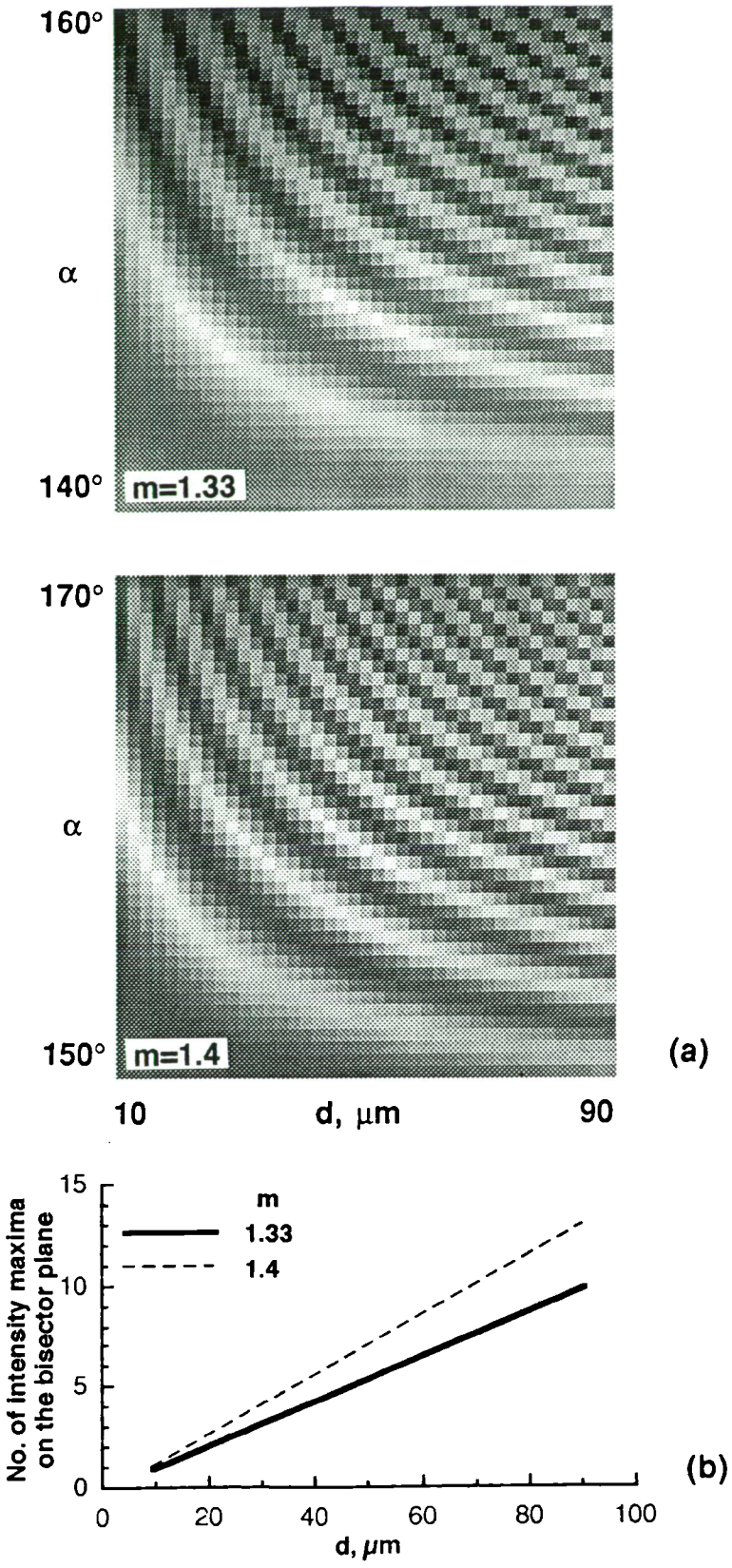


FIGURE 2.23 (a) Intensity distributions of the central fringes of the back-scattered light as a function of particle diameter.
(b) Number of intensity maxima of the central fringes of the back-scattered light over a range of scattering angle of 20°.

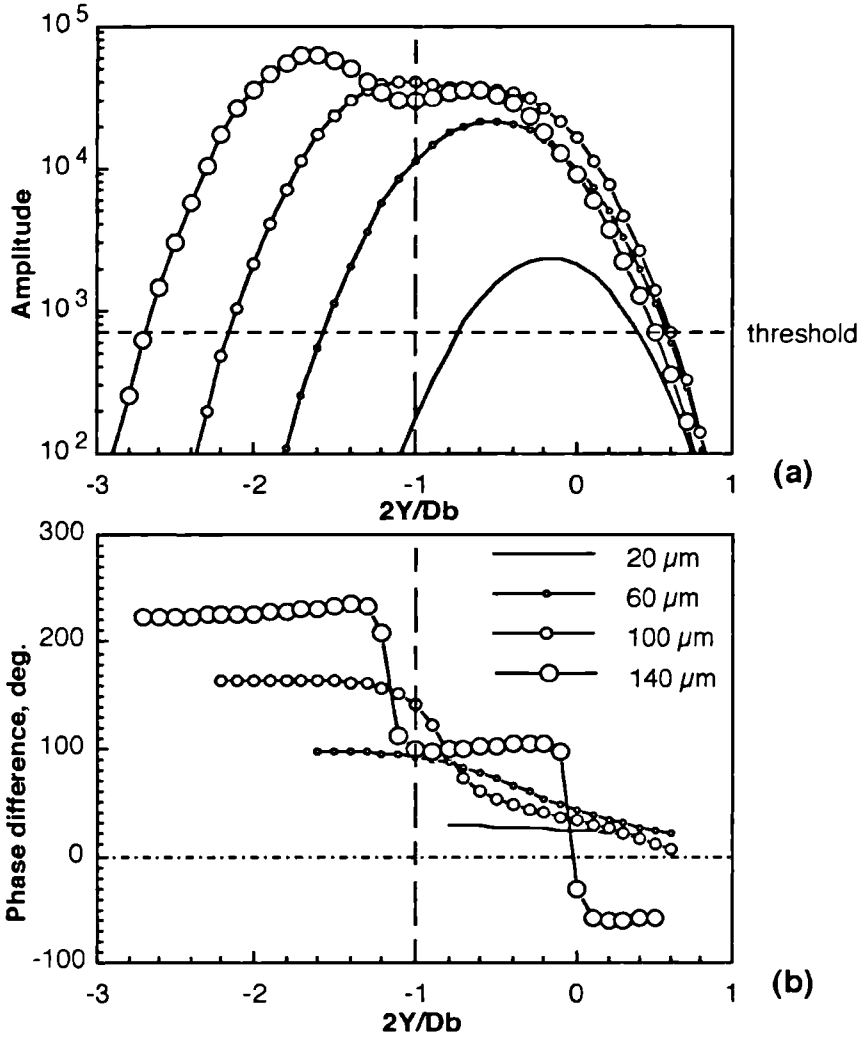


FIGURE 2.24 Variations of (a) amplitude of the modulation signal and (b) phase difference with particle trajectory at the off-axis light collection angle Ω = 160°. (threshold: the amplitude of a 10 μm particle)

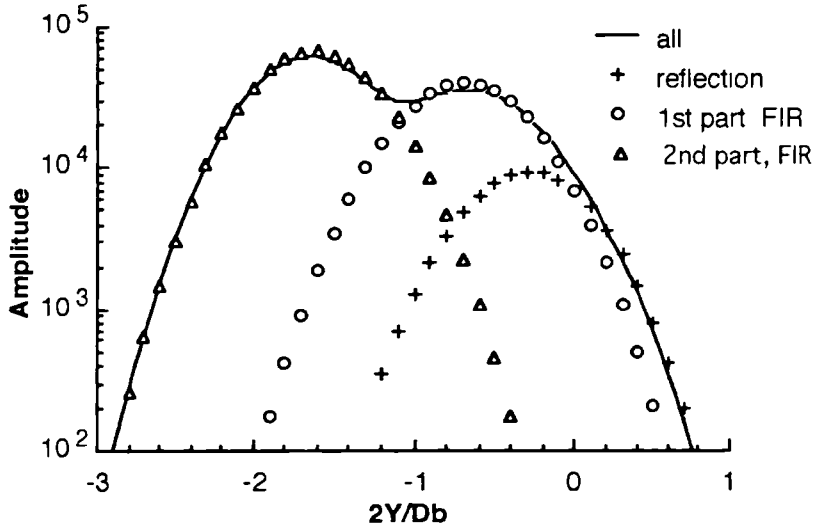


FIGURE 2.25 Amplitude profiles of the 140 μm particle of Figure 2.24a, considering separately the intensities of FIR and surface reflection.

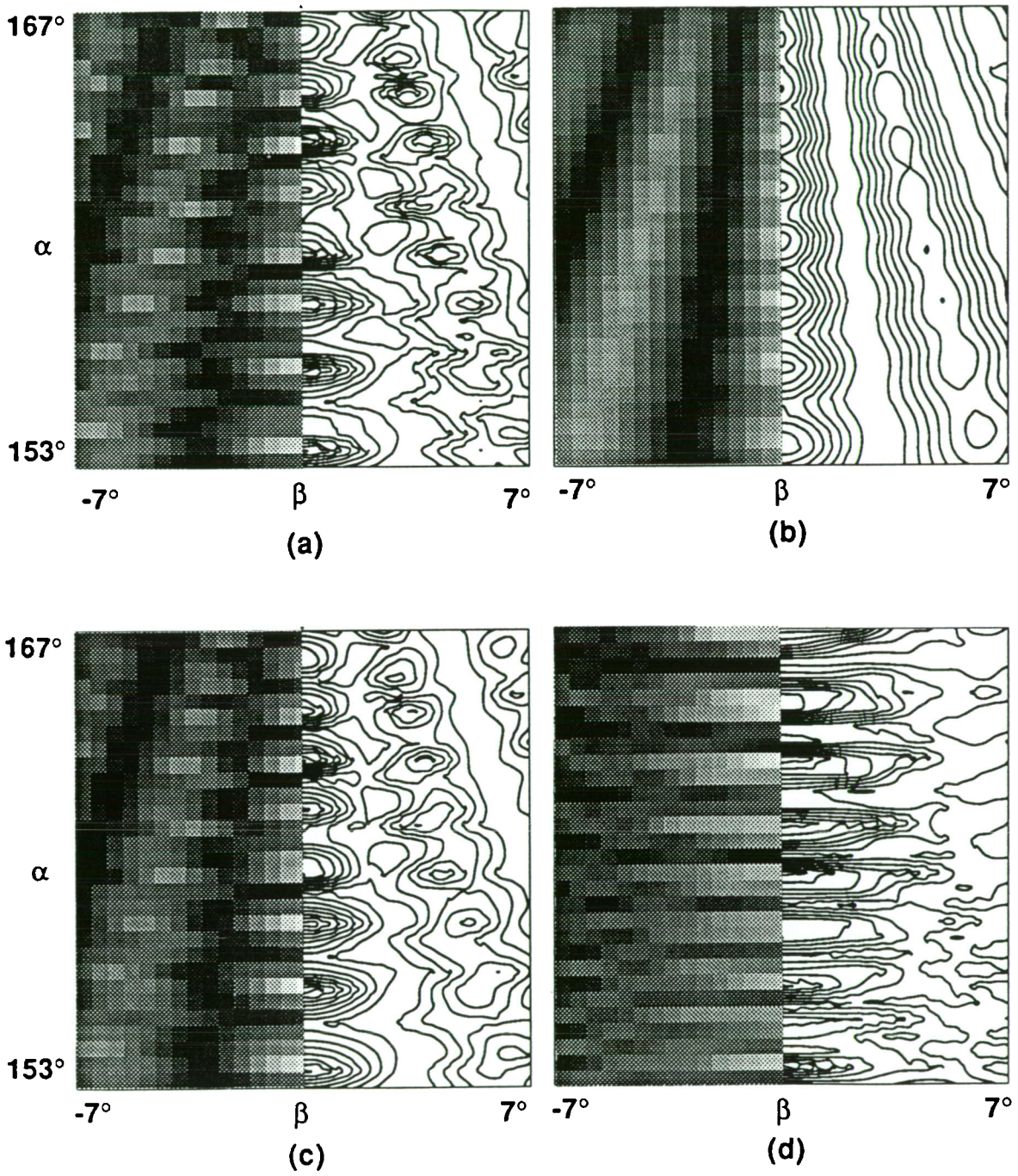


FIGURE 2.26 Intensity distributions of the back-scattered light of a 140 μm particle illuminated by (a) uniform intensity and Gaussian intensity profiles at the trajectories of $2Y/D_b$ = (b) -1.6, (c) -0.5 and (d) 0.5, considering FIR and surface reflection.

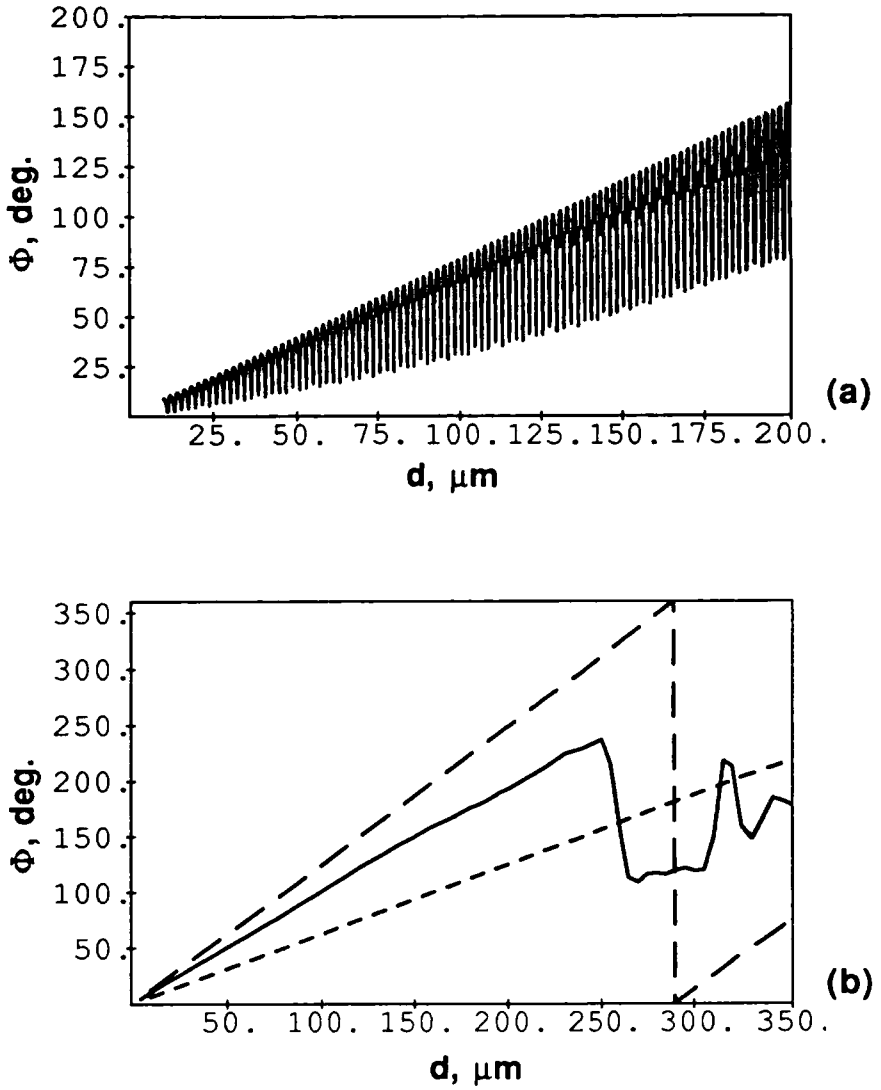


FIGURE 2.27 Response curves calculated between two points of (α, β) of (120°, 0°) and (120°, 2.5°), considering: (a) surface reflection and SIR; (b) surface reflection(— — —) and SIR(—— ——) and that after integration of intensity over the apertures centred at the same points(———).

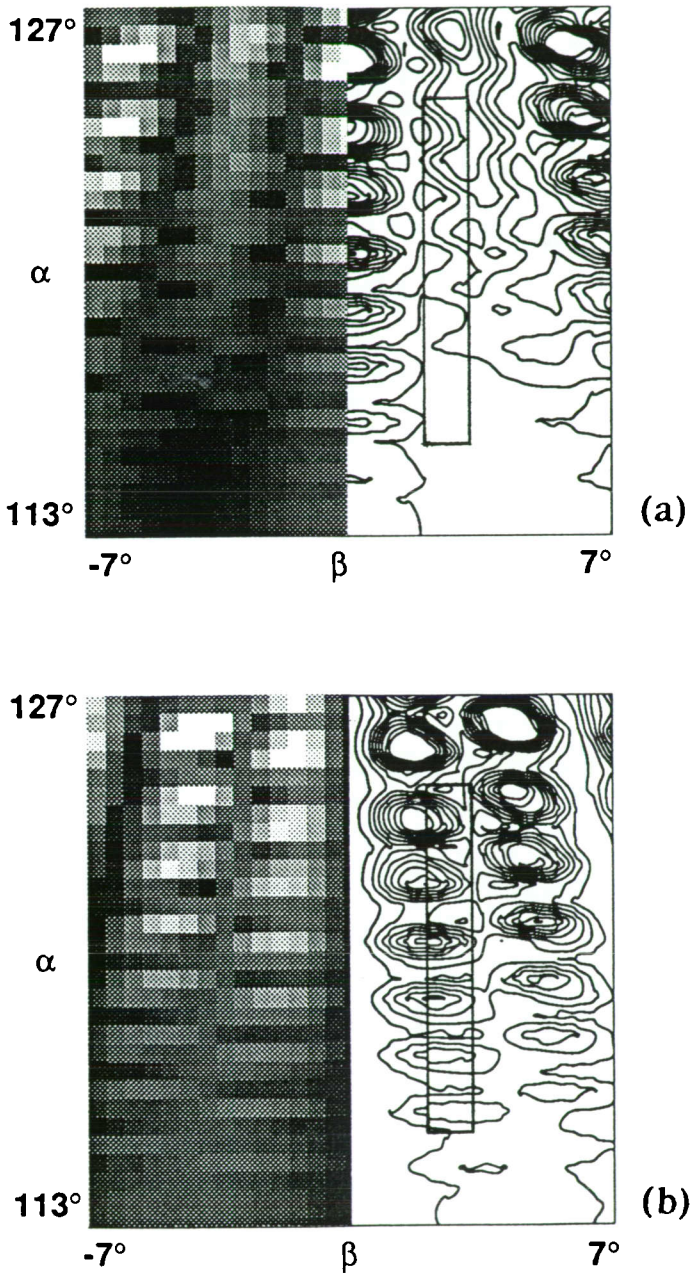


FIGURE 2.28 Intensity distributions of the side-scattered light of a 200 μm particle, considering surface reflection and SIR. Particle was aligned with (a) a bright fringe and (b) a dark fringe in the probe volume.

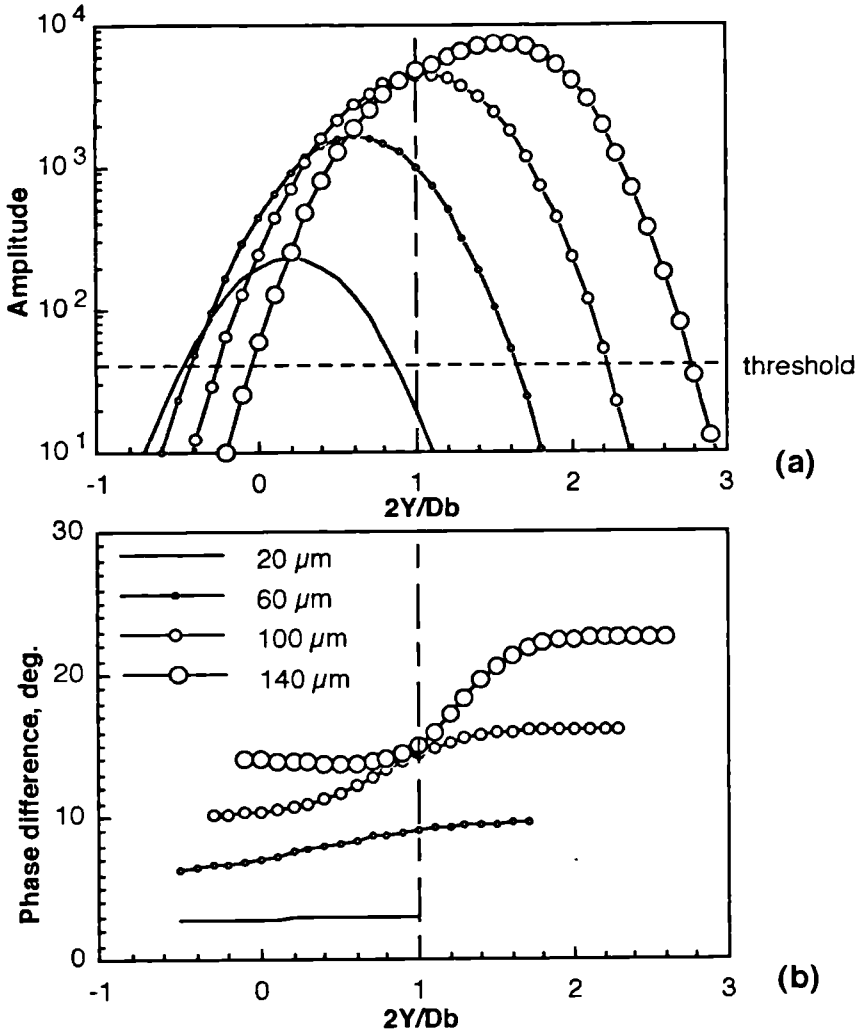


FIGURE 2.29 Variations of (a) amplitude of the modulation signals and (b) phase difference with particle trajectory at the off-axis light collection angle Ω = 104°. (threshold: the amplitude of a 10 μm particle)

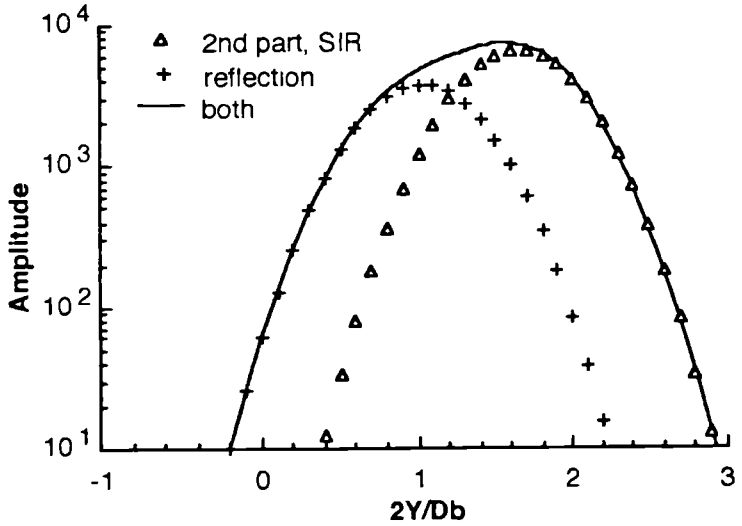


FIGURE 2.30 Amplitude profiles of the 140 μm particle in Figure 2.29a, considering separately the intensity of SIR and surface reflection.

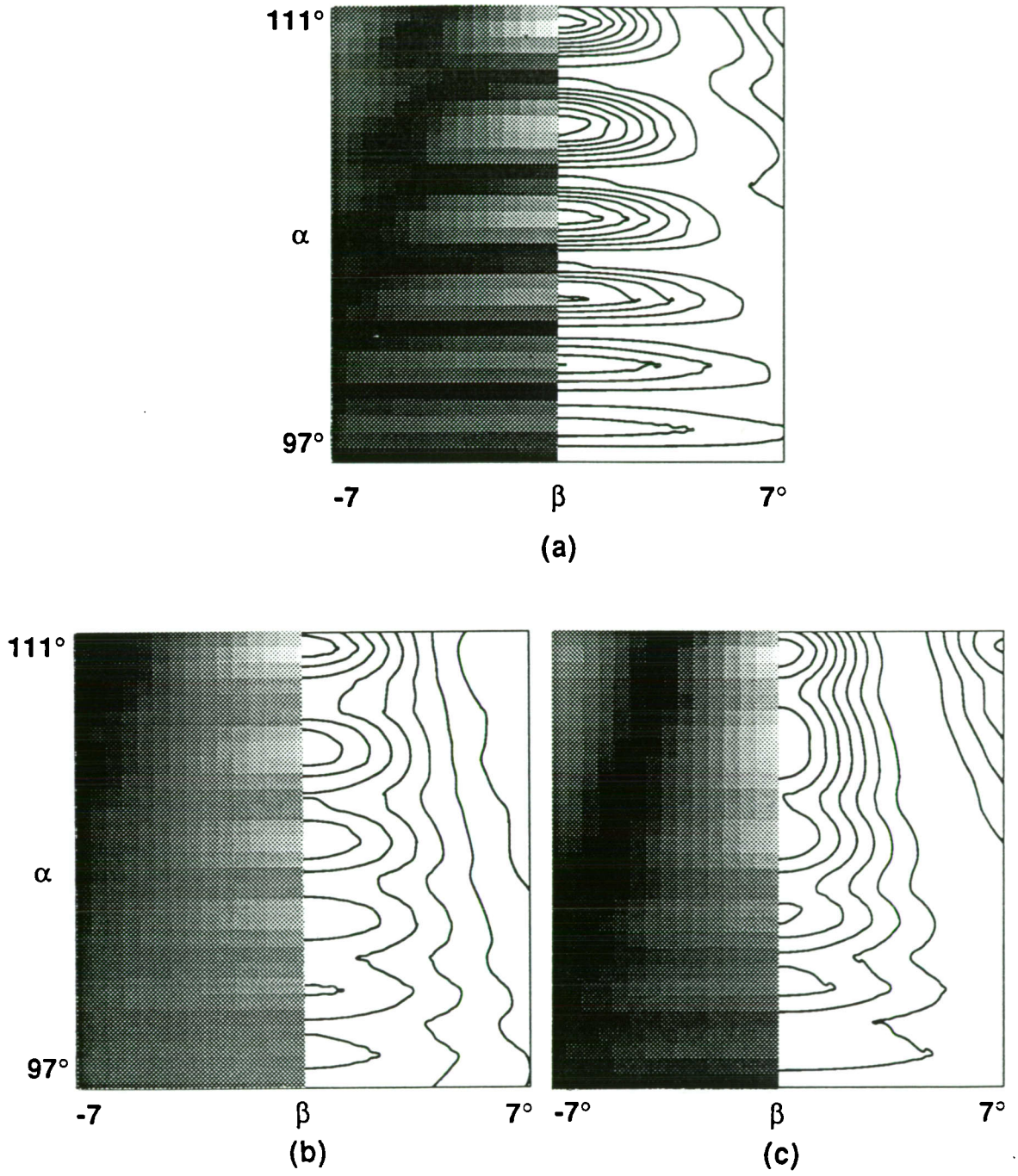


FIGURE 2.31 Intensity distributions of the side-scattered light of a 140 μm particle illuminated by (a) uniform intensity and Gaussian intensity profiles at the trajectories of $2Y/D_b$ = (b) 0.2 and (c) 2.2.

CHAPTER 3

Flow Characteristics of a Centrifugal Pump

3.1 INTRODUCTION

Centrifugal pumps are usually designed with fixed geometry and the performance is optimum at one operating condition, but a range of operating conditions may be required. The flows within rotors have attracted the interest of researchers for many years, but the complexities of rotating and stationary components and irregular geometries have implied measurement difficulties, so that investigations have been based largely on flow visualisation and wall pressure measurements (Acosta, 1954; Fischer and Thoma, 1954; Bowerman and Acosta, 1957; Senoo, Yamaguchi and Nishi, 1968; Lennemann and Howard 1970). Local velocities inside pump rotors have been reported, for example, by Binder and Knapp (1958), Howard and Lennemann (1971), Howard and Kittmer (1975) and Murakami, Kikuyama and Asakura (1980), but their results have not resolved the complex three-dimensional flow fields, and the accuracy and range of applicability has been limited by the intrusive nature of the probes. Efforts to resolve impeller flows have been paralleled by considerations of simpler rotating passages such as those of Fowler (1968), Johnston, Halleen and Lezius (1972), Moore (1973) and Rothe and Johnston (1976). A summary of the earlier works with pumps and rotating passages is provided in Table 3.1.

The development of laser velocimetry has allowed more detailed measurements within impeller passages and several investigations of the flows in pumps have been reported, for example those of Hamkins and Flack (1987), Flack, Hamkins and Brady (1987), Sideris and van den Braembussche (1987), Miner, Beaudoin and Flack (1989) and Paone, Reithmuller and van den Braembussche (1989), and are paralleled by those considering centrifugal

compressors, for example those of Eckhardt (1976, 1980), Adler and Levy (1979), Schodl (1980), Krain (1981, 1988), Khezzar, Vafidis and Whitelaw (1987) and Hah and Krain (1990). Recent reviews of the literature related to compressors have been provided by Cumsty (1989) and Whitefield and Baines (1990). The various investigations have considered non-uniform velocities, the importance of the secondary flows and interactions between impeller and diffuser. However, the measurements have been confined mainly to locations accessible through the inlet or exit and to limited regions of the impeller passages, often with ensemble-averaged velocities based on small samples so that little turbulence information has been reported. Moreover, some experiments, particularly with pumps, have been made with simplified geometries to allow optical access. A summary of these investigations of pump flows which have used laser velocimetry is provided in Table 3.2. Recent advances in numerical modeling should also be noted, and Moore, Moore and Timmis (1984), Martelli and Michelassi (1990) and Vu and Shyy (1990), for example, have presented results of turbulent flows in stationary and rotating components of turbomachines.

The application of laser-based instrumentation to liquid-flow pumps is complicated, even with the casing manufactured from a transparent material, by the refractive-index differences between air, casing and liquid. To overcome this problem, the inlet and exit ducts, the present casing and volute were manufactured from acrylic with the same refractive index as the liquid. This technique has been used to allow measurements of the flows in inlet ports of internal combustion engines by Yianneskis, Cheung and Tindal (1988), the flow in a model of the space-shuttle main engine mixing chamber by Thompson, Senaldi, Vafidis, Whitelaw and McDonald (1989), the flow in the coolant passages of an engine cylinder head by Liu, Margary, Vafidis and Whitelaw (1990) and two-phase flows by Nouri, Whitelaw and Yianneskis (1987) and Liu, Nouri, Tse and Whitelaw (1989). Details of the method have been documented by Nouri, Whitelaw and Yianneskis (1988).

The present work provides details of the turbulent characteristics of the flow in a centrifugal pump, with focus on the unsteady

effects related to the hydrodynamic generation of noise. According to Yuasa and Hineta (1979), the noise and vibration of pumps are closely related to the non-uniform velocity and pressure, especially near the cutwater, and the fluctuations are dominated by the fundamental and harmonics of the blade passing frequency. Preliminary experiments by Liu, Nouri, Vafidis and Whitelaw (1990), obtained with a similar pump running with lower flowrate, showed that the combination of laser velocimetry, transparent casing and fluid of the same refractive-index allowed detailed measurements except where the inlet pipe masked the inner part of the impeller. Their results also revealed differences of more than an order of magnitude between 1- and 360-degree averaged velocities and that the influence of the impeller passage on the flow in the volute was present up to at least half of the volute diameter. Complementary measurements of wall pressure and far-field sound intensity have been reported by Tse, Sabnis, McDonald and Whitelaw (1991) with the same pump arrangement.

The following section describes the flow configuration, the instrumentation and possible sources of measurement uncertainty. The results are presented and discussed in the third section with separate consideration given to the inlet and exit flows, the absolute and relative flows in the impeller passages and the flow in the volute passage. The report ends with a summary of the more important conclusions.

3.2 FLOW CONFIGURATION AND INSTRUMENTATION

Figure 3.1 shows the experimental arrangement, including the pump, the circuit for the temperature-controlled liquid, the laser velocimeter and the encoder which identified the shaft angle and rotating speed of the impeller. The centrifugal pump (Price model SC100-150) was driven by an electric motor (Leroy Somer Motor, LS80L2) at a speed of 2910 rpm (N) and circulated liquid from and to a 70 litre tank through 36 mm (D_i) and 28.5 mm (D_e) inlet and outlet pipes respectively. The impeller, Figure 3.2, had four backswept blades of 2.5 mm thickness (t) with the blade height tapered from 11.2 mm at an inner radius of 21 mm to 6.2 mm (Z_t) at the outer radius of the impeller of 62.7 mm (R_t). The

clearance between the impeller tip and shroud was adjusted to 0.5 mm, smaller than the manufacturer's nominal value, and the resulting passage width (Z_b) was 11.7 and 6.7 mm at the radii of 21 and 62.7 mm, respectively, where the circumferential cross-section areas of the passage were 1427 and 2572 mm^2. The curve of the impeller blade was a logarithmic spiral with blade angle of around 30 degrees in the entrance section between radii of 12 and 20 mm, and 58 degrees (β) in the discharge section between radii of 40 and 62.3 mm, with a smooth transition from 30 to 58 degrees between radii of 20 and 40 mm.

The original cast stainless steel casing of the pump was replaced by a cast acrylic component of rectangular external shape and internal dimensions identical to those of the metal components. This was achieved by moulding a core of the metal casing in silicon rubber, creating a casting of plaster of Paris, moulding a core of low melting-point alloy (MCP 70) and a second casting, this time of acrylic. The final cast was machined to provide flat external surfaces and polished on its internal and external surfaces. The finished acrylic casing was annealed at 82°C for 35 hours with slow heating and cooling. The final internal dimensions were measured and found to be within 0.5 mm of those of the original casing and volute.

The working fluid was a mixture of 31.8% by volume of 1,2,3,4-tetrahydronapthalene (tetraline) and oil of turpentine with density (ρ) and kinematic viscosity (ν) of 0.893 kg/m^3 and 1.64×10^{-6} m^2/s, respectively, at 25°C. The Reynolds number based on the impeller diameter (125.4 mm) and tip velocity (19.1 m/s) was 1.38×0^6. The mixture was maintained at a temperature of 25±0.2°C by a temperature controller (Eurotherm, type 818), with a heater and cooler installed within the storage tank and a platinum resistance sensor near the pump outlet to maintain a refractive index of 1.49, identical to that of the cast acrylic. The flowrate of the mixture was regulated between 2.52×10^{-3} and 4×10^{-4} m^3/s by a valve downstream of the pump outlet, which corresponded to a range of flow coefficients (Φ) between 0.054 and 0.0086. The flowrate was measured by a sharp edge orifice

meter, calibrated to an accuracy of better than 3%. The flow conditions of the experiment are provided in Table 3.3.

The motion in a rotating system involves a Coriolis force which is important when its magnitude is comparable with the other forces in the system, i.e. the inertial and viscous forces. The non-dimensional parameters of Ekman (Ek) and Rossby (Ro) numbers are defined based the ratio of viscous to Coriolis forces and inertial to Coriolis forces, respectively, and allow the estimation of the relative importance of the forces in the system. Typical values of the Ekman and Rossby numbers were calculated based on the impeller diameter and tip velocity as 3.4×10^{-7} and 0.5, respectively, and suggest similar magnitudes for the Coriolis and inertial forces and a smaller value for the viscous force, except in the boundary layer where the three can have similar values.

The design point of a pump with volute diffuser is determined from the criteria of equal angular momentum of the flow at the impeller discharge and at the throat of the volute (Karassik, Krutzsch, Fraser and Messina, 1976), usually corresponding to the condition of highest efficiency, and depends on the rotating speed. The flowrate at the design point of the pump running at 2910 rpm was 2.72×10^{-3} m^3/s (Q_n), based on theoretical velocities at impeller discharge plane and at throat of the volute, which is equivalent to a flow coefficient of 0.058. The experimental conditions comprised a range of flowrates from 93% to 15% of the design flowrate, Table 3.3. The performance of the pump is characterised by the head coefficients (Γ) of Figure 3.3 which shows that it is almost identical to that of the manufacturer's specification with the metal casing and is higher with the perspex casing by 18% near the design flow coefficient and by 15% near shut-down. The differences are due probably to the smaller impeller tip clearance ($\approx$ 0.5mm) and the machined and polished inner surfaces of the perspex casing which reduced the leakage flow and friction.

The laser velocimeter, Figure 3.1, was similar to that of Liu *et al.* (1990) and comprised a one watt argon-ion laser tuned to the green line (514.5 nm wave-length) and operating at powers from 0.1 to 0.8 watt depending on the angle of light collection. The

transmission optical components were based on a diffraction grating which divided the beam and provided frequency shifts up to 13 MHz. The collection optical system comprised a lens of 33 mm aperture and 200 mm focal length with a 100 μm diameter pinhole and a photomultiplier (EMI model 9817B). Rotation of the transmission optical components allowed the measurement of two orthogonal components of velocity, and the third component was measured by realigning the velocimeter. The optical components were secured to an optical bench which was translated in three orthogonal directions with accuracy of location better than 0.1 mm in each direction. A summary of the optical characteristics of the velocimeter is provided in Table 3.4.

The Doppler signal, based on natural contaminants in the liquid and with a data arrival rate up to $3x10^4$ per second, was processed by a frequency counter (TSI model 1990c) and interfaced to a microcomputer (IBM PC-AT), together with the pulse train from the optical shaft encoder with its resolution of 0.25 degrees. The digital information was collected in sequences of up to $1.4x10^6$ velocity values and used subsequently to provide angle-resolved velocity traces of up to 2300 rotation cycles or ensemble averaged values based on angular windows of one degree. The ensemble averaged velocity statistics in each angular window were calculated from sample sizes between 1000 and 4000 velocity values depending on the magnitude of the rms of the fluctuations.

The zero of the impeller shaft angle (Ø) on each revolution was identified by a marker pulse from the shaft encoder which was purposely arranged to coincide with one of the impeller blade tips. The alignment was made by illuminating the outer rim of the blade tip at around the middle of its height by a focused laser beam aligned on the plane of the volute circumferential angle (Ψ) of 330 degrees, and the reflected light was collected by a photomultiplier. Every time a blade tip passed that plane, a pulse was generated with its width corresponding to that of the blade tip, and a total of four pulses were generated in one revolution. The marker pulse from the shaft encoder was then aligned with the centre of one of the blade pulses by displaying them simultaneously on an oscilloscope. In this way, the marker of the

shaft encoder was aligned with the centre of the blade thickness at the outer rim of the impeller, and the origin of shaft angle Ø was aligned with the plane Ψ = 330 degrees.

The possible sources of uncertainty associated with laser velocimeters have been considered in many contributions, and only velocity gradient and statistical broadening were important here. Spatial gradients were greatest in the vicinity of the pressure and suction surfaces of the blades and the maximum uncertainties, minimised by the small effective length of the measurement volume (Table 3.4), were less than 0.5% in the estimates of the rms velocities; the corresponding angle-broadening errors were less than 1%. Statistical uncertainties were maintained unimportant by ensuring a sufficient number of velocity data in each ensemble average. Ensemble-averaged information over 360 degrees is presented at locations where the impeller influence is small. As a consequence of the above, the maximum uncertainties in the ensemble-averaged mean and rms velocities are not expected to exceed 2% and 5% of the local values respectively and should be less in the large majority of cases. The use of refractive index matching minimised positioning errors to less than 0.2 mm.

3.3 RESULTS AND DISCUSSION

The coordinate systems of the experiment are identified in Figure 3.2 and were chosen to facilitate presentation of results in different parts of the pump and in absolute and rotating frames. The inlet and exit flows are described by the stationary Cartesian coordinates, x-y-z, located in the inlet and exit pipes respectively, and the absolute flows in the impeller and volute are described by the cylindrical coordinates, r-θ-z, located in the volute with an additional set of cylindrical coordinates, r-θ-z, for the relative flow within the impeller. The impeller shaft angle Ø was measured in the counter-clockwise direction with its origin at Ψ = 330 degrees. The exit pipe was normal to the plane of Ψ = 330 degrees which was also the origin of the x-coordinate in the exit pipe. The relative angular coordinate Ω on the impeller was measured in a direction from suction to pressure surface with its

origin at the centre of the blade thickness. The velocity measurements were based on a stationary probe volume with the angle dependent velocity resolved according to the impeller shaft angle. The measuring stations of the flows in the impeller and volute are identified by the volute circumferential angle Ψ measured in the counter-clockwise direction from the cutwater which was on an angular plane 30 degrees to that of Ψ = 330 degrees.

The velocity measurements are presented in five sub-sections. The first describes the flows in the inlet and exit pipes where the velocity was insensitive to the rotation of the impeller and the data were averaged over 360 degrees. The second and third are concerned with the absolute and relative flows in the impeller passages and the influence of the volute, and the velocity is quantified by angle-resolved measurements to one degree of shaft rotation. The fourth sub-section considers the flow in the volute passage, and the last quantifies the slip factor based on integrations of angle-resolved velocities. The velocity values are normalised by the blade tip velocity (W_t = 19.1 m/s), except in the inlet and exit pipes where the bulk mean velocity in the exit pipe (U_e in Table 3.3) is used.

3.3.1 Flows in the Inlet and Exit Pipes

Profiles of axial mean velocity in the inlet pipe, 25 mm upstream of the impeller hub (z/D_i = 0.7) and on two orthogonal planes, are presented in Figure 3.4 and show symmetry along the z-diameter and asymmetry along the y-diameter, reflecting the asymmetric pressure distribution in the volute. Integration of the radial profiles resulted in mass flowrates within 1% and 4% of the values measured by the flow meter for $0.93Q_n$ and $0.57Q_n$, respectively, and with poorer agreement at lower flowrates due to increased asymmetry and flow separation. The boundary layer thickened with evident regions of flow reversal and swirl near the pipe wall and larger normalised cross-stream velocities at $0.29Q_n$ and $0.15Q_n$, in contrast to the more uniform flow at $0.93Q_n$ and $0.57Q_n$. The induced tangential velocity (the z-profile of V) has a maximum close to the outer radius and vanishes toward the axis, due to mis-matching of the inlet blades and flow angles at small

flowrates. The increased radial velocities (the y-profile of V) at small flowrates are associated with the less-uniform axial flow and separation, and due partly to the upstream influence of the expansion of the duct at a short distance downstream of the measuring station. The maximum negative axial velocities are U_e and $1.8U_e$ for $0.29Q_n$ and $0.15Q_n$, respectively, and occur close to the upper wall with induced tangential velocities up to $2.5U_e$ and $5.2U_e$. The increasing non-uniformity of the inlet velocity profiles at low flowrates is likely to cause variation of impeller passage flow and this is quantified in the following sections.

The rms of the fluctuating velocities in the inlet pipe, Figure 3.5, are asymmetric at the lowest flowrate and associated with the mean velocity distributions. The turbulence is near-isotropic except close to the outer radius where the flow rotated and separated at the lower flowrates. The minimum rms values on the centre of the pipe are $0.05U_e$, $0.07U_e$, $0.12U_e$ and $0.27U_e$ for Q/Q_n of 0.93, 0.57, 0.29 and 0.15, respectively, and are equivalent to local turbulence intensities of 8%, 11%, 20% and 43% based on the inlet bulk mean velocities U_i in Table 3.3. The maximum rms velocities coincide with large axial velocity gradients near the wall and flow reversal at small flowrates. The high turbulence intensities in the inlet pipe may be attributed to the straight inlet pipe of eight diameters in length connected to an upstream flexible hose.

The distributions of axial mean velocity in the diverging section of the exit pipe ($x = 1.8D_e$), a short distance downstream of the cutwater, and in the straight section ($x = 3.2D_e$), are presented in Figures 3.6 and 3.7, respectively, and show qualitative axial symmetry with a minimum in the central region at $0.93Q_n$. A region of streamwise flow separation occurred close to the wall ($z/R = -1$) in the diverging pipe at $0.57Q_n$, Figure 3.6, and changed position and increased with decrease in flowrate to increase the non-uniformity of the velocity profiles. The separated wake, inferred by the orthogonal diametral profiles, occupies up to 5%, 20% and 35% of pipe diameter with negative velocity values up to $-0.15U_e$, $-0.88U_e$ and $-1.49U_e$ for Q/Q_n of 0.57, 0.29 and 0.15 respectively. The streamwise flow separation at lower flowrates

was accompanied by increased cross-stream velocities and caused the location of the separated wake to vary in the downstream straight pipe, Figure 3.7. The mean flow did not depend on the periodicity of the impeller rotation, and the poor match of flow angles and volute geometry in the upstream passage at off-design flowrates caused separation in the exit pipe.

The rms of the fluctuating velocities of Figure 3.8 are related to the mean values of Figure 3.7 in the straight pipe and are near-isotropic with uniform distributions at higher flowrates and increasingly anisotropy and spatial variations at the lower flowrates. The exit flow was fully turbulent with typical rms values of $0.17U_e$, $0.2U_e$, $0.65U_e$ and U_e for Q/Q_n of 0.93, 0.57, 0.29 and 0.15, respectively, and corresponding to 3% to 4% of the impeller tip velocity.

3.3.2 Flows in the Impeller Passages

The impeller discharge flow is characterised in Figures 3.9 and 3.10 by the circumferential profiles of the three components of mean velocity in the absolute frame on the mid-plane of the impeller passage at discharge, with Figure 3.10 highlighting the effects of flowrate. The velocities in the four impeller passages, Figure 3.9, show that the blade-to-blade variations and the passage-to-passage differences of velocity increase with decrease of flowrate, with the maximum differences between passages occurring close to the blade surfaces. Inspection of the impeller geometry showed maximum differences of 0.5 mm in passage width (Z_b) and up to one degree in blade circumferential spacing, and these imperfections were responsible for the observed passage-to-passage variations of velocity. The maximum differences in the radial and tangential velocities between passages were $0.025W_t$ and $0.06W_t$, respectively, at the highest flowrate, and increased to $0.03W_t$ and $0.16W_t$ at the lowest flowrate. The blade-to-blade variations of velocity in W, V and U components are up to $0.16W_t$, $0.14W_t$ and $0.09W_t$, respectively, at $0.93Q_n$ and increased to $0.25W_t$, $0.32W_t$ and $0.12W_t$ at $0.15Q_n$.

The variations of discharge velocity with flowrate are more clearly illustrated in Figure 3.10 which considers one impeller passage,

as in the remainder of this paper. It should be noted that the velocity values belong to an absolute frame so that the tangential velocity is much larger than the other two components and the normalised value will be unity at the blade surfaces, i.e. at $\Omega = 2$ and 88 degrees. The results show uniform tangential and axial components of velocity, except close to the surfaces of the blades, with the radial component increasing from suction (SS) to pressure (PS) surfaces at the flowrate of $0.93Q_n$. Decrease of flowrate caused the decrease of radial velocity and increase of velocity gradient between blade surfaces leading to radial flow reversal near the suction surface at $0.15Q_n$. The tangential velocity in the absolute frame also decreased with the radial velocity in accord with the increased slip effect, and a more detailed discussion is provided in sub-section 3.3.5. The axial velocity component has increased values with changes of sign at small flowrates suggesting increasing complexity of the secondary flow as discussed in detail in the later text.

It is obvious that these complexities and large blade-to-blade variations of velocity limit the value of investigations by methods without angle-resolving ability and, as has been point out by Liu *et al.* (1990), the ensemble-averages over 360 degrees can lead to over- or under-estimation of the local velocity by more than 100%. Figure 3.10 shows that the rms velocities are near-uniform and near-isotropic at high flowrates, and that the decrease of flowrate caused the increase of rms values and the blade-to-blade variations, with peak values close to the suction surface and in the wake region, as reported by Moore (1973) in a rotating diffuser, Flack *et al.* (1987) in a centrifugal pump and Kjork and Lofdahl (1989) in a centrifugal fan.

A clear picture of the impeller flow is given by Figure 3.11 in terms of mean velocity vectors in the absolute frame at $0.93Q_n$ and by Figure 3.12 in the relative frame at the flowrates from $0.93Q_n$ to $0.15Q_n$. The results were obtained by measurements at six radial and three axial locations on the plane of $\Psi = 330$ degrees and correspond to combinations of angle-resolved radial and tangential velocities at each point. The absolute flow of Figure 3.11 shows that the velocity increases radially, as a consequence

of the work done by the impeller, with the outward angle higher at the pressure surface and lower at the suction surface. The outward angles of the vectors are small and approach zero close to the shroud, suggesting a tendency towards radial flow reversal.

It should be noted that the flow fields of Figures 3.11 and 3.12 was constructed from Eulerian measurements at stationary points on the plane of Ψ = 330 degrees and corresponded to the behaviour of the flow passing the probe volume. However, the results are presented as the mean flow behaviour centred around the measuring point (±45 degrees in the present case), as illustrated in the figure, which is justified provided the relative flow is invariant with rotation. Since the geometry of the volute is asymmetric with pressure distributions a function of the circumferential angles, the relative flow in the impeller passages may be subject to upstream effects due to the pressure field. The extent of variation of relative flow with the volute circumferential angle was examined by the measurements on the planes of Ψ = 60 and 240 degrees, and the results are presented in sub-section 3.3.3.

The relative flow on the mid-plane of the passage in Figure 3.12 generally follows the curvature of the blade at the flowrate closest to the design point ($0.93Q_n$) with departures from blade curvature at inner radii close to the hub and a less regular flow close to the shroud. The reduction of flowrate decreased the velocity vectors and increased the flow angle (the angle between radius and relative velocity vector), and the flow tended to decelerate towards the suction side of the passage and accelerate towards the pressure side, Figure 3.12, $0.57Q_n$, $0.29Q_n$ and $0.15Q_n$. The obedience of the mean flow to the blade curvature is suggested by the mean flow angles in Figures 3.13 and 3.14. The flow angles of Figure 3.13 on the mid-plane at $0.93Q_n$ increased along the radius with values smaller than the blade angle (58 degrees) at inner radii and larger than the blade angle at discharge. The flow angles remained close to the blade angle near the pressure surface where the streamlines followed the blade curvature. The flow angles at discharge were larger than the blade angle at all flowrates, Figure 3.14, and decreased almost linearly from suction

to pressure surfaces and increased monotonically with the decrease of flowrate, leading to values larger than 90 degrees at the smallest flowrate where the radial flow was reversed.

Figure 3.12 also shows a tendency for the velocity vectors to change direction and to form vortices, more evident at small radii and close to the shroud, as the flowrate decreased. The velocity vectors at $r/R_t = 0.71$ had a tendency to diminish on the pressure side of the passage at lower flowrates, $0.29Q_n$ and $0.15Q_n$, in contrast to the larger vectors on the suction side of the passage, suggesting an eddy within the blade passage. Measurements at smaller radii close to the concave surfaces of the blades were limited by the obstruction of the inlet pipe and the backward curved blades, combined with the near 90 degrees angle of light collection optimised to eliminate reflection from the impeller surface. Measurements were obtained over the outer 35% of the impeller radius and all the way along the periphery of the passage at discharge ($r/R_t = 1$) and up to 63% at the inner radius of $0.65R_t$. The inward velocity vectors close to the shroud are common for an unshrouded impeller design, due to the radial pressure gradient and the relative motion of the shroud and impeller, which increased in magnitude and angle as the flowrate was decreased leading to radial flow reversal at radii up to $0.71R_t$ at the smallest flowrate. The increasing irregularity of the flow and separation at off-design conditions are related to the centrifugal and Coriolis acceleration, the irrotational nature of the flow and viscosity and are discussed in the following paragraphs.

The centrifugal and Coriolis forces are balanced by radial and blade-to-blade pressure gradients from inner to outer radii and from suction to pressure surfaces, respectively. The static pressure is therefore lower on the suction surface and higher on the pressure surface. Since the pressure at discharge is dominated by that of volute, the pressure gradient along the suction surface is stronger to give rapid deceleration of the flow. The pressure gradient from one surface to another gives rise to secondary flows in which the boundary layer fluid is transported from pressure to suction surfaces along the walls of the hub and shroud, and the core fluid is convected in the opposite direction,

leading to accumulation of low energy fluid on the suction side of the passage. The tendency for separation to occur on the suction side of the passage had also been reported by Dean and Senoo (1960) and Eckhardt (1976, 1980) with compressor rotors.

Fowler (1968), Moore (1973) and Rothe and Johnston (1976) had investigated flows in two-dimensional channels with converging and diverging angles, and Johnston, Halleen and Lezius (1972) considered a straight channel, rotating in a span-wise direction. They concluded that rotation enhanced the tendency towards stall which occurred on the suction surfaces of their ducts, and that the Coriolis acceleration stabilised the turbulent boundary layers on suction surface and destabilised them on pressure surface, resulting in local suppression of turbulent mixing in the suction-side boundary layer and consequent tendency for stall. However, the backward curvature of the blade causes streamline curvature and can generate forces opposite to that due to rotation and with similar magnitude to enhance the tendency of stall on the convex surface of the blade.

Potential flow in the impeller passages can be represented by superposition of a through-flow and a relative eddy, Stanitz (1952). The relative eddy is due to the irrotational nature of the flow and has the angular velocity of rotation but the opposite direction. In the present case, it rotated in a clockwise direction and was bounded by the blades surfaces consistent with acceleration and deceleration along the suction and pressure surfaces respectively, and acceleration from suction to pressure surfaces at large radii and the opposite at small radii. It caused the departure of streamlines from blade curvature, so that the flow angles were larger than the blade angle at discharge and the impeller head output was less than the theoretical value.

The radial mean velocities of Figure 3.15 show the deceleration and acceleration along the suction and pressure surfaces respectively, and the reversed flow close to the shroud. The relative eddy is evident in the profiles at small radii where a clockwise-rotating vortex exists at $0.15\Omega_n$, in agreement with the trend predicted by Stanitz (1952) with potential theory where recirculation existed on the pressure surface. This vortex

decreased in size and moved closer to the suction surface towards outer radii, due to the backward leaning geometry of the passage, and the radial flow on the pressure side of the passage was enhanced at discharge. Similar trends exist at higher flowrates, but the vortex is less obvious due to the stronger through-flow.

The streamwise and cross-stream velocities of Figures 3.16 and 3.17 were obtained by resolving the radial and tangential components. The streamwise component of Figure 3.16 increased uniformly with radius with smaller variations between hub and shroud and across the passage than the radial component. The variations with flowrate were also less for the streamwise velocity and this, together with the more uniform distributions, suggests that the non-uniform distributions in radial component were mainly caused by the secondary flows. Flow reversal in streamwise direction was observed at small radii, close to shroud, and in the pressure side of the passage at the smallest flowrate, and is related to the near-stagnation region of Figure 3.12.

Figure 3.17 shows that the cross-stream component of mean velocity had positive and negative values at $r/R_t = 0.71$ and only negative values at discharge and increased from hub to shroud and from pressure to suction surfaces due to the relative motion of the impeller and the shroud, influenced by the curvature of the blade and the relative eddy. The velocity on the shroud surface, $z/Z_b = 1$, is the cross-stream component of the tangential velocity relative to the impeller, i.e. $-0.38W_t$, $-0.48W_t$ and $-0.53W_t$ at $r/R_t = 0.71$, 0.9 and 1 respectively, with the arrow indicating the relative motion. Decrease of flowrate increased the secondary flow at $r/R_t = 0.9$ and 1, and the cross-stream velocities on the mid-plane at discharge, $z/Z_b = 0.5$ and $r/R_t = 1$, were up to $0.1W_t$, at $0.93Q_n$ and $0.35W_t$ at $0.15Q_n$ close to the suction surface. The magnitude of the cross-stream velocity at $r/R_t = 0.71$ was more uniform with flowrate, but the changes of sign suggest the formation of vortices due to passage pressure gradients and leakage flow, and a counter-clockwise vortex is evident close to the suction surface at $r/R_t = 0.9$ for the small flowrates. Similar vortices have been reported by Eckhardt (1976), Farge, Johnson and Maksoud (1989) and Ishida, Senoo and Ueki (1990) with

their centrifugal compressors and by Engenda and Rautenberg (1987) with a centrifugal pump and were attributed to the combined effects of the pressure gradients, the blade tip leakage flow and the impeller-shroud relative motion. The passages of those earlier investigations had smaller aspect ratios and tip clearance-to-blade height ratios than the present impeller which may limit the extent of the leakage flow, so that the relative motion of the impeller and shroud would dominate, particularly at large radii where the tangential velocity of the relative motion was high.

The axial component of velocity (not shown in figure) is smaller than the other two components particularly in the central region of the passage and at small radii. Larger axial velocities occur at discharge and Figure 3.10 shows that the maximum and minimum are within $\pm 0.1 W_t$. The axial velocities close to blade surfaces at smaller radii support form of the vortices discussed above.

3.3.3 Variations of Relative Flow in the Impeller

Centrifugal pumps use volutes to collect the discharge from the impeller and are arranged to match the impeller discharge flow at the design flowrate. The cross sectional area of the passage is a function of the circumferential angle (Ψ) to maintain a constant angular momentum of the flow (Karassik *et al.*, 1976) with a cutwater to separate the outlet duct. The asymmetric shape of the volute generates circumferential pressure distribution which depends on the operating condition (Iversen *et al.*, 1960; Sideris and van den Braembussche, 1987), and off-design operation results in larger pressure variations which, in turn, affect the flow in the impeller and pump performance (Bowerman and Acosta, 1957; Hamkins and Flack, 1987). The results in this sub-section describe the impeller flow measured at the circumferential angles Ψ of 60, 240 and 330 degrees at a flowrate of $0.57Q_n$.

The relative flows for Ψ of 60 and 240 degrees, Figure 3.18, correspond to the passage of Figure 3.12 and are similar to that at Ψ = 330 degrees (Figure 3.12, $0.57Q_n$), with the velocity vectors and flow angles smaller at the smaller angles. The measurements at Ψ of 60 and 240 degrees allowed closer to the suction surface

where the region of higher velocity at r/R_t = 0.65, 0.71 and 0.8, indicating acceleration due to the relative eddy, is clearly identified in Figures 3.18b and 3.18c, which was less obvious in Figure 3.12.

The profiles of velocity and flow angle on the mid-plane of the passage at discharge are shown in Figures 3.19 and 3.20, respectively, for the three locations and have lower mean values for the radial component and higher mean values for the absolute tangential component at Ψ = 60 and 240 degrees, Figure 3.19, with the rms values similar at the three locations. The results suggest a variation of flowrate, and this is supported by the higher absolute tangential velocities for lower radial velocities. Figure 3.20 shows larger flow angles and uniform distribution at Ψ = 60 degrees, in contrast to lower values and larger variation at Ψ = 330 degrees, again suggesting the influence of the volute, and is related to the slip effect of the last sub-section. The radial velocity profiles were averaged over 360 degrees and resulted in $0.08W_t$, $0.092W_t$ and $0.116W_t$ for the profiles of Ψ = 60, 240 and 330 degrees respectively. Area averages of the radial velocity profiles on the three axial planes over the peripheral area of the passage at discharge resulted in lower values of $0.044W_t$, $0.053W_t$ and $0.059W_t$ due to velocity gradients from hub to shroud. The results confirm that passage flowrates depend on the circumferential angles of the volute, with that at Ψ = 60 and 240 degrees 25% and 10%, respectively, lower than that at Ψ = 330 degrees. These variations of passage flowrate are associated with a flowrate of $0.57Q_n$ and could cause uneven momentum of discharge from the multiple passages of the impeller which, together with the volute pressure distribution, could give a net radial thrust exerting on the impeller.

3.3.4 Flow in the Volute Passage

The results in this sub-section consider the flow in the volute which stem from the impeller discharge. Velocities were measured in detailed for the flowrate of $0.57Q_n$ with sample results for higher and lower flowrates.

Figure 3.21 shows that the streamwise component of mean velocity at Ψ of 60, 240 and 330 degrees in the volute at $0.57Q_n$ had a tendency to decelerate along the passage, and that the velocity varied with impeller shaft angle. The results at shaft angles $\emptyset$ = 0, 30 and 70 degrees are presented to identify the variations, based on velocity traces over 360 degrees. The radial profiles are characterised by velocity maxima at the impeller discharge with near-uniform distribution close to the volute wall. The profile close to the cutwater, x/D_e = 1.15, has sharp gradient towards the cutwater and rapid deceleration on the back surface of the wall (z = -1, Figure 3.2), due to the influence of the cutwater and the divergence of the outlet duct. The deceleration along the passage of the volute is due to the geometry and operating conditions that the flow decelerates and static pressure increases in the circumferential direction at flowrates below the design point (Binder and Knapp, 1958; Bowerman and Acosta, 1957; Hamkins and Flack, 1987). Flow acceleration and static pressure increasing in the circumferential direction would occur for the flowrates above the design point (Sideris and van den Braembussche, 1987). Similar characteristics of volute flows have been reported by van den Braembussche and Hände (1990) in a simplified geometry with a straight conical channel.

The rms velocities associated with the mean values of Figure 3.21 are presented in Figure 3.22 and show larger values at Ψ = 60 degrees and near the cutwater where the maximum was $0.94W_t$ and the variations with shaft angle up to $0.2W_t$, indicating the local unsteadiness of the flow due to the interaction of the impeller and the cutwater. Local maxima of the rms velocity are also associated with velocity gradients of the mean flow.

The details of the flow near the cutwater are further identified in Figure 3.23 by the mean velocity vectors on the plane z = 0 at five shaft angles and show large change near the cutwater with the vectors away from the cutwater insensitive to the rotation of the impeller. The stagnation point, inferred from the vectors, was on the outer surface of the lip at $0.57Q_n$, similar to the results of Miner, Beaudoin and Flack (1989), and moved towards the inner surface at higher flowrates. The location of the stagnation point

may control out- or in-flow through the cutwater clearance at flowrates above and below the design point and separation when the stagnation point occurs at extreme positions (Binder and Knapp, 1958).

The decrease of flowrate caused a general decrease in circumferential velocity, Figures 3.21 and 3.24, and increased variation with shaft angle, as is evidenced by the typical values of the streamwise mean velocity of the near-uniform profiles at Ψ = 330 degrees of $0.56W_t$, $0.53W_t$, $0.42W_t$ and $0.39W_t$ for Q/Q_n of 0.93, 0.57, 0.29 and 0.15 respectively, with variations of up to $0.06W_t$ at $0.93Q_n$ and $0.11W_t$ at $0.15Q_n$ based on 360-degree traces of velocity. The results are associated with the non-uniform discharge flow of the impeller, and the values of the periodic variations of the mean velocity with impeller rotation were equivalent to around 11% of local velocity at $0.93Q_n$ and 28% at $0.15Q_n$.

Figure 3.25 shows the cross-stream mean flow in the volute in terms of velocity vectors on the plane of Ψ = 330 degrees at five shaft angles and for flowrates of $0.93Q_n$ and $0.57Q_n$, obtained by resolving the radial and axial components of velocity. The transverse flow is mainly radially outward with little signature of the impeller rotation at $0.93Q_n$, except close to the impeller and in the region of small vectors. The cross-stream velocities decreased with flowrate which caused the formation of a counter-clockwise circulation. The flow in the outer region (r/R_t>1.13) of the cross section is almost insensitive to impeller rotation with the signature of blade passing detected only close to the impeller.

The variations of velocity with impeller rotation decayed in the outlet, Figure 3.26, with the velocity traces at x/D_e = 1.8 and 3.2 the same as the measurements of Figures 3.6 and 3.7 where the velocities were 360-degree averaged. The variations of velocity in streamwise (U) and radial (V) directions were of the same order of magnitude and decreased with axial distance faster for the lower flowrate. Measurements at x/D_e = 3.2, two exit pipe diameters downstream of the cutwater, and at the centre of the pipe (not shown in figure) showed that velocities varied slightly for the flowrates up to around $0.8Q_n$ and larger variations for

higher flowrates. These variations corresponded to 14% and 6% of the local bulk mean velocity in the exit pipe for 100% and 80% of the design flowrate respectively. The separated wake and vorticity in the exit pipe of Figure 3.6 are expected to be responsible partly for the variations of mean velocity at lower flowrates.

3.3.5 Slip Factors

The angle-resolved radial and tangential velocities quantified the transfer of angular momentum to the flow and the slip factor inside the impeller. The normalised angular momentum of the flow (M) and slip factor (S), according to Hamkins and Flack (1987), are calculated from the area- and mass-averaged radial and tangential velocities by integration of the measured angle-resolved values at each radial station. The expressions for M and S are defined as,

$$M = \frac{r\,\tilde{w}}{R_t^2\,\omega} \tag{3.1}$$

$$S = \frac{\tilde{w}}{r\omega - \hat{v}\tan\beta} \tag{3.2}$$

The slip factor is based on the ratio of the actual to theoretical values of absolute tangential velocity, and the angular momentum is normalised by the radius of impeller and angular speed of rotation, and both were evaluated at each radial station of measurement.

Figure 3.27 shows that the angular momentum of the flow increases with radius, as expected, to reach maxima of 0.62 and 0.66 at the discharge plane for $0.93Q_n$ and $0.29Q_n$ respectively. The tendency for the angular momentum to reach maxima inside the impeller is evident at $0.29Q_n$ and may be attributed to reverse blade loading at low flowrate according to Hamkins and Flack (1987). The ideal value of angular momentum based on the area-averages of measured radial velocity can be obtained by dividing equation 3.1 by equation 3.2, and the results suggest that the flow loses momentum along the radius with larger loss for the lower flowrate. The departure of angular momentum from ideal is due

partly to the slip effect and partly to friction and is quantified by the slip factor of Figure 3.28 which has a trend opposite to that of angular momentum. The slip factor was larger than unity at small radii, supporting the effect of a relative eddy, and is in contrast to that reported by Hamkins and Flack (1987) who measured in the region of larger radii ($0.8 \leq r/R_t \leq 1$) where the slip factor was always less than one.

Figure 3.29 shows that the slip factors at the impeller discharge increased monotonically with flowrate, and they are compared with the theoretical values of Stodola (μ) and Busemann (σ), defined by (Wiesner, 1967; Dixon, 1975):

$$\mu = 1 - \frac{\pi \cos \beta}{n} \tag{3.3}$$

$$\sigma = \frac{A_1 - A_2 \frac{V_R}{W_t} \tan \beta}{1 - \frac{V_R}{W_t} \tan \beta} \tag{3.4}$$

The formula of Stodola was obtained assuming no through-flow and the value of μ was 0.58 based on β of 58 degrees and n of 4. The Busemann slip factor σ was calculated using the theoretical radial velocity V_R in Table 3.3, with A_1 equal to 0.69, which is a constant depending on the number of blades and the blade angle, and A_2 equal to unity. The experimental value at $0.93Q_n$ was 0.78 which was around 15% and 25% larger than the theoretical values of Busemann and Stodola, respectively. The slip factors calculated by the velocities measured at Ψ of 60, 240 and 330 degrees at $0.57Q_n$ were within 6% with each other in spite of variations in passage flowrate of up to 25%, again demonstrating the influence of the volute.

3.4 CONCLUSIONS

Measurements of turbulent flow in a centrifugal pump with an unshrouded impeller with four backward leaning blades and a single volute have been made by laser-Doppler velocimetry close to the recommended flowrate and at lower flowrates. A

transparent casing with refractive index identical to that of the fluid allowed detailed examination of the inlet, a large part of inter-blade region, the volute and the outlet of the pump. The more important findings are summarised below:

1. The impeller flow departed from blade curvatures at off-design conditions with increased blade-to-blade variations of relative velocity, in contrast to a generally well-guided flow at the design flowrate. Decrease of flowrate from the design point caused deceleration of radial flow on the shroud surface and on the suction surface of the blades and increase of secondary flows and vorticity in the passages. The radial velocity reversed close to the suction surface at flowrates below 30% of the design point and close to the shroud surface at all flowrates. The velocity measurements confirmed the influence of the relative eddy by higher velocity on the suction surface and near-stagnation flow near the pressure surface at small radii and lower flowrates. However, the geometry of the passage enhanced the influence of the relative motion between the shroud and impeller surfaces and the viscous effects, which, together with the leakage flow through the tip clearance of the blades, caused the secondary flow to be mainly from suction to pressure surface with vortices close to blade surfaces at smaller radii.

2. The unsteady effects of the impeller discharge are caused mainly by the blade-to-blade variations of the flow and partly by the variations in blade-passage geometry and with the circumferential angle of the volute. The measurements confirmed differences of the angle-resolved velocities between the four impeller passages, which increased with the decrease of flowrate and with maximum differences close to the surfaces of the blades. Differences in mean velocity of up to 2.5% and 6% of the impeller tip velocity for the radial and tangential components, respectively, were measured close to the design flowrate and up to 3% and 16% at the flowrate close to shut-down, and were related to the differences of up to 0.5 mm in blade dimensions and up to one degree in blade circumferential spacing. The variations of relative flow in the passages with the circumferential angle of the volute were identified by the velocities obtained at three circumferential

angles of 60, 240 and 330 degrees downstream of the cutwater. The measurements at 57% of the design flowrate showed variations up to 25% of the discharge flowrate from the same passage at the three locations, which would caused a radial thrust to be exerted on the impeller.

3. The velocities in the volute passage decelerated in the circumferential direction at 57% of the design flowrate where the geometry of the volute was over-sized. The decrease of flowrate increased the variations of velocity with impeller rotation, and the cross-stream flow formed a circulation, due to the increased non-uniformity of the impeller discharge flow and separation on the shroud surface. The variations of velocity decayed in the exit pipe and was around 4% of the impeller tip velocity at the design flowrate and a near constant level of around 1% for the flowrates below 80% of the design value at a station two pipe diameters downstream of the cutwater.

4. The results confirmed a continuous increase of angular momentum with radius to a maximum at discharge close to the design flowrate and larger departures of angular momentum from ideal at small flowrates due to the slip effect. The slip factor was larger than unity inside the impeller and decreased with radius. The slip factor at impeller discharge increased monotonically with flowrate, and the value of 0.78 at 93% of the design flowrate was around 15% and 25% larger than the theoretical values of Busemann and Stodola respectively.

REFERENCES

Acosta, A.J. (1954) An experimental and theoretical investigation of two-dimensional centrifugal pump impellers. *Trans. ASME*, **76**, 749.

Adler, D. and Levy, Y. (1979) A laser-Doppler investigation of the flow inside a backswept, closed, centrifugal impeller. *J. Mech. Eng. Sci.*, IMechE, **21**, 1, 1.

Binder, R.C. and Knapp, R.T. (1958) Experimental determinations of the flow characteristics in the volutes of centrifugal pumps. *Trans. ASME*, **80**, 649.

Van den Braembussche, R.A. and Hände, B.M. (1990) Experimental and theoretical study of the swirling flow in centrifugal compressor volutes. *J. Turbomachinery*, Trans. ASME, **112**, 38.

Bowerman, R.D. and Acosta, A.J. (1957) Effect of the volute on the performance of a centrifugal-pump impeller. *Trans. ASME*, **79**, 1057.

Cumpsty, N.A. (1989) Compressor Aerodynamics, Longman, U.K.

Davis, M.C. and Flack, R.D. (1990) Laser velocimetry measurements in a laboratory vaned diffuser. *Experiments in Fluids*, **8**, 1.

Dean, Jr. R.C. and Senoo, Y. (1960) Rotating wakes in vaneless diffusers. *J. Basic Eng.*, Trans. ASME, **82**, 563.

Dixon, S.L. (1975) Fluid Mechanics, Thermodynamics of Turbomachinery. Pergamon Press.

Eckhardt, D. (1975) Instantaneous measurements in the jet-wake discharge flow of a centrifugal compressor impeller. *J. Eng. for Power*, Trans. ASME, **97**, 337.

Eckhardt, D. (1976) Detailed flow investigations within a high-speed centrifugal compressor impeller. *J. Fluids Eng.*, Trans. ASME, **98**, 390.

Eckhardt, D. (1980) Flow field analysis of radial and backswept centrifugal compressor impellers. Part 1: flow measurements using a laser velocimeter. in Performance Prediction of Centrifugal Pumps and Compressors, ASME-paper, 77.

Engeda, A. and Reutenberg, M. (1987) Comparisons of the relative effect of tip clearance on centrifugal impeller. *J. Turbomachinery*, Trans. ASME, **109**, 545.

Farge, T.Z., Johnson, M.W. and Maksoud, T.M.A. (1989) Tip leakage in a centrifugal impeller. *J. Turbomachinery*, Trans. ASME, **111**, 244.

Fischer, K. and Thoma, D. (1954) Investigation of the flow conditions in a centrifugal pump. *Trans. ASME*, **76**, 141.

Flack, R.D., Hamkins, C.P. and Brady, D.R. (1987) Laser velocimeter turbulence measurements in shrouded and unshrouded radial flow pump impellers. *Int'l J. of Heat and Fluid Flow*, **8**, 1, 16.

Fowler, H.S. (1968) The distribution and stability of flow in a rotating channel. *J. Eng. for Power*, Trans. ASME, **90**, 229.

Hah, C. and Krain, H. (1990) Secondary flows and vortex motion in a high-efficiency backswept impeller at design and off-design conditions. *J. Turbomachinery*, Trans. ASME, **112**, 7.

Hamkins, C.P. and Flack, R.D. (1987) Laser velocimeter measurements in shrouded and unshrouded radial flow pump impeller. *J. Turbomachinery*, Trans. ASME, **109**, 70.

Howard, J.H.G. and Kittmer, C.W. (1975) Measured passage velocities in a radial impeller with shrouded and unshrouded configurations. *J. Eng. for Power*, Trans. ASME, **97**, 207.

Howard, J.H.G. and Lennemann, E. (1971) Measured and predicted secondary flows in a centrifugal impeller. *J. Eng. for Power*, Trans. ASME, **93**, 126.

Ishida, M., Senoo, Y. and Ueki, H. (1990) Secondary flow due to the tip clearance at the exit of centrifugal impeller. *J. Turbomachinery*, Trans. ASME, **112**, 19.

Iversen, H.W., Rolling, R.E. and Carlson, J.J. (1960) Volute pressure distribution, radial force on the impeller, and volute mixing losses of a radial flow centrifugal pump. *J. Eng. for Power*, Trans. ASME, **82**, 136.

Johnston, J.P., Halleen, R.M. and Lezius, D.K. (1972) Effects of spanwise rotation on the structure of two-dimensional fully developed turbulent channel flow. *J. Fluid Mech.*, **56**, 3, 533.

Karassik, I.J., Krutzsch, W.C., Fraser, W.H. and Messina, J.P. (editors) (1976) Pump Handbook. McGraw-Hill Inc.

Khezzar, L., Vafidis, C. and Whitelaw, J.H. (1987) Laser velocimetry for the measurement of air velocity in a centrifugal compressor. Imperial College, Fluids Section Report FS/87/36.

Kjork, A. and Lofdahl, L. (1989) Hot-wire measurements inside a centrifugal fan impeller. *J. Fluids Eng.*, Trans. ASME, **111**, 363.

Krain, H. (1981) A study on centrifugal impeller and diffuser flow. *J. Eng. for Power*, Trans. ASME, **103**, 688.

Krain, H. (1988) Swirling impeller flow. *J. Turbomachinery*, Trans. ASME, 110, 122-128.

Lennemann, E. and Howard, J.H.G. (1970) Unsteady flow phenomena in rotating centrifugal impeller passages. *J. Eng. for Power*, Trans. ASME, **92**, 65.

Liu, C.H., Margary, R., Vafidis, C. and Whitelaw, J.H. (1990) Flow in the coolant passages of an internal combustion engine cylinder head. *Exp. in Fluids*, **10**, 50.

Liu, C.H., Nouri, J.M., Vafidis, C. and Whitelaw, J.H. (1990) Experimental study of the flow in a centrifugal pump. in Proc. 5th Int'l Symp. on Appl. of Laser Techniques to Fluid Mechanics, Lisbon, Portugal, 9-12 July, 1990.

Liu, C.H., Nouri, J.M., Whitelaw, J.H. and Tse, D.G.N. (1989) Particle velocity in swirling, confined flow. *Comb. Sci. and Tech.*, **68**, 131.

Martelli, F. and Michelassi, V. (1990) Using viscous calculations in pump design. *J. Fluids Eng.*, Trans. ASME, **112**, 272.

Miner, S.M., Beaudoin, R.J. and Flack, R.D. (1989) Laser velocimeter measurements in a centrifugal flow pump. *J. Turbomachinery*, Trans. ASME, **111**, 205.

Moore, J. (1973) A wake and an eddy in a rotating, radial-flow passage. Part 1: experimental observations. *J. Eng. for Power*, Trans. ASME, **95**, 205.

Moore, J., Moore, J.G. and Timmis, P.H. (1984) Performance evaluation of centrifugal compressor impellers using three-dimensional viscous flow calculations. *J. Eng. for Gas Turbine and Power*, Trans. ASME, **106**, 475.

Murakami, M., Kikuyama, K. and Asakura, E. (1980) Velocity and pressure distributions in the impeller passages of centrifugal pumps. *J. Fluids Eng.*, Trans. ASME, **102**, 420.

Nouri, J.M., Whitelaw, J.H. and Yianneskis, M. (1988) A refractive index matching technique for solid/liquid flows. In Laser Anemometry in Fluid Mechanics 3, Ladoan, 335.

Nouri, J.M., Whitelaw, J.H. and Yianneskis, M. (1987) Particle motion and turbulence in dense two-phase flow. *Int'l J. Multiphase Flow*, **13**, 729.

Paone, N., Riethmuller, M.L. and van den Braembussche, R.A. (1989) Experimental investigation of the flow in the vaneless diffuser of a centrifugal pump by particle image displacement velocimetry. *Exp. in Fluids*, **7**, 371.

Rothe, P.H. and Johnston, J.P. (1976) Effects of system rotation on the performance of two-dimensional diffusers. *J. Fluids Eng.*, Trans. ASME, **98**, 422.

Schodl, R. (1980) A laser-two-focus (L2F) velocimeter for automatic flow vector measurements of turbomachineries. *J. Fluids Eng.*, Trans. ASME, **102**, 412.

Sideris, Th.M. and van den Braembussche, R.A. (1987) Influence of a circumferential exit pressure distortion on the flow in an impeller and diffuser. *J. Turbomachinery*, Trans. ASME, **109**, 48.

Stanitz, J.D. (1952) Some theoretical aerodynamic investigations of impeller in radial- and mixed-flow centrifugal compressor. *Trans. ASME*, 74, 473-497.

Thomas, R.N., Kostrzewsky, G.J. and Flack, R.D. (1986) Velocity measurements in a pump volute with a non-rotating impeller. *Int'l J. Heat and Fluid Flow*, **7**, 1, 11.

Thompson, B.E., Senaldi, J., Vafidis, C., Whitelaw, J.H. and McDonald, H. (1989) Flow in a model of the SSME main injector bowl. in Proc. CASI 1st Canadian Symposium on Aerodynamics, Ottawa, Canada, 4-5 Dec. 1989.

Tse, D.G.N., Sabnis, J.S., McDonald, H. and Whitelaw, J.H. (1991) Active control of pressure, sound and velocity of centrifugal pumps. Scientific Research Associates Inc., Report R91-920036-A2.

Vu, T.C. and Shyy, W. (1990) Viscous flow analysis as a design tool for hydraulic turbine components. *J. Fluids Eng.*, Trans. ASME, **112**, 5.

Whitfield, A. and Baines, N.C. (1990) Design of Radial Turbomachines. Longmans.

Wiesner, F.J. (1967) A review of slip factor for centrifugal impellers. *J. Eng. for Power*, Trans. ASME, **89**, 558.

Yianneskis, M., Cheung, R.S. and Tindal, M.J. (1988) A method of investigating flows in inlet ports of complex shape. in Proc. Int'l Conf. on Combustion in Engines, IMechE, London, 10-12 May.

Yuasa, T. and Hineta, T. (1979) Fluctuation flow behind the impeller. *Bulletin of the JSME*, **22**, 174, 1746.

TABLE 3.1 Investigations of flows in centrifugal pumps and rotating passages made by non-laser based techniques

Authors (Year)	*Experimental Techniques*	*Pump Configuration*	*Operating Range (Spec.)*	*Quantities Measured*	*Main Findings*
Acosta (1954)	passage fixed pressure probe	• laboratory pump • shrouded impeller with parallel hub and shroud; D_t=305 mm; Z_t=24 mm; β=60° log spiral blades; n=2, 4 and 6 • vaneless diffuser	N=150 to 200 rpm; Φ=0.14 to 0.31	static pressure	• experimental data correlated well with the prediction by potential theory when the inlet flow to the vanes is optimised
Fischer & Thoma (1954)	dye-injection visualisation and rotoscope	• laboratory pump • shrouded impeller; D_t=280 mm; Z_t=20 mm; β=62° log spiral blades; n=6 • vaneless diffuser	N=450rpm Φ=0.2 to 1.58 Φ_n	N/A	• flow patterns different from the predictions of potential theory • high velocity and wake regions observed near pressure and suction surfaces, respectively

TABLE 3.1 Continued (1)

Authors (Year)	*Experimental Techniques*	*Pump Configuration*	*Operating Range (Spec.)*	*Quantities Measured*	*Main Findings*
Bowerman & Acosta (1957)	static pressure tap; total-head probe; torque meter	• laboratory pump • shrouded impeller with parallel hub and shroud; Dt=262 mm; Zt=30 mm; β=66.5° log spiral blades • three 2-D double volutes with log spiral walls to match 0.75, 1 and 1.2 of impeller design flowrate (Φ_i)	Φ=0 to 0.22 (Φ_i=0.117)	static and dynamic pressure in volute; shaft power	• volute flow qualitatively similar to potential flow with the degree of departure depending on flowrate • volute flow subjected to real fluid effects due to impeller discharge • the presence of the volute affected the performance of impeller to give a different pump characteristics at off-design operation • efficiency highest near the matching point of the impeller-volute combination
Binder & Knapp (1958)	pitot tube with slide valve to synchronise impeller rotation	• commercial pumps • double suction impeller; D_t=350, 317mm; Z_t=43, 39 mm; β=67.2°, 70°; n=8, 7 • single volute	N=2000; 2500 rpm (N_{sUS} =1400, @2500 rpm; =1720 @2900 rpm)	velocity and pressure in volute	• radial velocity distributions depended on flowrates with non-uniformity at high and low flowrates • out- and in-flow in the cutwater region at high and low flowrates, respectively • non-uniform velocity and pressure distributions related to the unbalanced radial force on the impeller

TABLE 3.1 Continued (2)

Authors (Year)	*Experimental Techniques*	*Pump Configuration*	*Operating Range (Spec.)*	*Quantities Measured*	*Main Findings*
Iversen, Rolling & Carlson (1960)	static pressure taps and probe; strain-guaged bearing housing	• commercial pump • shrouded impeller; D_t=258 mm; Z_t=13 mm; β=67.5° log spiral blades; n=9 • single volute	N=1000 rpm; Q=0 to 300 GPM	static pressure in volute; shaft radial force	• confirmed the correlation between the shaft radial force and the volute circumferential pressure distribution • the magnitude and direction of net shaft radial forces varied with flowrate • the radial force was a minimum around the best efficiency point
Fowler (1968)	passage fixed hot-wire probe; surface flow visualisation	• 2-D channels with fixed height of 80 mm and 4° converging (w_1=152 mm), parallel (w_1 =135 mm) and 10° diverging (w_1=94 mm) side walls; • rotation in span-wise direction	$Re=3x10^3$ to $4x10^4$; Rn=0 to 2.1; $Rn=\frac{\omega w_1}{U}$	passage exit velocity	• convergence and divergence affected flow stability and had less effect on flow patterns • the non-uniformity of velocity depended on the rotation number (Rn) and Reynolds number (Re) • flow in the channel sensitive to downstream obstacles and adjacent channels

TABLE 3.1 Continued (3)

Authors (Year)	*Experimental Techniques*	*Pump Configuration*	*Operating Range (Spec.)*	*Quantities Measured*	*Main Findings*
Lennemann & Howard (1970)	hydrogen bubble tracer	• laboratory pump • shrouded and unshrouded impeller with parallel hub and shroud; D_t=457 mm; Z_t=21 mm; β=64° log spiral blades; n=14 • vaneless diffuser	N=140rpm partial capacity (Φ_n=0.118 @140rpm)	N/A	• rotating stall with frequency lower than blade passing frequency at partial capacity influenced by the secondary flow patterns • tip clearance influenced the secondary flow and the stall characteristics in the unshrouded impeller
Howard & Lennemann (1971)	passage fixed hot-film probe; hydrogen bubble tracer	• similar to Lennemann & Howard (1970)	N=140rpm Φ=0.13 (Φ_n=0.118 @140rpm)	primary and secondary velocities	• the deviation of streamwise velocity from those of usual primary flow was related to the secondary flow pattern
Johnston, Halleen & Lezius (1972)	static pressure taps; hydrogen bubble tracer	• rectangular channel with height of 279 mm and width (w_1) of 39 mm • fully developed flow rotating in span-wise direction	Re up to $35x10^3$; Rn up to 0.57	static pressure	• boundary layer on the suction surface stabilised and thicker with the transition to turbulent flow suppressed • large scale vortices developed on the pressure side boundary layer due to local destabilisation

TABLE 3.1 Continued (4)

Authors (Year)	*Experimental Techniques*	*Pump Configuration*	*Operating Range (Spec.)*	*Quantities Measured*	*Main Findings*
Moore (1973)	hot-wire probe; 5-hole pitot tube; static pressure taps	• 2-D diffuser with fixed height and entrance width (w_1) of 76 mm; 15° divergence angle; A_2/A_1=3.1 • rotation in span-wise direction	Re=$5x10^6$ Rn=0.46 to 1.78	mean and rms velocity; flow angle; static pressure	• large wake region on the suction surface at large flowrate and related with the secondary flow along the shroud and hub boundary layer from pressure to suction side • a pressure side eddy was observed at small flowrate
Howard & Kittmer (1975)	passage fixed hot-film probe; hydrogen bubble tracer	• similar to Lennemann & Howard (1970) • β=68° log spiral blades; n=7 • vaneless diffuser	N=140rpm $\Phi=1.11\Phi_n$ (Φ_n=0.134 @140rpm)	primary and secondary velocities	• stream-wise flows similar for the shrouded and unshrouded impellers with no tendency of separation • secondary flow patterns characterised by double vortices and a single vortex for the shrouded and unshrouded impellers, respectively, with the later influenced by tip leakage flow

TABLE 3.1 Continued (5)

Authors (Year)	*Experimental Techniques*	*Pump Configuration*	*Operating Range (Spec.)*	*Quantities Measured*	*Main Findings*
Rothe & Johnston (1976)	static pressure taps; hydrogen bubble tracer	• 2-D diffuser with fixed height of 279 mm and entrance width (w_1) of 39 mm; A_2/A_1=1.4 to 2.6 • rotating in span-wise direction	Re up to $3x10^4$; Rn up to 0.2	static pressure	• the stall pattern was more stable with rotation and occurred only on the suction surface • the suppression of turbulent mixing and shear stresses in the suction boundary layer and the Coriolis acceleration enhanced the stall to occur in the diffuser
Yuasa & Hineda (1979)	microphone; hot wire probe; anechoic chamber	• shrouded impeller with parallel hub and shroud; D_t=278 mm; Z_t=12 mm; β=35°; n=6 • vaneless diffuser	Re=$5x10^5$ Φ=0.116 and 0.206	velocity and pressure behind the impeller discharge	• air replaced water as working fluid • pressure fluctuations affected by both viscous wake and circulation within blade passages • velocity and pressure fluctuation dominated by blade passing frequency and its harmonics with amplitudes decreasing with harmonic number and radius

TABLE 3.1 Continued (6)

Authors (Year)	*Experimental Techniques*	*Pump Configuration*	*Operating Range (Spec.)*	*Quantities Measured*	*Main Findings*
Murakami, Kikuyama & Asakura (1980)	3-hole yaw probe; oil film surface flow visualisation	• shrouded impeller; D_t=339 mm; Z_t=23 mm; β=63° log spiral blades; n=3 and 7 • single volute	N=400rpm Φ=0.33 to 1.28Φ_n (Φ_n=0.098 @400rpm)	primary and secondary velocities; static pressure	• flow of the 7-blade impeller was better guided and coincided well with prediction by potential theory • flow of the 3-blade impeller deviated from prediction at both design and off-design operations with separation on pressure surface at inner radii • Busemann and Stodola slip factors correlated well with measurements for the 7-blade impeller, but under-estimated for the 3-blade impeller
Engeda & Rautenberg (1987)	pressure transducer; torque meter	• five commercial pumps • shrouded and unshrouded mixed-flow impeller; D_t=404 to 185 mm; Z_t=17 to 60 mm; β=62° to 66°; n=6 • single volute	N_s=0.33, 0.57, 0.83, 1.23 and 1.51; δ/Z_t=0.01 to 0.16	head; flowrate; shaft power	• increase of tip clearance caused a decrease of head, flowrate, input power and efficiency • no evident dependence of tip clearance effect on specific speed

TABLE 3.2 Investigations of flows in centrifugal pumps made by laser velocimetry

Authors (Year)	*Experimental Techniques*	*Pump Configuration*	*Operating Range (Spec.)*	*Quantities Measured*	*Main Findings*
Thomas, Kostrzewsky & Flack (1986)	LDV	• laboratory pump • shrouded impeller with parallel hub and shroud; D_t=203.2 mm; Z_t=12.7 mm; β=74° log spiral blades; n=4 • 2-D single volute	Φ=1.2 and 1.6Φ_n	V, W	• impeller replaced by two 32-vane swirlers to simulate the discharge flows • radial and circumferential non-uniformity of velocity in the volute attributed to geometric mismatching of discharge flow angles and volute angle
Hamkins & Flack (1987)	LDV	• laboratory pump • shrouded and unshrouded impeller with parallel hub and shroud; D_t–203.2 mm; Z_t=12.7 mm; β=74° log spiral blades; n=4 • 2 D single volute	N=620rpm Φ=0.4 to 1.35Φ_n; δ/Z_t=0.06; 0.08 (N_{sUS} =1200, Φ_n=0.063)	V, W	• passage vortex in the unshrouded impeller was caused by tip leakage and relative wall motion • slip factor decreased with radius and decreased with flowrate • angular momentum increases uniformly with radius at impeller-volute matched flowrate but had a peak at inner radius at lower flowrate

TABLE 3.2 Continued (1)

Authors (Year)	*Experimental Techniques*	*Pump Configuration*	*Operating Range (Spec.)*	*Quantities Measured*	*Main Findings*
Flack, Hamkins & Brady (1987)	LDV	• similar to Hamkins & Flack (1987)	N=620rpm Φ=0.2 to $1.35\Phi_n$ (N_{sUS} =1200, Φ_n=0.063)	V, W, v', w', $\overline{v'w'}$	• more uniform velocity and lower turbulence level with shrouded impeller • normal stress higher with negative shear stress values on the suction surface
Sideris, van den Braembussche (1987)	LDV; static pressure taps	• shrouded mixed flow impeller; D_t=204 mm; Z_t=20 mm; β=63.5° log spiral blades; n=8 • vaneless diffuser followed by a volute	N=300rpm Q=0.0026, 0.0054 and 0.0066 m^3/s	V, W and static pressure in vaneless diffuser	• static pressure in the volute increased, near constant and decreased with circumferential positions for low, medium and high flowrates, respectively. • circumferential variations of velocity in the diffuser due to pressure were confirmed
Miner, Beaudoin & Flack (1989)	LDV	• similar to Hamkin & Flack (1987); • passage height increased to Z_t=24.6 mm	N=620rpm Φ=0.4 to $1.06\Phi_n$ (N_{sUS} =1583, Φ_n=0.063)	V, W	• non-axisymmetric impeller flow at design flowrate • radial flow reversal at 40% design flowrate • free-vortex-like flow in the volute with blade passing rapidly damped with radius

TABLE 3.2 Continued (2)

Authors (Year)	*Experimental Techniques*	*Pump Configuration*	*Operating Range (Spec.)*	*Quantities Measured*	*Main Findings*
Paone, Riethmuller, van den Braembussche (1989)	PIDV	• similar to Sideris & van den Braembussche (1987)	N=300rpm Q=0.0026, 0.0054, 0.0066 m^3/s	Instan-taneous velocity vectors in vaneless diffuser	• well guided flow at high flowrate • flow separation on suction surface at low flowrate • slip factors of 0.9 and 0.55 at impeller discharge for low and high flowrate, respectively
Davis & Flack (1990)	LDV	• laboratory vaned diffuser with swirler generated inlet flow and downstream baffle vanes • D_1=270 mm; D_2=390 mm; Z_t=12.7 mm; β=70°; n=0, 2,4, 6 and 8	$\Phi > \Phi_n$	V, W, v', w'	• swirler discharge flow had 14° incident angle to the diffuser vane to represent the condition of larger-than-design flowrate • large region of separation behind the diffuser vanes with counter rotating vortex pair

TABLE 3.3 Experimental conditions

Flow conditions	**I**	**II**	**III**	**IV**
Q (m^3/s)	2.52×10^{-3}	1.57×10^{-3}	8×10^{-4}	4×10^{-4}
Q/Q_n	0.93	0.57	0.29	0.15
Φ	0.054	0.034	0.017	0.0086
Γ	0.446	0.512	0.554	0.568
N_s	0.425	0.304	0.203	0.142
N_{sUS}	917	647	443	303
Inlet pipe				
U_i (m/s)	2.47	1.54	0.79	0.39
Re_i	54500	34000	17300	8670
Exit pipe				
U_e (m/s)	3.94	2.46	1.25	0.63
Re_e	69000	43000	22000	11000
Impeller passages				
V_R/W_t	0.056	0.035	0.018	0.009
W_R/W_t	0.9	0.94	0.97	0.98

TABLE 3.4 Characteristics of the laser-Doppler velocimeter

Transmitting optics		
Laser: 1 watt Ar-ion laser		
max. operating power	400	mW
wave-length	514.5	nm
Beam intersection angle	9.69	deg
Measurement volume diameter at $1/e^2$ intensity	52	μm
Measurement volume length at $1/e^2$ intensity	620	μm
Fringe spacing	3.04	μm
Number of fringes	17	
Frequency shift	0-13	MHz
Receiving optics		
Focal length of collimating lens	200	mm
Focal length of focusing lens	100	mm
Diameter of pinhole	100	μm
Effect length of measurement volume for 90° collection angle	200	μm

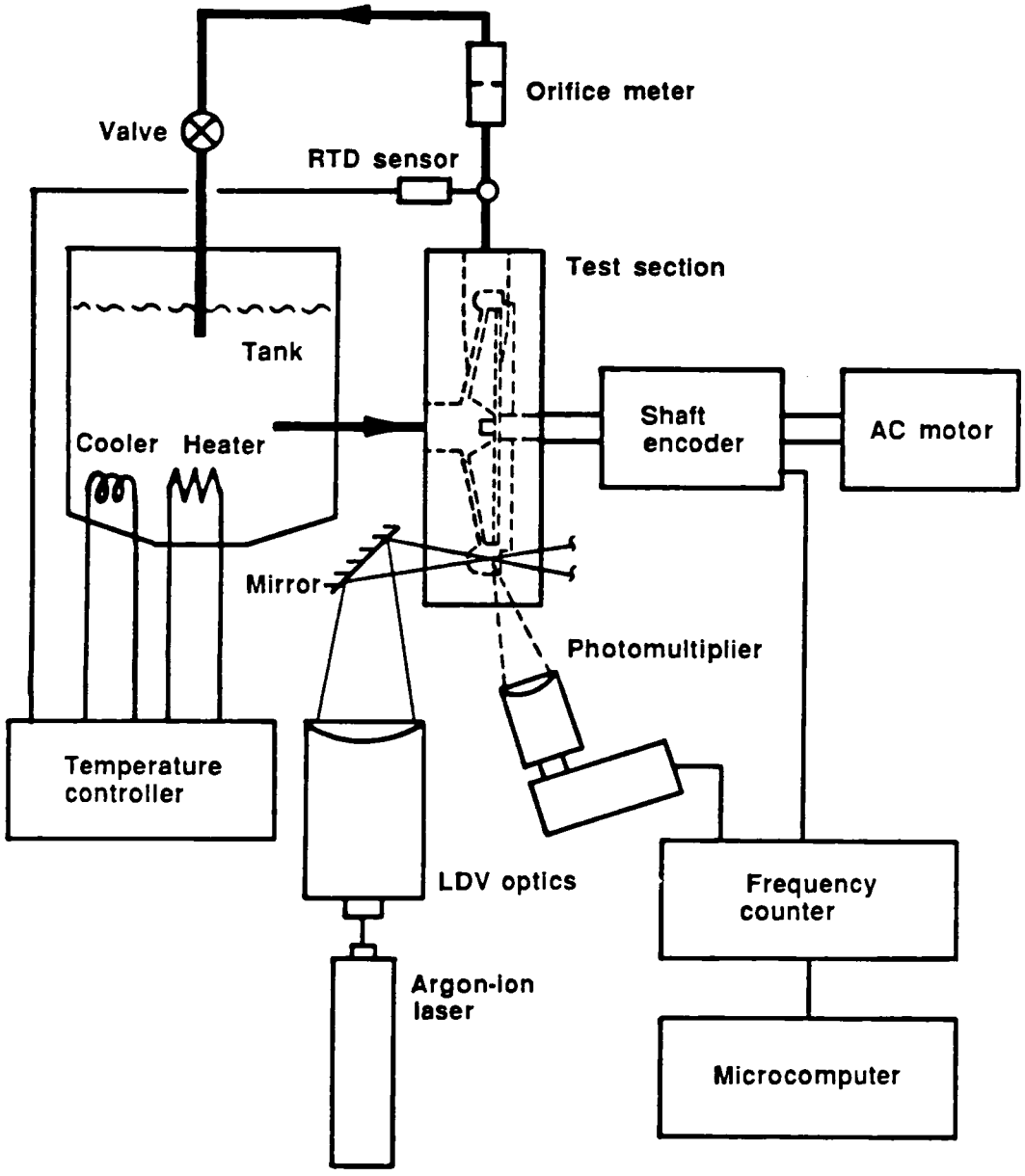


FIGURE 3.1 Flow configuration and instrumentation.

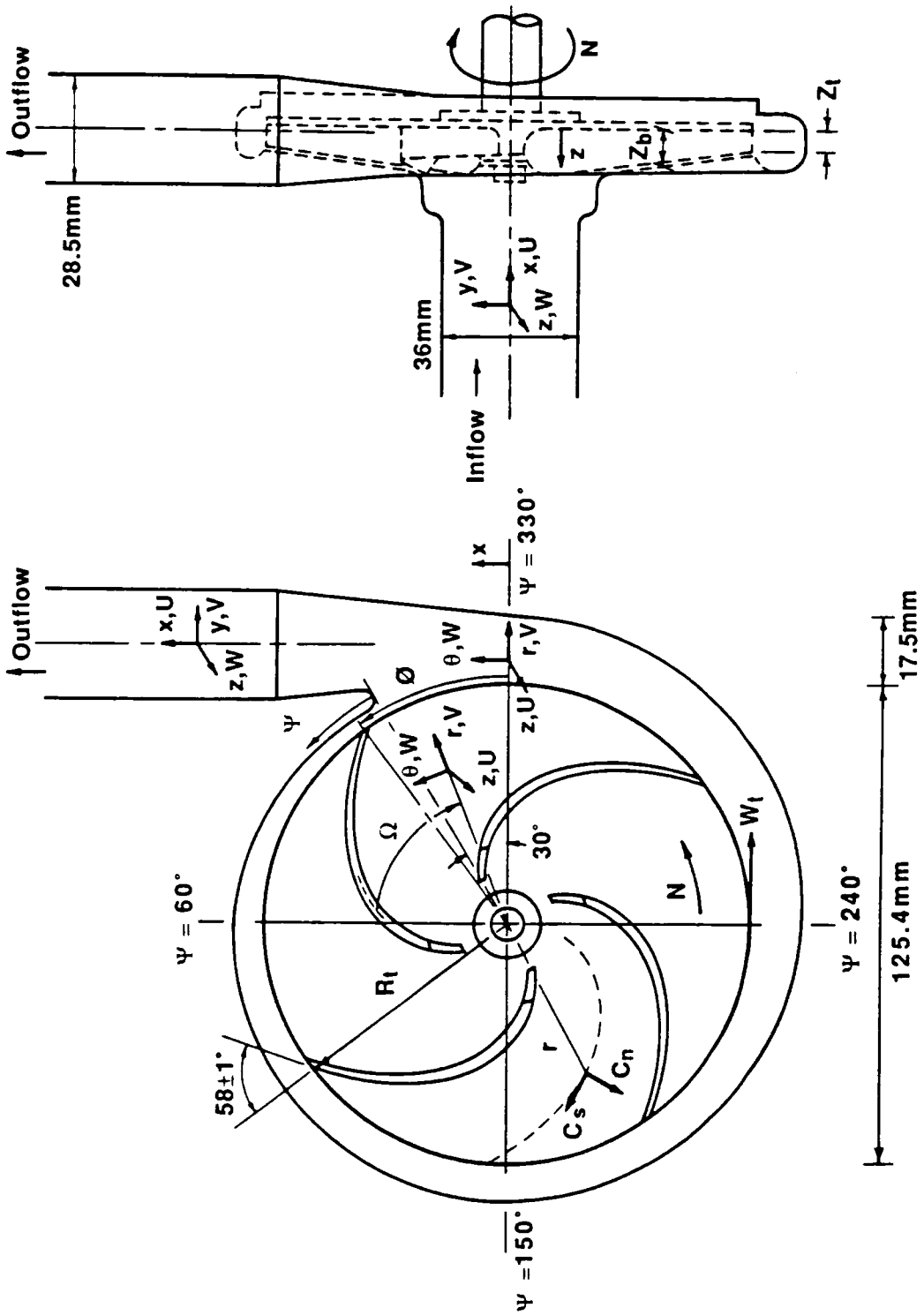


FIGURE 3.2 Dimensions of the centrifugal pump and coordinate systems.

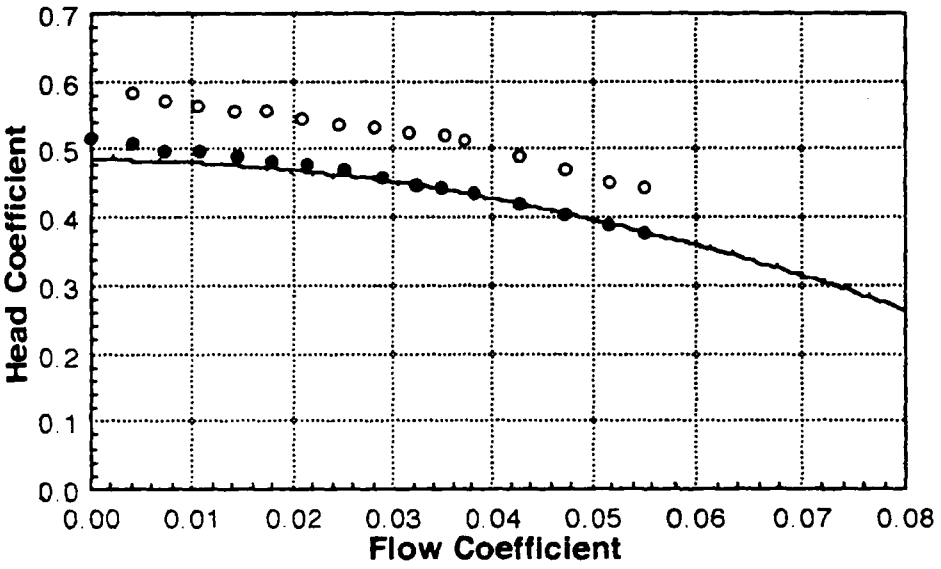


FIGURE 3.3 Head coefficient of the pump running at 2910 rpm. (o perspex casing; • metal casing; —— manufacturer's specification)

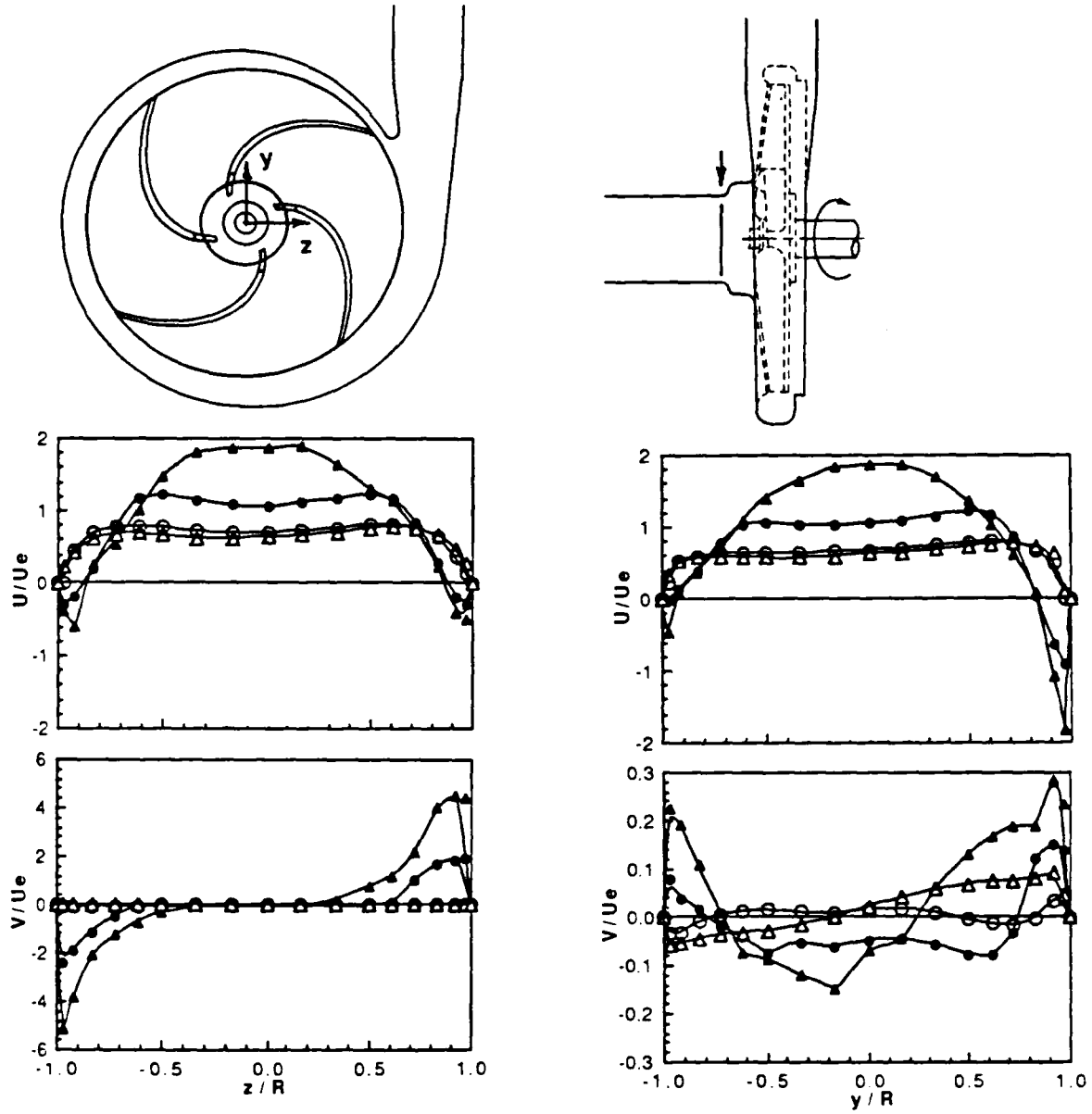


FIGURE 3.4 Radial profiles of x-component (U/U_e) and y-component (V/U_e) of mean velocity at the axial station z/D_i of 0.7 in the inlet pipe and **flowrates** of $0.93Q_n$ (Δ), $0.57Q_n$ (o), $0.29Q_n$ (•) and $0.15Q_n$ (▲).

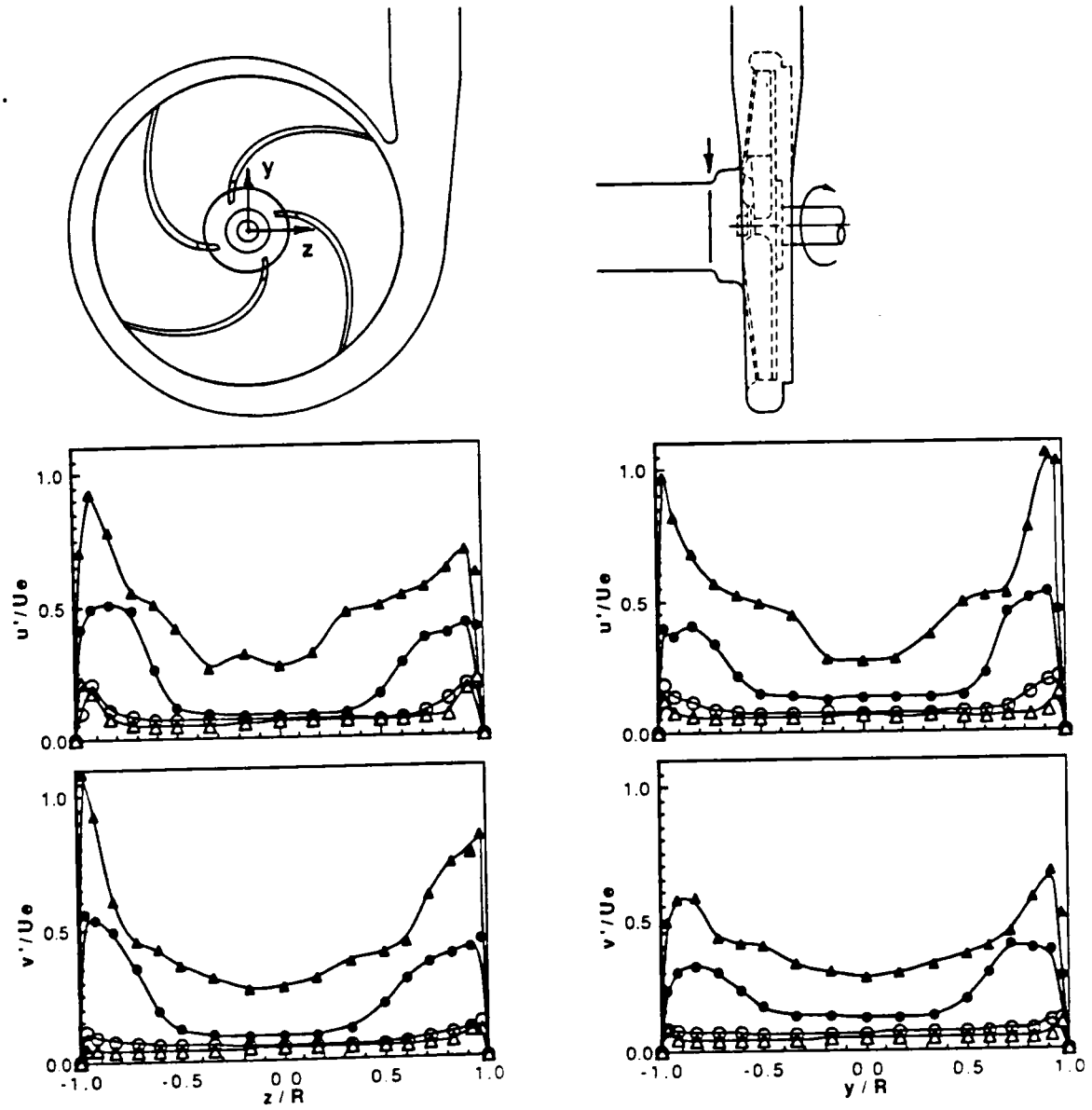


FIGURE 3.5 Radial profiles of x-component (u'/U_e) and y-component (v'/U_e) of rms velocity at the axial station z/D_i of 0.7 in the inlet pipe and flowrates of $0.93Q_n$, $0.57Q_n$, $0.29Q_n$ and $0.15Q_n$. (see Figure 3.4 for symbols)

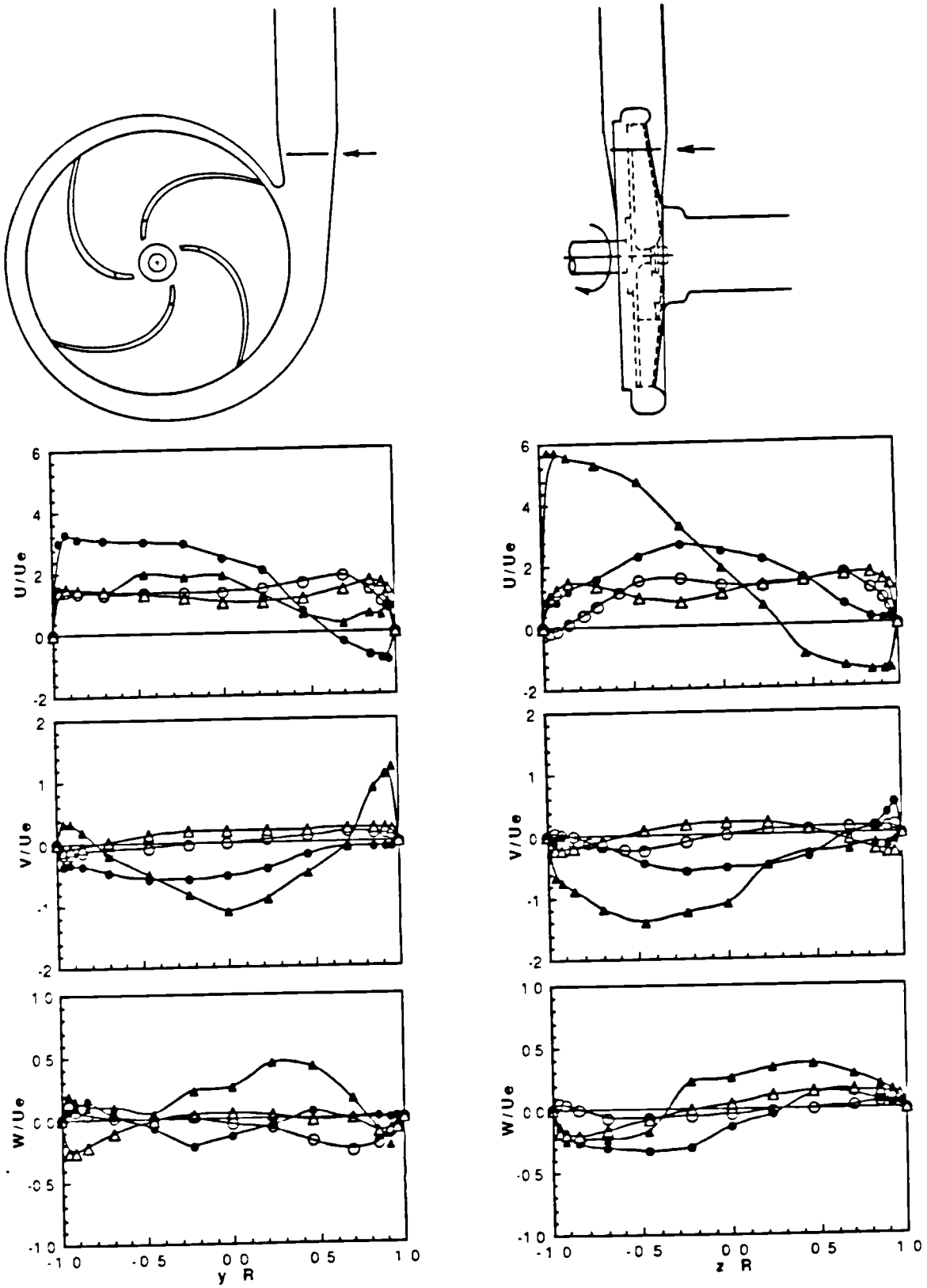


FIGURE 3.6 Radial profiles of x-component (U/U_e) and y-component (V/U_e) of mean velocity at the axial station x/D_e of 1.8 in the exit pipe and flowrates of $0.93Q_n$, $0.57Q_n$, $0.29Q_n$ and $0.15Q_n$. (see Figure 3.4 for symbols)

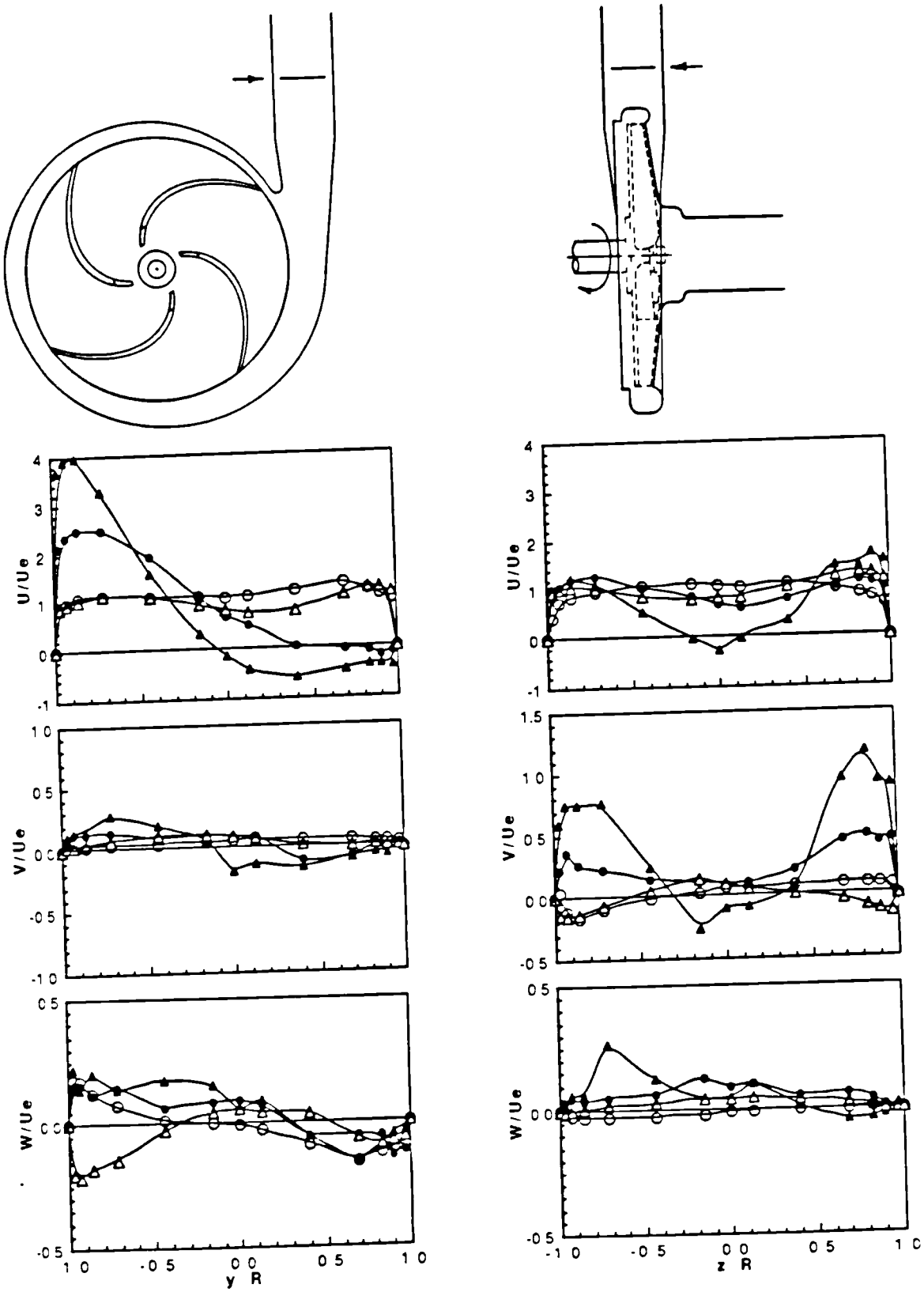


FIGURE 3.7 Radial profiles of x-component (U/U_e) and y-component (V/U_e) of mean velocity at the axial station x/D_e of 3.2 in the exit pipe and flowrates of $0.93Q_n$, $0.57Q_n$, $0.29Q_n$ and $0.15Q_n$. (see Figure 3.4 for symbols)

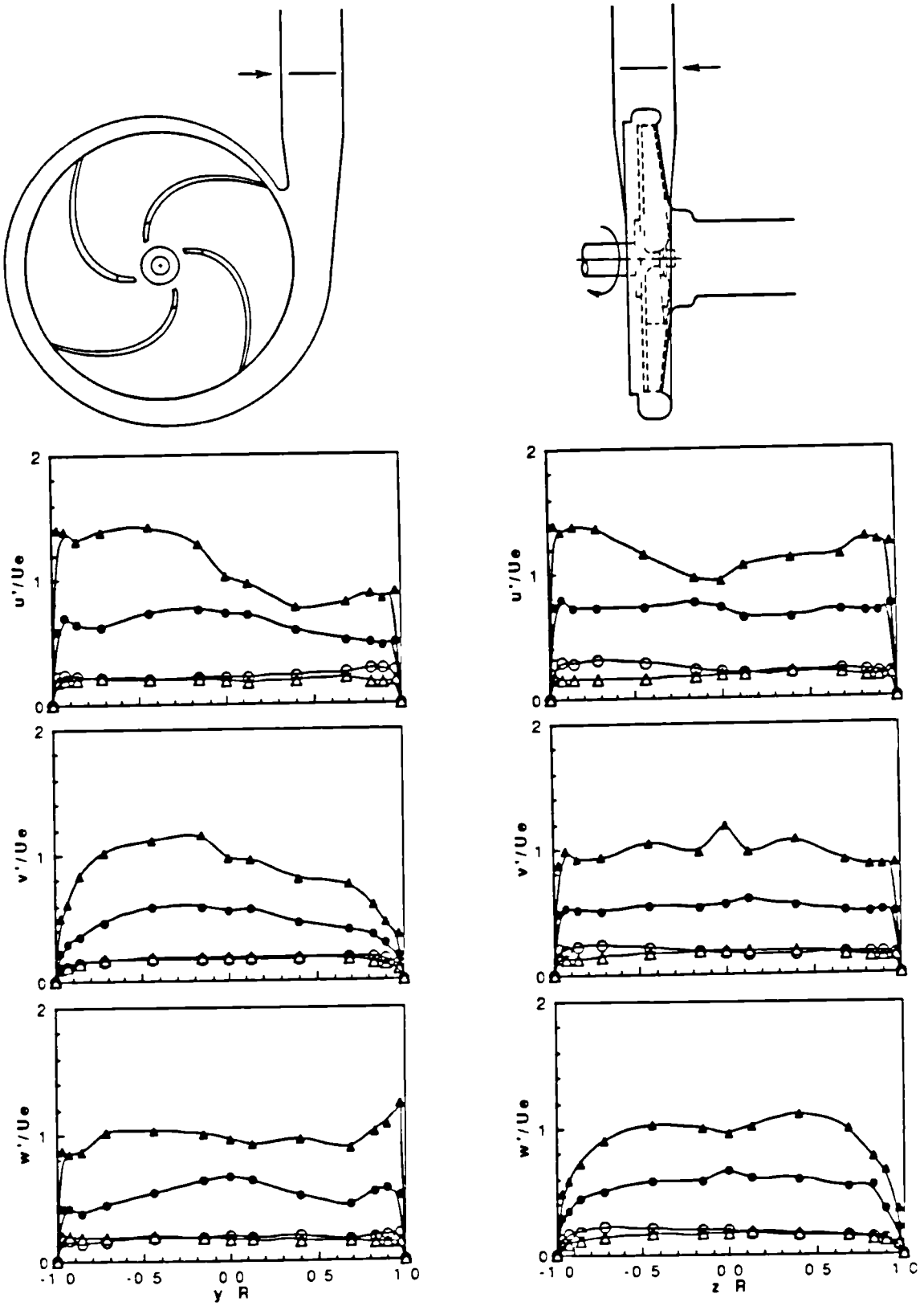


FIGURE 3.8 Radial profiles of x-component (u'/U_e) and y-component (v'/U_e) of rms velocity at the axial station x/D_e of 3.2 in the exit pipe and flowrates of $0.93Q_n$, $0.57Q_n$, $0.29Q_n$ and $0.15Q_n$. (see Figure 3.4 for symbols)

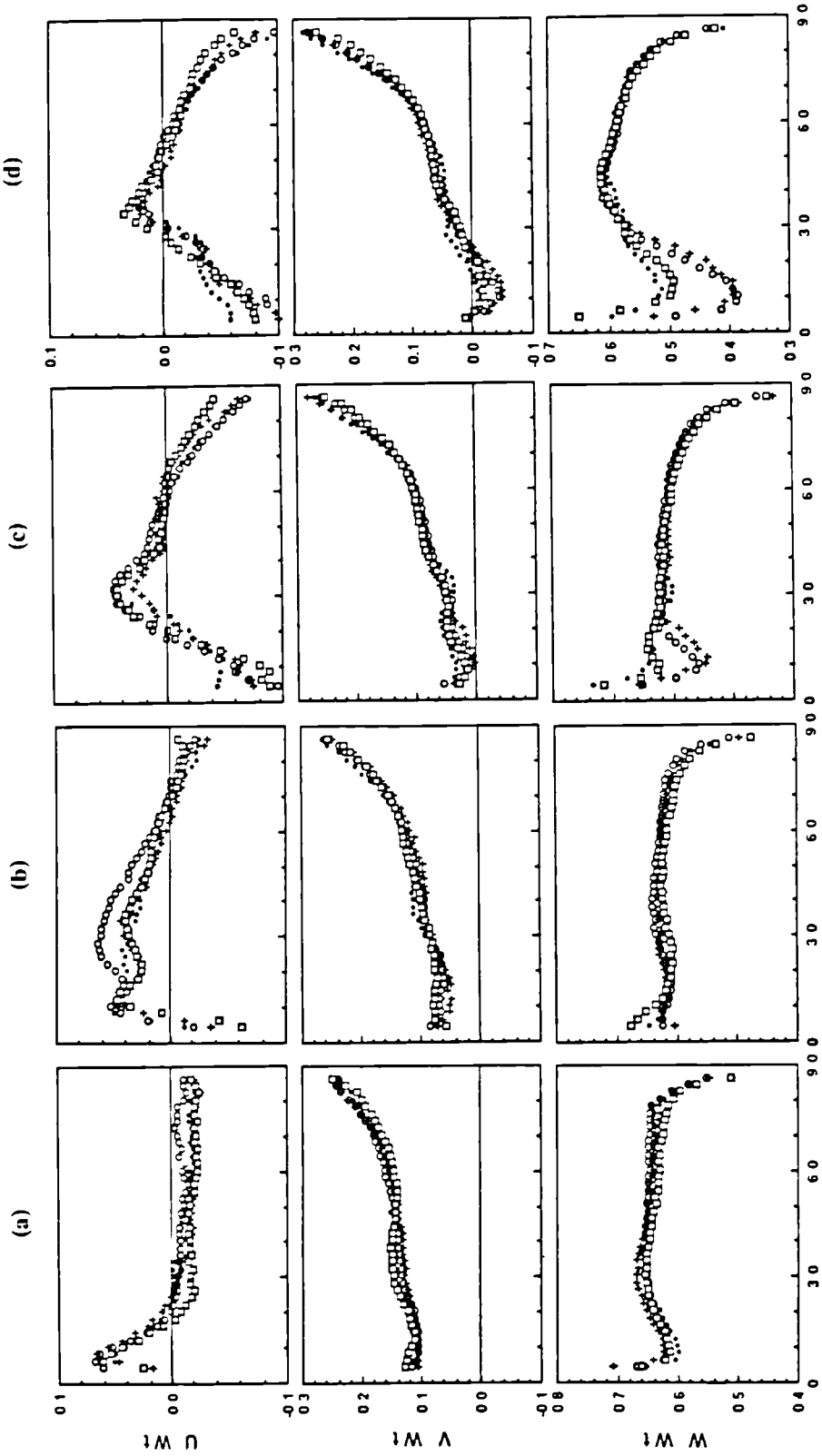


FIGURE 3.9 Blade-to-blade distributions of angle-resolved axial (U/W_t), radial (V/W_t) and tangential (W/W_t) components of mean velocity on the mid-plane of the impeller passage at discharge, z/Z_t=0.5 and r/R_t=1, measured at Ψ=330 degrees and the flowrates of (a)$0.93Q_n$,(b) $0.57Q_n$, (c)$0.29Q_n$ and (d)$0.15Q_n$. Symbols for each of the four impeller passages.

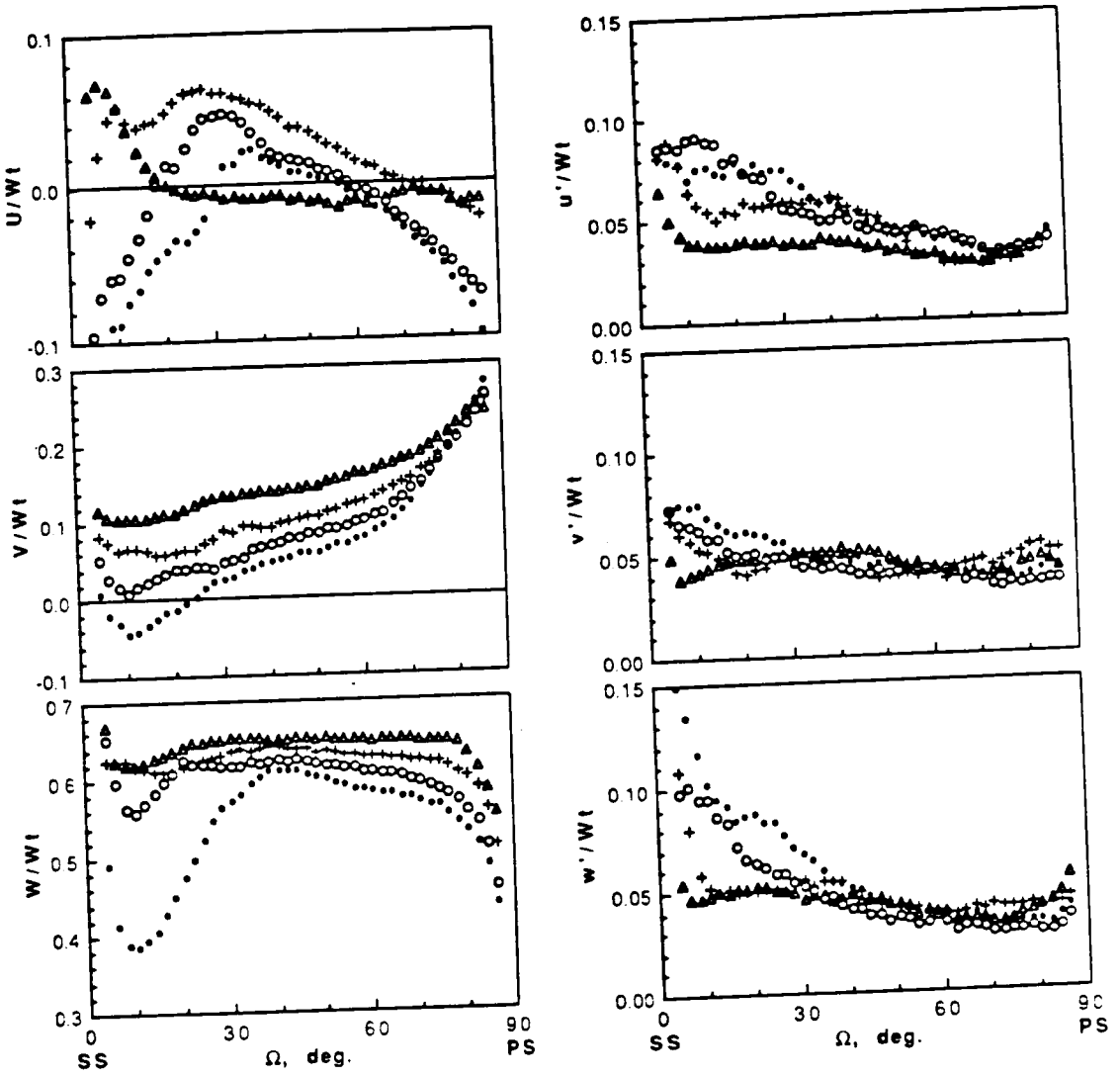


FIGURE 3.10 Blade-to-blade distributions of angle-resolved axial (U/W_t and u'/W_t), radial (V/W_t and v'/W_t) and tangential (W/W_t and w'/W_t) components of mean and rms velocities on the mid-plane of the impeller passage at the discharge, $r/R_t=1$ and $z/Z_t=0.5$, measured at $\Psi=330$ degrees and the flowrates of $0.93Q_n$(▲), $0.57Q_n$(+), $0.29Q_n$(o) and $0.15Q_n$(•).

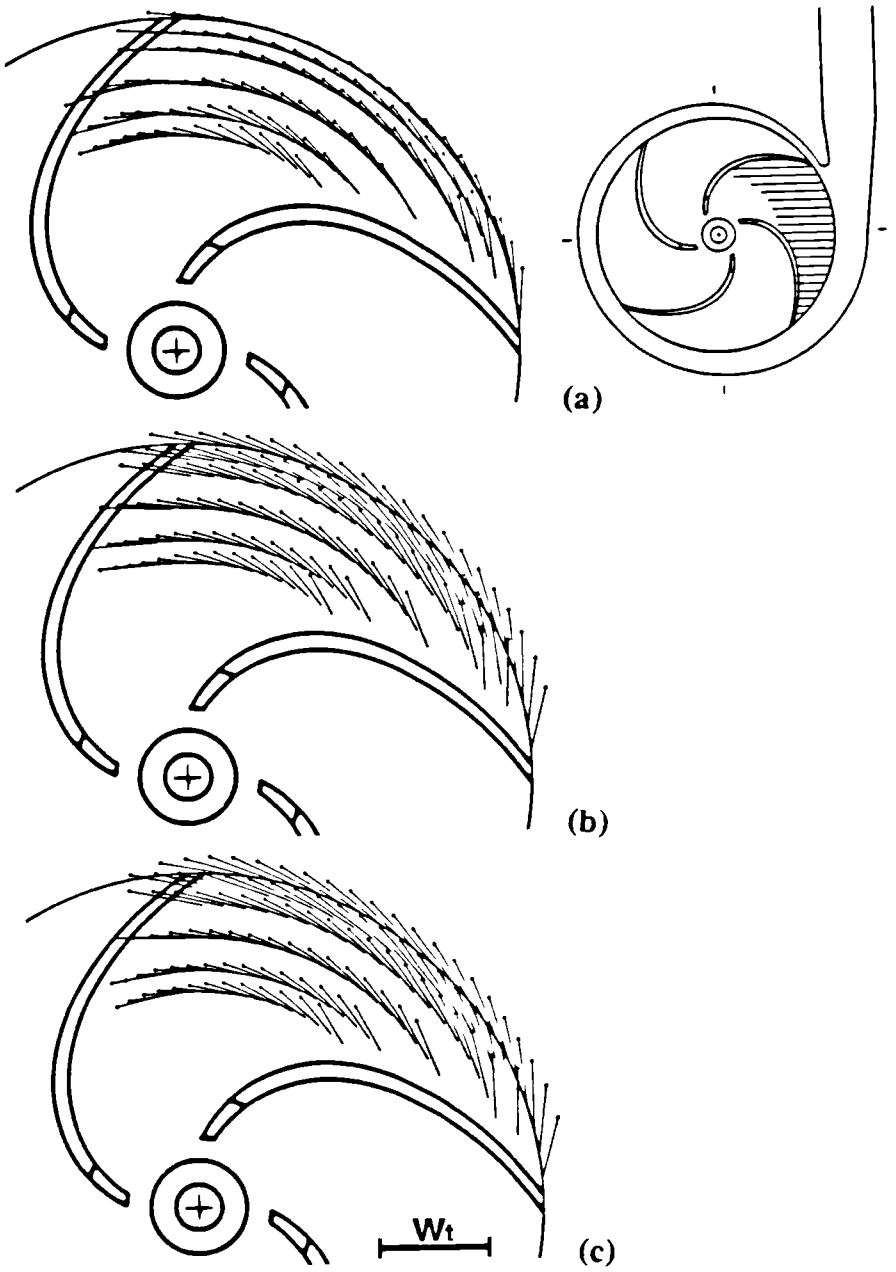


FIGURE 3.11 Mean velocity vectors of the absolute flow in an impeller passage at the flowrate of $0.93Q_n$ measured at Ψ=330 degrees. Radial locations r/R_t=0.65, 0.71, 0.81, 0.9, 0.95 and 1.
(a)plane 1 mm from the shroud
(b)the mid-plane of the blade height
(c)plane 1 mm from the impeller hub

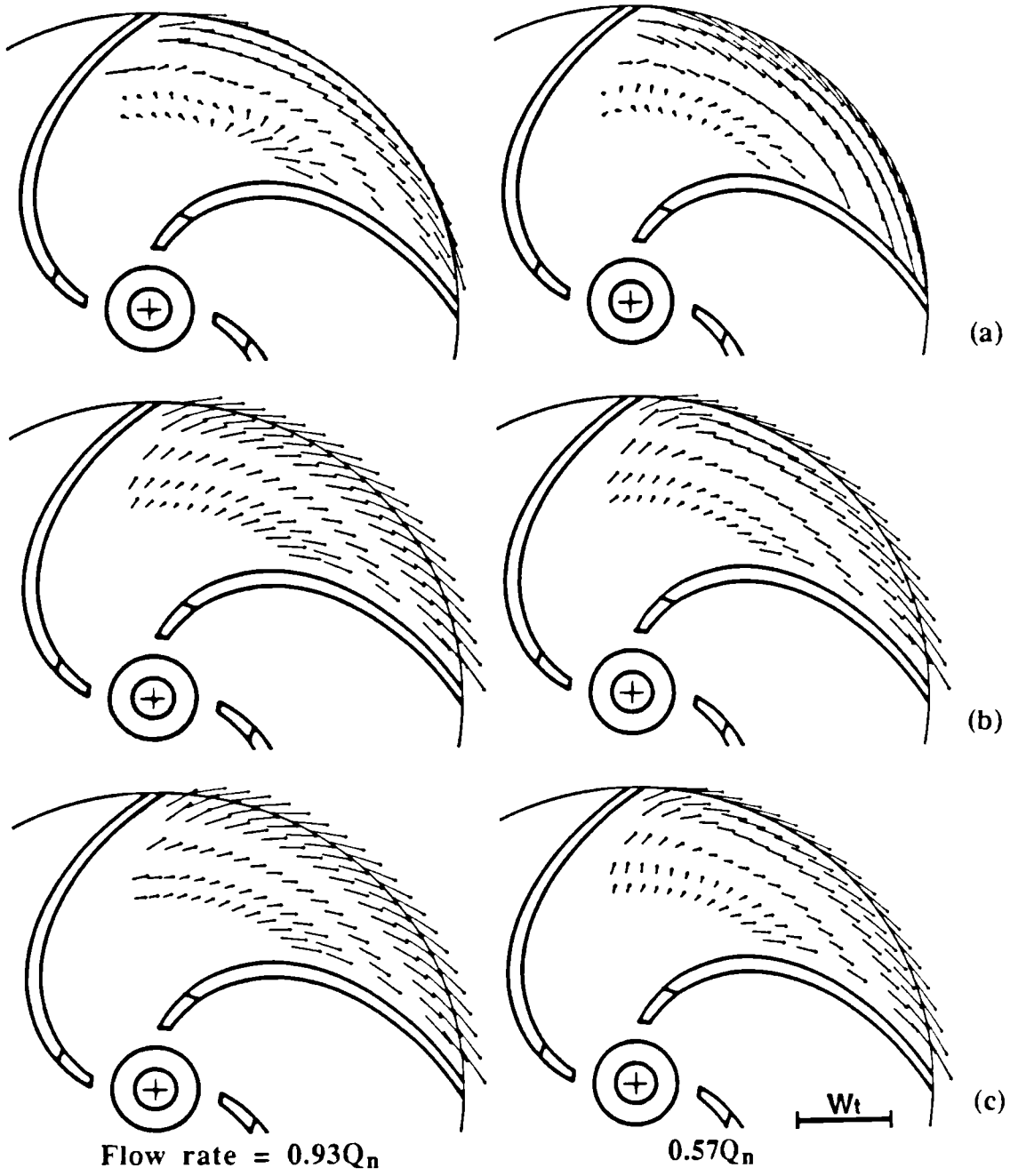


FIGURE 3.12 Mean velocity vectors of the relative flow in an impeller passage at the flowrates of $0.93Q_n$, $0.57Q_n$, $0.29Q_n$ and $0.15Q_n$ measured at Ψ=330 degrees.
(see Figure 3.11 for radial locations)
(a) plane 1 mm from the shroud
(b) the mid-plane of the blade height
(c) plane 1 mm from the impeller hub

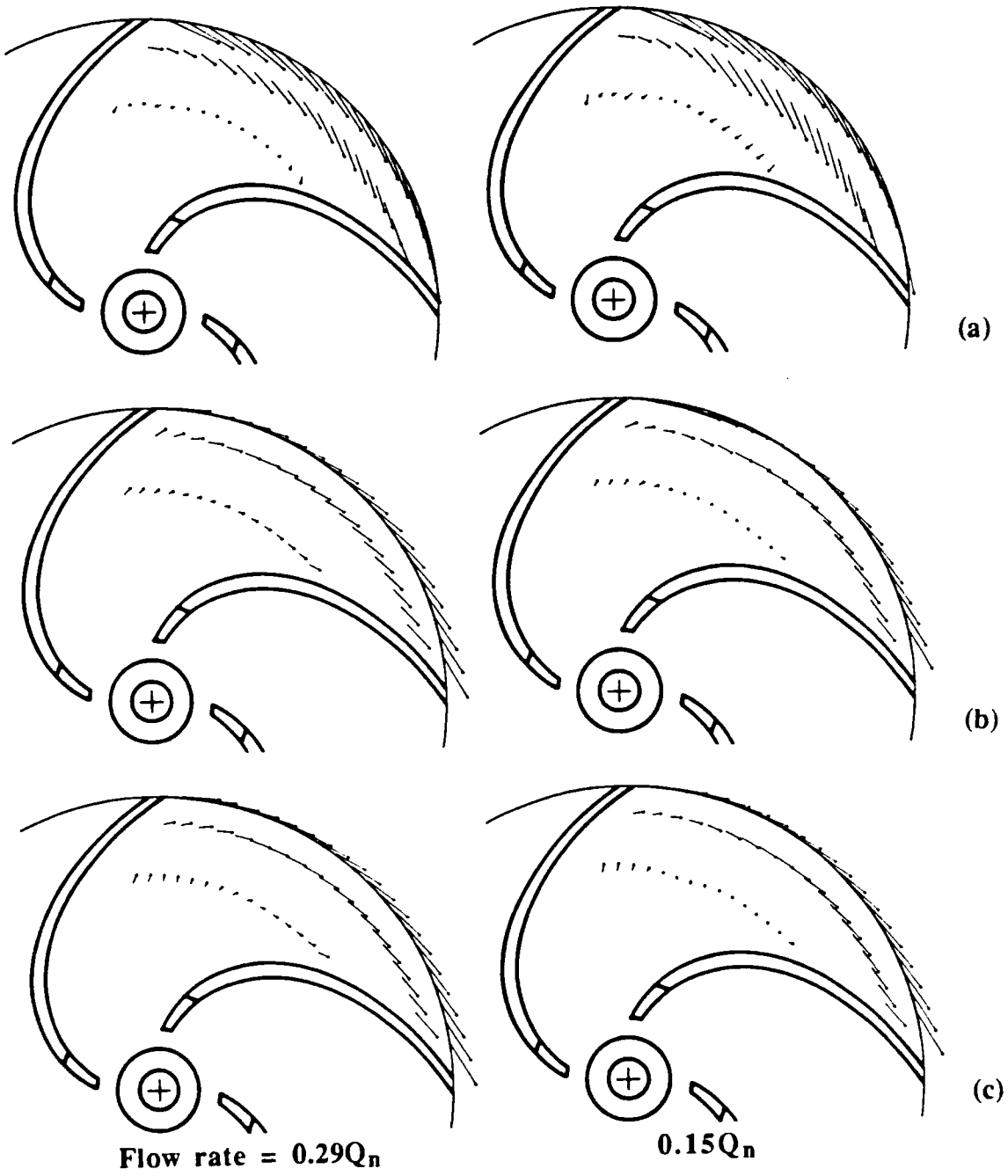


FIGURE 3.12 Continued.

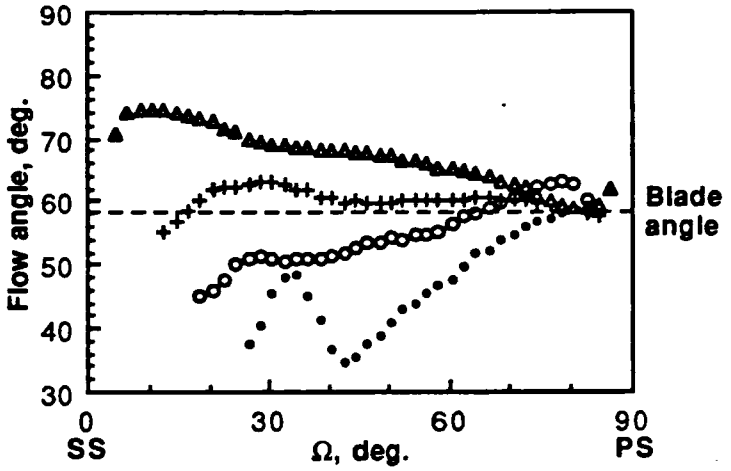


FIGURE 3.13 Blade-to-blade distributions of mean flow angle on the mid-plane of the impeller passage, z/Z_t=0.5, at the flow-rate of $0.93Q_n$ measured at Ψ=330 degrees with the radial locations r/R_t=0.7(•), 0.8(o), 0.9(+) and 1(Δ).

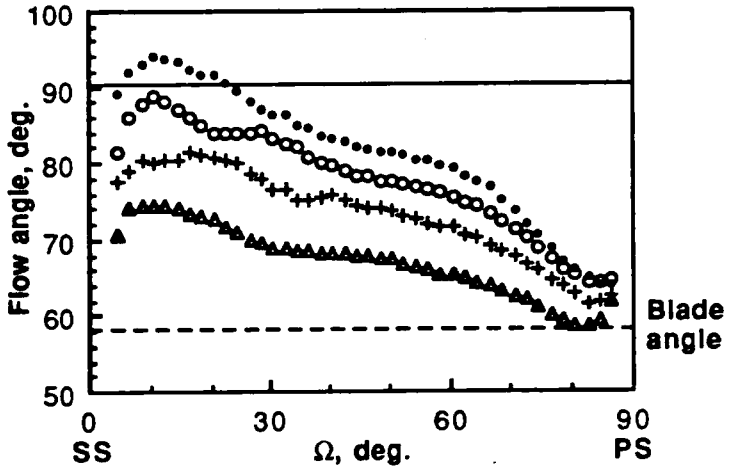


FIGURE 3.14 Blade-to-blade distributions of mean flow angle on the mid-plane of the impeller passage at discharge, z/Z_t=0.5 and r/R_t=1, measured at Ψ=330 degrees.
(see Figure 3.10 for symbols)

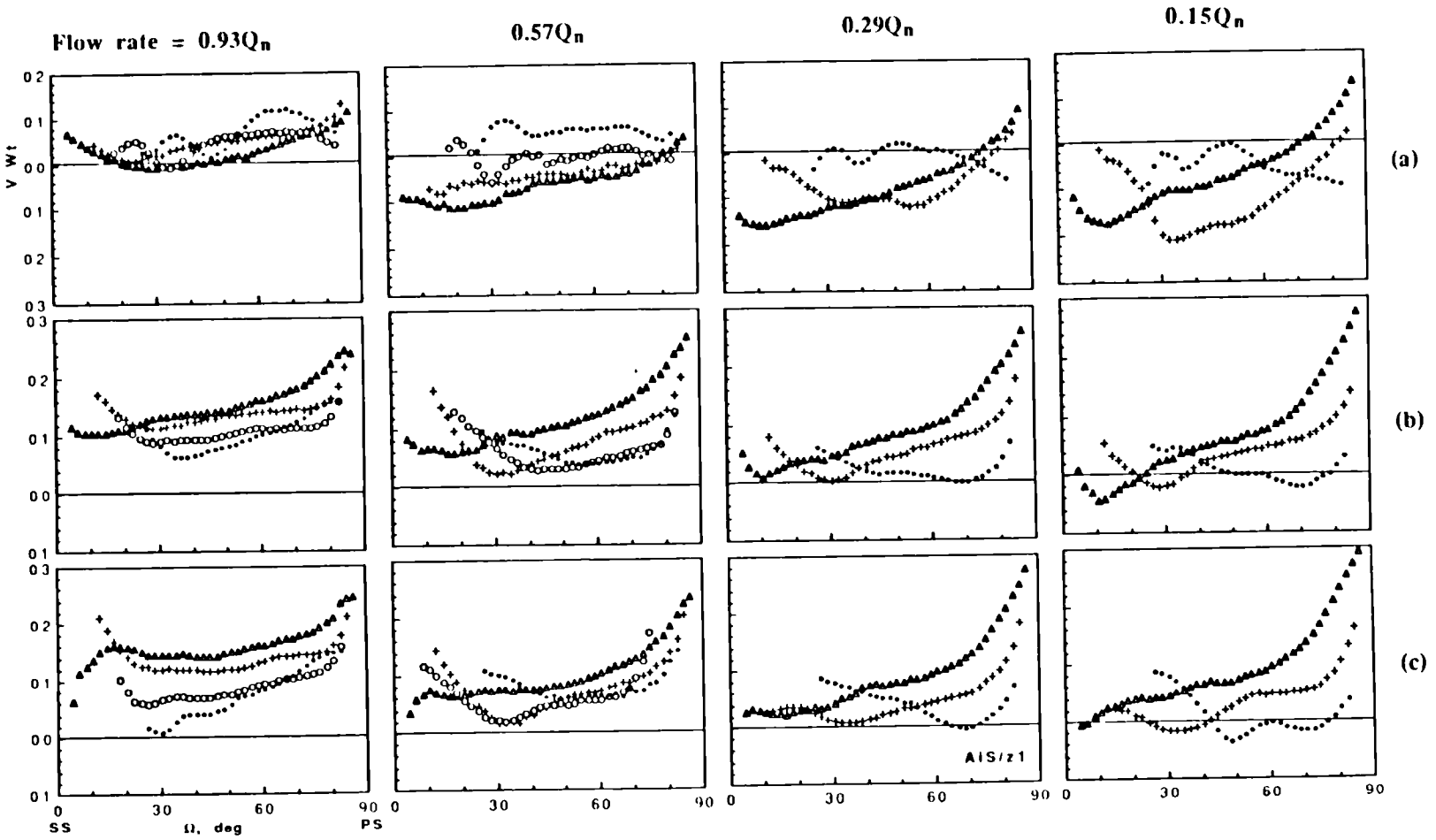


FIGURE 3.15 Blade-to-blade distributions of angle-resolved radial component of mean velocity (V/W_t) at the flowrates of $0.93Q_n$, $0.57Q_n$, $0.29Q_n$ and $0.15Q_n$ measured at Ψ=330 degrees. (see Figure 3.13 for symbols)
(a) plane 1 mm from the shroud
(b) the mid-plane of the blade height
(c) plane 1 mm from the impeller hub

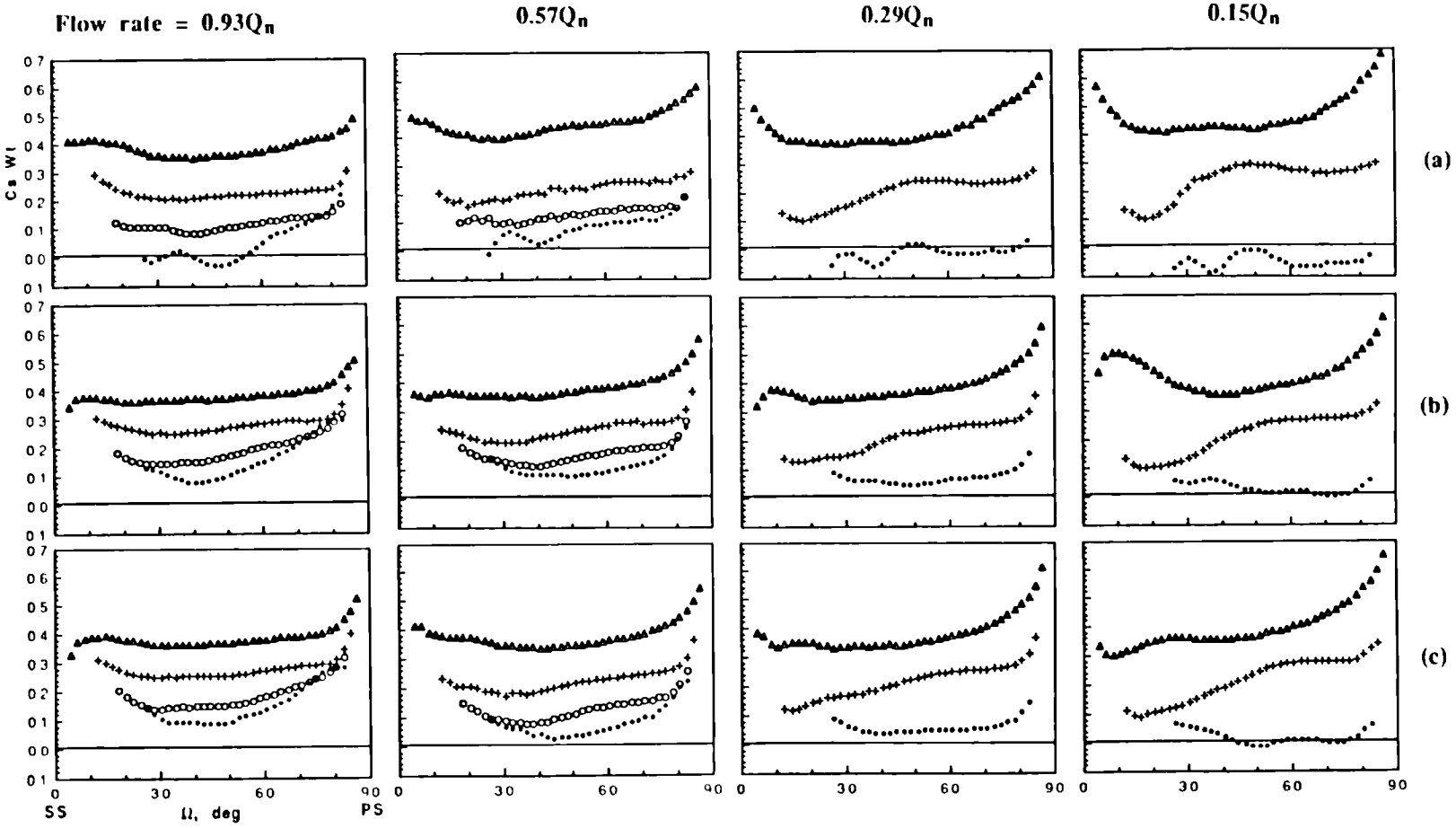


FIGURE 3.16 Blade-to-blade distributions of angle-resolved streamwise component of mean velocity (C_s/W_t) at the flow-rates of $0.93Q_n$, $0.57Q_n$, $0.29Q_n$ and $0.15Q_n$ measured at Ψ=330 degrees. (see Figure 3.13 for symbols)
(a) plane 1 mm from the shroud
(b) the mid-plane of the blade height
(c) plane 1 mm from the impeller hub

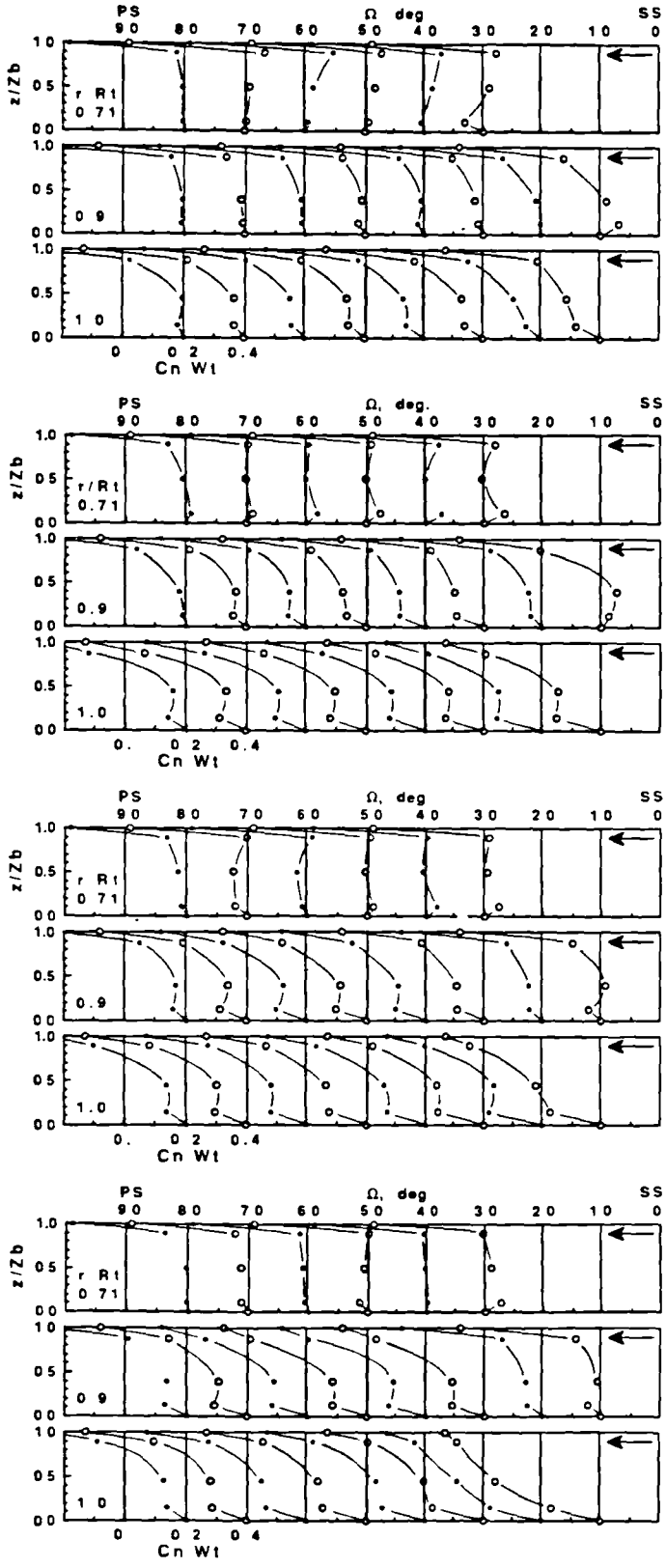


FIGURE 3.17 Angle-resolved cross-stream mean velocity (C_n/W_t) in an impeller passage measured at Ψ=330 degrees with the radial planes of r/R_t of 0.71, 0.9 and 1 and the flowrates of (a)$0.93Q_n$, (b)$0.57Q_n$, (c)$0.29Q_n$ and (d)$0.15Q_n$.

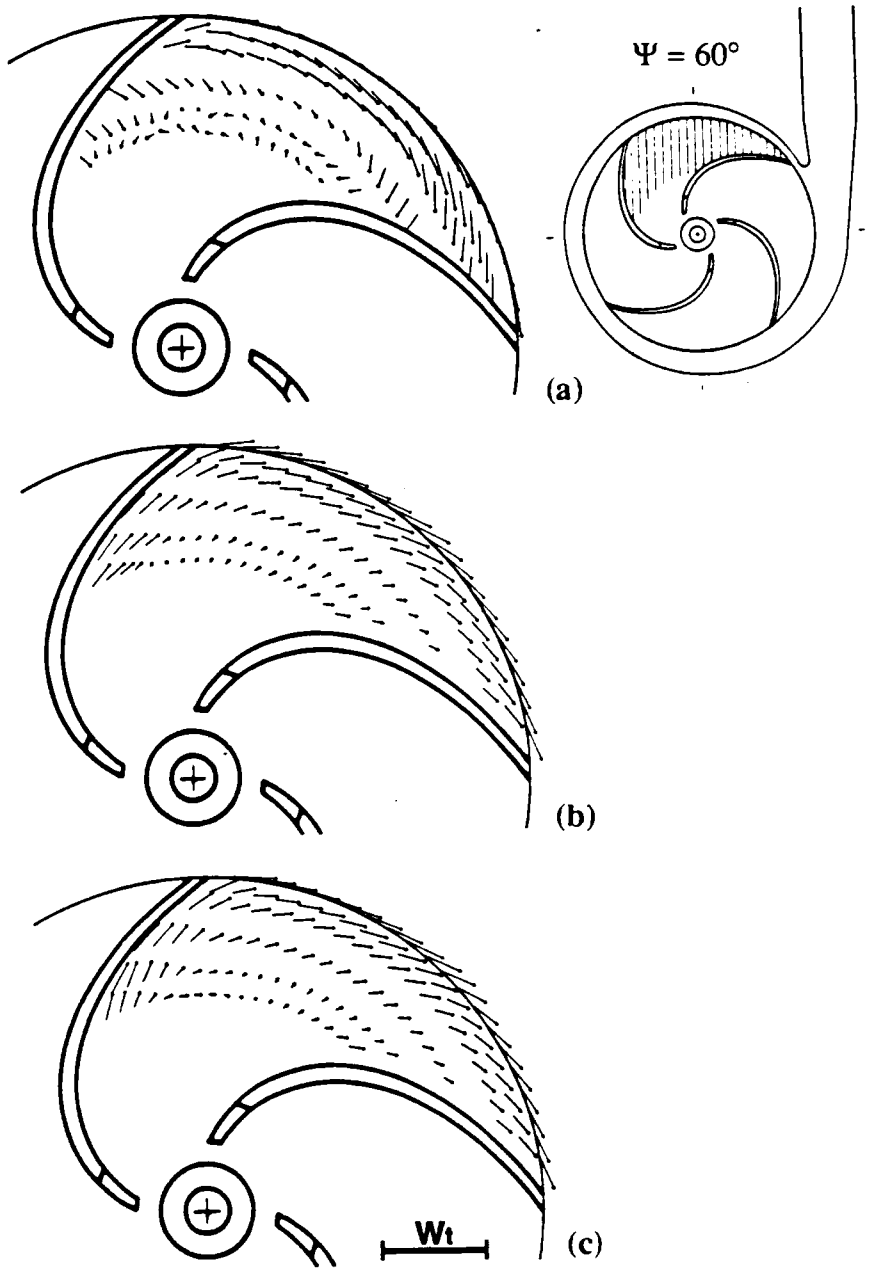


FIGURE 3.18 Mean velocity vectors of the relative flow in an impeller passage at the **flowrate** of $0.57Q_n$ measured at Ψ=60 and 240 degrees. (see Figure 3.11 for radial locations)
(a) plane 1 mm from the shroud
(b) the mid-plane of the blade height
(c) plane 1 mm from the impeller hub

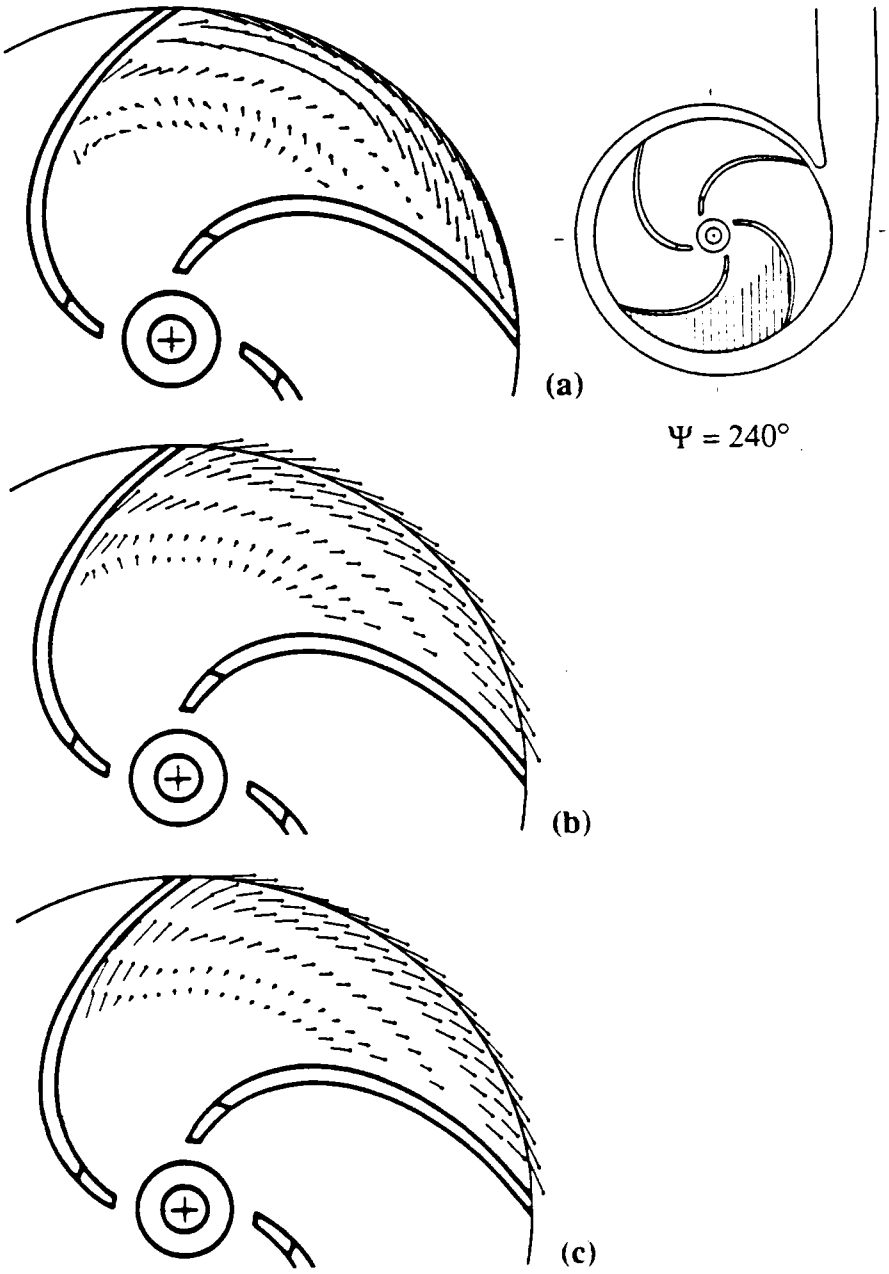


FIGURE 3.18 Continued.

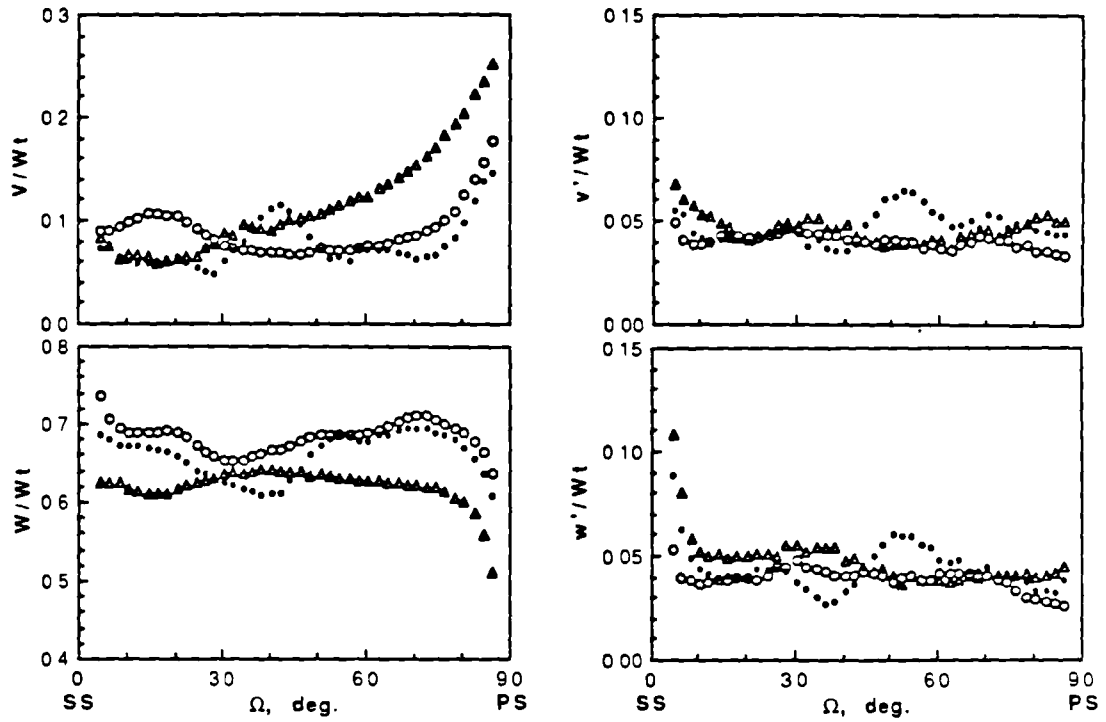


FIGURE 3.19 Blade-to-blade distributions of angle-resolved radial (V/W_t and v'/W_t) and tangential (W/W_t and w'/W_t) components of mean and rms velocities on the mid-plane of the impeller passage at discharge, z/Z_t=0.5 and r/R_t=1, at the flowrate of $0.57Q_n$ measured at Ψ=60(•), 240(o) and 330(Δ) degrees.

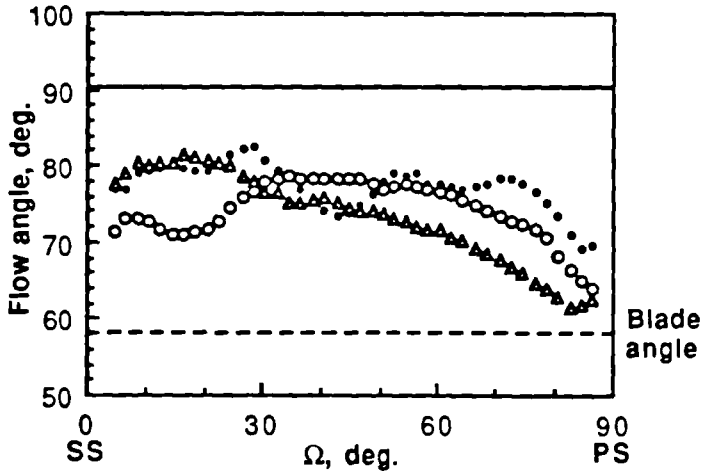


FIGURE 3.20 Blade-to-blade distributions of flow angle on the mid-plane of the impeller passage at discharge, z/Z_t=0.5 and r/R_t=1, at the flowrate of $0.57Q_n$ measured at Ψ=60, 24 and 330 degrees. (see Figure 3.19 for symbols)

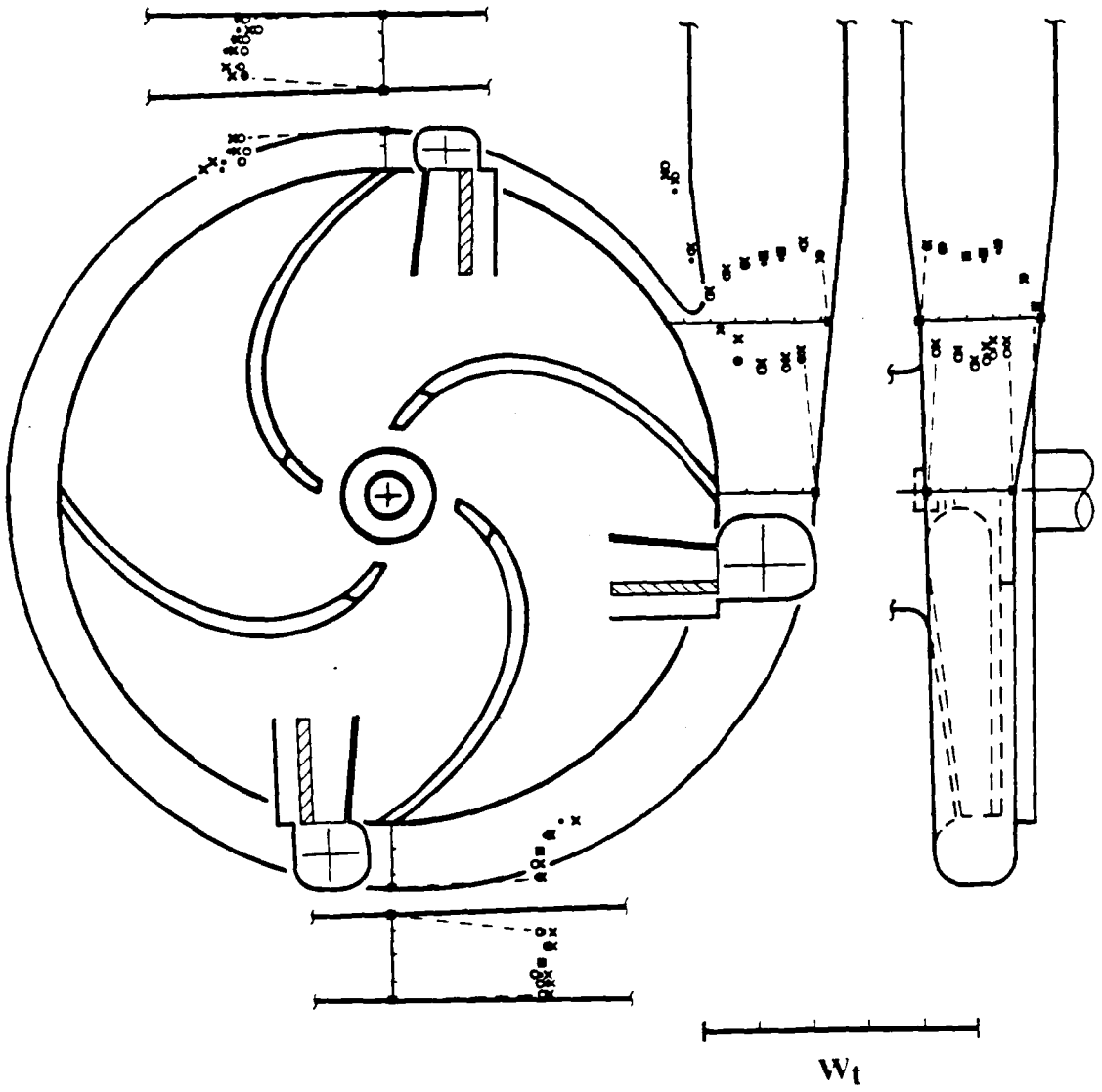


FIGURE 3.21 Angle-resolved tangential component of mean velocity (W/W_t) in the volute passage at the flowrate of $0.57Q_n$. Impeller shaft angles Ø=0(o), 30(•) and 70(×) degrees.

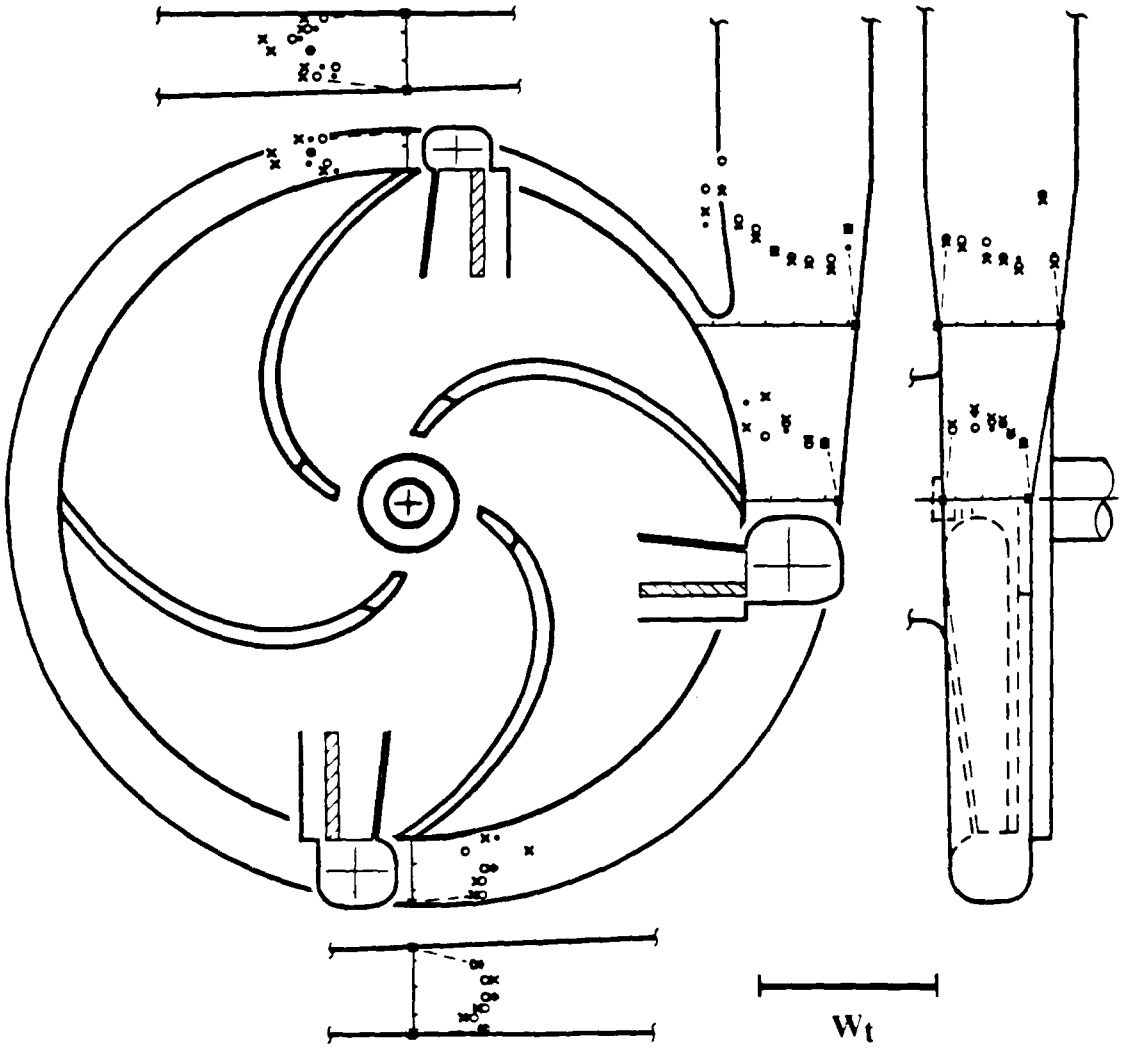


FIGURE 3.22 Angle-resolved tangential component of rms velocity (w'/W_t) in the volute passage at the flowrate of $0.57Q_n$.
(see Figure 3.21 for symbols)

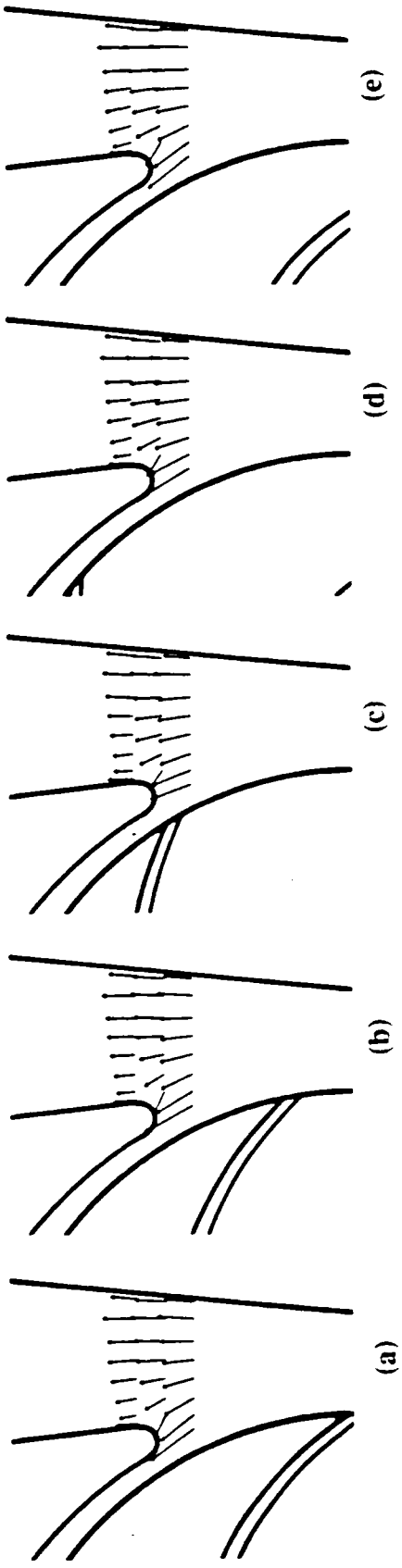


FIGURE 3.23 Mean flow vectors on the plane of z=0 close to the cutwater at the flowrate of 0.57Q_n. Impeller shaft angles Ø= (a)0, (b)10, (c)30, (d)50 and (e)70 degrees.

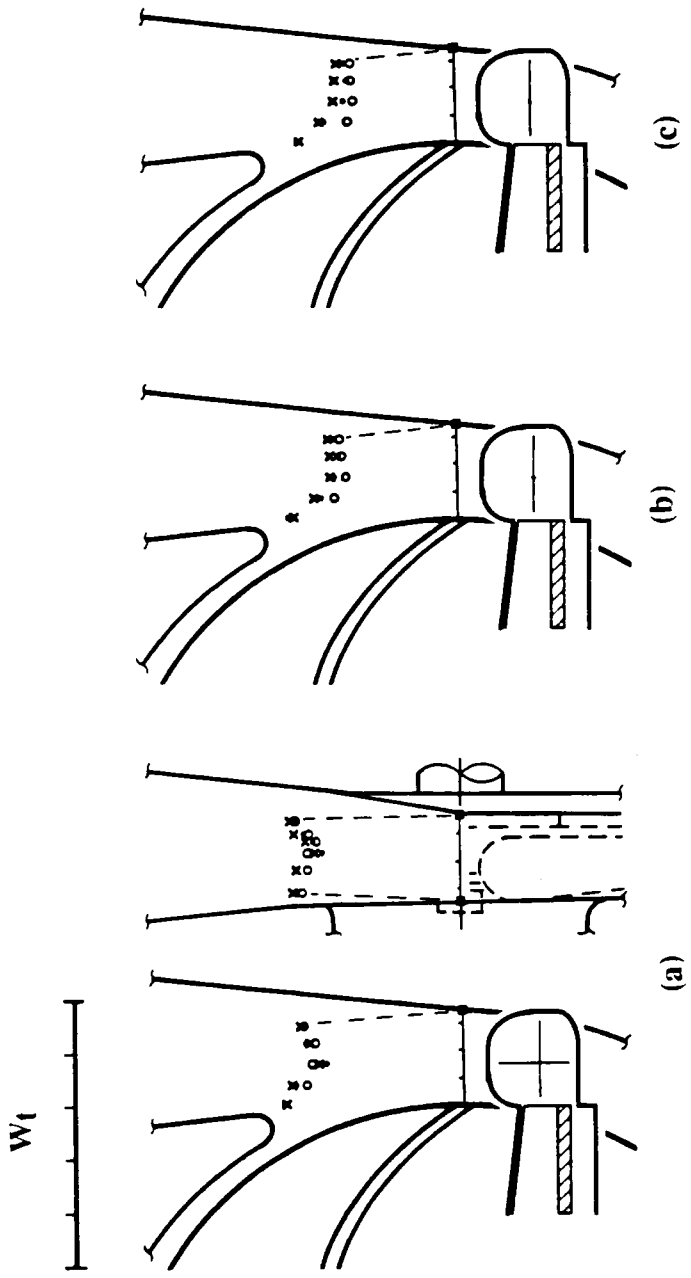


FIGURE 3.24 Angle-resolved tangential component of mean velocity (W/W_t) in the volute passage measured at Ψ of 330 degrees with the flowrates of (a)$0.93Q_n$, (b)$0.29Q_n$ and (c)$0.15Q_n$. (see Figure 3.21 for symbols)

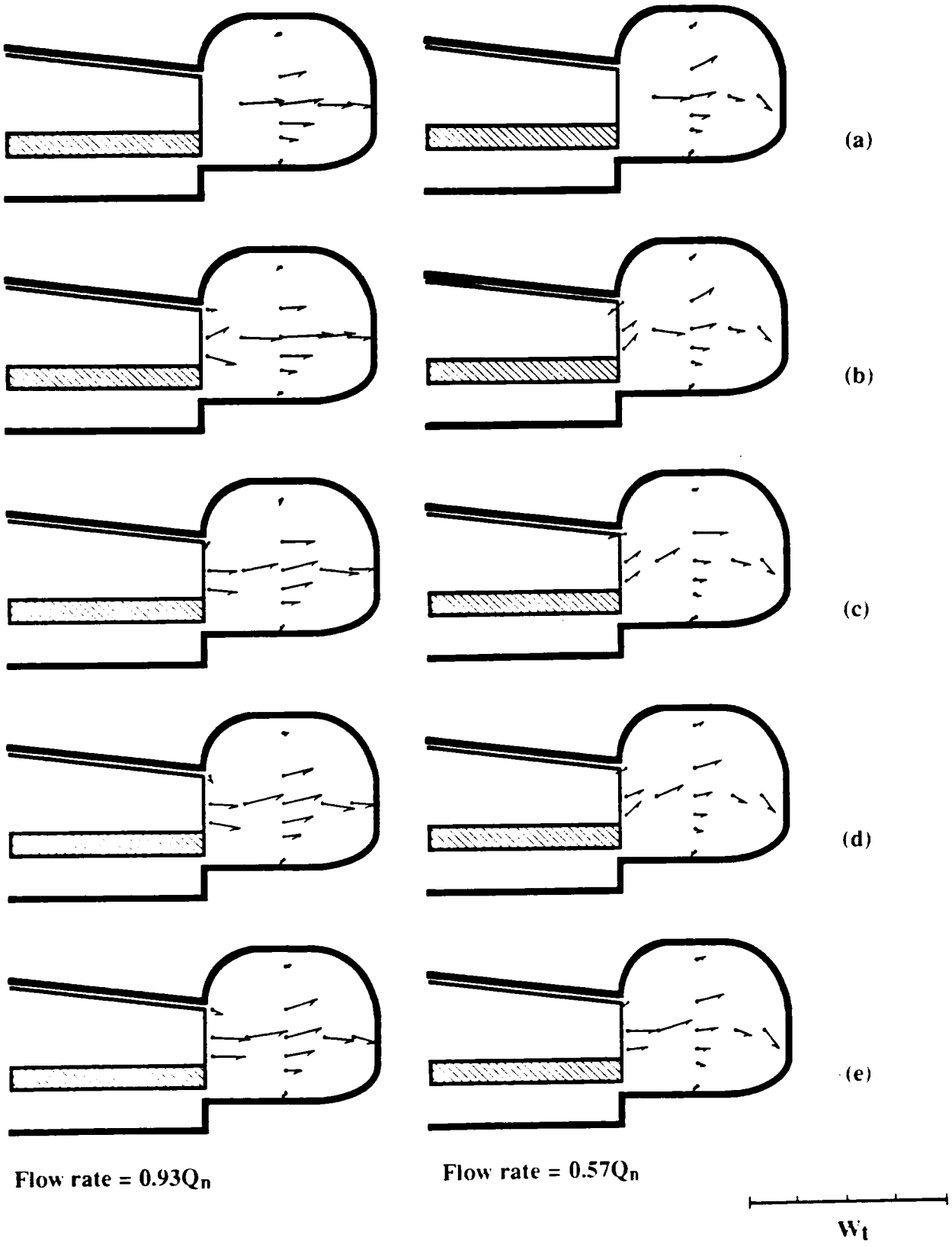


FIGURE 3.25 Cross-stream mean flow in the volute on the plane of Ψ=330 degrees at the **flowrates** of $0.93Q_n$ and $0.57Q_n$. Impeller shaft angles Ø=(a)0, (b)10, (c)30, (d)50 and (e)70 degrees.

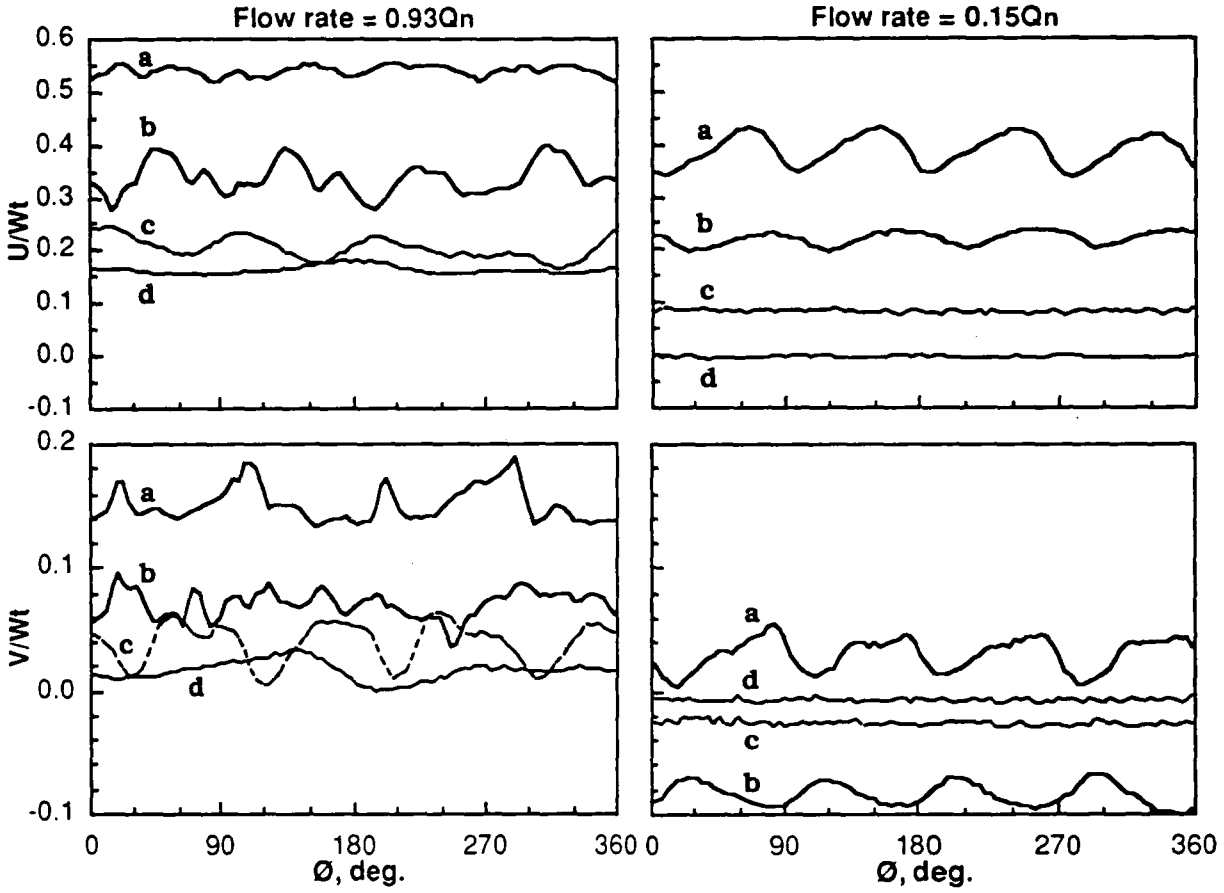


FIGURE 3.26 Angle-resolved axial (U) and radial (V) components of mean velocity traces on the centreline of the exit pipe at axial locations x/De=(a)0, (b)1, (c)1.8 and (d)3.2.

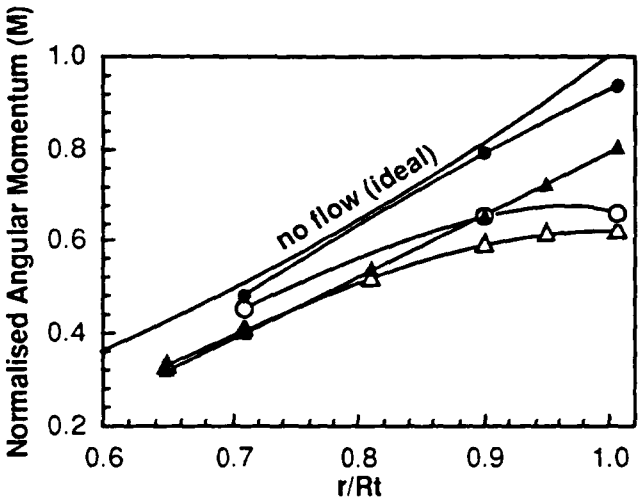


FIGURE 3.27 Radial distributions of angular momentum (M) at the flowrates of 0.93Qn (Δ , ▲) and 0.29Qn (O , ●). (open symbol: experiment; block symbol: theoretical value)

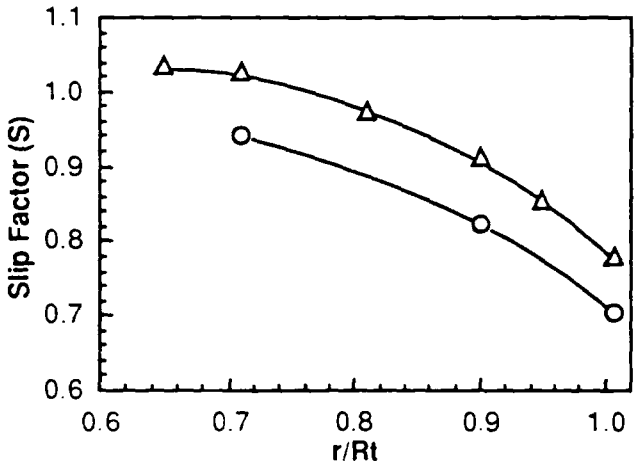


FIGURE 3.28 Radial distributions of slip factor (S) at the flowrates of 0.93Qn (Δ) and 0.29Qn (O).

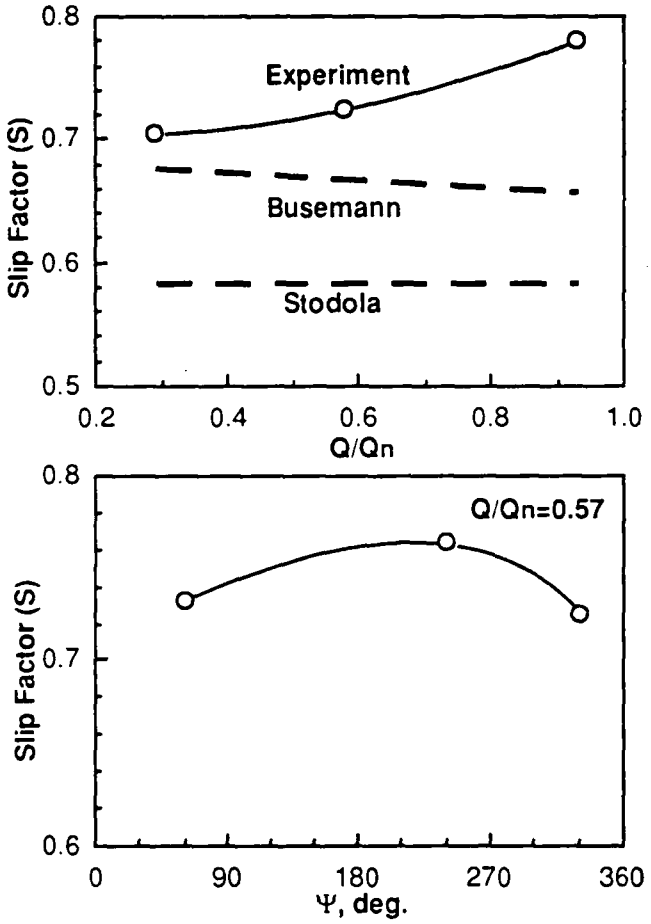


FIGURE 3.29 Variations of slip factor (S) with **flowrate** and volute circumferential angle at impeller discharge, r/Rt=1.

CHAPTER 4

Particle Velocities in a Swirling, C onfined Flow

4.1 INTRODUCTION

The burners of many furnaces comprise a co-axial flow of fuel and air into a diffuser arrangement, often referred to as a quarl, which is provided to cause a stable region of recirculation and the lower velocities necessary for a stable flame. This recirculation also provides increased residence time for less volatile fuels to vaporise and burn. Examples of this type of flow include the gas- and coal-fuelled flames of Milosavljevic, Taylor and Whitelaw (1988a,1988b,1990) and the kerosene-fuelled flame of Hardalupas, Taylor and Whitelaw (1989a). The isothermal flows investigated here occurred in a geometrical arrangement with dimensions similar to one of the burners of Milosavljevic *et al.* (1988a) and velocity characteristics were measured with two main purposes. The first was to provide information of the recirculating flow within the quarl and its influence on the downstream flow and the second to determine the behaviour of solid beads, first in the central jet and then in the annulus.

The flow configuration, solid beads and fluid were arranged to have the same refractive index so as to allow measurements by laser-Doppler velocimetry without refraction at the curved inner wall and by the beads. In principle, this should permit measurement with volume concentration of beads from zero to unity but unavoidable inclusions of gas within the beads scattered light and limited the mean concentration to a maximum of 0.143 within the annulus (0.113 within the burner). The velocimeter was operated with forward-scattered light and three orthogonal components of mean velocity, normal and shear stress were measured.

The flow in the annulus passed through swirl vanes which resulted in a swirl number of 1.38 in the absence of the beads and, with ratios of the bulk mean velocity in the central jet to that in the annulus up to unity, ensured a toroidal vortex partly within the quarl in addition to the corner vortex in the sudden expansion downstream of the quarl. It is well known that the energy made available by combustion can lead to important differences between isothermal and combusting flow, see for example So, Ahmed and Mongia (1985), Heitor and Whitelaw(1986) and Jones and Tober (1988), so that extrapolation from one to the other should be undertaken with care. On the other hand, it is desirable that physical understanding should be available without the added complications of heat transfer and combustion. Some previous investigations of related isothermal flows include those of Habib and Whitelaw (1980), Altgeld, Jones and Wilhelmi (1983) and So *et al.* (1985), but none has considered burner-furnace arrangements such as those of Milosavljevic *et al.*

The two-phase flow investigation makes use of plexiglass spheres of mean diameter 510 and 700 μm with Stokesian time constant

$$\tau_p = \frac{d_p^2 \ \rho_p}{18 \ \mu} \tag{4.1}$$

of around 12 and 22 ms, respectively, which are of the same order as the turbulent time scales in the mixture of tetraline and turpentine, used to match the refractive index of the plexiglass geometry and beads, in the region downstream of the sudden expansion. Thus, it is to be expected that the beads will follow the mean flow and turbulent fluctuations in the downstream region. In the jet and annulus, however, the turbulent time scales are much shorter, of the order of 2ms, so that the turbulent Stokes number, defined by

$$St_t = \frac{\tau_f}{\tau_p} = \frac{\upsilon_{eff,f}}{u_f^2 \ \tau_p} \tag{4.2}$$

is of order 0.1 and the beads can be expected to respond to the mean flow but not to the turbulence. With volume concentrations greater than around 0.003, as in the upstream region of the

present flows, particle-to-particle interactions can occur with results which may modify these preliminary statements. It should be noted that particles of pulverised coal in burners are also not expected to be responsive to the higher turbulent frequencies and occur with high volume concentrations.

The following section describes the flow configuration, boundary conditions and the laser velocimeter. The results are presented and discussed in the third section and the paper ends with a summary of the more important conclusions.

4.2 FLOW CONFIGURATION AND INSTRUMENTATION

The flow arrangement of Figure 4.1 includes the test section of Figure 4.1b. Two centrifugal pumps delivered a mixture of 31.8% by volume of tetraline and turpentine from a supply tank to the settling chamber where, after passing through a section of honeycomb, it flowed into a pipe and an annulus formed by two 1.05 m long coaxial, straight pipes. The flowrates to the pipe and annulus were measured by calibrated orifice plates to be 1.96×10^{-3} m^3/s for the annular flow and varied from zero to 1.48×10^{-3} m^3/s for the central pipe flow with precision of better than 3%. The temperature of the mixture was controlled to 25.15±0.02°C so that its refractive index was 1.489 identical to that of the plexiglass material used to form the test section. A detailed description of the matching technique has been given by Nouri, Whitelaw and Yianneskis (1988).

The test section was machined from a rectangular block of plexiglass and carefully annealed at 85°C for 24 hours with a slow heating and cooling rate. The outside rectangular shape avoided asymmetric refraction of light beams and the circular cross-section of the inner surfaces and coaxial pipes were not observed because of the identical refractive index of the fluid. The inner diameter of the central pipe was 14.9 mm, with an outer diameter of 20.9 mm and an inner diameter of the outer pipe of 38.1mm to form the annulus which was fitted with a nine vane swirler of angle 60 degree, 133 mm upstream of the inlet to the diffuser.

The swirl number was calculated to be 1.38, based on the expression of Beer and Chigier (1972).

The last 10mm of the outside diameter of the central pipe was tapered to allow gradual merging of the central and annular flows and the diffuser, connected to the outer pipe, had a half angle of 25 degree over a length of 38.1mm at which axial location there was a sudden expansion from a diameter of 73.6 mm to one of 147 mm. The confining geometry of this diameter extended for 420 mm before converging with a half angle of 30 degree to the exit pipe of diameter 38.1 mm.

It was essential to separate the beads after they had passed through the model so that they could be added separately to the central pipe and annulus. This was achieved with a screen with blockage ratio arranged so that the beads in the size ranges considered here could not pass through. The flowrates of the mixture were identical to that of the 0.25 mass-flow ratio in the single-phase flow experiments with beads added after the flowrate had been measured. In the absence of the beads, natural contaminants in the fluid scattered light to allow measurements of its velocity characteristics. The bulk flow and fluid properties for the two-phase measurements are given in Table 4.1 together with the mean diameters of the beads and the range of volume concentrations. Additional information of the nature of the beads is given in Table 4.2.

Careful microscopic examination of the beads showed that between 20 and 50% of their volume was made up of gas with refractive index different from that of the plexiglass and fluid. These inclusions scattered light so that the velocity of the beads could be measured but limited the concentration with which the measurements could be obtained for each distance over which the light had to pass. Thus, the maximum volume concentration in the burner was 0.113; measurements at higher values were possible but with signal quality which caused reduction in accuracy.

The laser-Doppler velocimeter comprised a 5 mW helium-neon laser and optical components which provided two beams of light which intersected and scattered light to be observed in the

forward in-line direction. The main characteristics of the optical system are provided in Table 4.3. The signal from the photomultiplier was processed by a frequency counter interfaced to a microprocessor and led to values of mean velocity and normal stress with overall uncertainty of better than 2 and 5% of the local values. Single-phase velocity measurements were made first, with light scattered from natural contaminants. The sensitivity of the photomultiplier and the intensity of the scattered light incident upon the photomultiplier were then reduced until no signal corresponding to liquid flow could be detected. The beads were then inserted and their mean and rms velocity components were measured. A number of Reynolds shear-stress values were also obtained and are available in the report of Liu, Nouri, Tse and Whitelaw (1989).

4.3 RESULTS AND DISCUSSION

Results in this section are presented in three sub-sections: the first concerns the characteristics of the single phase flow at a range of swirl number and comprises the baseline data to compare against the velocity of beads; the second and third sub-sections concern the velocity of beads suspended in the flow of the central jet and the annulus, respectively, and consider the effects of bead size and concentration.

4.3.1 Single-Phase Flow

The mean velocity measurements of Figure 4.2 correspond to liquid flow at three axial locations, including the jet-exit plane, $z/D = 0.02$, and confirm that asymmetries are small. Integration of these profiles led to mass-flows within 5% on either side of the axis and similar interpretation of profiles measured further downstream were within 6% of each other. The shape of the axial-velocity profiles at $z/D = -0.79$ suggests fully-developed flow in the central pipe.

The single-phase results are presented in Figure 4.3 in the form of streamlines deduced from measurements of the axial components of velocity obtained at streamwise stations

corresponding to z/D of -0.26, 0.02, 0.1, 0.25, 0.38, 0.5, 1, 1.4, 2, 3, 4, 5, 7.5 and 10. The integration was performed with radial steps of 0.05 to 0.1D and the interpolation of the resulting locations of constant stream function make use of a surface regression routine. The results in the near field correspond to four values of the ratio of mass-flow in the central pipe to that in the annulus and the downstream region is shown for three of them. The mass-flow ratio of 0.25 corresponded to equal bulk mean velocities for the two flows and was used for the subsequent two-phase flow investigation.

The main features of the near field are the region of recirculating flow behind the step and the toroidal vortex which has a major axis parallel to the wall of the quarl and an extent which depends on the mass-flow ratio. The length of the separation region caused by the sudden expansion increases by some 20% with decreasing mass-flow ratio from 0.77 to zero and the inner vortex increases by a much larger amount. At a mass-flow ratio of 0.77, the results do not show a vortex within the quarl although, with more detailed measurements, a small vortex might be revealed. Further downstream, however, a weak flow structure is apparent and beyond z/D of around three, the velocity is nearly uniform across the vessel. With a mass-flow ratio of 0.25, a small vortex is apparent in the quarl region and the downstream flow structure has disappeared although there is a substantial turning of the flow with consequent regions of high velocity flow close to the axis and wall and a substantial region of low velocity flow in between. The vortex increases considerably in length as the mass-flow ratio is decreased further and, with no flow in the central pipe, extends from z/D of less than unity to more than two. The turning of the downstream flow noted with the mass-flow ratio of 0.25 moves downstream with increasing ratio.

It is difficult to extrapolate the results of Figure 4.3 to those of a combusting flow but it can be expected that both the strength and extent of the toroidal vortex is likely to be decreased with increase of mass-flow ratio. Also, and as shown by the review of Pascau (1985), the downstream flow is accelerated so that the reversal does not occur. Of the present sequence of flows, that

with a mass-flow ratio of 0.25 appears to offer the best arrangement for combustion in that the stabilisation region of the flame would be contained within the quarl and for a short distance downstream; and the downstream flow will be made unidirectional by the energy of combustion. It is, however, evident that the radial location of the vortex is controlled in part by the degree of swirl in the annulus and it is likely that an optimum swirl number will exist for each mass-flow ratio of the central jet.

4.3.2 Beads Suspended in the Central Jet

The centreline distributions of the mean velocity components in three orthogonal directions and the corresponding rms values, Figure 4.4, show that the results with beads of average diameter of 510 μm and with concentration of 0.001 by volume, are in close agreement with those of the single-phase flow. There is a tendency, however, for the larger beads (700 μm) to have higher velocities within the pipe and in the near-field of the jet and to lag the single-phase flow in the downstream recovery region. The larger beads show similar trends but, when the concentration is increased to 0.004, the bead velocities are greater than those of the single-phase flow by around 15% suggesting that the terminal velocity is representative of a collection of beads. The bead velocities approach those of the single-phase with increasing distance as should be expected since the particle and mean-flow time scales become similar.

Swirl has caused the finite crossflow velocity on the axis since it introduces precession of a vortex core which, in this case, has small amplitude but an axis different from that of the geometry. The frequency of the precession appears to be around 5Hz and the deviation of the flow axis from that of the geometry around 3mm or $0.04R$ at $z/D = 7.5$. As we shall see, however, the same trend is present with beads in the annulus and also existed with the single-phase flow

Figures 4.5 and 4.6 show that the 700 μm beads with the initial concentration of 0.004 continue to lead the single-phase flow but only in terms of the axial velocity component. After the diffuser,

they tend to lag the single-phase flow in the central *jet* although the local concentration has undoubtedly reduced. There is also a tendency for the beads to lag the single-phase swirl-velocity component in the inner region and this is expected since the annular jet has to accelerate the beads diffusing from the central region. The results suggest that the vortex pattern of Figure 4.3 is little influenced by the addition of beads which indicate a similar flow behaviour.

Since the Stokes number is low within the quarl, anisotropy of the normal stresses can be expected due to the fan-spreading effect discussed by Hardalupas, Taylor and Whitelaw (1990) and is evident on Figure 4.4, with similar effects evident in the normal stresses measured at radial locations within the quarl. Downstream of the sudden expansion, the Stokes number is of the order unity and the beads can be expected to follow turbulent fluctuations and this is also evident in Figure 4.4.

4.3.3 Beads Suspended in the Annulus

Figure 4.7 shows the centreline distributions where the 700μm beads were added to the annulus and for volume concentrations up to 0.085. Those beads which have diffused to the axis arrive from a region of low velocity so that the velocity lead evident in Figure 4.4 is absent and the beads tend to decelerate more with increasing concentration as the region of minimum axial velocity is approached. This trend continues downstream of the diffuser where the beads tend to lag the single-phase flow by an amount which increases with concentration. As in the previous case, the flow has a finite crossflow velocity on the axis and a tendency for the beads to exhibit better symmetry than the flow. The normal stresses are unaffected by bead concentration except in the diffuser as the mean velocity tends to a minimum and the fluctuation levels increase with concentration. The large values of normal stress in the region of the minimum axial velocity are undoubtedly associated with fan spreading rather than with turbulence.

Figure 4.8 is concerned with the flow in the annulus. It is evident that the radial distribution of the velocity components is

dependent upon the bead concentration with a tendency to move the maximum axial and tangential velocities to smaller radii as the concentration is increased. The results encompass a range of volume concentrations up to 0.113 and the trend is almost monotonic. The radial distribution of volume concentration of beads, on the other hand, is skewed to larger radii, as a consequence of the imposed swirl and there is a radially outwards velocity component at z/D of -0.26. There is also clear suppression of the axial normal stress at larger radii where the local concentrations exceed the quoted spatially-averaged value and of a reduction in the tangential normal stress throughout the flow with increasing concentration. Careful consideration of Figures 4.8 and 4.9 shows a link between the profiles of axial mean velocity and volume concentration in that the former is similar to the single-phase velocity at the concentration of 0.018 although bead-to-bead interactions are likely. At higher concentrations and for locations between r/R of 0.7 and 0.85, the velocities exceed those of the single-phase flow as in the central jet and again due to high concentrations giving rise to larger terminal velocities than those of a single bead.

It is noteworthy that velocity measurements were achieved with a volume concentration of 0.113 in the annulus which implies that the light beams have to cross eight surfaces, a total of 200mm of plexiglass, the fluid and the beads.

The influence of the swirler on the annulus flow, as shown by Figures 4.8 and 4.9, has implications for the flow downstream of the exit plane of the annulus and pipe so that it is likely that the bead concentration will be small close to the axis. This influence is evident only at the larger radii where a considerable suppression of fluctuation levels is evident. At z/D of 0.38, however, the mean axial velocity at small radii has been much reduced by the beads of the annulus and in contrast to the results of Figure 4.6. In this case, the lower velocity in the annulus is transported to the centreline by beads whose axial velocity has been further reduced by the interaction of their radial and tangential components with the liquid flow of the central jet. Again, however, the vortex structure of Figure 4.3 is clearly

represented by the beads particularly at its downstream extremity. Downstream of the diffuser, the bead concentrations have reduced and the beads and liquid behave in a similar manner in accordance with the similar value of the bead and flow time constants. Indeed the normal stresses of the single-phase flow are identical to those of the bead by the 2D location, but are not shown here

4.4 CONCLUSIONS

The isothermal, single-phase flow in the near-quarl region shows the expected toroidal vortex for mass-flow ratios of 0.25 and less and for higher value indicates a flow pattern which is unlikely to be useful as a basis for combustion in that flame stabilisation will occur downstream of the quarl if at all. A further region of recirculation may occur on the bluff end of the central pipe, corresponding to the zero mass-flow ratio, and can assist flame stabilisation although this is unlikely to be useful with liquid or solid fuels. The possible existence of an optimum swirl number is likely to be further complicated with non-gaseous fuels, since the large droplets or particles will be preferentially centrifugal so that a Stokes number

$$St_\omega = \frac{18\ \mu}{\rho_p\ \omega\ d_p^2} \qquad (4.3)$$

and a burning time scale should also be considered.

The two-phase flows confirm the behaviour expected by consideration of the particle and flow time scale, and also the presence of fan spreading which may be mistaken for turbulence. At very high concentrations of beads, the mean velocity profiles are distorted and turbulence is considerably suppressed. There is no evidence here of turbulence augmentation by beads at any concentration but it is evident that the terminal velocity corresponds to a group of beads with high concentration.

An important effect of the swirl imposed by the vanes in the annulus is to centrifuge the beads to large radii and thereby to cause local regions of high concentration and turbulence

suppression. This has important consequences for burners since the fuel tends to be removed from the flame zone and turbulent fluctuations, assist mixing-controlled combustion. This effect of swirl was noted for much lower swirl numbers by Hardalupas *et al.* (1989a) and it is evident that a compromise is required between the need for swirl assist in the formation of a region of recirculation to stabilise the flame and to increase residence time, and the need to avoid centrifuging fuel away from the flame.

Finally, the results confirm that the use of plexiglass for the containing vessel and particles and an appropriate temperature and concentration of tetraline and turpentine allows the examination of two-phase flows with volume concentrations greater than could otherwise be achieved. Thus, velocity measurements has been made with a mean concentration of 0.113 in a complex geometry, and may be contrasted with values of 0.01 by Nouri, Whitelaw and Yianneskis (1984) in water, 0.14 by Nouri, Whitelaw and Yianneskis (1987) in a simple jet with tetraline and turpentine and of 0.004 by Hardalupas, Taylor and Whitelaw (1989) in a jet of air. The concentration has been limited by our inability to find beads without inclusions of gas.

REFERENCES

Altgeld, H., Jones, W.P., & Wilhelmi, J. (1983) Velocity measurements in a confined swirl driven recirculating flow. *Exp.s in Fluids*, **1**, 73.

Beer, J.M., and Chigier, N.A. (1972) Combustion Aerodynamics. Applied Science.

Habib, M.A. and Whitelaw, J.H. (1980) Velocity characteristics of confined coaxial jets with and without swirl. *J. Fluids Eng.*, Trans. ASME, **102**, 47.

Hardalupas, Y.,Taylor, A.M.K.P. and Whitelaw, J.H. (1989a) Velocity and particle flux characteristics of turbulent particle-laden jet. *Proc. Roy. Soc.*, Lond. A., **246**, 31.

Hardalupas, Y., Taylor, A.M.K.P. and Whitelaw, J.H. (1990) Velocity and size characteristics of liquid-fuelled flames stabilised by a swirl burner. *Proc. Roy. Soc.*, Lond. A, **428**, 129-155.

Heitor, M.V. and Whitelaw, J.H. (1986) Velocity, temperature and species characteristics of the flow in a gas-turbine combustor. *Comb. and Flame*, **64**, 1.

Jones, W.P., and Tober, A. (1988) Velocity, composition and temperature fields in an axisymmetric model combustor. Proc. 4th Int. Symp. on Application of Laser Anemometry to Fluid Mechanics.

Liu, C.H., Nouri, J.M., Tse, D.G.N. and Whitelaw, J.H. (1989) Particle velocities in a swirling, confined flow. Imperial College, Fluids Section Report FS/89/09.

Milosavljevic, V., Taylor, A.M.K.P., & Whitelaw, J.H. (1988a) Velocity, temperature and concentration characteristics of quarl burners. Imperial College, Fluids Section Report FS/88/23.

Milosavljevic, V., Taylor, A.M.K.P., & Whitelaw, J.H. (1988b) Stability limits of pulverised coal burners. Imperial College, Fluids Section Report FS/88/53.

Milosavljevic, V., Taylor, A.M.K.P., & Whitelaw, J.H. (1990) The influence of burner geometry and flowrates on the stability and symmetry of swirl-stabilised non-pressurised flames. *Comb. and Flame*, **80**, 196.

Nouri, J.M., Whitelaw, J.H. and Yianneskis, M. (1984) The flow of dilute suspension of particles around axisymmetric baffles. Imperial College, Fluids Section Report FS/84/18.

Nouri, J.M., Whitelaw, J.H., & Yianneskis, M. (1987) Particle motion and turbulence in dense two-phase flows. *Int. J. Multiphase Flow*, **13**, 729.

Nouri, J.M., Whitelaw, J.H., & Yianneskis, M. (1988) A refractive index matching technique for solid/liquid flows. In Laser Anemometry in Fluid Mechanics 3, Ladoan, 335.

Pascau, A. (1985) A review of experimental data on inert and reacting, and confined and unconfined swirling flows. Imperial College, Chem. Eng. Dept., Internal Report.

So, R.M.C., Ahmed, S.A., Mongia, H.C. (1985) Jet characteristics in confined swirling flow. *Exp. in Fluids*, **3**, 221.

TABLE 4.1 Flow and fluid properties of two-phase flow

	Central Jet		*Annulus*	*Exit pipe*
Mass flowrate (10^{-3} m^3/s)	0.48		1.9	2.38
Bulk mean velocity (m/s)	2.75		2.38	2.08
Hydraulic diameter (m)	14.9		31.8	8.1
Reynolds number	25122		46400	48600
Fluid density (kg/m^3)	894			
Fluid viscosity (cSt)	1.631			
Beads in the central jet				
Beads diameter (μm)	510	700		
C_v in the central jet (%)	0.5	2.0		
C_v in the burner (%)	0.1	0.4		
Beads in the annulus				
Beads diameter (μm)	700	700	700	700
C_v in the annulus (%)	2.3	6.8	10.5	14.3
C_v in the burner (%)	1.8	5.4	8.5	11.3

TABLE 4.2 Bead characteristics

Mean diameter (μm)	510	700
Size range (μm)	425 to 600	600 to 800
Material	Diakon	Diakon
Density (kg/m^3)	1180	1180
Terminal velocity (m/s)	0.07	0.08
Reynolds number ($V_t\ d_p/\nu$)	22	34
Response time (ms)	12	22
Turbulent Stokes number ($\tau_f\ /\tau_p$) at the jet exit plane of the central jet	0.17	0.1

TABLE 4.3 Optical characteristics of laser-Doppler velocimetry

Half angle of the beam intersection (deg.)	8.93
Fringe spacing (μm)	2.038
Number of fringes without frequency shift	32
Diameter of the control volume at $1/e^2$ intensity (μm)	66.7
Length of the control volume at $1/e^2$ intensity (μm)	425.
Maximum frequency shift (MHz)	±4.91
Frequency to velocity conversion (ms^{-1}/MHz)	2.038

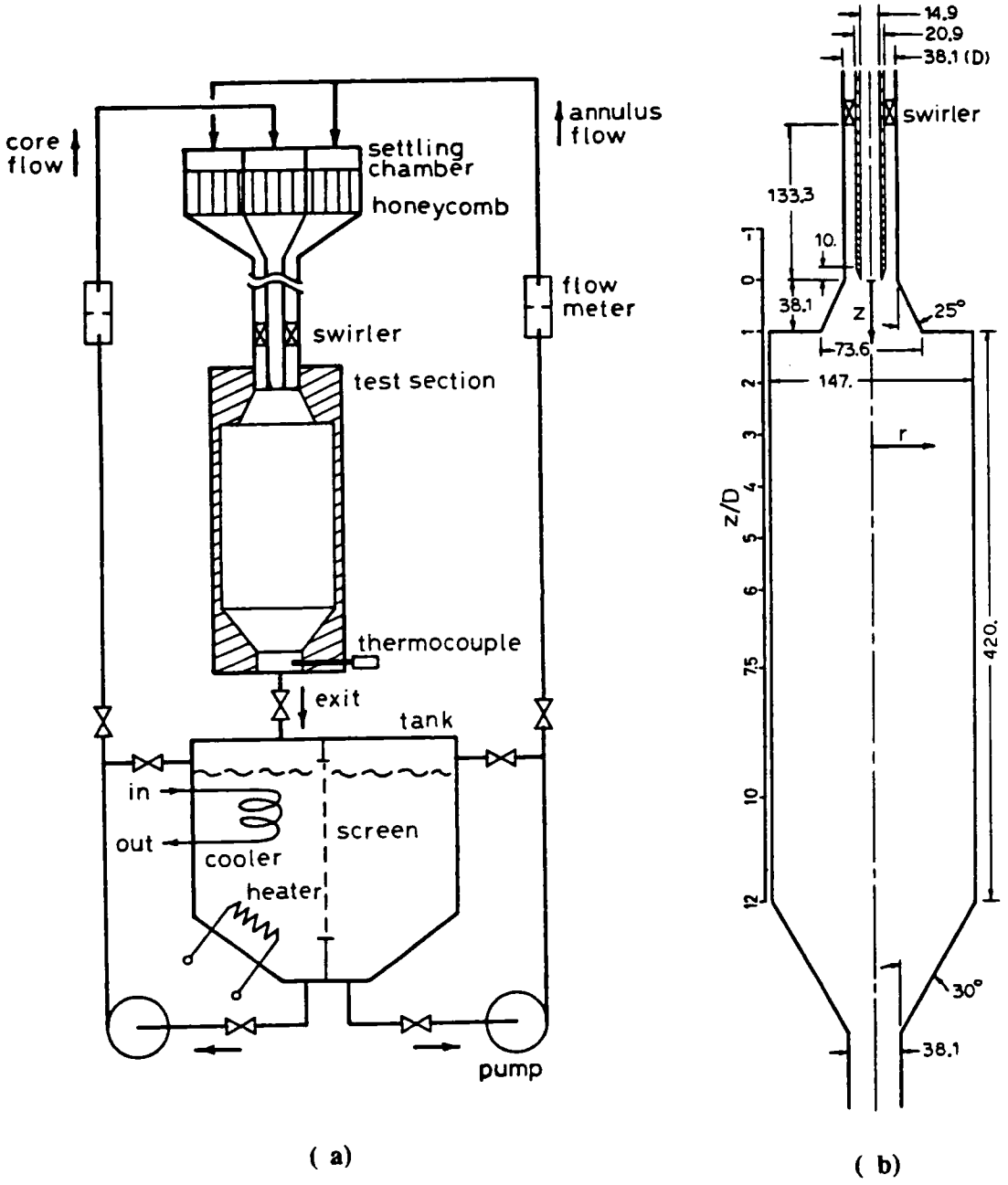


FIGURE 4.1 Flow circuit and model. (dimension in mm)

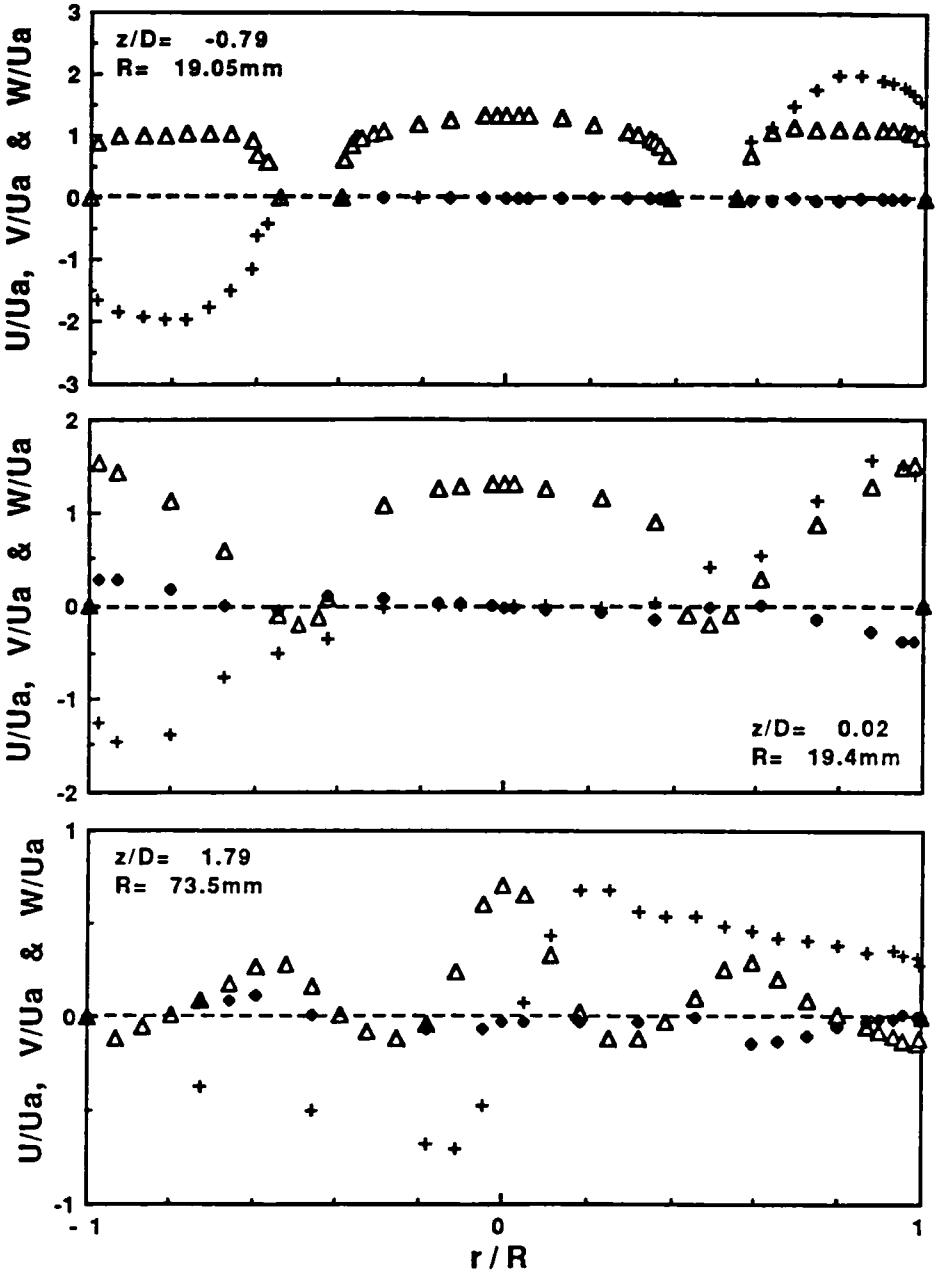
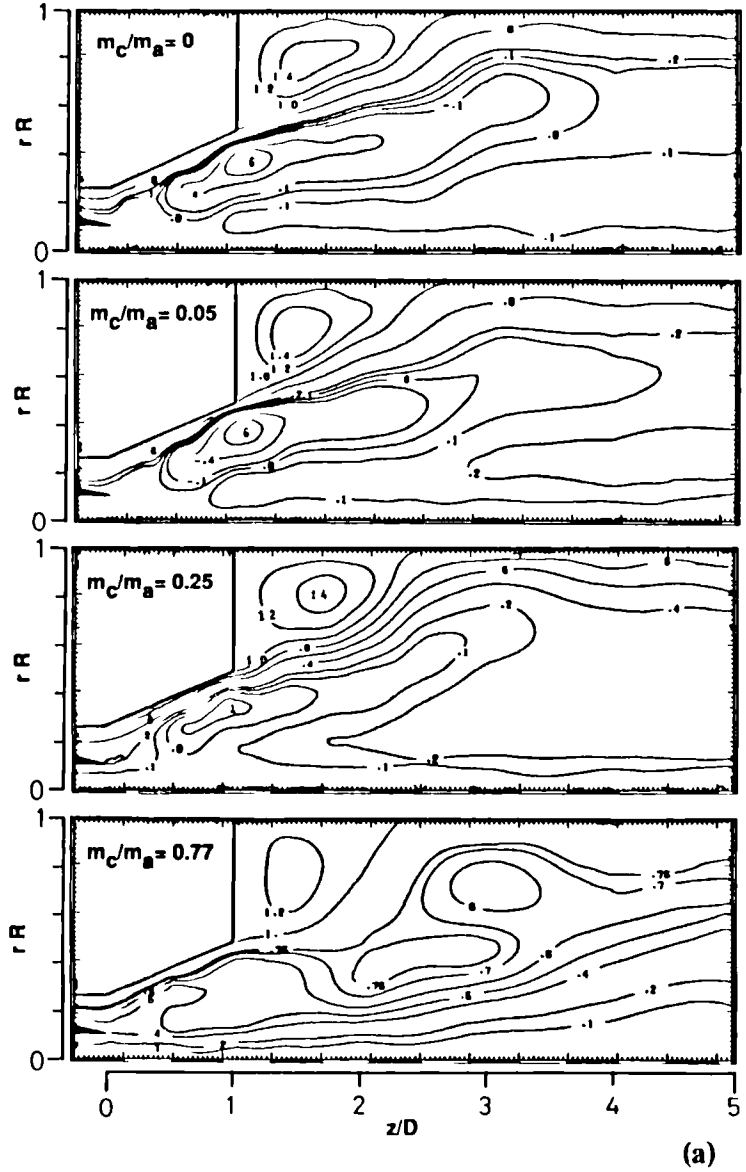


FIGURE 4.2 Symmetry of mean velocities at different axial locations. (△ U/U_a, ◆ V/U_a, + W/U_a)



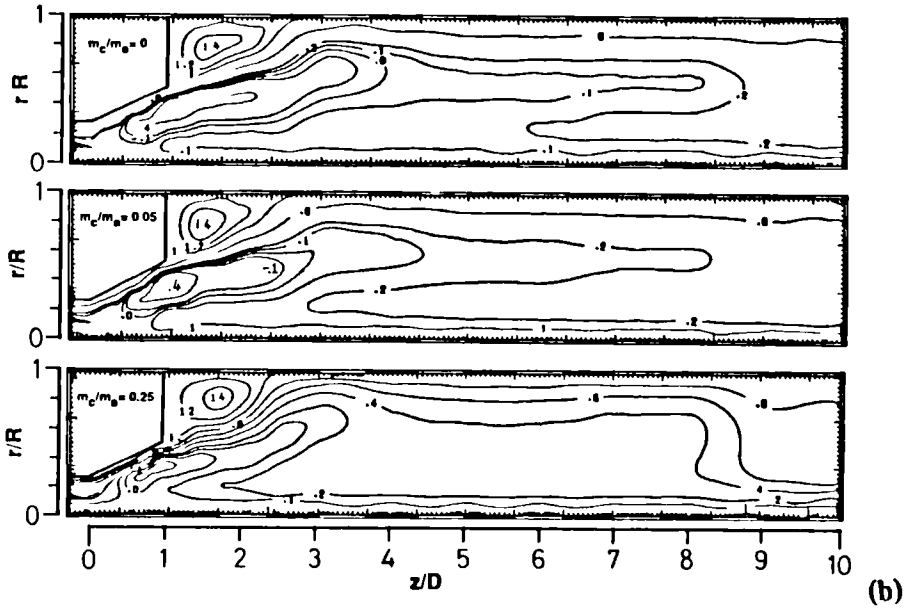


FIGURE 4.3 Streamline of single-phase flow with different mass-flow ratio of central jet and annulus flow. (a) near field; (b) overall flow.

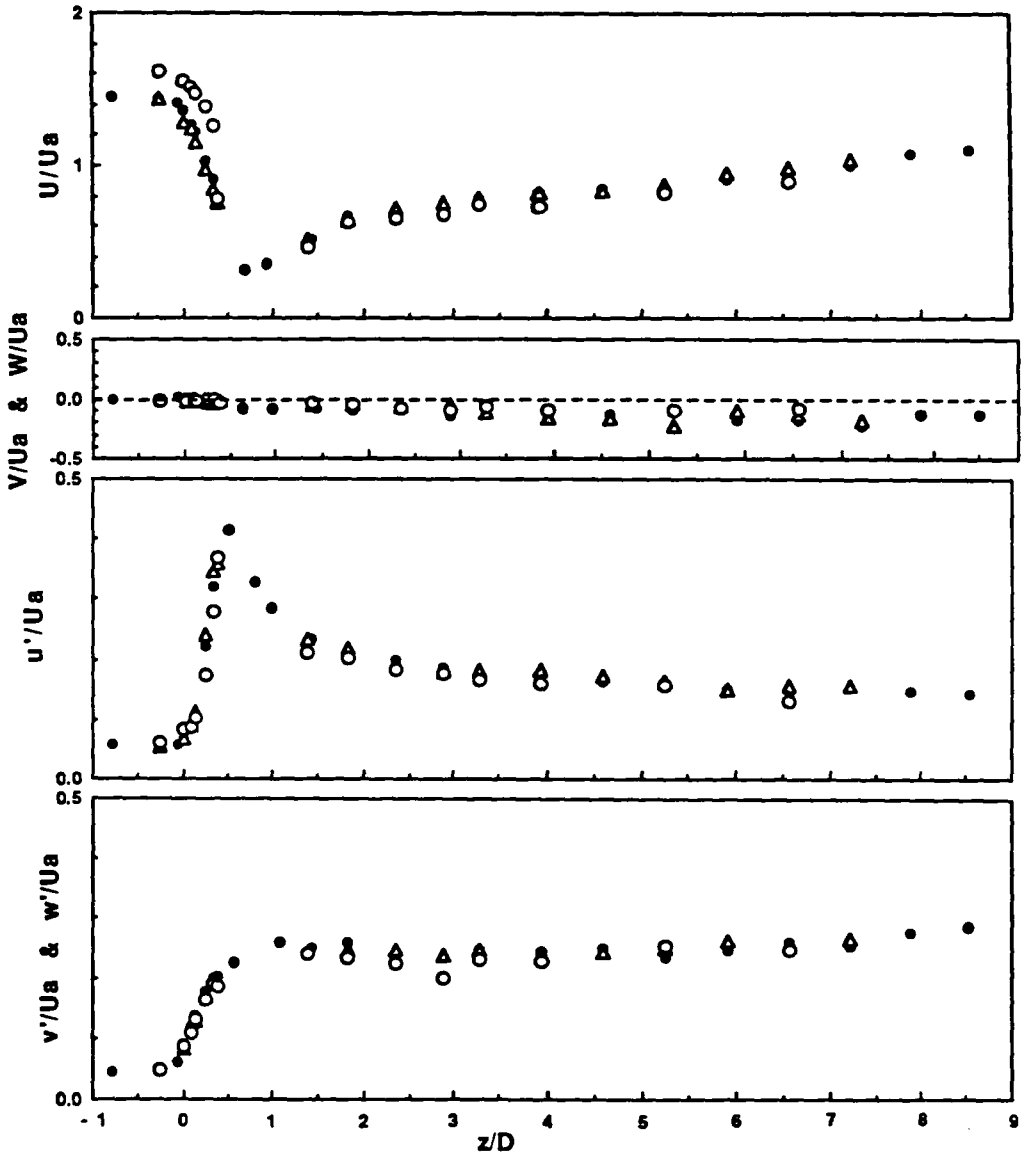


FIGURE 4.4 Bead mean and rms velocities on centreline.
(● single-phase; beads suspended in the central jet:
△ 510 μm beads with C_v=0.1%; ○ 700 μm beads with C_v =0.4%)

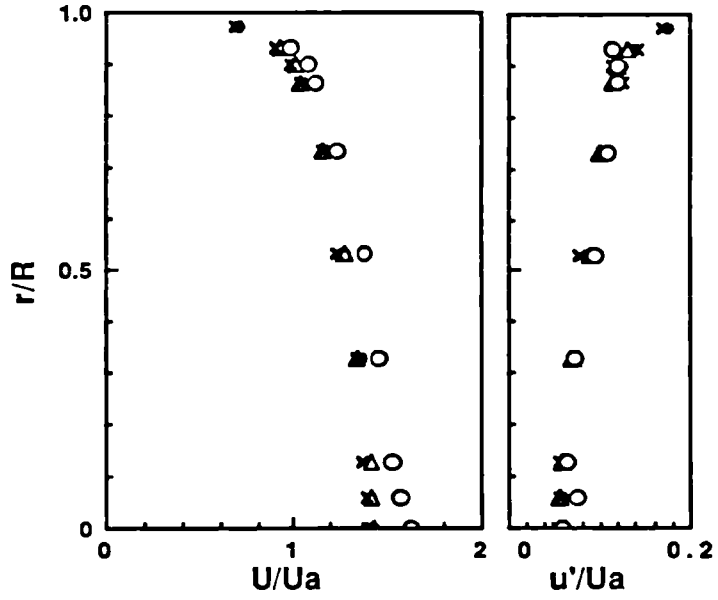


FIGURE 4.5 Radial distribution of bead mean and rms velocities of central jet on plane of z/D= -0.26 and R=7.45mm. (● single-phase; beads suspended in the central jet: △ 510 μm beads with C_v=0.1%; × 700 μm beads with C_v=0.1%; o 700 μm beads with C_v =0.4%)

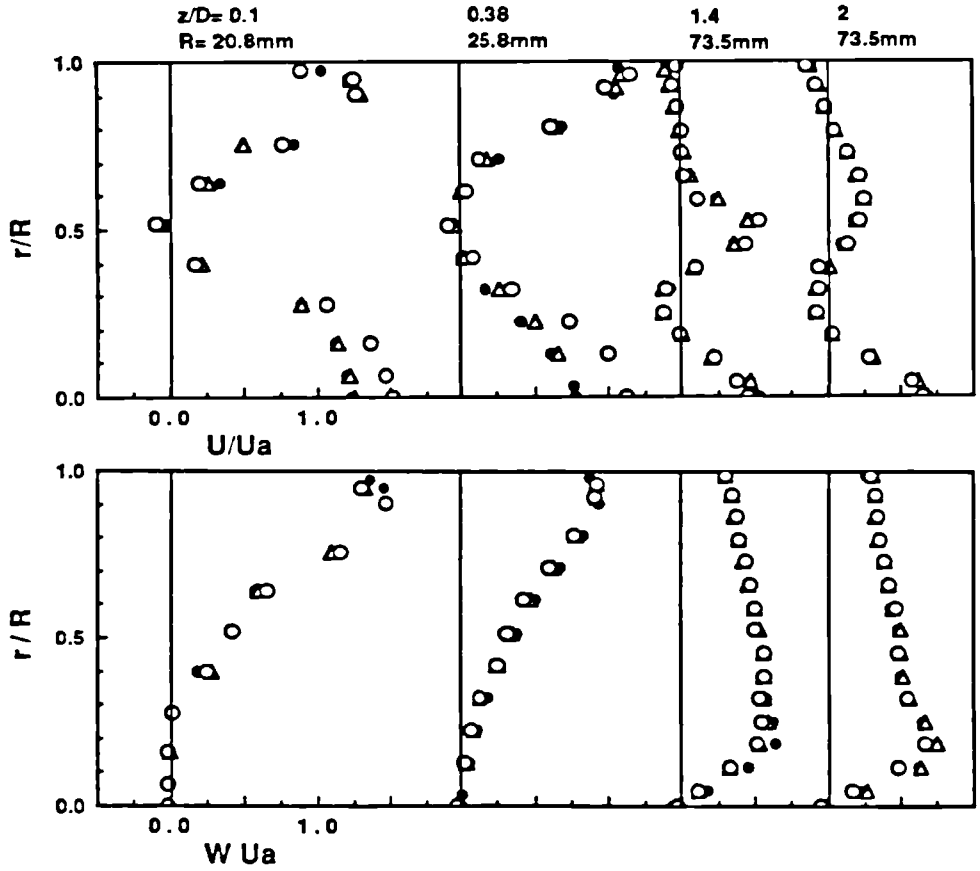


FIGURE 4.6 Radial distribution of bead mean velocities; beads suspended in the central jet.
(see Figure 4.4 for legend)

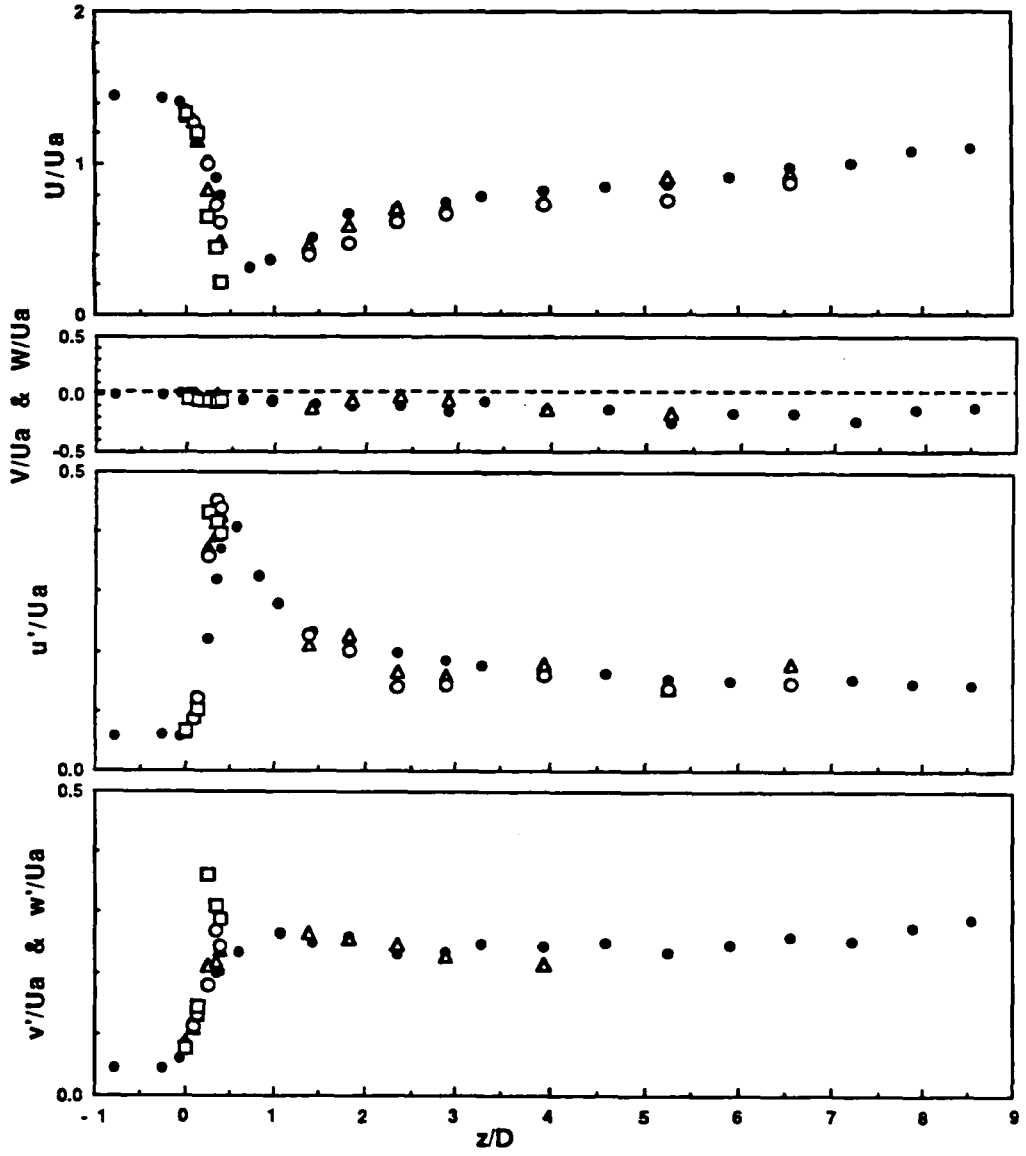


FIGURE 4.7 Bead mean and rms velocities on centreline. (● single-phase; 700 μm beads suspended in the annulus: △ C_V=1.8%; ○ C_V=5.4%; □ C_V=8.5%)

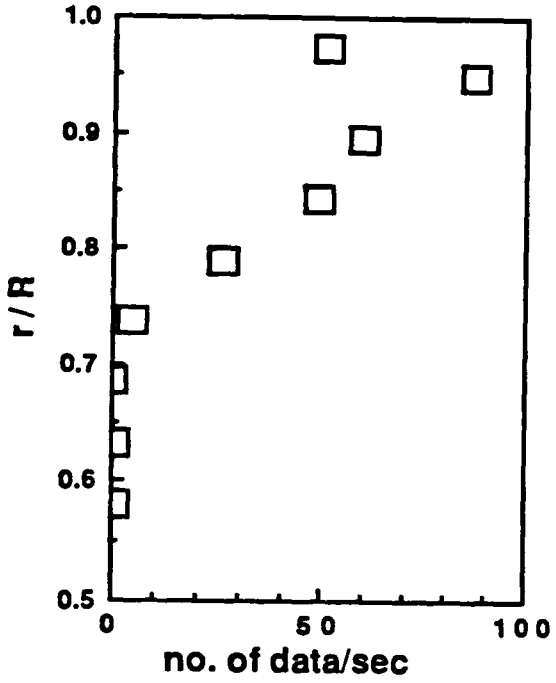


FIGURE 4.8 (a) Data rate of 700μm beads suspended in the annulus on plane of z/D= -0.26 at C_v =8.5%.

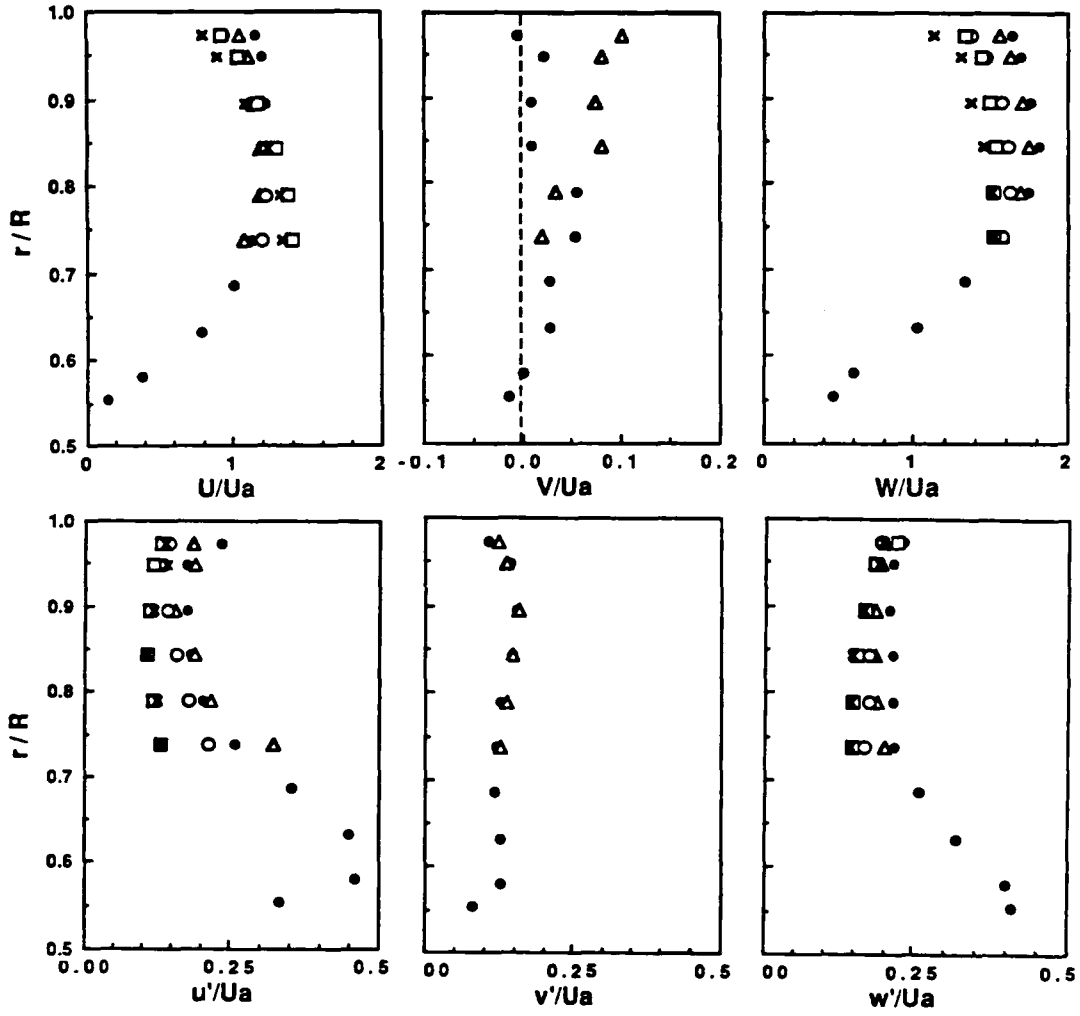


FIGURE 4.8 (b) Radial distribution of bead mean and rms velocities in the annulus on plane of z/D= -0.26 and R=19.5mm. (● single-phase; 700μm beads suspended in the annulus: △ C_v =1.8%; o C_v =5.4%; □ C_v =8.5%; × C_v =11.3%)

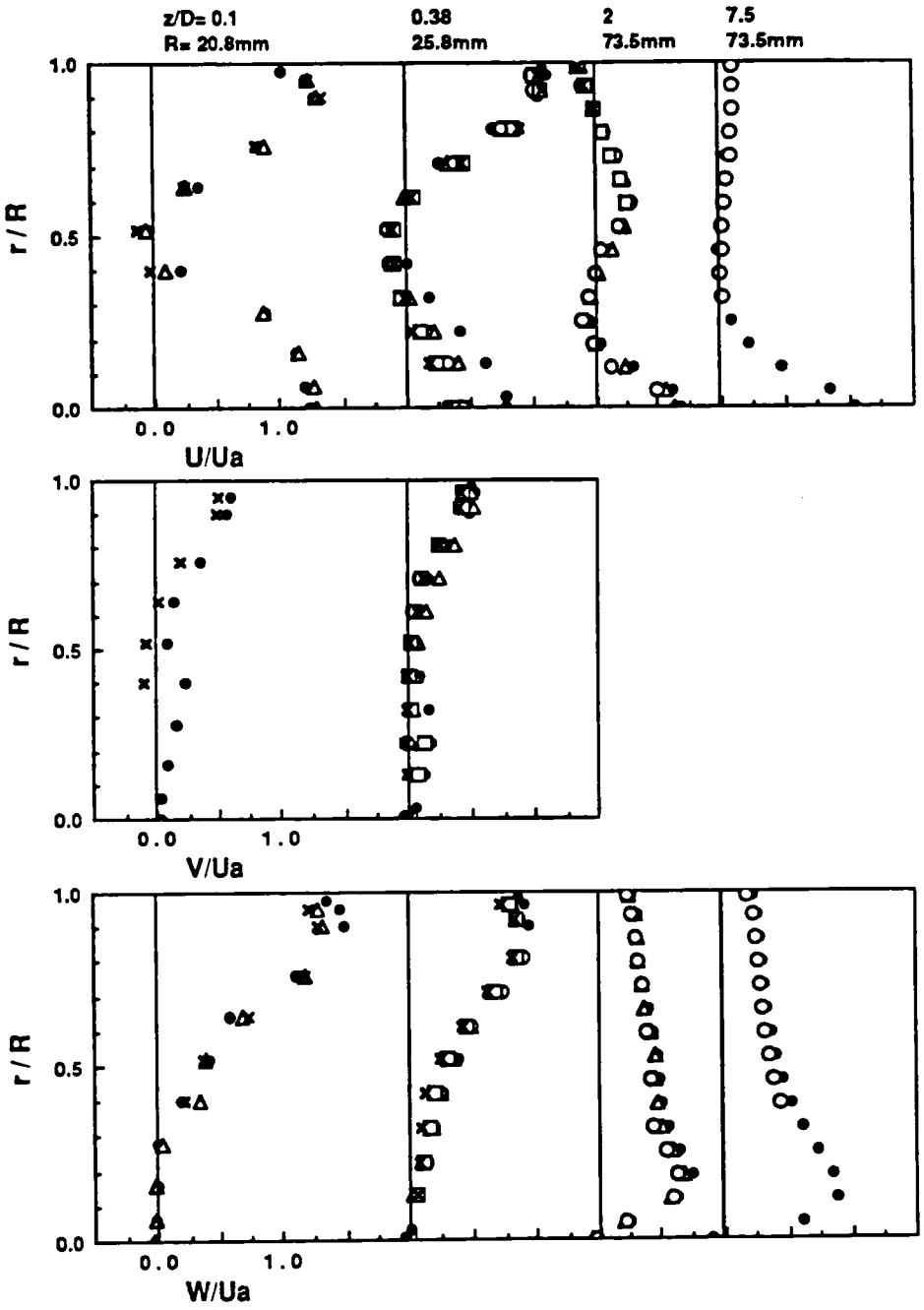


FIGURE 4.9 Radial distribution of bead mean velocities; bead suspended in the annulus.
(see Figure 4.8b for legend)

CHAPTER 5

Experiments with Disk Stabilised Kerosene-Fuelled Flames

5.1 INTRODUCTION

Flame stability in industrial burners and gas turbine combustors is usually achieved by recirculation generated by swirl or bluff-bodies with spray nozzles used to atomise the fuel in a wide range of droplet diameters. Knowledge of the behaviour of fuel droplets can be important for the improvement of stability and combustion efficiency and early studies include the photographs of McCreath and Chigier (1973) and the measurements by laser Doppler velocimetry of El Banhawy and Whitelaw (1981), but without detailed information of droplet sizes. Recently, instantaneous velocity and size measurements of fuel droplets have been obtained in non-swirling flames by Mao *et al.* (1986), Kawazoe *et al.* (1990) and McDonell and Samuelsen (1988) and in swirling flames by Hardalupas *et al.* (1990a, b and 1991) and Edwards *et al.* (1990) and the results show that the inertia and burning time of different droplet sizes affects the combustion efficiency. In addition, photographic studies of water sprays at the exit of annular air flows have been examined by Li and Tankin (1989) who showed the strong influence of the air flowrate on the spray characteristics.

These results explain many of the phenomena important to the combustion of two-phase flows and provide some guidance for scaling, particularly in terms of the various time scales of the flows. It is known, for example, that the droplets are likely to respond to the fluctuations of the continuous phase as their Stokes number, the ratio of the response time of the droplets to the timescale of the continuous phase flow, decreases towards and below unity, so that droplets of different sizes travel in different directions in regions of reverse flow with consequences for flame

stabilisation. In flames, the burning time of the droplets is an additional timescale relative to the isothermal flow, which affects the droplet behaviour in the flame. However, no work exists providing local droplet characteristics in flames stabilised by bluff bodies and recent work on droplet behaviour in isothermal flows behind bluff bodies (Rudoff *et al.*, 1988 and Brena de la Rosa and Bachalo, 1991) does not provide information on the scaling parameters influencing the droplet motion or detail information of the local fuel flux.

The present work examined the fuel droplet characteristics in non-combusting and combusting flows stabilised by bluff bodies and in burner geometries with and without a diffusing quarl, using a phase-Doppler velocimeter. The measurements of droplet velocity and flux characteristics in three 5 μm wide size classes, 10, 30 and 50 μm, explain the mechanisms which stabilise the flame in liquid fuelled bluff body combustors and quantify the influence of the stabilising disk diameter and the presence of the quarl on flame stability, flame length and combustion efficiency. Also, the tendency of the large droplets to be centrifuged by the streamline curvature of the recirculation vortices outside the reaction zone, either in the cold air stream and eventually at the exhaust or on the wall of the quarl, was quantified and scaled by their centrifuge Stokes number. The data form part of a pattern of results obtained in two burner sizes, see for example Hardalupas *et al.* (1990a, b and 1991) and Milosavljevic (1992) and assist in the provision of additional scaling parameters and the verification of those already known, as discussed in the following text. The experimental study includes photographic visualisation of the isothermal and combusting flows as well as measurements of droplet size, velocity and flux characteristics. Temperatures are included to add to the description of the flames in locations where the droplet concentration was sufficiently low to allow accurate measurements.

The following section describes the flow conditions and the experimental set-up. The results are presented and discussed in the third section which examines separately the velocity, size and flux characteristics of the liquid fuel droplets in isothermal

conditions and in flames stabilised by bluff-bodies without and with quarl and quantifies the effect of the quarl on combustion efficiency and stability. The paper ends by a summary of the more important findings.

5.2 FLOW CONDITIONS AND INSTRUMENTATION

Figure 5.1 shows the experimental arrangement which includes the kerosene-fuelled burner and the phase-Doppler velocimeter. The burner is similar to that of Milosavljevic (1992) with a constant air mass flowrate of 3.35×10^{-2} kg/s supplied through an upstream annular tube with inner and outer diameters of 18 (D_i) and 50.8 mm (D_o), respectively, as shown in Figure 5.2. Disk-shaped bluff-bodies with diameters, D_c, of 43.8, 38.2 and 31.6 mm, respectively, were positioned normal to the flow at the exit of the annulus and generated the recirculation zones essential for flame stabilisation; their blockage ratios were 0.74, 0.56 and 0.39. The area averaged air velocity in the annulus upstream of the disk was 15.4 m/s (U_a) and in the annulus at the exit of the disk was 51, 31 and 22 m/s (U_c), respectively, for 43.8, 38.2 and 31.6 mm diameter disks and the resulting Reynolds number was 53700 in the upstream annulus and 177000, 106000 and 76500 at the exit of the disk based on the outer diameter of the annulus D_o. The influence of a quarl of 50.8 mm length and 50° divergence angle positioned at the end of the annulus on the flame characteristics was examined.

Kerosene (Mobil Oil Company Ltd.) with the properties of Table 5.1 was supplied by a pump to an airblast atomiser (Delavan Type SN 30609-7) at a constant flowrate of 6×10^{-4} kg/s and atomised by an air flowrate of 6.53×10^{-4} kg/s to produce the 30° solid cone spray shown in Figure 5.3a by laser light sheet visualisation. The atomizing air corresponded to around 2% of the total air supplied to the burner. Fibre filters (Bolton type BQ and DQ) with 10 and 25 μm transmission were placed in the fuel supply circuit to remove potential contaminants. The equivalence ratio based on the atomising air was 13.6 and based on the overall air flowrate supplied to the burner was 0.26.

The velocity, diameter, flux and number density of the fuel droplets were measured by the phase-Doppler velocimeter described by Hardalupas (1989) which comprised transmitting optics based on a rotating grating as beam splitter and frequency shifter and integrated receiving optics which collected the light scattered from the measuring volume in the forward direction. The receiving optics were arranged to collect light at a forward scattering angle of 30 degree on the bisector plane of the two laser beams, as shown in Figure 5.1, to ensure that refraction dominated the scattered light. Quartz windows on the transmitting and receiving sides of the quarl provided optical access to the flow inside the quarl. The collected light was focused to the centre of a 100 μm collimating slit and passed through a mask with three evenly spaced rectangular apertures. The three light paths were each observed by a photomultiplier and the electrical signals processed by a purpose-built frequency counter and a mini-computer (PDP-11) to obtain the velocity and droplet-size information. The arrangement of the rectangular apertures is equivalent to collection of scattered light by three photomultipliers with their angular positions separated by 2.3 and 4.6 degrees and, combined with the arrangement of the transmitting light, allowed the measurement of droplet diameters up to 110 μm. The characteristics of the velocimeter are presented in Table 5.2.

The mean diameters were based on 7000 measurements resulting in statistical uncertainties of less than 2% (Tate, 1982) and the sizing accuracy of the instrument was less than 2 μm for droplets larger than 20 μm. The uncertainty is larger for the smaller droplets due to the tolerance of the phase-measuring electronic circuit and the oscillations existing on the response curve of the instrument (Hardalupas, 1989). Size uncertainties due to the variation of refractive index of kerosene in combustion is less than 7% for the present optical setup according to the analysis of Chapter 2, and the errors caused by the Gaussian intensity profile of the laser light is arround 5%. Droplet velocities were obtained in 20 size classes, with a 5 μm range in each size class, and the uncertainties were less than 2% and 5% for the mean and rms values, respectively, based on the average sample size of 1000 in

each class for the smaller sizes and around 500 for the 50 μm droplet size. The reduced number of measurements in the larger droplet size bins is due to the low number density of large droplets in the spray produced by the atomiser. The volume flux and number density of the liquid droplets were measured, as described by Hardalupas and Taylor (1989). The uncertainty of the flux measurements was around 30% in the dilute region of the spray due to uncertainties in the evaluation of the area of the probe volume for each size class and the rejection of measurements due to the validation procedure of the instrument (Bachalo *et al.*, 1988; Hardalupas and Taylor, 1989; Dodge *et al.*, 1987) and higher in the dense region due to attenuation of the laser beams resulting in decreased signal to noise ratio.

The time-averaged temperatures were obtained from a bare-wire thermocouple (Pt-$Pt_{13\%Rd}$, 300 μm diameter) and a digital voltmeter. The uncertainty of the temperature measurement, evaluated by comparison of the results with a 80 μm fine-wire probe, was around 100°K at 1800°K mainly due to radiation loss. The effect on the temperature measurement by droplet collisions with the thermocouple in the flame with the quarl was negligible due to the low number density of the liquid fuel droplets, less than $8x10^7$ m^{-3} as measured by the phase Doppler velocimeter. However, the temperature was not measured in the flame without the quarl due to influence of the liquid droplets, since the number density of droplets was several order of magnitudes higher than in the flame with the quarl.

5.3 RESULTS AND DISCUSSION

The local velocities were normalised with the area averaged air velocity in the annulus upstream of the bluff body, U_a, and axial and radial distances with the outer radius of the annulus, R. Velocities are presented in terms of the mean and rms values of fuel droplets within size classes of 10-15, 30-35 and 50-55 μm, which will be referred as the 10, 30 and 50 μm droplets.

The results are presented in three sub-sections. The first, sub-section 5.3.1, examines the spray characteristics without

combustion downstream of the bluff body with and without air flow in the annulus. Sub-section 5.3.2 presents the velocity, droplet size and flux characteristics in the flame stabilised by a disk bluff-body. The last sub-section examines the consequences of the presence of a quarl and of the stabilising disk diameter on the flame.

5.3.1 Characteristics of Droplets in Isothermal Flow

In an effort to examine the effect of the air flow in the annulus on the fuel spray, the droplets were visualised by a laser sheet and photographs of the isothermal spray without and with air in the annulus are shown on Figures 5.3a and 5.3b, respectively, for the 43.8 mm diameter disk. It is evident from the photographs that when the air was introduced in the annulus a large number of droplets lost their momentum and dispersed away from the centreline. This was caused by the air recirculation zone downstream of the bluff body, which increased the drag force on the droplets and made them lose their momentum faster than when no air stream was introduced in the annulus. The momentum of the recirculating air stream, which opposed that of the fuel spray, dispersed the droplets away from the centreline and made some droplet sizes move towards the bluff body. The droplets, which were captured by the recirculating air flow and eventually moved towards the bluff body, provided a stabilising mechanism for the flame, since they provided fuel at the base of the flame where they burned and generated heat to evaporate and ignite injected fuel. The mechanism that caused the spray to spread is similar to that observed by Li and Tankin (1989), for a hollow cone spray in their annular air flow.

The fidelity with which a given droplet size follows the mean air velocity can be quantified by the mean Stokes number, St_m, defined as

$$St_m = \frac{t_f}{\tau} \qquad (5.1)$$

where τ is the relaxation time of the droplets and t_f is the characteristic mean timescale of the flow, taken here as the ratio

of the outer diameter of the annulus (D_o) to the tip velocity at the exit of the disk (U_c). For the present flow, t_f was 1 and 2.3 ms for the 43.8 and 31.6 mm diameter disk respectively, giving rise to the characteristic time scales and Stokes numbers of Table 5.3 which justify the choice of the droplet sizes for which the velocity characteristics are presented, since the 10 μm droplets follow faithfully the mean air flow, the 30 μm droplets partially and the 50 μm droplets are nearly unaffected by the air flow.

Another parameter which limits the response of the droplets to the mean flow characteristics is the transit time Stokes number, St_{tr}

$$St_{tr} = \frac{t_{tr}}{\tau} \qquad (5.2)$$

where t_{tr} is the transit time of the droplets through the recirculation zone length and is quantified by the measured centreline droplet velocity and the length of the recirculation zone. The transit time of the droplet can be modified independently of the mean air flow characteristics by changing the operating conditions of the atomiser. So careful adjustment of both mean and transit Stokes numbers can affect the response of the droplets to the mean flow and improve the operation of the burner.

5.3.1.1 Spray droplet characteristics without co-flowing annular air

Preliminary measurements were obtained in the non-combusting fuel spray of Figure 5.3a, and Figure 5.4a shows that the mean velocities were around $0.2U_a$, $0.5U_a$ and $0.5U_a$ for 10, 30 and 50 μm droplets at the exit of the nozzle (z/R = 0.1) and increased monotonically to maximum values of $1.1U_a$, $1.5U_a$ and $1.4U_a$, respectively, at z/R = 0.8 and then gradually decreased to a common value of $0.65U_a$ at z/R = 3.6. The 30 and 50 μm droplets led the 10 μm droplets in the initial region due to different initial accelerations. The rms values at the exit of the nozzle were $0.46U_a$, $0.4U_a$ and $0.28U_a$ for the 10, 30 and 50 μm droplets respectively; they subsequently decreased and then increased

towards maximum values of $0.47U_a$, $0.5U_a$ and $0.4U_a$ at z/R = 0.6, 1.2 and 2, respectively. The behaviour of the spray was closely associated with the design of the nozzle, Figure 5.2, which provided swirling air and its effects are seen in the radial profiles of Figure 5.4b at z/R = 0.4 where the mean and rms velocities have a central minimum with the maximum values at r/R = ±0.08 and the mean velocities of 30 and 50 μm droplets lead that of the 10 μm droplets. The rms velocities of the 10 μm droplets were higher than those of the 30 and 50 μm droplets in the central region with the maximum value for the larger droplets at r/R = ±0.2. Higher rms velocities of the larger size droplets existed at the exit and were attributed to the fan-spreading phenomena (Hardalupas *et al.*, 1989). It may also be expected that the high mass (≈ 1) and volume loadings (≈ 0.1%) tend to suppress the gas phase rms velocities in the initial region.

The Sauter-mean diameters (SMD) of Figure 5.5a vary from around 50 μm in the near field of the centreline to less than 30 μm farther downstream with corresponding distributions which became narrower with distance from the nozzle and few droplets were larger than 55 μm which justified the choice of size ranges for the presentation of the velocity results. A radial profile of SMD at the axial location of z/R = 0.4 is also shown in Figure 5.5b with the larger droplets in a central region with an inner cone angle of around 30° and very few droplets at radii greater than r/R of 0.5. The spray in the region close to the nozzle was very dense and some ligaments could have been present to increase the measured SMD. Also, the large number density of droplets in the near field may have attenuated the incident laser light and reduced the observation of small droplets so that the distributions were skewed towards the larger droplets and the SMDs over-estimated. The SMD decreased with the axial distance from the nozzle partly because of droplet break-up and the entrainment of smaller droplets on the centreline and partly because the spray became less dense.

The characteristics of the SMD are directly related with those of the volume fluxes shown in Figure 5.6, and the flux of the 30 and 50 μm droplets was around two orders of magnitude larger than

that of the 10 μm droplets in the nearfield and in the core of the spray, r/R = ±0.18, Figure 5.6b, and gradually approached the flux of the 30 μm droplets in the downstream region (Figure 5.6a) at around z/R = 1. So the larger droplets of the spray carry most of the liquid fuel in the spray and their response to the air flow is very important for the operation of the burner.

5.3.1.2 The effect of air flow in the annulus on the spray characteristics

When air was introduced in the annulus a recirculation zone was established in the wake of the bluff body. The droplet behaviour inside the recirculation zone was identified in terms of the axial component of mean and rms velocities along the centreline, Figure 5.7, where the reduced back pressure increased the velocities close to the nozzle exit to around $0.32U_a$, $0.55U_a$ and $0.5U_a$ for the 10, 30 and 50 μm droplets and the initial axial velocity gradient from $3U_a/R$ and $4.3U_a/R$ without recirculation to $3.8U_a/R$ and $5U_a/R$ with recirculation for the 10 and 50 μm droplets, respectively. The resulting velocity maxima increased, relative to the development of the spray alone, to $1.3U_a$, $1.7U_a$ and $1.65U_a$ for 10, 30 and 50 μm droplets respectively. The effect of the adverse pressure gradient in the recirculation was to decelerate the mean and increase the rms velocity of the droplets between z/R = 0.6 and 1.2 and this was particularly evident with the 10 μm droplets whose mean axial velocity approached zero at z/R = 1.2. The rms velocity increased to $0.7U_a$, $0.83U_a$ and $0.75U_a$ close to the stagnation point for 10, 30 and 50 μm droplets, also as a result of the adverse pressure gradient, and diminished downstream to lower values for all droplets. The length of the recirculation zone was around 1.2R, as indicated by the minimum of the axial velocity of the 10 μm droplets in Figure 5.7. The transit time of the droplets through the recirculation zone length of the 43.8 mm disk was quantified by the measured mean axial velocity of droplets along the central trajectory and the recirculation zone length and was 8 ms for the 10 μm droplets and 3 ms for the 30 and 50μm droplets. The transit Stokes number was estimated and is given in Table 5.3 and shows that the 10 μm droplets had enough time to respond to the

recirculating flow, the 30 μm droplets could just respond and the 50 μm droplets would just travel through the recirculation zone.

The behaviour of droplets near the stagnation point observed by the velocity minimum in Figure 5.7, was clearly explained by their velocity probability density function (pdf) at z/R = 1.2 in Figure 5.8. They showed that 10 and 30 μm droplets moved either away from the nozzle (positive velocities) or towards the bluff body (negative velocities) while the 50 μm droplets moved only away from the nozzle. The reverse flow of the smaller droplet sizes was induced by the air recirculation downstream of the bluff-body which exchanged momentum with the forward-flowing spray, while the larger droplets failed to respond to the air and moved always away from the nozzle.

The centreline distribution of volume flux of droplets, Figure 5.9, remained near-constant as in the spray alone (Figure 5.6a), except in the region of the stagnation point, around z/R = 1.2, where the volume flux of the smaller droplet sizes decreased locally. So the amount of liquid fuel flux moving towards the bluff body on the centreline was small, as was also suggested by the photographs of Figure 5.3b, and the droplets moved mainly away from the axis after being decelerated on the centreline (Figure 5.7) and were then captured by the recirculating flow and moved backwards towards the bluff body.

5.3.2 Velocity, Droplet Size and Liquid Fuel Flux in the Flame Stabilised by a Bluff-Body

The disk stabilised flames had rich and lean flammability limits which tended to narrow with increasing disk diameter as the air velocity in the annulus increased, Figure 5.10a. The rich blowout of the flame was caused by the heat required by the fuel to burn. As the fuel flowrate increased, the generated heat close to burner was not enough to provide the additional heat to evaporate more fuel and the flame became cooler and eventually was blown off. The lean stability limits are more important for the low cost operation of the burner and became narrower as the bluff body diameter increased. It is of interest that Lefebvre *et al.* (1966) suggested a method for estimating the fraction of mass flow

entrained by a bluff-body flameholder, based on the blockage area and mean air velocity in the annular passage of the disk, and for the present experimental arrangement, this yielded relative values of recirculating air flowrate proportional to 0.91, 0.28 and 0.1 for the 43.8, 38.2 and 31.6 mm disks, respectively. The measurements presented below support also the increase of the recirculating air with the bluff body diameter. Thus, for constant overall equivalence ratio, the increase of disk diameter increased the amount of recirculating air which, in turn, decreased the local equivalence ratio inside the recirculation zone. So the narrower flammability limits of the flame stabilised by the larger disk diameter as a function of the overall equivalence ratio (Figure 5.10b) were justified by the lower local equivalence ratio inside the recirculation zone for the larger stabilising disk diameter.

The phase Doppler measurements were made in flames with Reynolds number of 53700 and overall equivalence ratio of 0.26. The flame stabilised by the 43.8 mm disk is shown in Figure 5.3c with the combustion zones identified by the bright yellow flame, signifying the presence of many droplets close to the outer radii of the disk and the light blue flame, signifying the burning of fuel vapour at the central region and at z/R around unity. The small droplets accelerated faster than the large ones, Figure 5.11, and the initial velocity gradients were $10.5U_a/R$, $8U_a/R$ and $7U_a/R$ and maximum velocities $2.9U_a$, $2.5U_a$ and $2.2U_a$ for 10, 30 and 50 μm droplets, respectively. The deceleration of the mean flow due to the recirculation zone was, however, similar to that of the non-combusting flow but, with the minimum axial velocity of $1.1U_a$ at the later axial location of $z/R = 2$ for the 10 μm droplets, rather than $z/R = 1.2$ (Figure 5.7) for the non-combusting flow. Thus, the stagnation point of the continuous phase was farther downstream than in non-combusting flow and the recirculation zone longer, due to the overall gas flow acceleration in combustion caused by the lower density of the combustion gases. Although the 10 μm droplets followed the mean air flow, the measured axial velocity near the stagnation point of the continuous phase was small but always positive. This was also observed by Edwards *et al.* (1990), who suggested that it was caused by the inability of 10 μm droplets to follow the instantaneous continuous phase flow

reversal. However, this effect was due to the short burning times of small droplets and will be explained in detail in the following paragraphs. The behaviour of the 30 and 50 μm droplets was similar to that of the 10 μm droplets with lower initial velocities and minimum values of $1.45U_a$ at $z/R = 2.4$.

The lifetime of burning droplets in the high temperature region of the flame was shorter than in isothermal flow and may be estimated from the expression of Kanury (1977) for isolated hydrocarbon fuel droplet burning in air:

$$t_b = \frac{d_o^2}{\lambda_b} \tag{5.3}$$

where d_o is the initial diameter of the droplet and λ_b is the burning constant equal to 10^{-6} m^2/s for kerosene. The values of t_b are given in Table 5.3. It is interesting to note that equation 5.3 shows no dependence on temperature. Using the values in Table 5.3 for different droplet sizes, it was found that the ratio of the burning time to the relaxation time, t_b/τ, was constant and around 0.4 for kerosene which suggests that the rate of change of droplet diameter was faster than its response to the flow and the former may dominate the behaviour of droplets in flame. Since the droplets burned as a cloud (Chiu and Liu, 1977; Bellan and Harstad, 1987), their burning time in the spray was influenced by the local oxygen content and droplet number density and the burning constant tended to be higher and burning time longer to give t_b/τ close to unity. However, values of t_b/τ around unity could still be partly responsible for the discrepancies between the velocity characteristics of the 10 μm droplets and the continuous phase in the flame. Also, the lack of seeding powder in the air flow in the annulus during the measurements, could contribute to those discrepancies (Schefer *et al.*, 1987), and bias the velocity measurements of the 10 μm droplets towards the atomising air flow.

In heterogeneous combustion, such as with liquid fuel sprays, the chemical reaction rate may be limited by the turbulent mixing of the gas phase reactants or the evaporation rate of liquid fuel. The former can be characterised by the Lagrangian integral time scale

of the turbulence, t_t, which was estimated around 0.3 ms in present flow according to Tennekes and Lumley (1972) by considering the lengthscale of the energy containing eddies of turbulence equal to the shear layer width (= 1/10 D_c) and their convection velocity, equal to u', was measured as $0.95U_a$. The latter was characterised by the evaporation time, t_b (Table 5.3). With constant turbulent time scale and the evaporation time a square function of droplet diameter, the reaction rate for the small droplet sizes is likely to be limited by mixing and, for the large droplet sizes, by their evaporation. The diameter at which the evaporation rate ceases to be the limiting timescale was that at which the Damkoehler number, D_a, defined by $D_a = t_t/t_b$, became of the order of unity (El Banhawy and Whitelaw, 1981), and occurred at around 20 μm and the related values of D_a are listed in Table 5.3.

The length of the recirculation zone, as suggested by the axial velocity minimum of the 10μm droplets along the centreline in the flame, was $1.1D_c$, $0.82D_c$ and $0.7D_c$ for the 43.8, 38.2 and 31.6 mm diameter disks respectively and independent of the Reynolds number. This was shorter than the $1.4D_c$ of Schefer *et al.* (1987) or the $1.5D_c$ of Chen *et al.* (1990) or the $2D_c$ of Taylor and Whitelaw (1984) due to different upstream and downstream conditions. The transit times of the droplets through the recirculation zone in the flame stabilised by the 43.8, 38.2 and 31.6 mm disks were 3, 2.4 and 1.9 ms respectively for all droplet sizes, while the burning times of the 10, 30 and 50 μm droplets, according to equation 5.3, are 0.1, 0.9 and 2.5 ms respectively. So, for the flame stabilised by the 43.8 mm disk, the burning times of droplets up to around 50 μm were smaller than their transit times through the recirculation zone, so that they could not survive to the end of the recirculation zone. So the measured droplets can either correspond to those which were initially larger and evaporated or to those which move faster than the mean velocity and so have shorter transit times than those indicated by the mean velocity. The droplets in the flame with the smaller disk had shorter transit time, so more droplets escaped downstream of the recirculation zone where they could be ignited to result in a longer flame. However, this did not

happen because the temperature there was too low to ignite the fuel due to the entrainment of cold air and resulted in a large amount of liquid fuel going to the exhaust system.

The recirculation zone can be identified by the mean flow vectors of the 10 μm droplets, and Figure 5.12 shows a toroidal vortex located adjacent to and driven by the shear layer established along the outer annular air flow as also identified in Figure 5.3c by the yellow flame close to the front face of the bluff-body. This result is similar to that of Schefer *et al.* (1987) in their bluff-body stabilised methane flame. A second vortex, smaller in scale and with direction opposite to that of the vortex created by the annular air flow, was located adjacent to the upstream portion of the fuel jet and bounded on the upstream side by the front surface of the bluff-body, and was driven mainly by the fuel jet. The mean flow vectors of the 30 μm droplets indicated vortices which extended only to $z/R = 0.4$, rather than around unity, and the 50 μm droplets retained forward direction at all locations.

The structure of the flow field shown by the velocity vectors of the 10 μm droplets is in accord with simple theories describing the near field flow characteristics of gaseous flames stabilised by bluff bodies. For example, the flow structure in a methane-fuelled bluff-body stabilised flame with axial fuel injection is characterised by two parameters, namely the vortex strength and the fuel-jet momentum, according to Chen *et al.* (1990). The vortex strength can be related to the area-averaged recirculating velocity and the radius of the vortex. The former is insensitive to fuel-jet momentum and around $0.3U_c$ in the present flame, i.e. 15.3, 9.3 and 6.6 m/s respectively for the 43.8, 38.2 and 31.6 mm disks, and the latter is comparable with the radius of the bluff-body, $D_c/2$. The momentum ratio, defined as the ratio of the air momentum flux to that of the liquid fuel momentum flux, identifies the transition of the flames from recirculation dominated to fuel-jet dominated as its value increases more than the critical value of 0.66 (Chen *et al.*, 1990). For the present case, the momentum flux of the fuel jet was equivalent to the momentum flux of the atomising air jet, which was proportional to U_{jet}, the maximum gas velocity along the centreline ($= 1.1U_a$), as

shown in Figure 5.11. The momentum flux of the air stream is proportional to U_c. Thus, the momentum ratio was proportional to $(U_{jet}/U_c)^2$ and corresponded to values of 0.1, 0.3 and 0.65 for the 43.8, 38.2 and 31.6 mm disk respectively. So the flames of the larger and the medium disk were recirculation-zone dominated as evidenced by the confined combustion zone in Figure 5.3c, and that of the smallest disk is close to transition as suggested by the momentum ratio.

The velocity profiles of Figure 5.13 show that the maximum negative velocity was around $-0.65U_a$ at $z/R = 0.1$ for the 10 μm droplets and indicate the amount of recirculating air, while the negative velocities of the 30 μm droplets were higher and at larger radii. The outward radial velocities of the 10 μm droplets were considerably lower than those of the larger droplets at $z/R = 0.1$, 0.4 and 0.8 with typical values of $0.3U_a$, $0.9U_a$ and $1.1U_a$ for 10, 30 and 50 μm droplets respectively and using these values their transit times along the radial width of the flame were estimated around 5.5, 1.8 and 1.5 ms, respectively. The radial transit times were shorter than the burning times (Table 5.3) of the 30 and 50 μm droplets and longer than that of the 10 μm droplets. Thus, droplets initially larger than 30 μm existed in liquid form at the edge of the high temperature reaction zone (bright blue and yellow region in Figure 5.3c) moving outwards and entered the outer cold annular air stream and were transported downstream without burning as was also confirmed by laser sheet visualisation. Droplets initially smaller than 30 μm could be burned completely in the reaction zone and, although their share of the total fuel volume flowrate was small, is contributed to the stability of the flame.

The degree of centrifuging of droplets due to the streamline curvature of the vortices can be quantified by the centrifuge Stokes number, St_ω, defined as: (Kriebel, 1961 and Dring and Suo, 1978)

$$St_\omega = \frac{18\,\mu}{\rho_d\,\omega\,d_o^2} \qquad (5.4)$$

where ρ_d and d_o are the density and initial diameter of the droplets, respectively, and μ the viscosity of the combustion gas (taken here as air). The angular velocity of the vortex, ω, on r-z plane can be estimated from $\omega = W/r$ with a typical value of vortex velocity $W = 0.3U_c$, equal to the recirculating air velocity, and the radius of the vortex $r = 0.25D_c$. The 10 μm droplets had moderate values of centrifuge Stokes number (Table 5.3), can followed faithfully the air flow. In contrast, the larger droplets have low St_ω and were centrifuged away from the vortices as indicated by their velocity vectors.

The rms velocity fluctuations close to the nozzle were mainly determined by the initial conditions and the atomisation process. The velocity fluctuations increased in the combusting flow relative to that without combustion (Figure 5.7) inside the primary reaction zone, up to $z/R = 2$, and a sample of the results is presented in Figure 5.11 and Figure 5.14. The swirling air was responsible for the wide range of droplet trajectory angles produced during the break-up process, ±15° for this spray which, when combined with the initially wide range of droplet axial velocities, caused the large rms fluctuations of the axial velocity, u', of the large droplets downstream of the nozzle due to the fan-spreading effect of Hardalupas *et al.* (1989) and the 50% anisotropy between u' and the rms fluctuations of the radial velocity, v', along the centreline (Figure 5.11). Both rms fluctuations, u' and v', were higher in the centre of the spray, lower in the recirculation zone and with radial maxima close to the shear layer of the spray (Figure 5.14). However, away from the centreline, the maximum values of v' of the 30 and 50 μm droplets at $z/R = 0.1$ were larger than those of u' mainly due to the centrifuging of the droplets by the jet driven vortex causing a fan spreading effect in the radial direction which was confirmed by examining the radial velocity pdf of the 30 and 50 μm droplets at $z/R = 0.1$ and $r/R \approx 0.3$, which had mainly radial velocity with outward direction. At the same point the radial velocity pdf of the 10 μm droplets had radially inward and outward velocities which resulted in larger v' than the larger droplets and was caused by the ability of the 10 μm droplets to respond to the gas phase

turbulence. This was confirmed by the values of the turbulent Stokes number defined as (Vames and Hanratty, 1988):

$$St_t = \frac{t_t}{\tau} \qquad (5.5)$$

where τ is the relaxation time of the droplet and t_t is the Lagrangian integral time scale of the turbulence, which was estimated earlier in the text of the order of 0.3 ms. The resulting values given in Table 5.3 show that the 10μm droplets, with a value of St_t close to unity, can follow the turbulent fluctuations but the larger droplets cannot.

The Sauter-mean diameter (SMD) along the centreline, Figure 5.15a, remained rather constant in the combusting flow up to z/R = 3, in contrast to the decrease observed in the non-combusting flow. The difference was caused partly by the dispersion and the burning of the droplets and partly by reduction of the laser light attenuation by the dense spray due to the evaporation of some droplets. A sample of the size distributions at z/R = 0.4, Figure 5.15a, shows that the most probable diameter of 40 μm for the non-combusting flow decreased to 15 μm for the combusting flow and confirmed the laser light attenuation close to the nozzle in the non-combusting flow. However, the SMD in the combusting flow was larger than that in the non-combusting flow downstream of the recirculation zone and caused by the faster evaporation of smaller droplets relative to the larger droplets. The radial distributions of SMD in the combusting flow (Figure 5.15b) were characterised by a near-constant central region with a value around 35 μm and initially lower values at the edge of the burning region (z/R = 0.1), which increased downstream (z/R = 0.8 & 1.2) as the smaller droplets burned and the larger droplets were centrifuged away from the centreline. At z/R = 2.4, the SMD was nearly uniform for r/R less than unity with a value between 30 and 40 μm which, together with Figure 5.3c, suggested that these were the droplet sizes escaping from the reaction zone without burning.

The centreline distribution of liquid fuel volume flux carried by the 10, 30 and 50 μm droplets, Figure 5.16, decreased

monotonically with axial distance from the nozzle in the combusting flow so that, at z/R = 2.4, it was some two orders of magnitude less than that at the origin and this suggests that, at least on the centreline, most of the fuel was burned or dispersed away from the centreline by the end of the secondary combustion region of Figure 5.3c. The radial distribution of fuel flux for each droplet size, conditionally sampled according to their axial velocity direction, is presented in Figure 5.17. The forward flux corresponding to droplets moving away from the nozzle was a maximum on the centreline, because of the influence of the spray, and the reverse flux of droplets moving towards the nozzle was negligible in the same region. The forward flux maintained similar values for the three sizes in the central region, but decreased radially in the recirculation zone where the flux for the 10 μm droplets was up to one order of magnitude less than the larger ones. The reverse flux, signifying the recirculating liquid fuel, existed only in the recirculation zone (up to z/R = 1.2) and was of the same order of magnitude for all three sizes, indicating that their reverse flux was large enough to contribute to the flame stability, although the direction of the time averaged velocity of the 50 μm droplets was always away from the stabilising disk. So careful implementation of the mean velocity information in the recirculation zone, particularly of the large droplets, is required and in some cases the fuel flux can be more relevant to combustion. Integration of the results suggested that the reverse flux was around 10% of the injected fuel and this was enough to stabilise the flame on the disk.

The dispersion of fuel in the flame is more clearly illustrated by the isoflowrate lines on the left hand half of Figure 5.18, deduced by integration of the measured radial profiles of net flux carried by 10, 30 and 50 μm and all droplet sizes. The measured total fuel flowrate at the initial measurement station (z/R = 0.3) was used to normalise the results, since the liquid fuel flowrate was not conserved in combustion because it burned. The results show that the fuel flowrate carried by 10, 30 and 50 μm size classes was 4%, 10% and 7% of the total fuel flowrate respectively. It is noted that the measurements identified only the fuel in liquid (droplet) form and did not take into account the fuel vapour. The annular air

driven vortex decelerated the spray and entrained fuel droplets into the recirculation region as can be clearly identified by the deflected isoflowrate line of the 10 μm droplets (Figure 5.18a) and this effect decreased with the increase of droplet size (Figures 5.18b and 5.18c). The similarity between the isoflowrate lines of the 50 μm droplets (Figure 5.18c) and those of all droplet sizes (Figure 5.18d) suggested that droplets larger than or around 50 μm carry most of the fuel flowrate in the flame.

5.3.3 Effect of a Quarl and of the Size of Bluff-Body

Photographs of the flames stabilised by the three disks and by the presence of a quarl are shown in Figure 5.19 and that stabilised by the quarl and the 43.8 mm disk (Figure 5.19a) allows direct comparison with that of Figure 5.3c without quarl. Combustion with the quarl was more intense with the flame filling the quarl and extending up to $z/R = 4.7$. The length of the flame increased with decrease of the stabilising disk diameter and reached z/R of 8.5 and 11.3 for the 38.2 and 31.6 mm disks respectively. The results confirmed that more droplets penetrated the recirculation zone of the smaller disk flame, so more fuel burned downstream of the recirculation zone resulting in a longer flame.

Figure 5.10b shows the flammability limits for the three disks with the quarl and are similar to those of Figure 5.10a except that no rich limit could be determined. The absence of rich limits was caused by the better combustion efficiency of the burner with quarl which provided enough heat to evaporate and burn the excess fuel. The lean extinction limit as a function of the overall equivalence ratio was more sensitive to disk diameter than for the flame without quarl due to the larger amount of recirculating air and the lower local equivalence ratio for the same overall equivalence ratio.

Measurements of temperature above the quarl, Figure 5.20, reveal a low temperature core together with high temperatures at larger radius, and the contours agree qualitatively with the photographs of Figure 5.19. The shorter flame, with the larger disk, was associated with higher temperatures at the quarl exit, and a maximum value of the order of 1700 °K at the outer periphery and

1300 °K at the centre. In contrast, the longer flame with the smaller disk had a maximum temperature of 1500 °K occurring farther downstream at the periphery with 1400 °K at the centre. The low temperature core at the centre, where the fuel spray was injected, was induced by the heat required to evaporate the droplets, while the reaction was intense at higher radius. The higher temperatures induced a secondary combustion region downstream of the recirculation zone where the unburned fuel droplets that penetrated the recirculation zone were ignited.

The centreline variations of axial mean velocity of droplets were similar for the two flames and that with the 43.8 mm disk is shown in Figure 5.21. The mean velocity in the upstream region, $z/R \leq 1.5$, was lower in the flame with the quarl due to the deceleration of the bulk flow by its diffusing confinement, which remained near-constant up to the quarl exit, $z/R = 2$, and decreased further downstream. The mean velocities of the 10 μm droplets were initially higher than those of the larger droplets with a hint of a minimum value at $z/R = 2$ in the flame stabilised by the largest disk, and around $z/R = 1.6$ for the flame stabilised by the small disk. These were considered as the length of the recirculation zone of the gas phase and, together with the centreline development of droplet axial velocity, estimated the transit times of droplets along the centreline which were longer than without the quarl by around 0.1 ms for all droplets. This difference was not large enough to justify the more efficient combustion that the photographs of flames with the quarl (Figure 5.19) indicate relative to those without quarl (Figure 5.3c). The time averaged centreline droplet velocity was formed by droplets which survived through the recirculation zone, and slow moving droplets were preferentially burned in the flame allowing only the fast droplets to remain in liquid form and be detected by the velocimeter. Thus, the velocity measurement of droplets remaining in liquid form were biased towards the faster moving droplets resulting in a measured short transit time of the droplets along the centreline. However, the volume flux of these droplets was reduced relative to the flame without quarl, because more droplets burned in the recirculation zone.

Figure 5.22 shows the radial profiles of mean axial velocity and indicates the nature of the recirculating region explaining the better combustion efficiency of the flame with the quarl. The near-zero axial velocity of the 10 μm droplets occurred at r/R = 0.8, 1. and 1.1 for the axial stations of z/R = 0.4, 0.8 and 1.2 respectively in the flame stabilised by the larger disk and at r/R = 0.7 and 0.8 at z/R = 0.4 and 0.8 for the smaller disk indicated a wider and stronger recirculation zone for the larger disk. The larger and stronger recirculation could retained more fuel droplets providing better mixing and burning inside the quarl to give a shorter length of flame stabilised by the larger disk and quarl, relative to that of the smaller disk (Figure 5.19) or that without the quarl (Figure 5.3c). The larger flowrate of recirculating air mixing with fuel inside the recirculation zone of the flame with the quarl accounted also for the local equivalence ratio lower than the overall equivalence ratio, and the flammability limits of Figure 5.10b.

A consequence of the quarl was the deposit of liquid droplet on the wall and the restriction of scattered light through the upper part of the optical windows, z/R>1.2. This is also undesirable since the flame can attach to the wall and shorten the life of large scale burners. Wall wetting was also observed in the swirling flames of Hardalupas *et al.* (1990a, 1991) and Milosavljevic (1992) and was attributed to the centrifuging of droplets by swirl which does not exist in the present flame; so another mechanism was responsible and is explained in the next paragraph. The same phenomenon has been observed in calculations of coal particles in flames stabilised by swirl for similar burner geometries (Lockwood and Mahmud, 1989; Godoy *et al.*, 1989 and was found to decrease combustion efficiency and increase emissions. Also coal particle deposition on the wall of the quarl can change the near-burner geometry and affect the stability of the flame.

Wall wetting is caused by the fast dispersion of fuel droplets away from the axis of the burner and the radial component of mean velocity, Figure 5.23, was near-uniform with an outwards value of around U_a and $1.5U_a$ for the 10 and 30 and 50 μm droplets, respectively, for r/R greater than 0.6 at the exit of the quarl

(z/R = 2.4). Information inside the quarl was limited by light detection but is expected to have similar trends as in the flame without the quarl (radial profiles of z/R = 0.4, 0.8 and 1.2 in Figure 5.13) with larger or similar values due to the expansion of the quarl. The large radial velocity close to the quarl was due to the centrifuging by the streamline curvature of the recirculation zone, as in the flame without the quarl. However, the flame without the quarl (Figure 5.3c) was not wider than the diameter of the stabilising disk and no droplets existed far from the reaction zone because of the large freestream velocity which carried the droplets downstream as soon as they left the recirculation zone. This did not happen with the quarl because the flame was wider due to the expansion of the flow and the location of the reaction zone close to the wall. The ratio of radial and axial residence times of droplets inside the quarl is important to quantify wall wetting and, when less than or equal to unity, will result in high probability of droplet deposition on the wall of the quarl. The radial transit time, t_r, based on the measured radial velocity of the 50 μm droplets at the exit of the quarl and the radius at the exit was 2 ms; the axial transit time, t_u, based on the length of the quarl and on the axial velocity of the 50 μm droplets was 2.5 ms, so the ratio of their transit times, t_r/t_u, was around 0.8. Since the burning time of the 50 μm droplets was larger than their transit times, droplets with initial size equal or larger than 50 μm could survive up to the exit of the quarl and reach the wall and since the ratio of their transit times, t_r/t_u, is less than unity, they will first reach the wall rather than the exit of the quarl and result in wall wetting. Proper control of the transit times can be achieved through the design of fuel injection devices to produce smaller droplet sizes or by a quarl large enough to ensure transit times smaller than the burning time of the larger droplets.

The Sauter Mean Diameters (SMD) of Figure 5.24 were around 20% larger in the flame stabilised by the smallest disk rather than the largest disk, except for the region of r/R between 0.8 and 1.2 at z/R = 0.8. According to the calculations of Kawazoe *et al.* (1990) the history of the SMD of a spray injected in a flame goes through a maximum, since it increases first due to faster evaporation of the smaller droplets, before decreasing as the spray proceeds in the

flame. This result is supported from our measurements since in the flame stabilised by the largest disk, where combustion was more intense, the SMD was smaller than in the smallest disk flame. At z/R = 0.8, the flame stabilised by the smallest disk filled the quarl up to r/R = 0.8, so that droplets at large radial distances were outside the flame and the rate of evaporation was negligible relative to the flame stabilised by the largest disk resulting in smaller SMD values in the smallest disk flame.

The radial distributions of liquid fuel flux carried by the 10, 30 and 50 μm droplets were integrated and the isoflowrate lines for the flame stabilised by the largest disk in the presence of a quarl are presented on the right hand half side of the Figure 5.18. The differences between the isoflowrate lines for the flames with and without the quarl was caused by the better combustion efficiency with the quarl. Most of the fuel injected at the centre of the flame with the quarl evaporated, burned or dispersed away from the centre much faster than in the flame without the quarl. The unburned fuel was mainly close to the quarl and resulted in the curved shape of the isoflowrate lines towards the wall. The effect was larger for the smaller droplet sizes (Figures 5.18a to 5.18c), but larger droplets were also found close to the wall supporting the wall wetting phenomenon explained earlier. The percentage of the total fuel flowrate carried by the 10, 30 and 50 μm was 1.2%, 10% and 6% respectively with most of the fuel carried by droplets larger than around 50 μm, as the similarity between the isoflowrate lines of the 50 μm and those of all sizes suggested (Figures 5.18c and 5.18d).

Integration of the radial profiles of the liquid fuel flux present in the flames stabilised by the large disk with and without quarl, Figure 5.25, shows that the liquid fuel flowrate decreased monotonically to 10% of the supplied flowrate up to the exit of the quarl, while 40% more liquid fuel remained in the flame without the quarl at the same distance from the nozzle. Although the figure indicates that the uncertainty of the absolute value of the measured fuel flowrate was 50% lower than that supplied by the nozzle, mainly due to the attenuation of the incident laser beams by the dense spray which reduced the data rate, the results

quantify the combustion efficiency of each burner at the last measured axial location (z/R = 2.4) as 88% in the flame with the quarl and 36% without the quarl.

The variation of the flame length with the air and fuel flowrates and the stabilising disk diameter was measured with the quarl, since it determined the length of the combustion chamber needed to burn the fuel. The Reynolds number was varied from 6000 to 50000 and the overall equivalence ratio up to 1.6. The flame lengths for the three bluff bodies and three fuel flowrates are presented in Figure 5.26 as a function of the ratio of the atomising air velocity to the air velocity in the annulus. The flame length scaled linearly with the fuel to air velocity ratio up to a value of 0.65, while the slope of the linear part of the curve increased with fuel flowrate. In common with the findings of Chen *et al.* (1990), the flame length was insensitive to the velocity ratio for values higher than 0.65, where the flame ceased to be dominated by the recirculation and became a jet flame. The decrease of the slope of the linear variation of the flame length with fuel flowrate was caused by the shift towards smaller sizes as the fuel flowrate decreased for constant air flowrate, and resulted in shorter droplet burning times and flame length.

The flame length plotted as a function of the overall equivalence ratio, Figure 5.27, suggests that an almost linear relation existed with its slope decreasing with the increase of the stabilising disk diameter. This happened because the recirculating air increased with the disk diameter and retained more fuel inside the recirculation zone to burn there rather than farther downstream. So, the relative change of the slope of the curves on Figure 5.27 suggests that the flame length as a function of equivalence ratio scales with the inverse of the disk diameter.

5.4 CONCLUSIONS

1. Velocity, droplet size, liquid fuel flux and temperature have been measured in kerosene-fuelled flames stabilised by bluff-bodies without and with a quarl diffuser by phase-Doppler velocimeter and photographic visualisation. The stabilising disk

diameters were 43.8, 38.2 and 31.6 mm resulting in blockage ratios of 0.74, 0.56 and 0.39 respectively. The equivalence ratio based on the overall air flowrate was 0.26 and based on the atomising air only was 13.6 and the Reynolds number based on the area averaged velocity upstream of the disk and the outer diameter of the annulus was 53700. The fuel was injected parallel to the axis of the burner using a commercial atomiser positioned at the centre of the stabilising disk. The quarl length was 50.8 mm and its divergence angle 50°. The flammability limits and the flame length were also measured as a function of the blockage and equivalence ratio for a range of Reynolds number between 6000 and 55000 and overall equivalence ratios up to 1.6.

2. The relative motion of a given droplet size class was characterised in terms of several timescale parameters : the mean Stokes number, St_m, and the transit time Stokes number, St_{tr}, indicating the fidelity to the mean air flow; the centrifuge Stokes number, St_w, indicating the tendency of the droplets to centrifuge due to air streamline curvature and the turbulent Stokes number, St_t, indicating the fidelity to the turbulent motion of the air. The 10 μm droplets can follow faithfully the mean and turbulent motion of the air. The 30 μm droplets respond partially to the mean air flow but not to the air turbulence and are partially centrifuged by the air streamline curvature. The 50 μm droplets are strongly centrifuged by the air streamline curvature. Since the transit time of the droplets through the recirculation zone can be modified by the atomisation process independent of the air flowrate in the annulus, both mean and transit Stokes numbers can be independently optimised to result in the best response of the droplets to the mean flow.

3. In the reacting flow, the droplet burning time was more important than the response of the droplets to the air flow, since it is shorter than their relaxation time. The ratio of the droplet burning time to their transit time through the recirculation zone indicated the chances that a droplet size class burned inside the recirculation zone. The transit time could be either along the radial direction away from the axis of the burner or along the axis of the burner. Droplet sizes larger than around 50 μm could

survive during their axial and the radial transit time through the recirculation zone and would contribute to fuel being lost to the exhaust.

4. The contributions of the 10, 30 and 50 μm droplet size classes to the total volume flux inside the recirculation zone was 4%, 10% and 7% respectively in the flame without the quarl and 1.2%, 10% and 6% in the flame with the quarl. Although the relative volume flux of the 30 μm droplets was larger, the volume flux carried by droplets larger than around 50 μm contributed the larger fraction to the total fuel flux, as was indicated by the similarity between the isoflowrate lines of the 50 μm droplets and those after integration over all the droplet size classes. When the flux of each size class was conditionally measured according to the direction of their axial velocity, then the reverse flux, denoting that directed towards the bluff body, of the 50 μm droplets was comparable with that of the smaller droplets. Considering that the mean motion of the larger droplets does not indicate recirculation and that the volume fluxes show their large contribution to the fuel remaining inside the recirculation zone, the interpretation of the velocity results without droplet flux information could be misleading. The total of reverse flux in the recirculation zone of the flame stabilised by the larger blockage ratio, 0.74, without the quarl was around 10% of the total injected fuel flowrate and was enough to stabilise the flame on the disk.

5. The parameter that affects the stability of the flame on the bluff body is the ratio of the momentum flux of the recirculating air to that of the liquid fuel jet. The momentum of the recirculating air increased the drag force on the droplets of the spray and spread them radially away from the axis where the recirculating vortices convected them towards the stabilising disk. For our flames, the momentum flux ratio was proportional to the ratio $(U_{jet}/U_a)^2$, where U_{jet} is the atomising air maximum centreline velocity and U_a the air velocity in the annulus. The results confirm that the recirculation zone dominated the flames stabilised by disks with blockage ratios of 0.74 and 0.56, while that corresponding to the smaller blockage ratio of 0.39 was close to the transition from recirculation to jet-dominated flames and the estimate of the

momentum ratio was 0.65, close to the critical value suggested by Chen *et al.* (1990) for gaseous fuel flames.

6. The effect of the presence of the quarl on the flames stabilised by the three disks resulted in more intense combustion close to the nozzle, with the flame stabilised by the largest diameter bluff body being shorter and having higher quarl exit temperature. There was a low temperature core at the centre, where the spray was injected, 1400°K and 1300°K for the larger and smaller disk respectively. High temperatures were observed at larger radius, 1700°K and 1500°K for the largest and smallest disks, respectively. The higher temperature induced a secondary combustion region downstream of the recirculation zone where the unburned fuel droplets that penetrated the recirculation zone were ignited. The presence of the quarl induced a larger recirculation zone which retained a larger part of the fuel and increased the amount of fuel burned in the near field. Integration of the flux results indicated that the liquid content of the flame stabilised by a blockage ratio of 0.74 was reduced by more than 40% due to the quarl and suggested that the combustion efficiency with and without the quarl were around 88% and 36% respectively.

7. The centrifuging of the droplets by the streamline curvature dispersed droplets from the axis and the isoflowrate lines indicated that a larger amount of fuel existed at large radii. The effect was more obvious with the quarl, since most of the fuel close to the axis burned or dispersed sideways and the isoflowrate lines were curved and directed to the wall consistent with the wall wetting. Although this effect has been observed in swirling flames (e.g. Hardalupas *et al.*, 1990a and 1991) and was attributed to centrifuging due to swirl, our results show that this can also be caused by streamline curvature of the recirculating vortices in bluff-body flames and suggests that all the flames stabilised by recirculation zones may suffer some centrifuging of the larger droplets. The tendency of the droplets to reach the wall of the quarl was quantified by the ratio of the radial residence time of the droplets in the flame relative to their burning time. Also the ratio of the axial to the radial burning time when smaller than

unity increased the probability of droplets reaching the wall of the quarl.

8. The lean flammability limits as a function of the overall equivalence ratio became worse with increase of the stabilising disk diameter without and with the quarl and this effect was larger for the flame with quarl. This was due to the larger amount of recirculating air induced by the larger disks or the presence of the quarl resulting in lower local equivalence ratio inside the reaction zone and leaner in the burning region. The rich flammability limits were caused by the increased requirement of heat to evaporate and burn the excess fuel, which could not be provided by the flame without the quarl and eventually the flame temperature reduced and combustion ceased. The flame with the quarl had no rich flammability limits.

9. The length of the flame with the quarl was found to scale linearly with the ratio of the velocity of the atomising air to that in the annulus, which was equivalent to the square root of the momentum ratio used by Chen *et al.* (1990) in their gaseous flame. The flame length remained constant for the velocity ratios above 0.66, when the flame became jet rather than recirculation zone dominated. The flame length varied linearly with the overall equivalence ratio and the slope of the curve decreased with disk diameter.

REFERENCES

Bachalo, W.D., Rudoff, R.C. and Brena de la Rosa, A. (1988) Mass flux measurements of a high number density spray system using the phase-Doppler particle analyzer. AIAA-paper-88-0236.

Brena de la Rosa, A. and Bachalo, W.D. (1991) Particle diagnostics and turbulence measurements in an isothermal spray under the influence of stabilising bodies. In Proc. of 5th Int'l Symp. of *Liquid Atomisation and Spray Systems* (ICLASS), Gaithersburg, U.S.A., paper 44, 423.

Bellan, J. and Harstad, K. (1987) Ignition of non dilute clusters of drops in convective flows. *Comb. Sci. and Tech.*, **53**, 75.

Chen, R.H., Driscoll, J.F., Kelly, J., Namazian, M. and Schefer, R.W. (1990). A comparison of bluff-body and swirl-stabilised flame. *Comb. Sci. and Tech.*, **71**, 197.

Chiu, H.H. and Liu, T.M. (1977) Group combustion of liquid droplets. *Comb. Sci. and Tech.*, **17**, 127.

Dodge, L.G., Rhodes, D.J. and Reitz, R.D. (1987) Drop size measurement techniques for sprays : comparison of Malvern laser-diffraction and Aerometrics Phase/Doppler. *Applied Optics*, **26**, 2144.

Dring, R.P. and So, M. (1978) Particle trajectories in swirling flows. *J. Energy*, **2**, 232.

Edwards, C.F. and Rudoff, R.C. (1990) Structure of a swirl-stabilised spray flame by imaging, laser Doppler velocimetry, and phase Doppler anemometry. In Proc. 23rd Symp. (Int'l) on Combustion, Combustion Institute.

El Banhawy, Y. and Whitelaw, J.H. (1981) Experimental study of the interaction between a fuel spray and surrounding combustion air. *Comb. and Flame*, **42**, 253.

Godoy S.G., Ismail M. and Lockwood, F.C. (1989) Measurements in a cylindrical pulverised coal furnace. Influence of swirl number on combustion performance. *Comb. Sci and Tech.*, **67**, 59.

Hardalupas, Y., Milosavljevic, V.D., Taylor, A.M.K.P. and Whitelaw, J.H. (1991) In-quarl measurements of liquid fuel velocity, mass flux and concentration distributions. Imperial College, Thermofluids Section Report TF/91/03.

Hardalupas, Y., Taylor, A.M.K.P. and Whitelaw, J.H. (1989) Velocity and particle flux characteristics of turbulent particle-laden jet. *Proc. Roy. Soc.*, Lond. A, **426**, 31.

Hardalupas, Y., Taylor, A.M.K.P. and Whitelaw, J.H. (1990a) Velocity and size characteristics of liquid-fuelled flames stabilised by a swirl burner. *Proc. Roy Soc.*, Lond., A, **428**, 129.

Hardalupas, Y., Taylor, A.M.K.P. and Whitelaw, J.H. (1990b) Liquid fuel mass flux, fraction and concentration distributions in a swirl-stabilised flame. Imperial College, Fluids Section Report FS/90/09.

Hardalupas, Y. (1989). Experiments with isothermal two-phase flow. Ph.D. Thesis, University of London.

Hardalupas, Y. and Taylor, A.M.K.P. (1989) On the measurement of particle concentration near a stagnation point. *Exp. in Fluids*, **8**, 113.

Kanury, A.M. (1977) Introduction to Combustion Phenomena. 2nd Ed., Gordon & Breach, New York.

Kawazoe, H., Ohsawa, K. and Fujikake, K. (1990) LDA measurement of fuel droplet sizes and velocities in a combustion field. *Comb. and Flame*, **82**, 151.

Kriebel, A.R. (1961) Particle trajectories in a gas centrifuge. *Trans. ASME, J. Basic Eng.*, **83**, 333.

Lefebvre, A.H., Ibrahim, A.R.A.F. and Benson, N.C. (1966) Factors affecting fresh mixture entrainment in bluff-body stabilised flames. *Comb. and Flame*, **10**, 231.

Li, X. and Tankin, R.S. (1989) Spray behaviour in annular air streams. *Comb. Sci and Tech.*, **64**, 141.

Lockwood, F.C. and Mahmud, T. (1989) On the prediction of pulverised coal flame stability. *Comb. Sci. and Tech.*, **66**, 319.

Mao, C.-P., Wang, G. and Chigier, N.A. (1986) An experimental study of air-assist atomiser spray flames. In *21st Symp. (Int'l) on Comb.*, The Combustion Institute, 665.

McCreath, C.G. and Chigier, N.A. (1973) Liquid-spray burning in the wake of a stabiliser disk. In Proc. 14th Symp. (Int'l) on Combustion, Combustion Institute, 1355.

McDonell, V.G. and Samuelsen, G.S. (1988) Evolution of the two-phase flow in the near field of an air-blast atomiser under reacting and non-reacting condition. In Proc. of 4th Int'l Symp. on Appl. of Laser Anemometry to Fluid Mechanics, July 1988, Lisbon, Portugal.

Milosavljevic, V. (1992) Ph.D. Thesis, University of London. (in preparation)

Rudoff, R.C., Houser, M.J. and Bachalo, W.D. (1988) Experiments on spray interactions in the wake of a bluff body. *J. Eng. for Gas Turbines and Power*, Trans. ASME, **110**, 86.

Schefer, R.W., Namazian, M. and Kelly, J. (1987) Velocity measurements in a turbulent non-premixed bluff-body stabilised flame. *Comb. Sci. and Tech.*, **56**, 101.

Tate, R.W. (1982) Some problems associated with the accurate representation of droplet size distributions. In Proc. of 2nd Int'l Conf. on Liquid Atomisation and Spray Systems (ICLASS), Wisconsin, U.S.A.

Taylor, A.M.K.P. and Whitelaw, J.H. (1984) Velocity characteristics in the turbulent near wakes of confined axisymmetric bluff bodies. *J. Fluid Mech.*, **139**, 391.

Tennekes, H. and Lumley, J.L. (1972) A First Course in Turbulence. MIT Press.

Vames, J.S. and Hanratty, T.J. (1988) Turbulent dispersion of droplets for air flow in a pipe. *Exp. in Fluids*, **6**, 94.

TABLE 5.1 Properties of kerosene†

Chemical Formula	$C_{12}H_{26}$
Relative density at 15 °C	0.8
Kinematic viscosity at 40 °C, cSt	<0.5
Lower specific energy, MJ/kg	42.8
Flash point, °K	>311
Boiling point, °K	>410
Vapour Pressure at 20 °C, mmHg	<0.1
Stoichiometric F/A ratio (in mass)	0.0676

† Mobile Oil Company Limited

TABLE 5.2 Characteristics of the phase-Doppler velocimeter

Transmitting optics		
Laser: 1 watt Ar-ion laser		
operating power	400	mW
wavelength	514.8	nm
Beam intersection angle	4.85	deg.
Measurement volume length at $1/e^2$ intensity	1979	μm
Measurement volume diameter at $1/e^2$ intensity	84	μm
Fringe spacing	6.07	μm
Number of fringes	13	
Frequency shift	0-3	MHz
Receiving optics		
Focal length of collimating lens	600	mm
Location of receiving optics		
from forward scatter angle	30	deg.
Equivalent aperture at collimating lens:		
dimension of rectangular aperture	45 x 6	mm
separation between aperture 1 and 2	24	mm
separation between aperture 1 and 3	48	mm
Magnification	1/2	
Spatial filter slit width	100	μm
Effective length of measuring volume	200	μm
Phase angle-to-diameter conversion factor		
for channel 1 and 3	0.306	μm/deg

TABLE 5.3 Characteristics of kerosene droplets

d_p, μm	τ, ms	t_b, ms	D_a	St_m[a]	St_{tr}[b]	St_t[c]	St_ω[d]
10	0.25	0.1	3	4	32	1.2	2.9
30	2.2	0.9	0.3	0.45	1.36	0.14	0.32
50	6.2	2.5	0.12	0.16	0.48	0.05	0.11

[a] t_f is 1 ms
[b] isothermal flow
[c] t_t is 0.3 ms
[d] ω is approximated as $0.3U_c/0.25D_c$

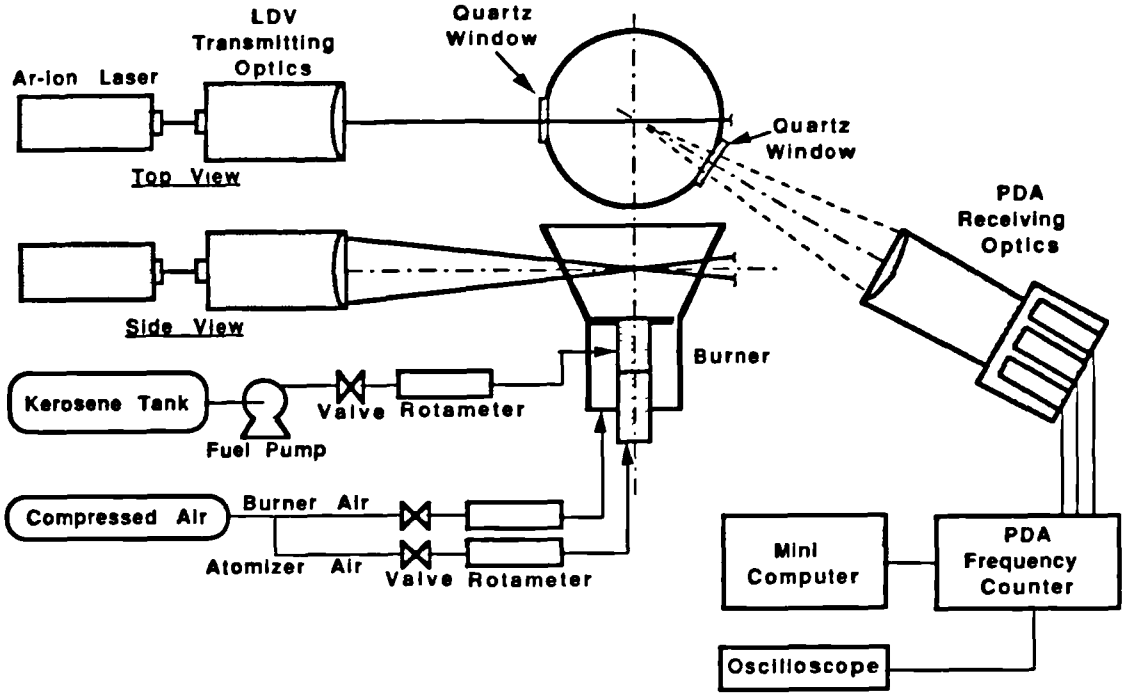


FIGURE 5.1 Schematic of the experimental system.

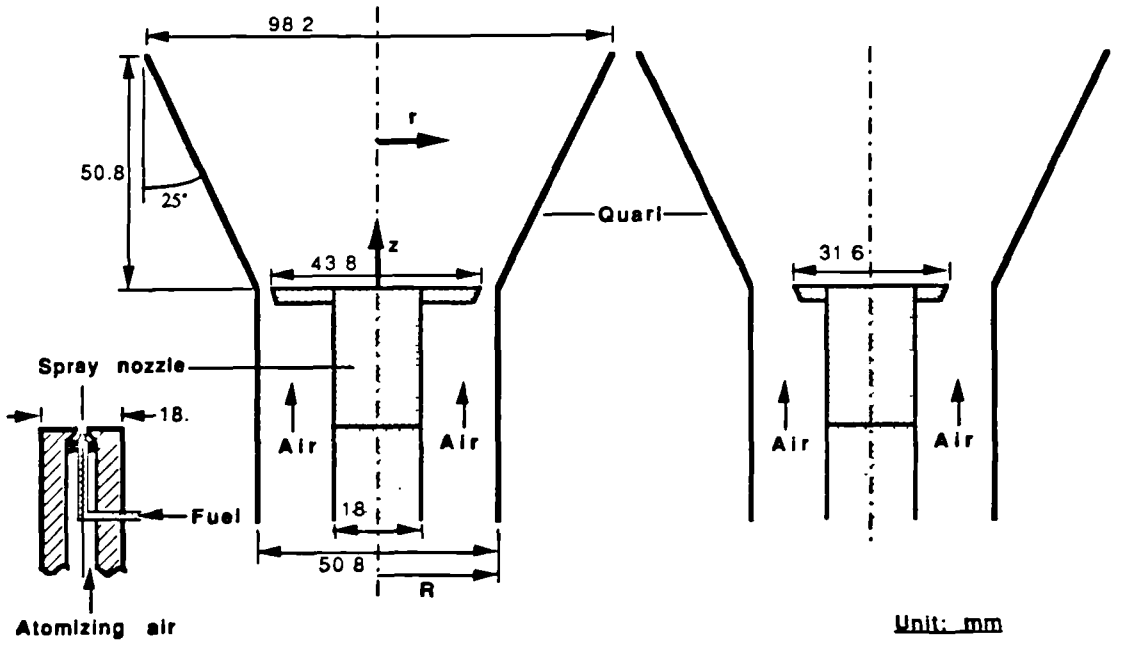


FIGURE 5.2 Dimensions and coordinates of the kerosene burner.

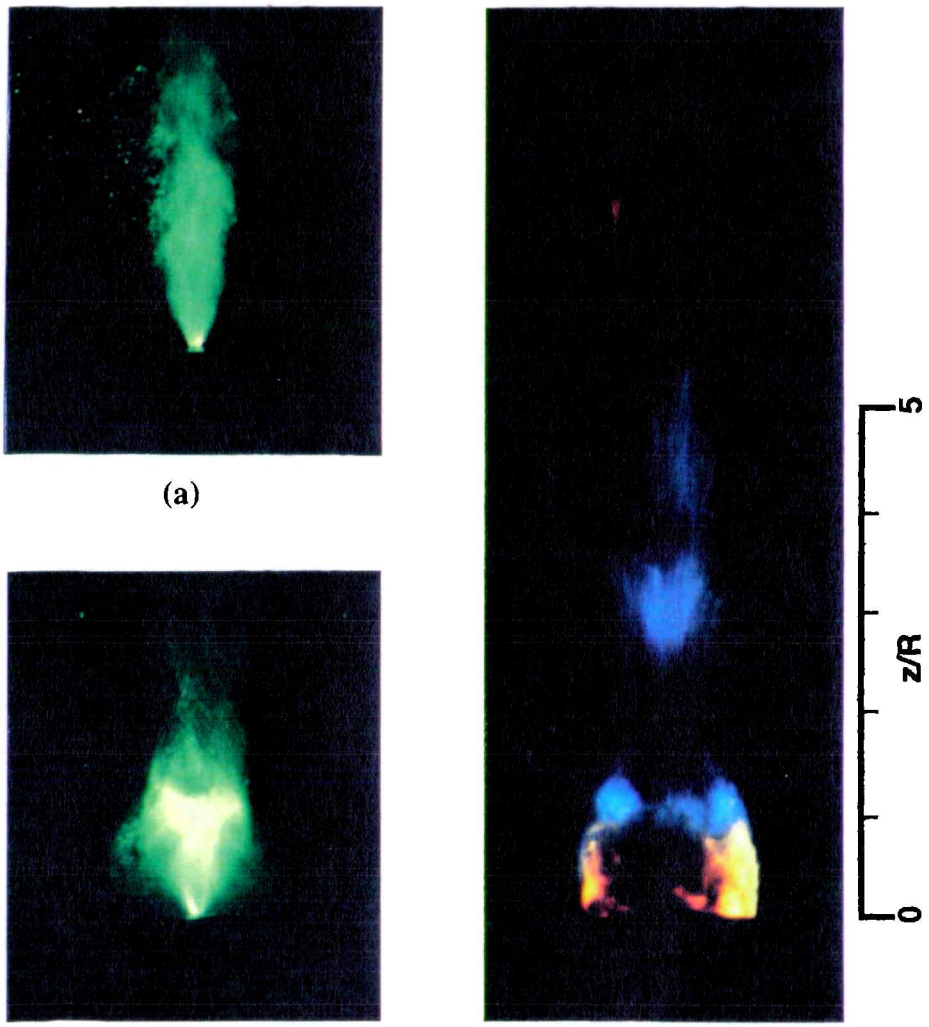


FIGURE 5.3 Kerosene flame stabilised by a 43.8 mm disk bluff-body.
(a) sheet-lighted non-combusting spray;
(b) sheet-lighted non-combusting flow;
(c) combusting flow.

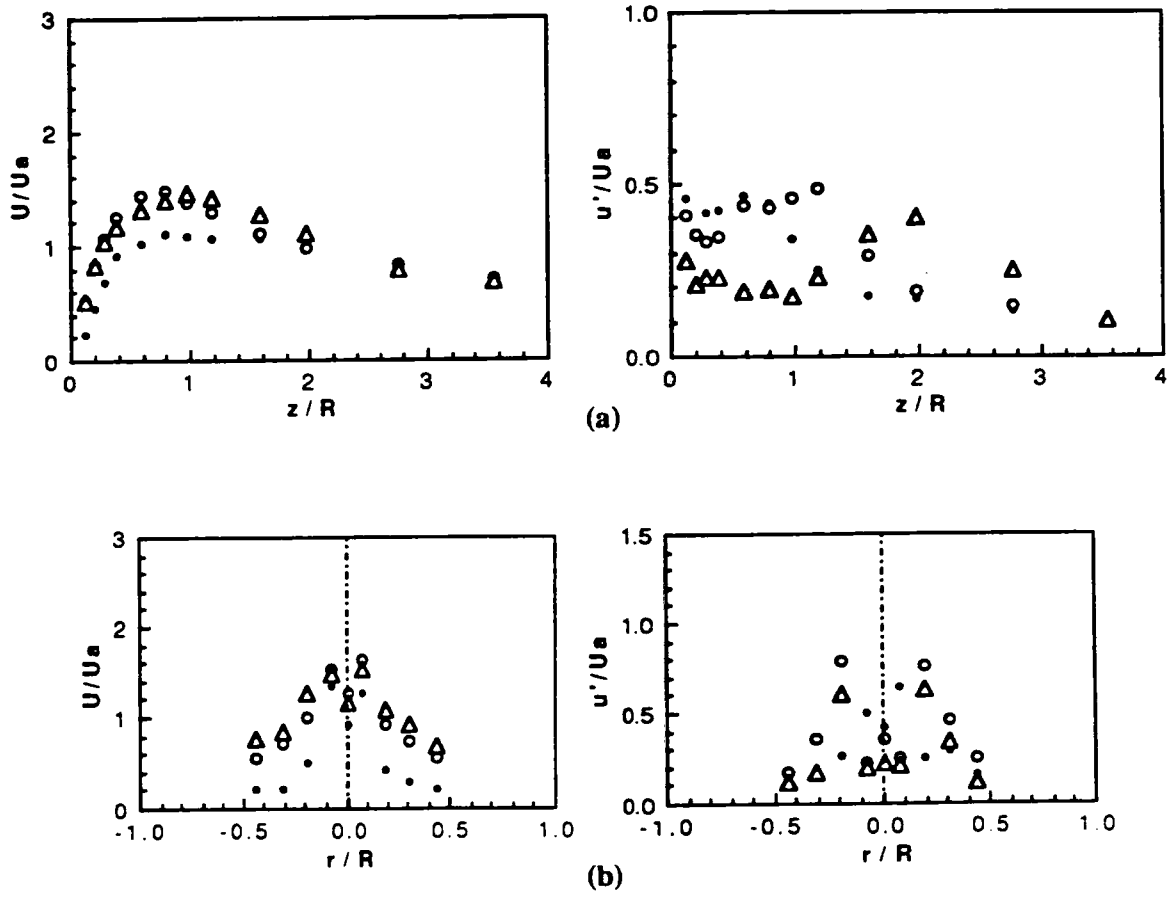


FIGURE 5.4 Axial component of mean (U/U_a) and rms (u'/U_a) velocities of fuel droplets in the non-combusting spray. (a) along the centreline; (b) radial profile at z/R=0.4. (• 10 μm, o 30 μm and △ 50 μm droplets)

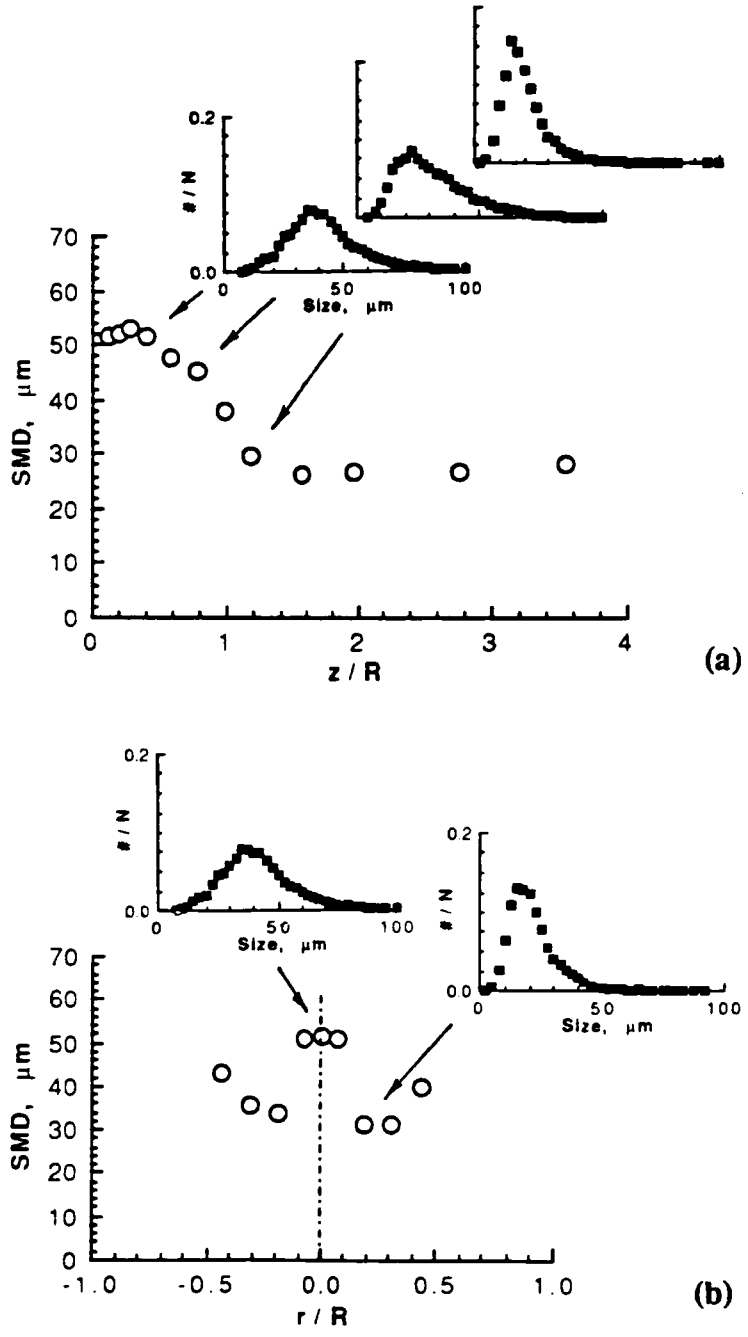


FIGURE 5.5 Sauter-mean diameter (SMD) and size distributions (#/N) of fuel droplets in the non-combusting spray.
(a) along the centreline; (b) radial distribution at z/R=0.4.

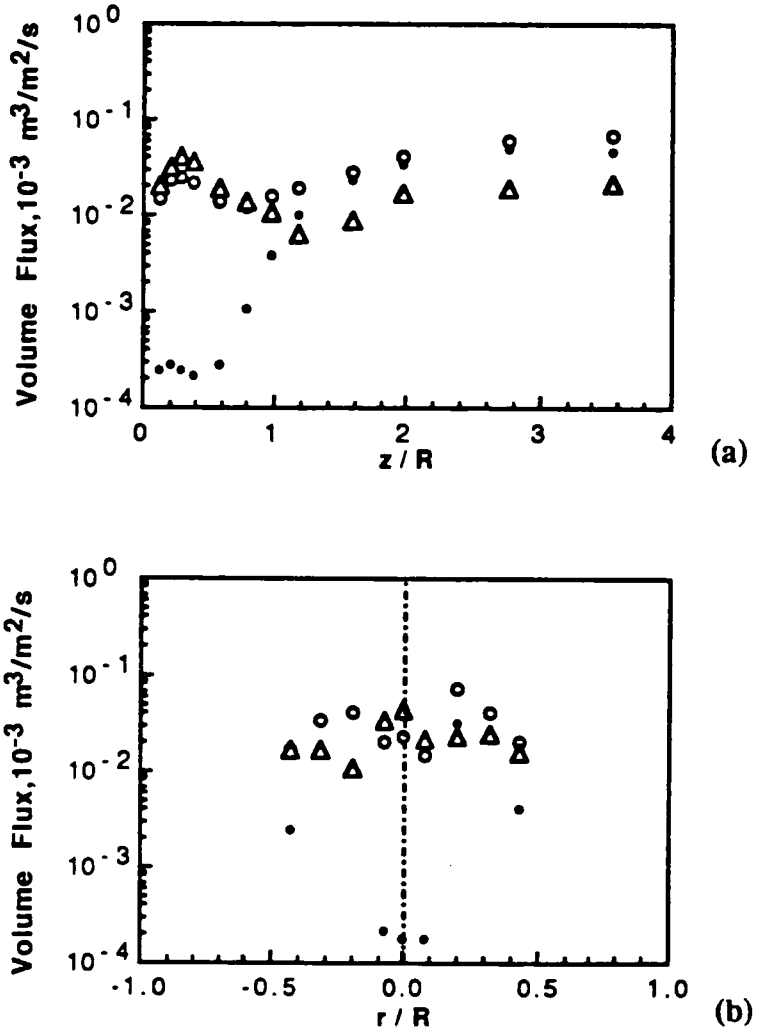


FIGURE 5.6 Volume flux of fuel droplets in the non-combusting spray. (see Figure 5.4 for symbols)
(a) along the centreline; (b) radial distribution at z/R=0.4.

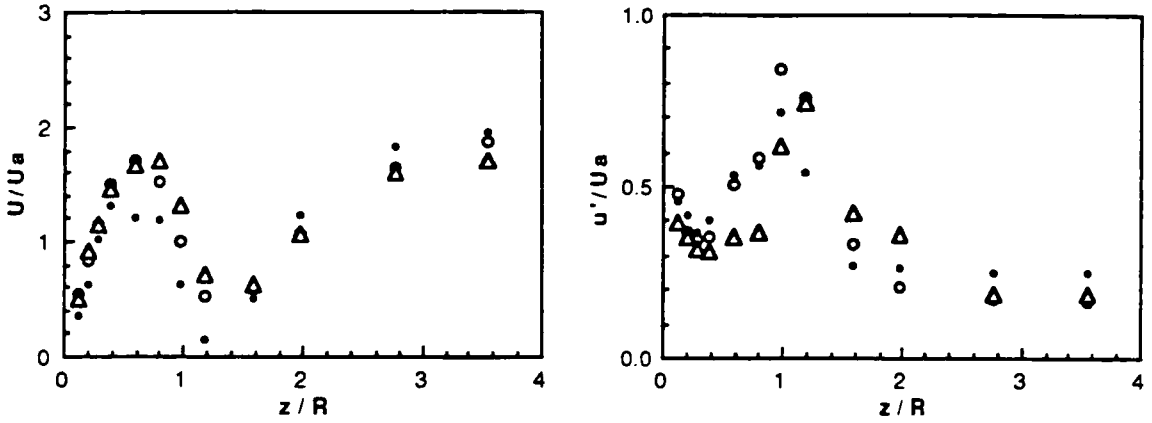


FIGURE 5.7 Axial component of mean (U/U_a) and rms (u'/U_a) velocities of fuel droplets along the centreline in the non-combusting flow downstream of a 43.8 mm disk bluff-body. (see Figure 5.4 for symbols)

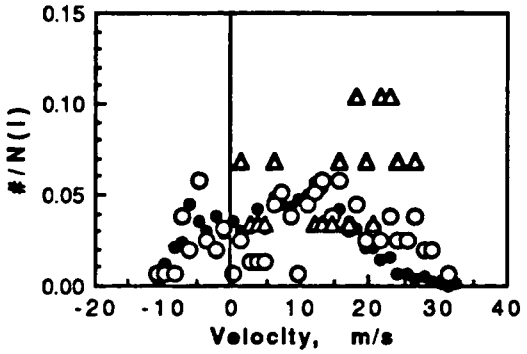


FIGURE 5.8 Velocity probability density function of fuel droplets at z/R=1.2 on the centreline of Figure 5.7.

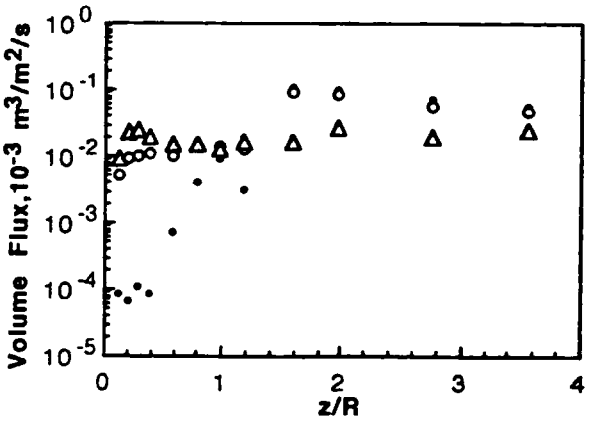


FIGURE 5.9 Volume flux of fuel droplets along the centreline in the non-combusting flow downstream of a 43.8 mm disk bluff-body. (see Figure 5.4 for symbols)

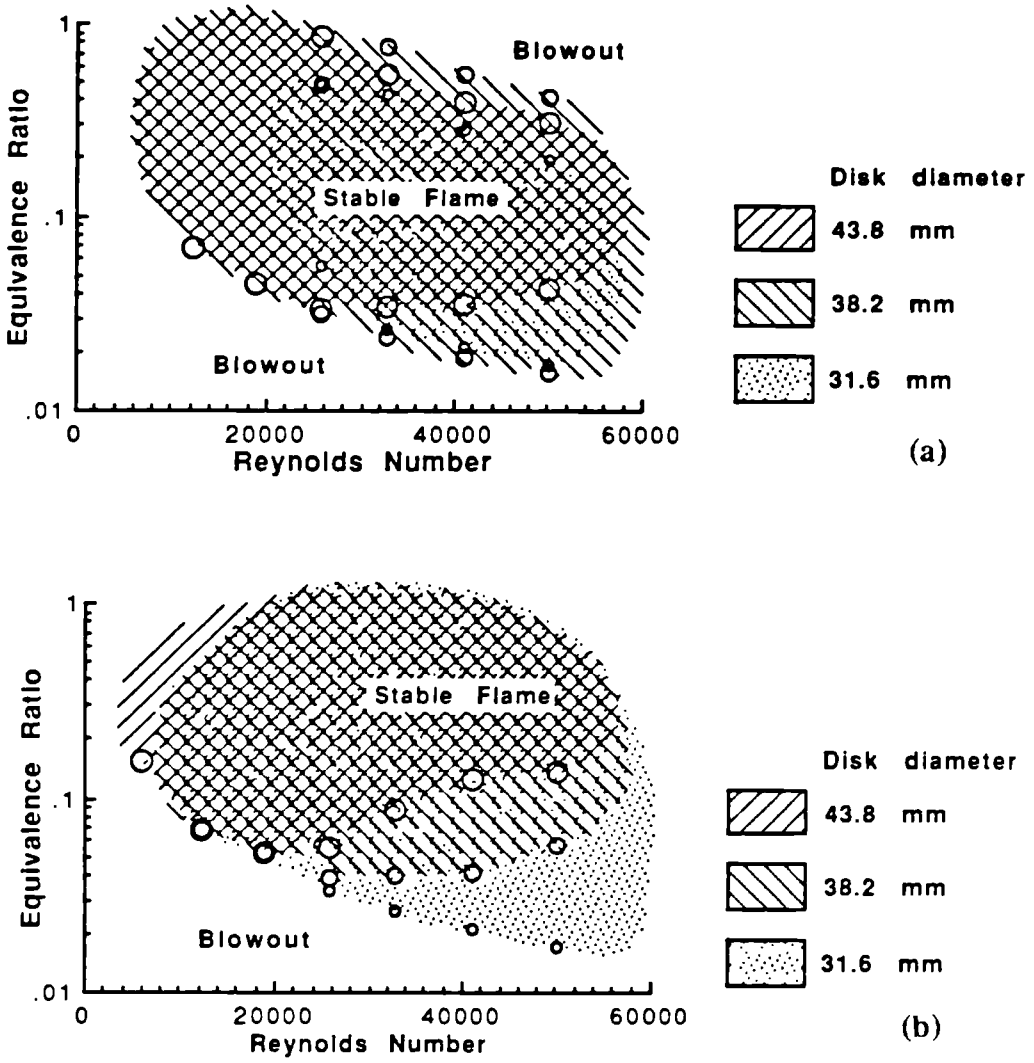


FIGURE 5.10 Flammability limit of the kerosene flames stabilised by flat disk bluff-bodies. Shaded area represents the region with stable flame.
(a) without quarl; (b) with quarl.

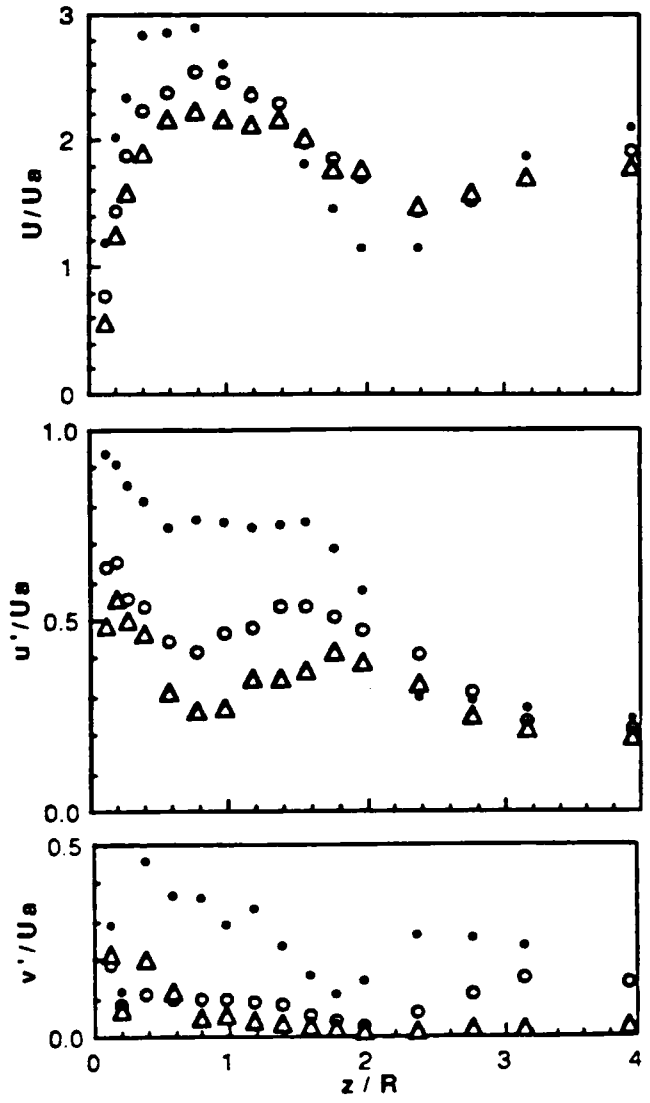


FIGURE 5.11 Axial and radial components of mean (U/U_a) and rms (u'/U_a and v'/U_a) velocities of fuel droplets along the centreline in the flame stabilised by a 43.8 mm disk bluff-body. (see Figure 5.4 for symbols)

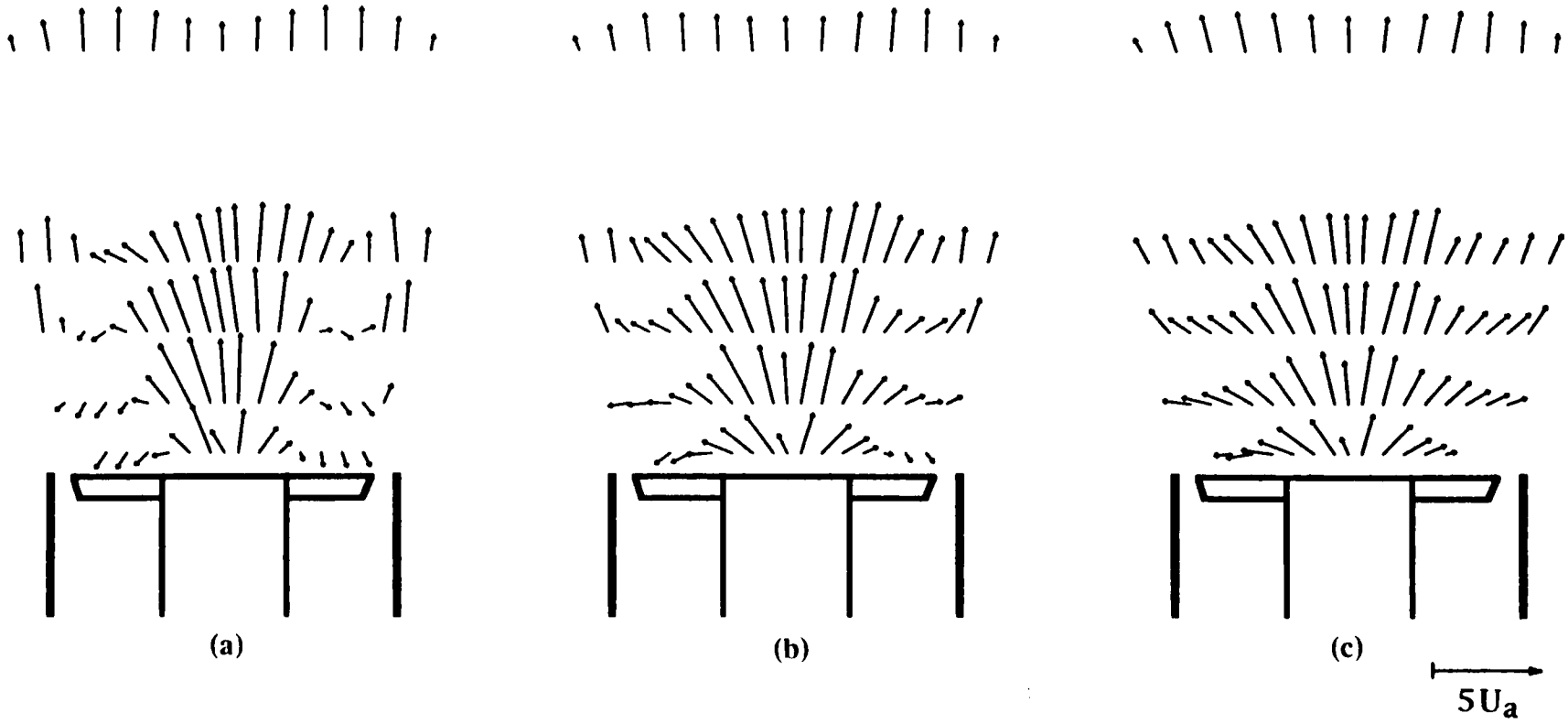


FIGURE 5.12 Mean velocity vectors of fuel droplets on a radial cross-section in the flame stabilised by a 43.8 mm disk bluff-body, with the radial profiles at the axial stations z/R of 0.1, 0.4, 0.8, 1.2 and 2.4.
(a) 10 μm, (b) 30 μm and (c) 50 μm droplets.

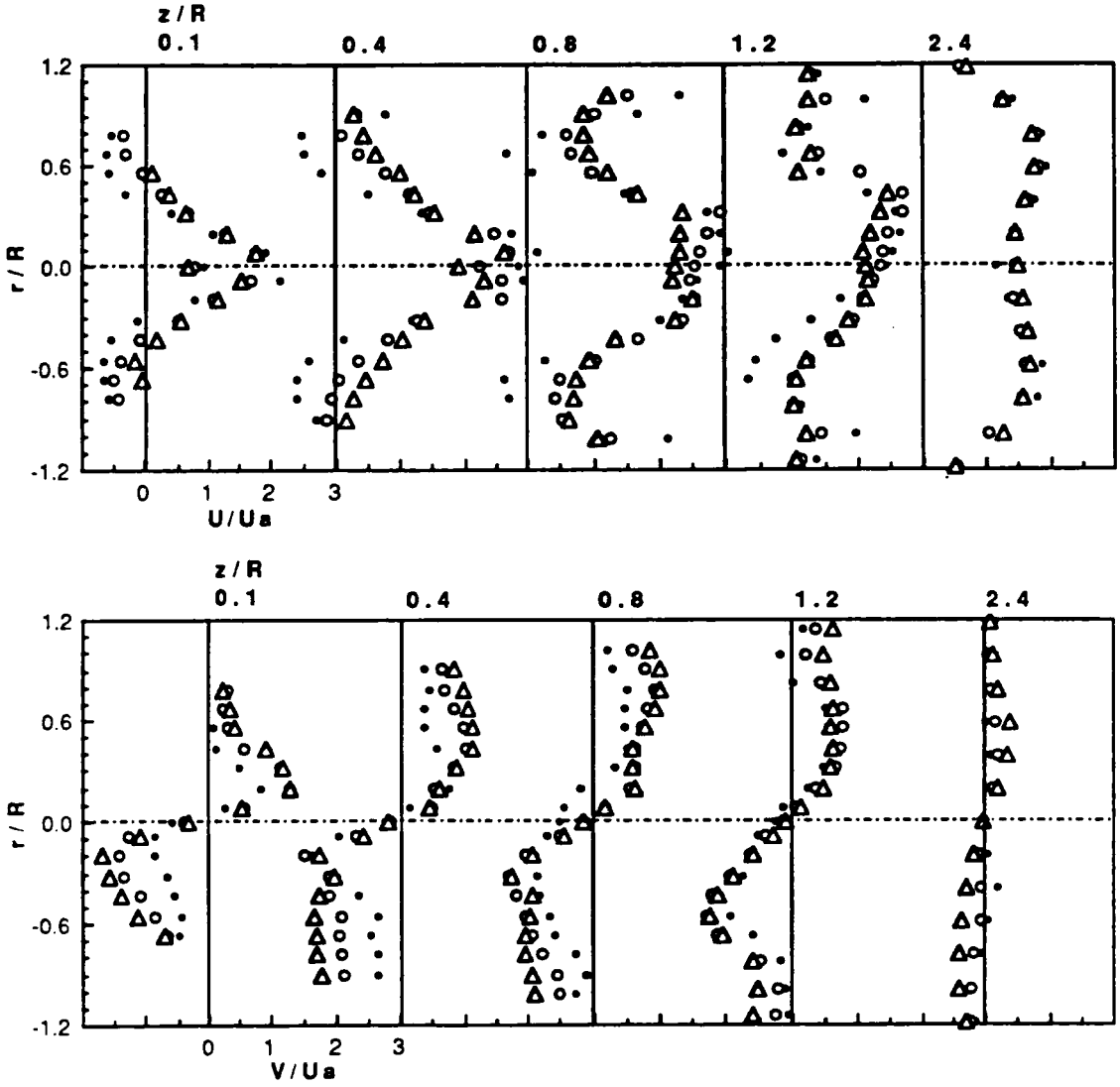


FIGURE 5.13 Radial profiles of axial (U/U_a) and radial (V/U_a) components of mean velocity of fuel droplets in the flame stabilised by a 43.8 mm disk bluff-body.
(see Figure 5.4 for symbols)

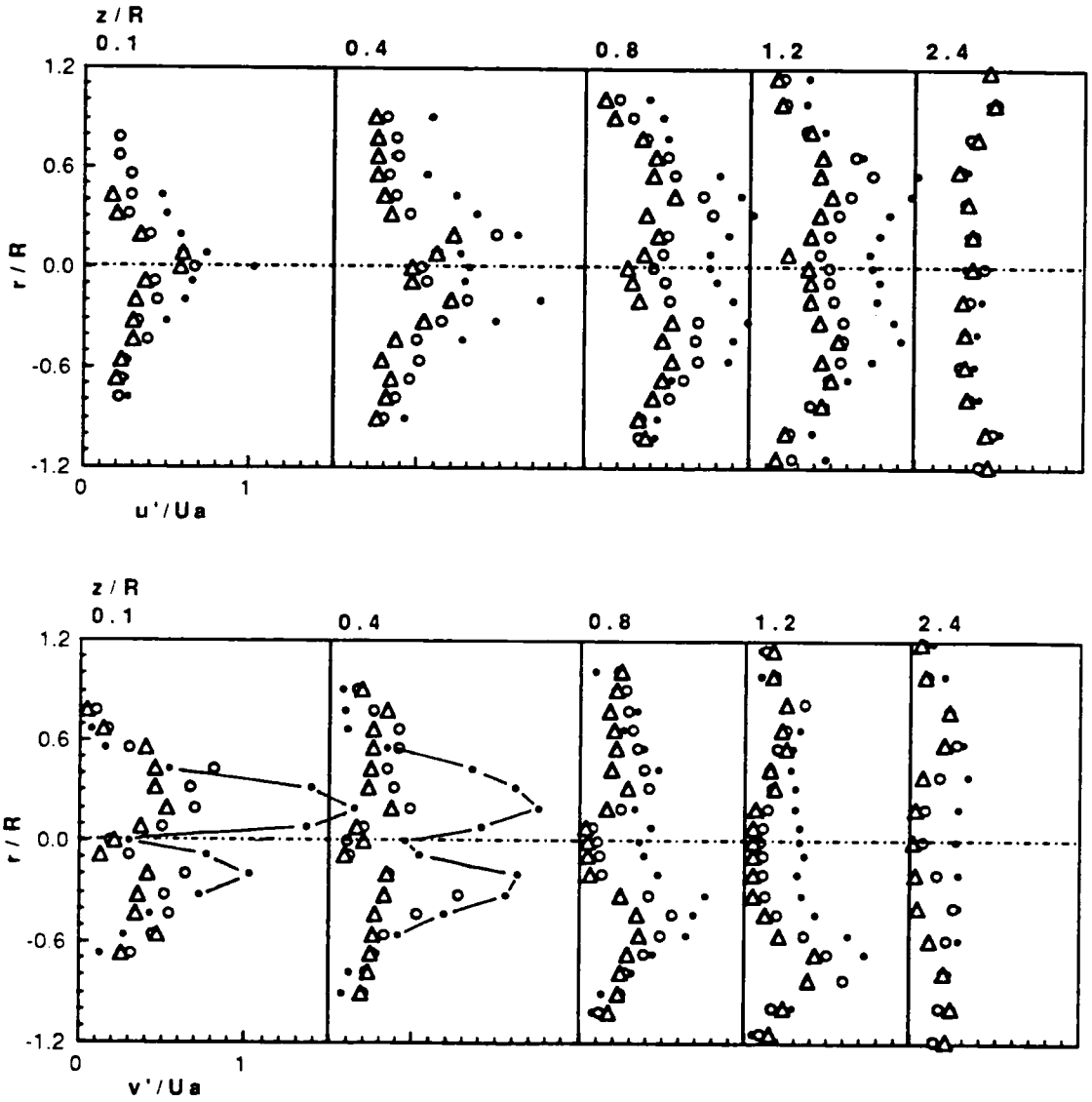


FIGURE 5.14 Radial profiles of axial (u'/U_a) and radial (v'/U_a) components of rms velocity of fuel droplets in the flame stabilised by a 43.8 mm disk bluff-body.
(see Figure 5.4 for symbols)

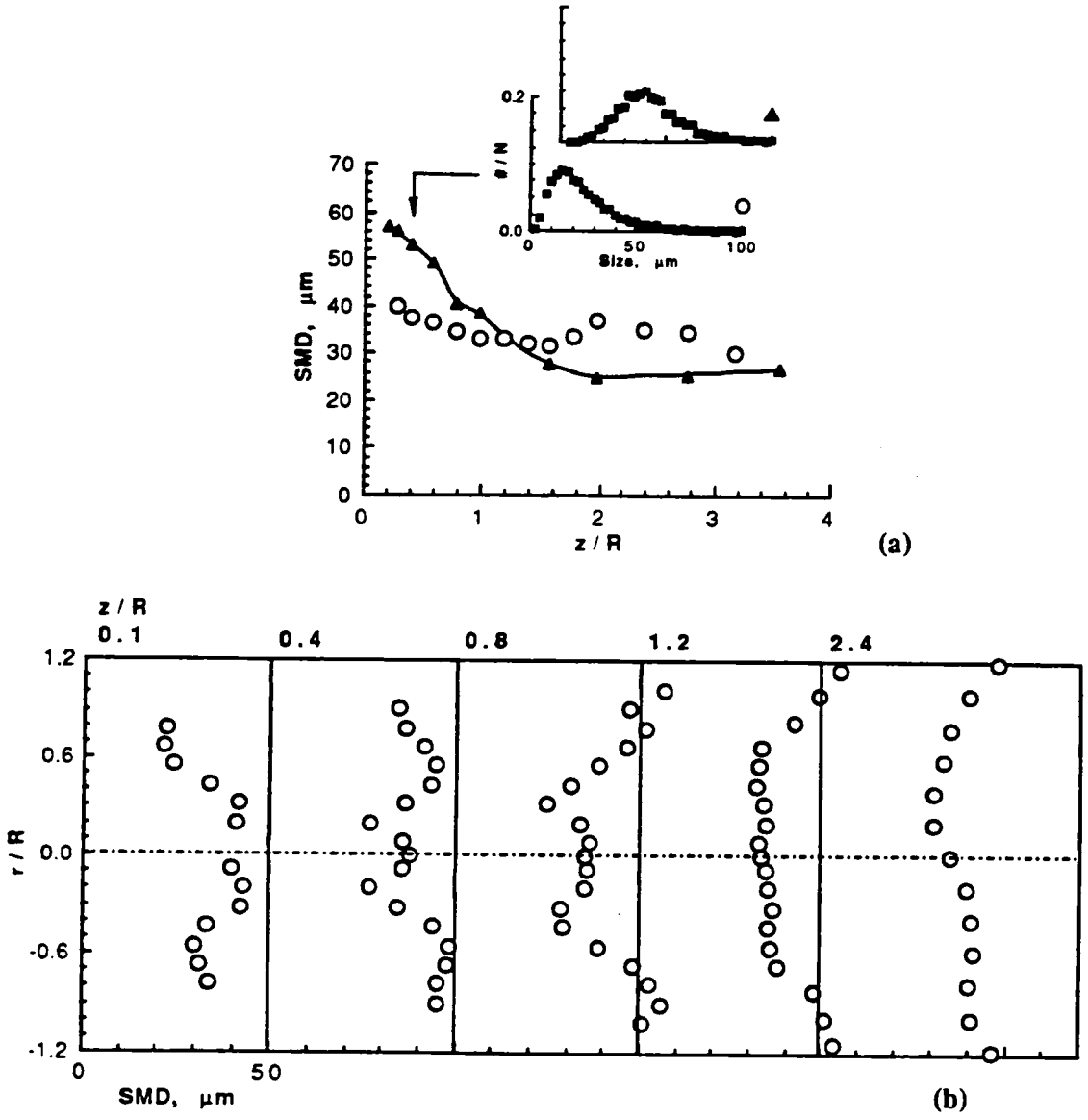


FIGURE 5.15 Sauter-mean diameter (SMD) and size (#/N) distributions of fuel droplets in the flame stabilised by a 43.8 mm disk bluff-body.
(▲ non-combusting flow; o combusting flow)
(a) along the centreline;
(b) radial distributions in combusting flow

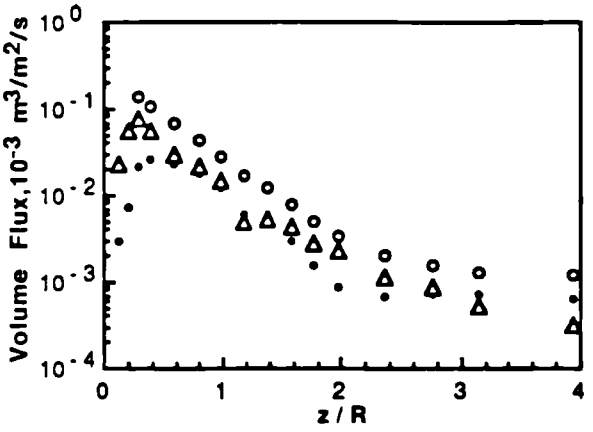


FIGURE 5.16 Volume flux of fuel droplets along the centreline in the flame stabilised by a 43.8 mm disk bluff-body. (see Figure 5.4 for symbols)

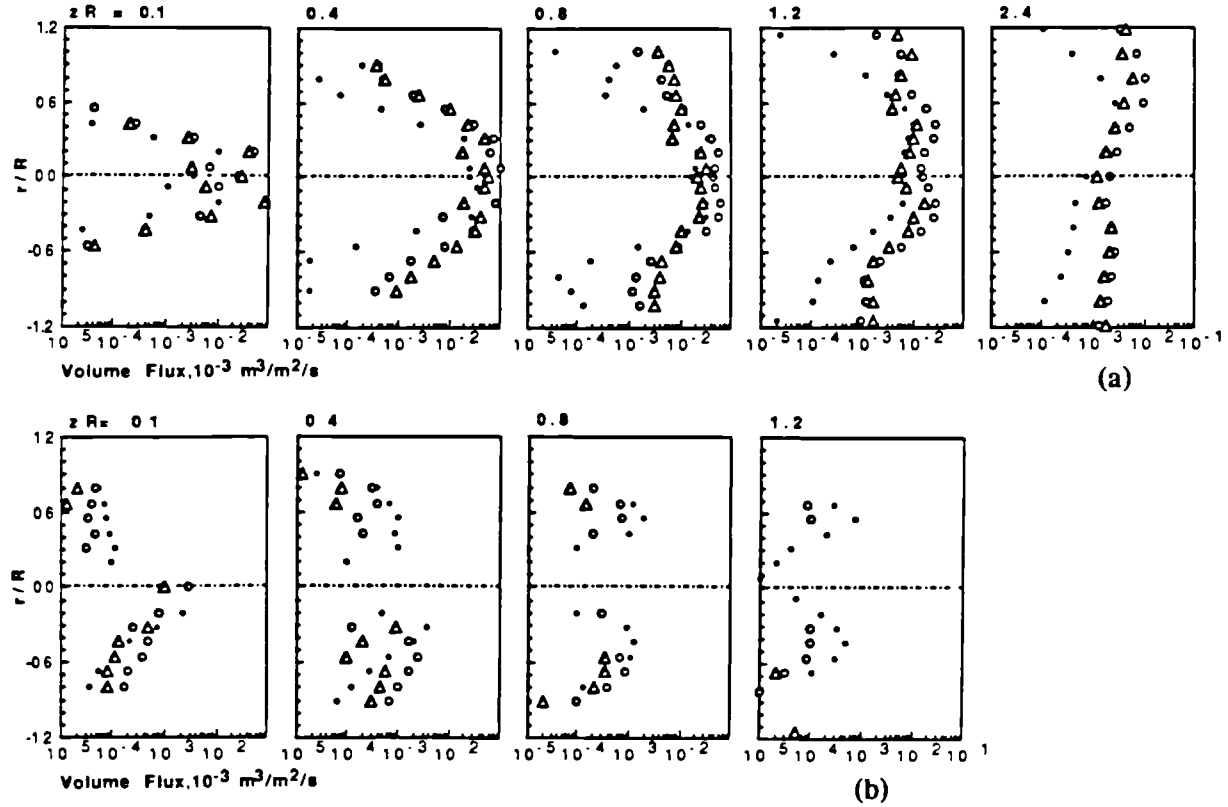


FIGURE 5.17 Radial distributions of volume flux of fuel droplets in the flame stabilised by a 43.8 mm disk bluff-body. (see Figure 5.4 for symbols)
(a) forward flux; (b) reverse flux.

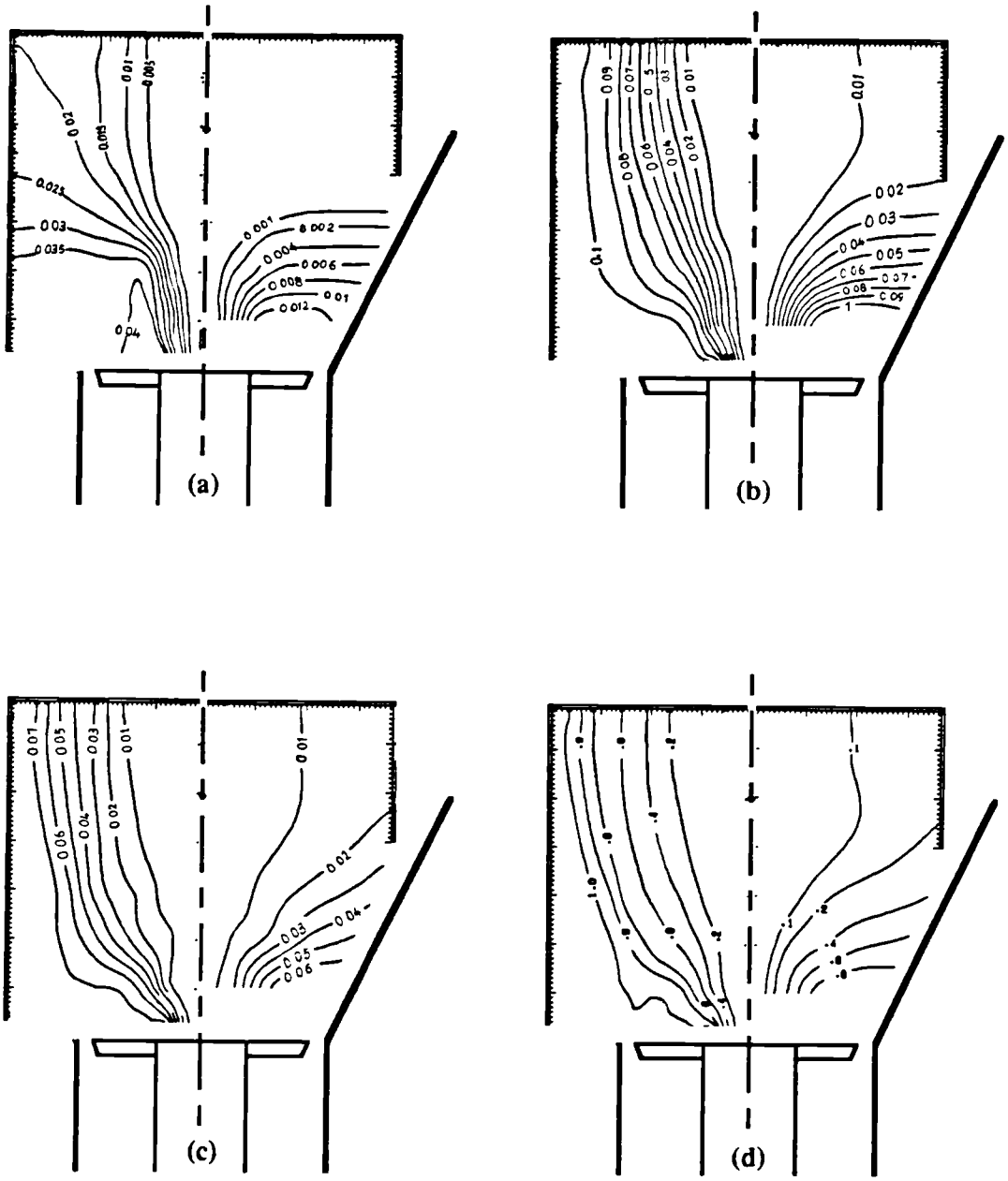


FIGURE 5.18 Isoflowrate lines of liquid fuel in the flames stabilised by a 43.8 mm disk bluff-body.
(Left: without quarl; right: with a quarl)
(a) 10 μm, (b) 30 μm and (c) 50 μm droplets;
(d) all sizes of droplets.

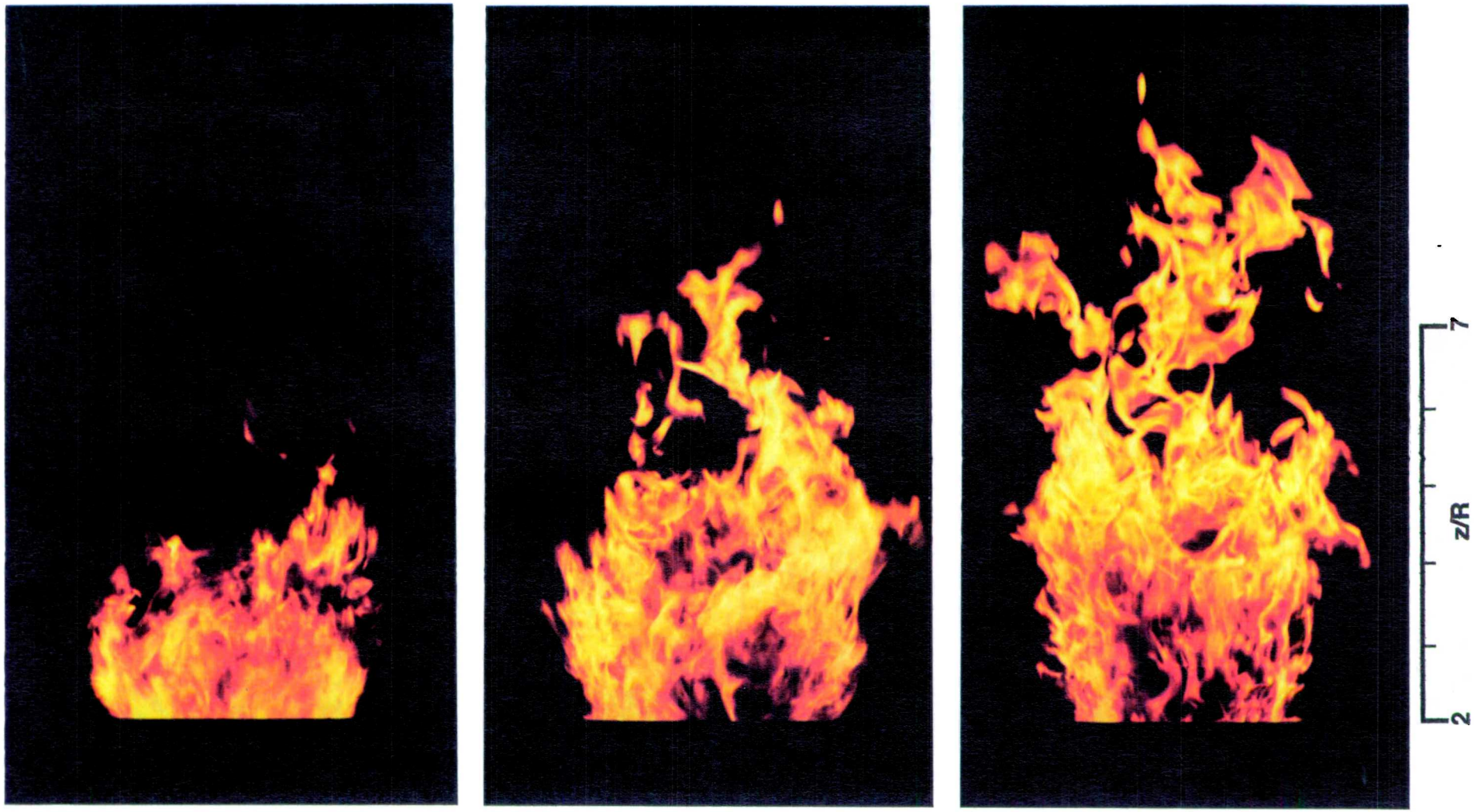


FIGURE 5.19 Kerosene flames stabilised by bluff-body with a quarl. (a) 43.8 mm, (b) 38.2 mm and (c) 31.6 mm disks.

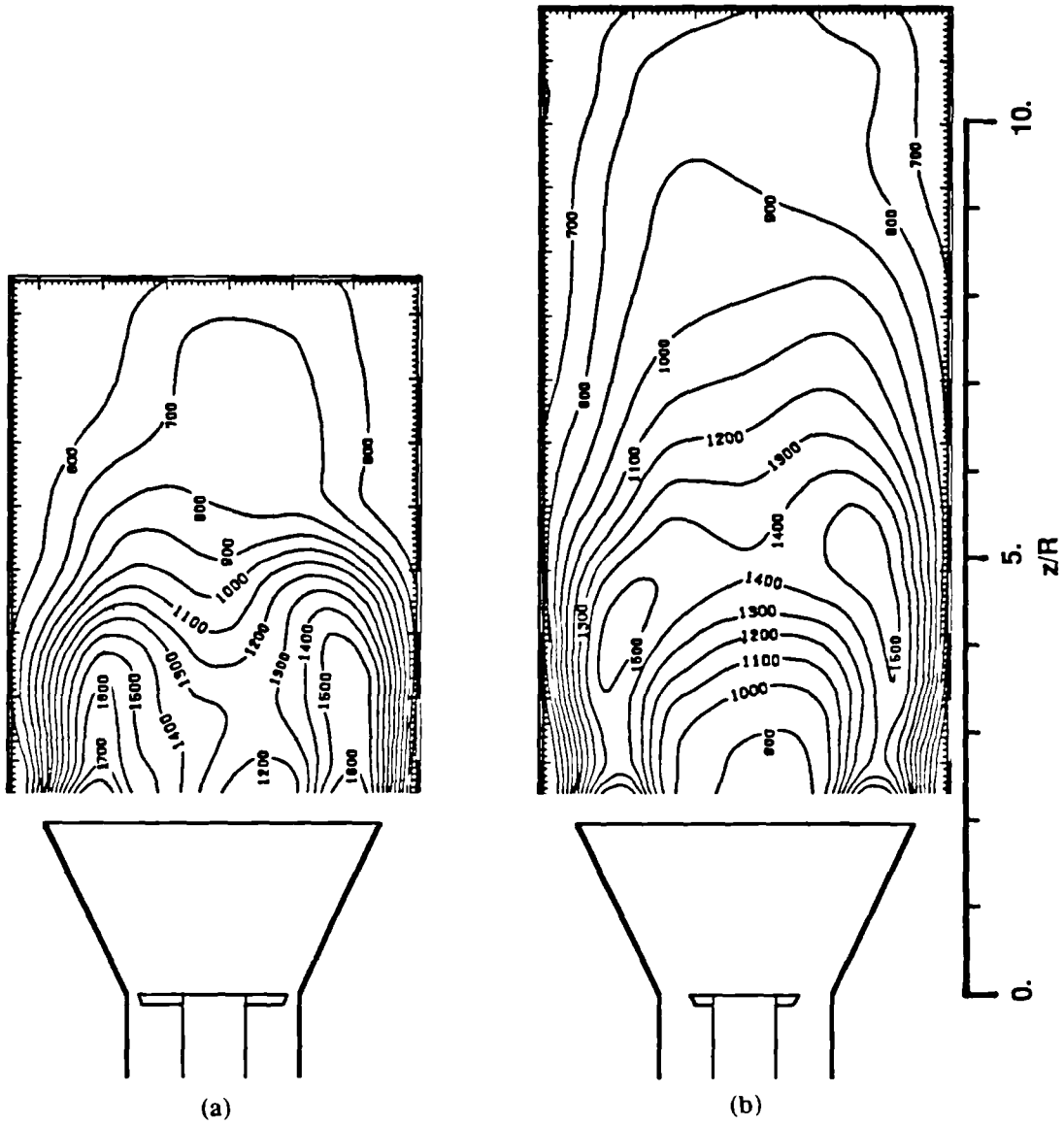


FIGURE 5.20 Temperature (°K) isotherms in the flames stabilised by bluff-body with a quarl.
(a) 43.8 mm and (b) 31.6 mm disks.

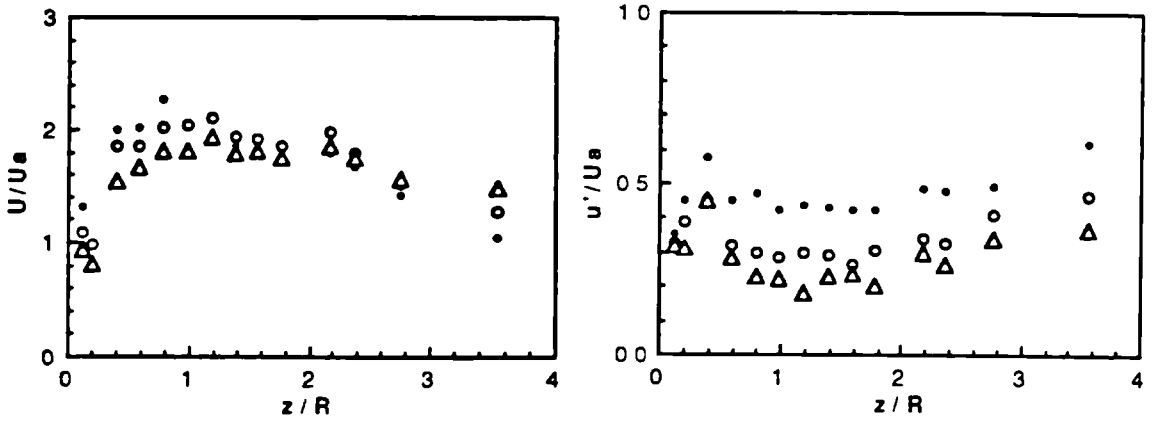


FIGURE 5.21 Axial component of mean (U/U_a) and rms (u'/U_a) velocities of fuel droplets along the centreline in the flame stabilised by a 43.8 mm disk bluff-body with a quarl. (see Figure 5.4 for symbols)

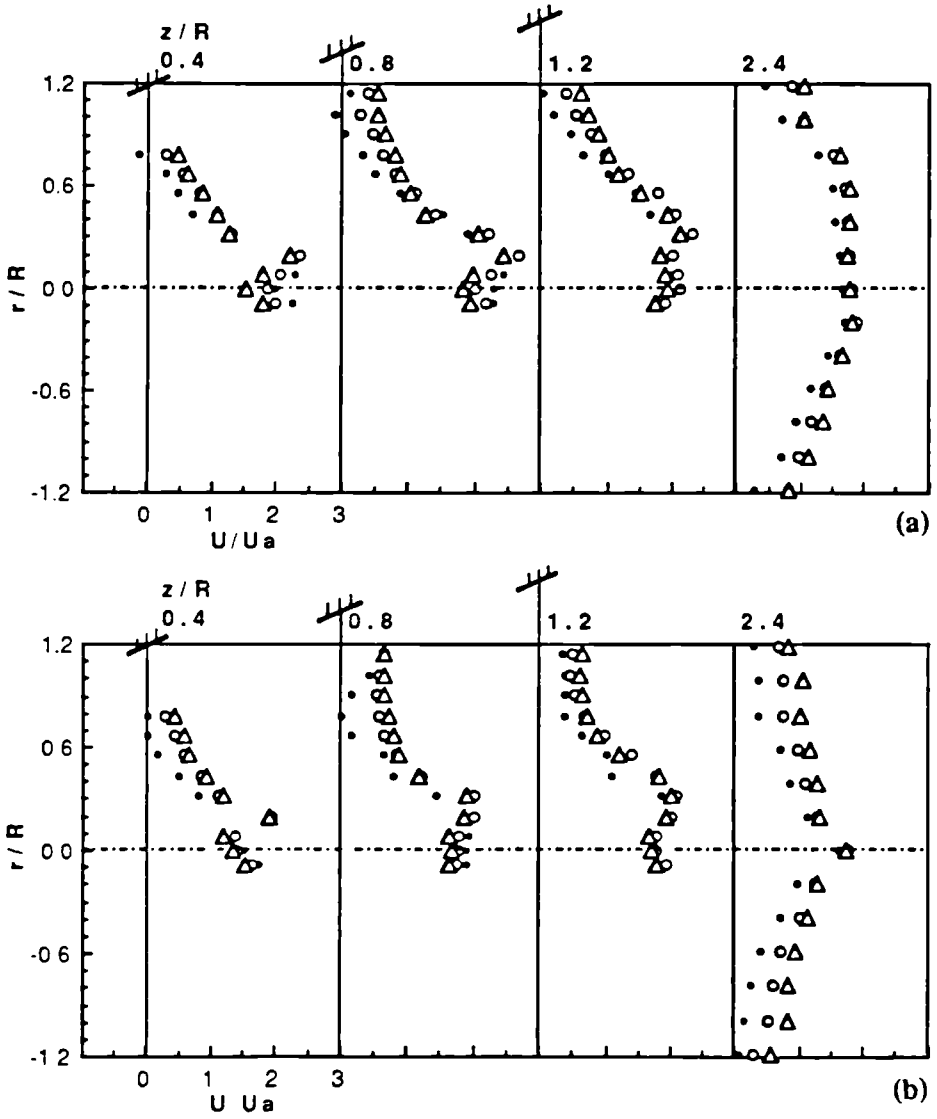


FIGURE 5.22 Radial profiles of axial component of mean velocity (U/U_a) of fuel droplets in the flames stabilised by bluff-body with a quarl.
(see Figure 5.4 for symbols; //// wall of the quarl)
(a) 43.8 mm and (b) 31.6 mm disk.

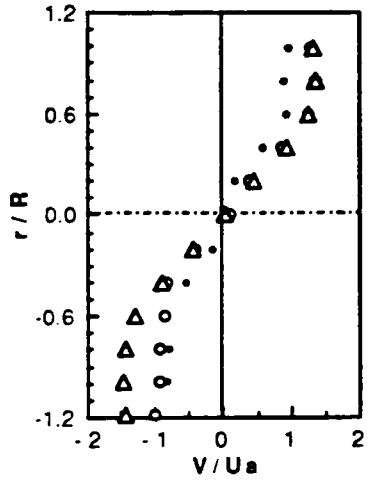


FIGURE 5.23 Radial profiles of radial component of mean velocity (V/U_a) of fuel droplets at the exit of the quarl (z/R=2.4) in the flame stabilised by a 43.8 mm disk bluff-body with a quarl. (see Figure 5.4 for symbols)

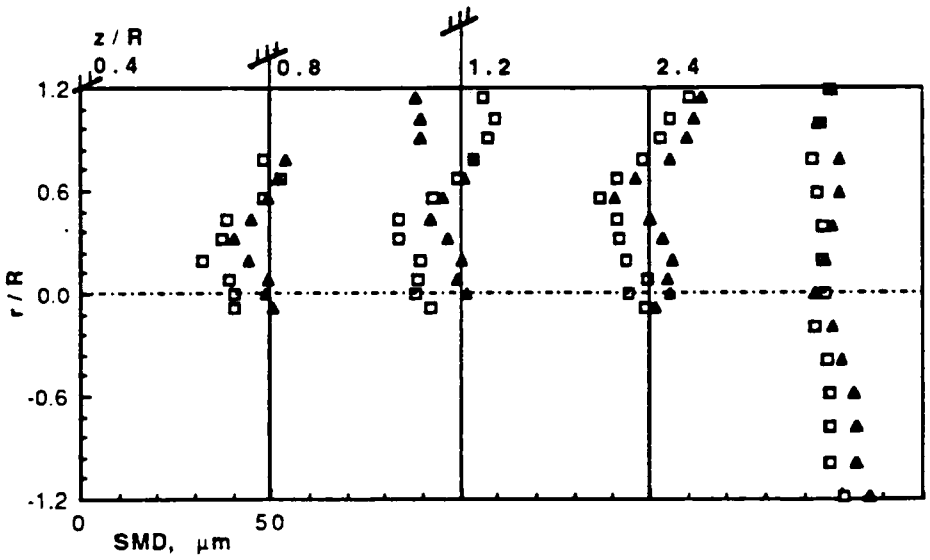


FIGURE 5.24 Radial distributions of Sauter-mean diameter (SMD) of fuel droplets in the flames stabilised by a 43.8 (□) and a 31.6 mm (▲) disk bluff-bodies with a quarl. (//// wall of the quarl)

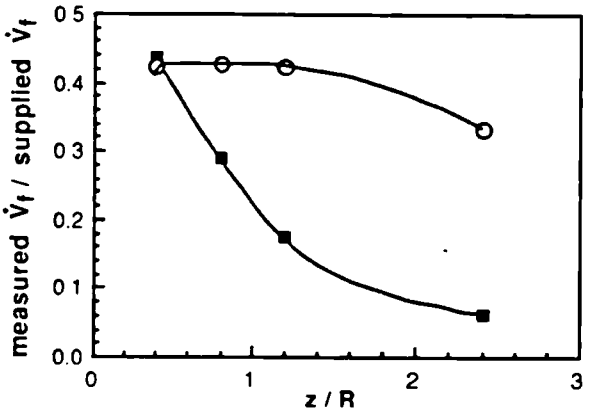


FIGURE 5.25 Flow rate of fuel droplets in the flames stabilised by a 43.8 mm disk bluff-body at different radial planes along the axis of the burner.
(o without quarl; ■ with a quarl)

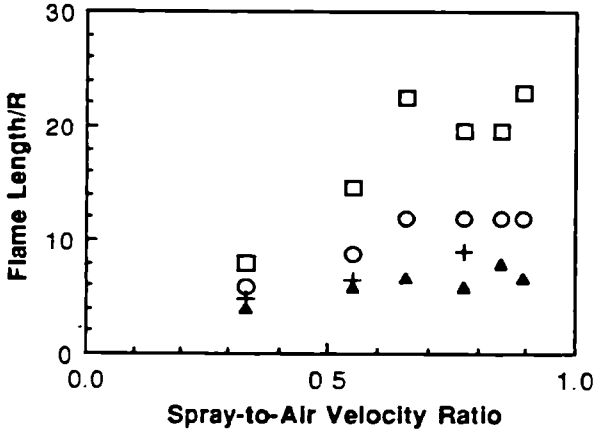


FIGURE 5.26 Variation of flame length with spray-to-air velocity ratio in the flames stabilised by bluff-body with a quarl. (fuel flowrate: ▲ 30 cc/min; o 50 cc/min; □ 100 cc/min and + 45 cc/min of PDA measurements)

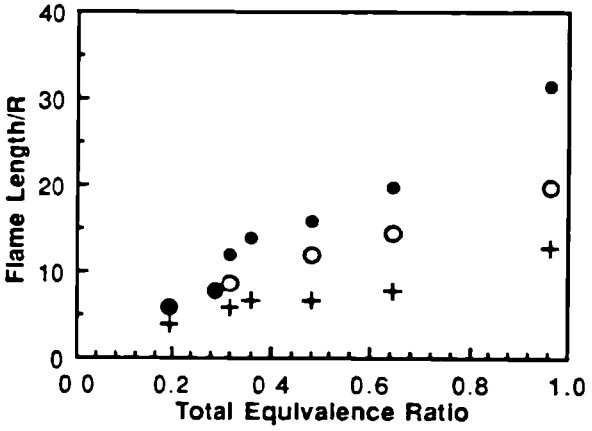


FIGURE 5.27 Variation of flame length with equivalence ratio in the flames stabilised by bluff-body with a quarl.
(+ 43.8 mm, o 38.2 mm and • 31.6 mm disks)

CHAPTER 6

Summary Conclusions and Recommendations

6.1 SUMMARY CONCLUSIONS

The thesis has described measurements of velocity characteristics in a centrifugal pump and of velocity and size characteristics of the two-phase flows in burner configurations. The results were obtained with laser- and phase-Doppler velocimetry, with the method of refractive index matching used to improve optical access where necessary. An analysis of the phase-Doppler velocimetry was conducted to improve the knowledge of the technique. Further results concerned the velocity characteristics of the coolant flow of an internal combustion engine and the size and velocity characteristics of droplets produced by a vaporiser of a gas-turbine combustor have also been obtained and are reported in the appendices. Details of the conclusions of each investigation are provided in chapters 2 to 5 and appendices. The following paragraphs summarise the more important findings, and recommendation for further research are provided in section 6.2.

1. The phase-Doppler velocimetry to size transparent particles is preferred with forward-scattered light due to larger intensity and domination of refracted light. The analysis suggested that kerosene droplets can be sized in combustion with uncertainties less than 7% at a scattering angle of 30° which is reduced at a 70° angle with correspondingly smaller intensity. Sizing with back- and side-scattered light is dominated by mixing of at least two light contributions, which requires the receiving optics to be placed close to the bisector plane of the beams, with the scattering angle determined by the refractive index of the particle and the linear phase-diameter relationship limited by a critical value of phase difference for a particular optical arrangement. The uncertainties of sizing due to refractive index were found to be of

the order of 100% with back- and side-scattered light. The Gaussian intensity profile caused sizing errors which at a scattering angle of 30° are reduced to around 5% with the Doppler signals validated by phase ratio and amplitude, and which are up to 100% and 26% with back- and side-scattered light, respectively, for particles larger than the probe diameter and up to 20% and 5% for a particle-to-probe diameter ratio of 0.24.

2. The impeller flows in the centrifugal pump departed from blade curvatures at off-design flowrates, with the secondary flow mainly from suction to pressure surfaces of the blades and dominated by the influences of the relative motion between shroud and impeller surfaces and leakage. Separation was observed in the inlet and exit pipes and close to the suction surface of the blades at flowrates below around 30% of the design condition, with separation on the shroud surface at all flowrates. Geometrical imperfection caused the passage velocity, measured with one-degree resolution of shaft rotation, to vary from one passage to another by up to 2.5% and 6% of the impeller tip velocity for the radial and tangential components, respectively, close to the design flowrate and up to 3% and 16% close to shutdown. The passage velocity varied also with the circumferential angle of the volute, and this variation is responsible for the differences of passage discharge up to 25% at a medium flowrate. The slip factor was found to be larger than unity inside the impeller, which decreased with radius and increased with flowrate, and the value of 0.73 at the discharge at 93% of the design flowrate was around 15% and 25% larger than the theoretical values of Busemann and Stodola respectively.

3. The investigations with the burner flows quantified the decrease in size of the toroidal vortex, caused by the swirler in the annulus, with increasing flowrate of the central jet. An effect of swirl was to centrifuge particles towards larger radii with local increases of concentration, and this caused distortion of velocity profiles and suppression of turbulence at high concentrations. The results were made to an overall volume fraction of particles of 0.113, and this was possible with the method of refractive index matching. In the liquid-fuelled flames, a disk was used to

generate the recirculation zone and to minimise centrifuging. However, centrifuging of fuel droplets was observed due to the streamline curvature of the vortex downstream of the disk, and droplets tended to be removed from the region of reaction and to cause wetting of the wall of a quarl. The effect of centrifuging was quantified by a centrifuge Stokes number and increased with the size of droplets so that droplets larger than 50 μm had burning times longer than the transit times from axis to the wall and were responsible for wall wetting. Particles/droplets in the two-phase flows were found to behave in the manners expected by considering the time scales of the discrete and continuous phases, and droplets smaller than 10 μm followed the recirculation of the gas phase in the flames. The burning time scale of the droplets is important in combustion since it is shorter than the relaxation time, and the estimations of transit times based on droplet velocity confirmed that only sizes larger than 50 μm survived through the recirculation zone, to contribute to unburned liquid fuel in the downstream flow with a quarl. The presence of the quarl enhanced combustion with the length of the flame increasing with decrease of blockage ratio of the disk and, for a blockage ratio of 0.74, the content of liquid fuel in the flame at a downstream station, corresponding to 1.2 diameters of the disk, was reduced by more than 40% with the quarl. It was observed that the lean flammability limit was worse with larger blockage ratios and with the quarl due to increased amount of recirculating air to reduce local equivalence ratio.

4. The coolant flow in the cylinder head of an internal combustion engine is determined mainly by the geometry of the flow passages and is insensitive to variations of upstream and downstream conditions. The investigation with a particular design found that the coolant was not distributed in the manner expected by design, and there were regions of low coolant flow where larger cooling was needed. The use of a transparent model with refractive index matching facilitated the detailed measurements by laser-Doppler velocimetry.

5. The performance of the vaporiser of a gas-turbine combustor depends on the operating conditions and atomisation. It was found

that higher inlet temperatures and flowrates of air resulted in smaller droplet diameters and flux of liquid fuel at the exit of the vaporiser, and an injector with six radial jets provides better atomisation than that with an axial jet. The performance of the vaporiser was improved with combustion, and better vaporisation was evidenced by a shorter flame with the region of intense combustion at an upstream station. It was found that the vaporiser deteriorated with time and more rapidly with high fuel flowrates due to carbon build-up at fuel impingement points.

6.2 RECOMMENDATIONS

The following paragraphs suggest areas for further work:

1. The analysis of the phase-Doppler technique assumed transparent and non-absorbing particles although there are many two-phase flow situations where the particles may absorb light. The effect of absorption causes competition of intensity for different light contributions due to differences in optical path length, and the sizing response curves may be modified. The consequences need to be examined together with the effect of the Gaussian intensity profile, and the method of geometric optics can be used as the basis for these further investigations.

2. It is known that the generation of pump noise is related to vibrations of solid walls, such as casing, piping and other structure, which is caused partly by unsteady effects of the flow. However, little is known about the interaction between the flow and casing and the mechanisms of the fluctuating forces. Further work should emphasize this area and use the technique of laser-Doppler velocimetry and refractive index matching together with measurements of pressure fluctuation.

3. One consequence of the liquid-fuelled flames was carbon deposition on the surface of the disk due to burning of liquid fuel on the surface where the mixing with air was insufficient. Although the fuel burnt close to the disk contributed to the stability of the flame, the deposition was undesirable as it accumulates with time to change the geometry of the bluff-body

and the flame. Frequent removal of the deposition is necessary to maintain a normal flame. A method to minimise the deposition is to introduce air through the bluff body to enhance local mixing and to form a layer of air protection, and the bluff-body can be made with air transpiration holes or slots. Further study of the characteristics of bluff-body with air transpiration may benefit the design of combustors and burners.

APPENDIX A

Flow in the Coolant Passages of an Internal Combustion Engine Cylinder Head†

†Experiment in Fluids, Vol. 10, pp. 50-54.

Experiments in Fluids 10, 50 54 (1990)

Experiments in Fluids

© Springer-Verlag 1990

Flow in the coolant passages of an internal combustion engine cylinder head

C.H. Liu, C. Vafidis and J.H. Whitelaw

Fluids Section, Mechanical Engineering Dept., Imperial College, London SW7 2BX, U.K

R. Margary

Centro Ricerche Fiat, Orbassano, Torino, Italy

Abstract. Detailed measurements of the coolant flow field have been made in the water passages of the cylinder head of an internal combustion engine. They were obtained by casting a transparent acrylic model of the cylinder head and using a mixture of hydrocarbon fluids at a predetermined temperature and concentration which ensured that the refractive index of the fluid was identical to that of the acrylic. This arrangement allowed the use of laser Doppler velocimetry to measure local velocities throughout the cooling passages. The results show that the flow was unevenly distributed with around three quarters of the total passing through the exhaust-port-side passages and larger coolant velocities close to the top of the head than close to the gas face. The results of this study aimed to assist the improvement of the specific cylinder head design.

1 Introduction

The general trend towards increased performance of internal combustion engines implies the need for greater control of the coolant flow in the passages of the cylinder head and block. The study of such flows using traditional probe techniques is not a simple task and the structure of engines precludes the use of optical techniques except through locally arranged windows. An alternative method would be to construct a transparent model of an engine cylinder head and this, in principle, would allow optical access to the cooling passages. However, the complex geometry of the various passages combined with the different refractive indices of the transparent model walls and cooling fluid imply refraction of light so that only qualitative studies by visualization methods are feasible.

This difficulty can be by-passed by matching the refractive index of the working fluid to that of the solid transparent boundary, as shown for example by Zizzelmar and Molerus (1978), Elphic et al (1982), Yianneskis and Whitelaw (1983), Dybbs and Edwards (1986), Thompson et al. (1987), Nouri et al (1988), Thompson et al (1989), Liu et al. (1989) and Liu et al (1990), and careful choice of fluid can ensure that its viscosity and density are similar to those of the appropriate working fluid. Our earlier work has shown that a mixture of oil of turpentine with 31.8% by volume of tetrahydronaphthalene (Tetraline) meets this requirement for water and matches the refractive index of common clear cast acrylics but calls for particularly careful treatment of the acrylic models to avoid chemical attack by the solvent mixture which leads to formation of stress cracks and crazing. As a consequence, an essential part of the present work was the casting and subsequent treatment of the acrylic model.

The following section describes the cylinder head and the techniques used to produce the transparent acrylic replica. The application of the refractive index matching technique is also described together with the laser Doppler velocimeter. The third section presents some of the results of this study and discusses their implications. The paper ends with a summary of the more important conclusions.

2 Flow configuration and instrumentation

The geometry of the cylinder head coolant passages is shown in Fig. 1. The coolant enters through one passage, leading to the inlet of a head-mounted pump, and exits through two (or three) outlets, one of which would normally lead to the cylinder block. The flow was maintained at a design flow rate of 1.22×10^{-3} m^3 s, corresponding to a Reynolds number of 3.16×10^4, based on the bulk mean velocity of 1.72 m s and the inlet duct diameter of 30 mm. The cooling passage comprises four geometrically similar sections in series, with the first and last accommodating the coolant inlet and outlets. Each section is arranged to cool a region of the head associated with an intake and an exhaust port.

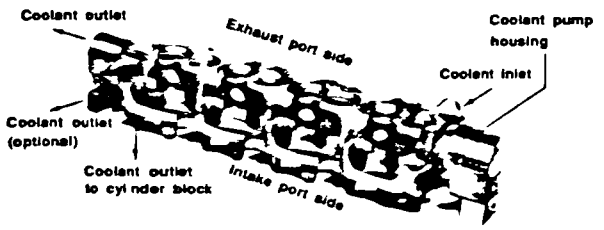


Fig. 1. Fusible core of the cylinder head coolant passages

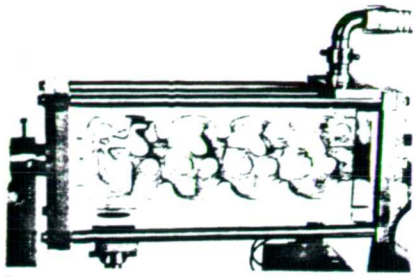


Fig. 2. Acrylic model of the cylinder head coolant passages

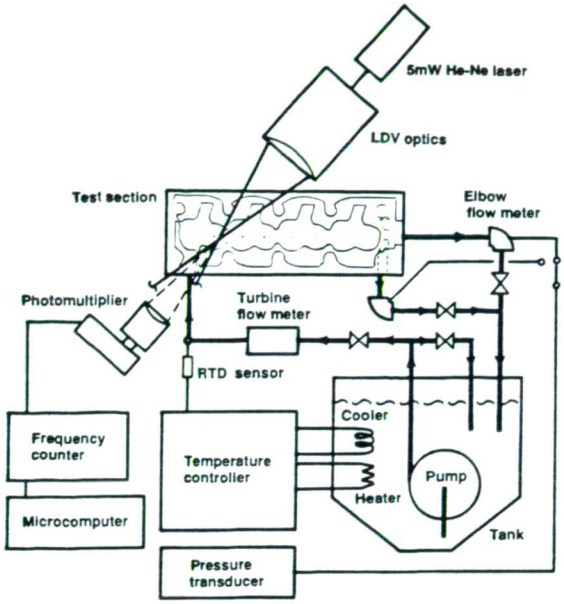


Fig. 3. Flow configuration and instrumentation

A fusible core, shown in Fig. 1, was taken from the mould of the production cylinder head and acrylic (Transpalite SS from Stanley Plastics Ltd) was cast around it in a liquid form to produce, after curing, a solid block with rectangular external shape, as shown in Fig. 2. The fusible core was made of a eutectic alloy (MCP 70 from Mining and Chemical Products Ltd) and was melted-out from the casting during the final stages of the curing process, when the acrylic temperature reached 70°C, leaving behind the intricate internal geometry of the coolant passages. The external surfaces were machined and polished and the model annealed with a slow heating cycle to a maximum temperature of 80°C at which it was held for 36 h before subsequent slow cooling to ambient conditions. A 16-vane swirler was then fitted in the housing intended for the water pump to simulate the coolant pump outflow and the model arranged on a table on top of the tank from which the mixture of turpentine and Tetraline was pumped, as shown in Fig. 2 and 3. Figure 2 also shows the acrylic model in plan view and the repeated four sections are in evidence. It can also be seen that the surface finish of the cooling passages varies, with roughness similar to that which can be expected in the production head. Nevertheless, and with few exceptions, the flow passages were optically accessible.

Table 1. Characteristics of the laser-Doppler velocimeter

Laser wavelength	632.8	nm
Beam intersection angle	11.9	deg
Measurement volume length at $1/e^2$ intensity	774	μm
Measurement volume diameter at $1/e^2$ intensity	81	μm
Fringe spacing	3.042	μm
No. of fringes	26	
Frequency shift	0.7	MHz

The flow circuit shown in Fig. 3 involved a submersible centrifugal pump located in a 0.07 m^3 tank and connected to the acrylic head with stainless steel piping with a turbine flow meter fitted to allow measurement of the flow rate. The mixture of turpentine and Tetraline was maintained at a constant temperature of 25 ± 0.02 °C with a heater and cooler inside the tank and a platinum resistance sensor a short distance upstream of the inlet to the model. The fluid left the model from its two exits, with flow rates which could be controlled by valves, and returned to the tank via two elbow flow meters, calibrated to allow direct measurement of the flow in the two exits. The pressure drop across the model was measured with a differential pressure transducer which was also used with the elbow flow meters.

The laser Doppler velocimeter was similar to that described by Liu et al. (1989) and comprised a 5 mW Helium-Neon laser and a transmitting optical arrangement based on a rotating diffraction grating. The optical characteristics of the velocimeter are given in Table 1. The light scattered from natural contaminants was collected at forward-scatter angles which depended on the measurement location. The Doppler signal was processed by a frequency counter (TSI 1990c) interfaced to a microcomputer. The optical components were arranged on a milling table which allowed translation in three directions with accuracy better than 0.1 mm. Measurements of the mean and rms values of three orthogonal components of velocity were obtained with an estimated error better than 2% and 5% respectively, mainly stemming from the finite sample sizes.

3 Results and discussion

Velocity measurements were obtained mainly on the three horizontal planes of Fig 4 which also shows the flow configuration, measurement locations and the position of the swirler, simulating the coolant pump. A sample of the results is shown in Fig. 4 and 5 and corresponds to a flow configuration where 60% of the exit flow passes through the outlet normally connected to the cylinder block. Measurements were also obtained for a lower flow rate of 0.83×10^{-3} m^3 s, with 60% of the flow passing through the optional outlet,

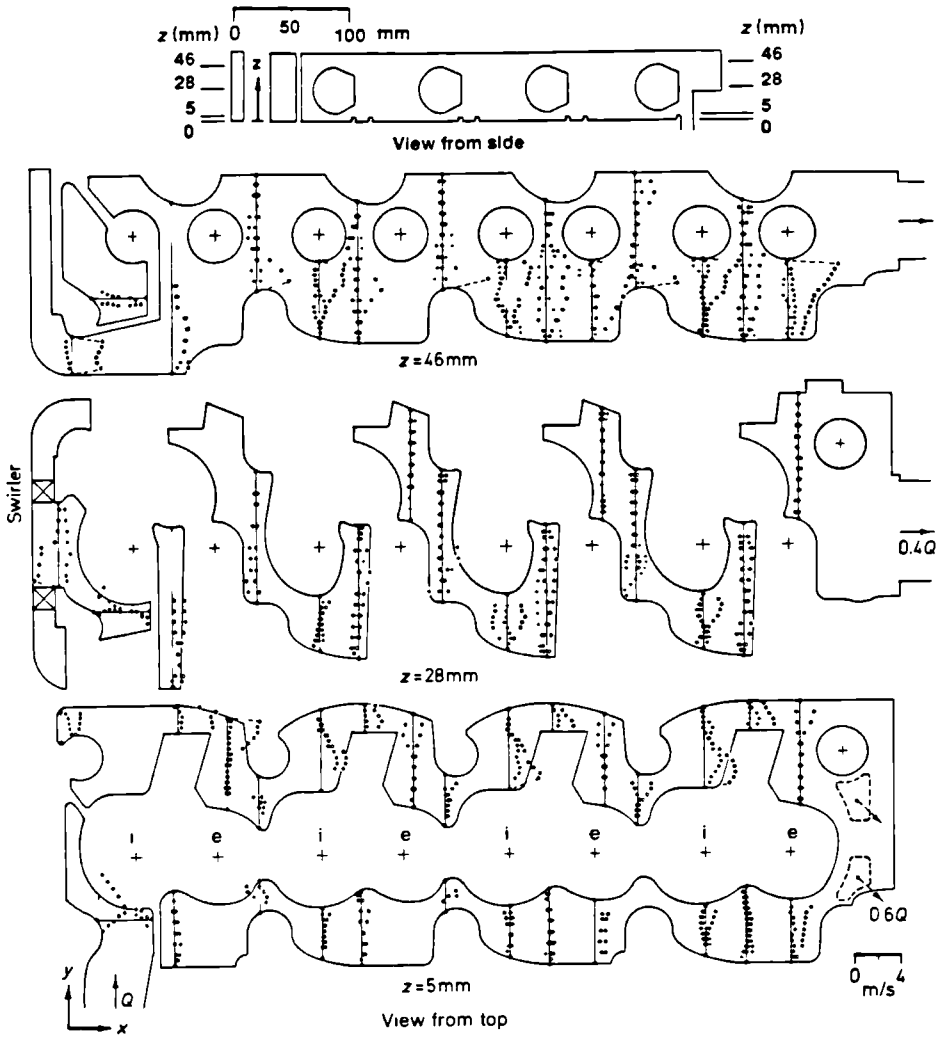


Fig. 4. Profiles of mean velocity (volume flow rate $Q = 1.22 \times 10^{-3}$ m^3 s: (o) x-component (• y-component. (+) z-component. i centre of intake valve. e centre of exhaust valve

and with a blockage in the first of the four sections. The results of these measurements. as well as those of the normal stress distribution. are not presented in the figures but are discussed in the following paragraphs.

The results of Fig 4 correspond to three orthogonal components of mean velocity and show that the flow is mainly unidirectional with generally much lower velocities close to the surface of the head located on the cylinder block gas face) and some regions of reverse flow particularly close to the valve guides There is an obvious tendency of flow similarity in the four sections but detailed differences are evident particularly in the inlet and outlet regions and also. though to a lesser extent. in the two middle sections Integration of the velocity profiles at successive lateral planes of the four sections led to volume flow rates indicating that three quarters of the flow passed through the exhaust-port-side passages The integrated total flow was within 5 o of that measured by the turbine flow meter, a fact that increased the confidence level of the velocity measurements

A simpler view of the flow is provided by Fig 5 which presents the results in the form of magnitudes of the coolant velocity vectors which were usually dominated by the x-component. Three components of velocity have not been measured in all regions of the flow, as indicated by Fig 4. so that the results of Fig 5 are more sparse than those of Fig 4, in many of these regions, however. the magnitude of the velocity vector can be expected to be very small The results suggest that poor cooling can be expected in the l west plane. particularly at the exhaust port side of the cylinder head where the velocity magnitudes are close to zero and this is c ntrary to usual requirements Examination of the geometry of the cooling passages sh ws that the narrowest passages at the exhaust port side are situated close to the block so that the flow naturally tends towards the upper part of the

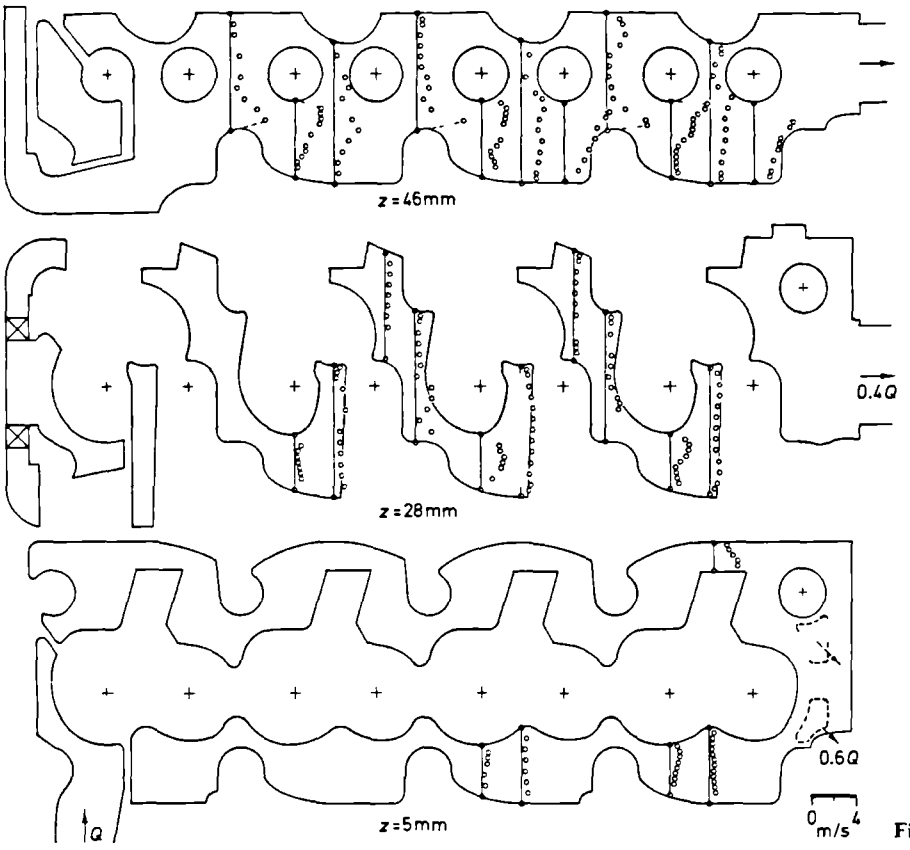


Fig. 5. Profiles of velocity magnitude

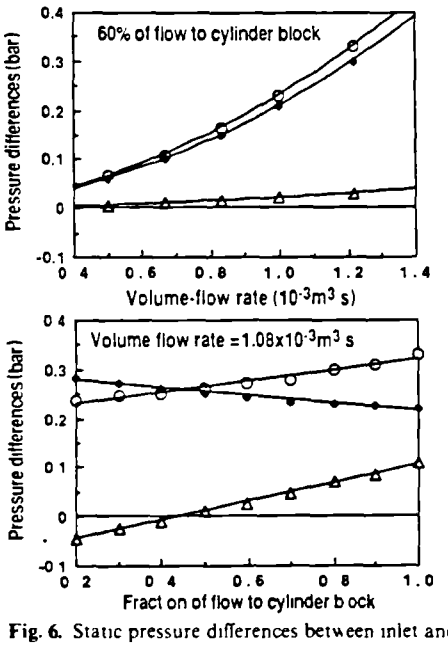


Fig. 6. Static pressure differences between inlet and outlets (● $P - P_2$, (○ $P - P_3$, (△ $P - P_3$ P static pressure at inlet, P_2 static pressure at main outlet, P_3 static pressure at passage to cylinder block

cylinder head. Although geometrical and production constraints limit the extent of possible modifications of the coolant passage shapes, a number of recommendations has been made for the improvement of the coolant velocity field in terms of local magnitudes and, therefore, heat transfer rates.

The change in the outlet configuration to allow 60% of the flow to pass through the optional outlet had effects which were local to the exit region with no effect on the flow in the upstream cooling passages. Also, it was found that the effect of a complete blockage of the flow in a passage of the first section was local so that the flow in the second section was very similar and the flow patterns in the third and fourth sections identical to those without the blockage. A reduction of flow rate by 3% also resulted in similar flow patterns in all sections of the cylinder head. These results suggest that the coolant flow in the complex passages was Reynolds independent for the practical range of engine operating conditions and insensitive to manufacturing tolerances and outlet configurations.

The Reynolds normal stresses were available at all locations of the mean velocity measurements of Fig. 4 and were near isotropic with magnitudes of around 0.3 m/s in regions of near-zero mean velocity and up to 1 m/s in regions where the mean velocity achieved the maximum value of around

4 m s. These fluctuation levels are consistent with turbulent flow and confirm that local heat transfer will occur in regions of near-zero mean velocity though of lesser magnitude than in regions of finite mean velocity.

Static pressure differences between the inlet and the two outlets are shown in Fig 6 which confirms that they were a quadratic function of the volume flow rate, with a pressure drop of around 0.32 bar at a flow rate of 1.22×10^{-3} m^3 s. The pressure difference between the two outlet ports varies with flow partition and tends to zero when 45% of the coolant flow is diverted to the cylinder block.

4 Summary and conclusions

Measurements of local velocities and pressure losses were made in a transparent model of the coolant passages of an internal combustion engine cylinder head. The model was manufactured in clear acrylic using a fusible core casting technique. Velocity data were obtained by laser Doppler velocimetry and by matching the refractive index of the working liquid to that of the acrylic model. The results show that the coolant flow was mainly unidirectional along the longitudinal direction with three quarters of the flow rate passing along the exhaust port side of the cylinder head. Lower coolant velocities were observed in regions near the cylinder block and at the exhaust port side of the cylinder head where higher velocities are normally required to increase heat transfer. Recommendations for small modifications of the coolant passages could be made based on the detailed velocity field measurements obtained. A change of the coolant outlet configuration and the blockage of a passage had only local effects on the flow field, allowing for manufacturing tolerances and modifications of the coolant flow system with little effect on the detail of the coolant flow field. The variation of pressure drop across the model with flow rate and the flow similarity for two practical flow rates also suggested that the flow was fully turbulent and, therefore, the flow patterns insensitive to engine operating conditions.

Acknowledgements

The authors are glad to acknowledge financial support from Fiat Research Centre in Orbassano and technical assistance from Stanley Plastics Ltd Dr R Rinolfi, Ing G Cipolla and Dr R Mascellini of Fiat were helpful at all stages of the work and P. Stanley and D Turner of Stanley Plastics were essential in the provision of the working model

References

Dybbs, A.; Edwards, R. V 1986 An index matched flow system for measurements of flow in complex geometries In Laser anemometry in fluid mechanics 2 pp. 171 184 Lisbon· Ladoan

Elphic, I G ; Martin, W W Currie, I G. 1982: Application of LDA to high Reynolds number cross flow. In· Proc. 2nd Int. Symp on Applications of Laser Anemometry to Fluid Mechanics. Lisbon, Portugal

Liu, C. H.; Nouri, J. M.; Whitelaw, J. H., Tse, D. G. N. 1989 Particle velocities in a swirling, confined flow. Comb. Sci. Technol. 68, 131-145

Liu, C. H., Nouri, J M.; Vafidis, C.; Whitelaw, J. H 1990 Experimental study of the flow in a centrifugal pump In: Proc. 5th Int. Symp. on applications of laser anemometry to fluid mechanics. Lisbon, Portugal

Nouri, J M.; Whitelaw, J H ; Yianneskis, M. 1988: A refractive index matching technique for solid/liquid flows. In· Laser anemometry in fluid mechanics 3 pp 335-346. Lisbon· Ladoan

Thompson, B. E.; Vafidis, C., Whitelaw, J. H. 1987: The application of refractive index matching technique for LDV flow measurements in a model of the SSME main injector bowl. Imperial College, Fluids Section, Report FS 87 23

Thompson, B E.; Senaldi, I., Vafidis, C.; Whitelaw, J. H.; McDonald, H 1989 Flow in a model of the SSME main injector bowl In: Proc. CASI 1st Canadian Symp. on Aerodynamics. Ottawa, Canada

Yianneskis, M.; Whitelaw, J H. 1983: Velocity characteristics of pipe and jet flows with high particle concentrations. Imperial College, Fluids Section, Report FS 83 22

Zizzelmar, R.; Molerus, O. 1978: Investigation of solid-liquid pipe flow with regard to turbulence modification In· Proc. Int Symp. on momentum, heat and mass transfer in two-phase energy and chemical systems. Dubrovnik, Yugoslavia

Received April 29, 1990

APPENDIX B

Vaporiser Performance†

C.H. Liu, R. Perez-Ortiz and J.H. Whitelaw

Department of Mechanical Engineering,
Imperial College of Science, Technology and Medicine.
Exhibition Road, London SW7 2BX, U.K.

ABSTRACT

Measured values of fuel droplet velocity, size and flux are presented for a vaporiser based on a T-shaped duct with upstream atomisation by a single axial jet and by six radial jets. They were obtained for a practical range of kerosene and air flow rates and inlet air temperatures with the vaporiser in free air and in a sector of an annular combustor with combustion. Phase-Doppler velocimetry was used to measure droplet velocity and size distributions and was complemented by photographic visualisation of the flames within the combustor.

The results obtained outside the combustor, and without combustion, showed that the Sauter-mean diameter of the droplets ranged from 20 to 60 μm and the liquid fuel flux from 0.2% to 30% of the total fuel as the inlet air temperature was increased from that of ground-idle to that of full power. The droplet size and liquid fuel flux also diminished with increase in air flow rate, and an arrangement of six radial jets resulted in better atomisation than an axial arrangement. The corresponding fluxes with combustion were in the range between 0.1% to 8% as a consequence of heat transfer from combusting gases to the vaporiser tubes.

Experience with the vaporiser operating within the combustor at fuel-flow rates and inlet air temperatures representative of take-off showed that the vaporiser performance could deteriorate rapidly due to the formation of carbon deposits particularly in the region where the flow impinged on the cross tube. The deposits led to reduced heat transfer and vapourisation with a consequently larger proportion of larger droplets and a tendency for the region of intense combustion to move downstream.

†To appear in Proceeding of Institute of Mechanical Engineering

1. INTRODUCTION

Most gas-turbine engines are fuelled by atomisers which spray liquid fuel into the combustor with performance which depends on the nature of the atomiser and the air and fuel flow rates. These devices are expensive and involve small annular and circular passages. An alternative is the so-called vaporiser described by Sotheran (1984) and used, for example, in some small engines. This requires atomisation of the fuel in the upstream region of the tube and secondary atomisation as the fuel-air mixture impinges on surfaces and turns corners. The process of vapourisation is assisted by heating the air supply and by heat transfer from the hot gases within the combustor to the vaporiser and to the atomising droplets within it. The flow from the vaporiser is directed towards the head of the combustor so that further atomisation and vapourisation may occur. The simplicity of the device makes it attractive but little is known about the details of its performance.

The experiences of Chow, Senda and Whitelaw (1989) and of Chow and Whitelaw (1991) with vaporiser-fuelling devices were generally satisfactory in their model of a Gem combustor with velocity, temperature and concentration distributions similar to those measured by Bicen, Tse and Whitelaw (1987) with gaseous fuel. It was noted that there was a tendency for lower temperatures and combustion efficiency with the liquid fuel, but the general nature of the flow and, in particular, the location of

NOMENCLATURE

A/F	air-to-fuel ratio
d	droplet diameter
$\dot{m}_f$	fuel flow rate
$\dot{m}_v$	vaporiser air flow rate
pdf	probability density function
SMD	Sauter-mean diameter
T_{air}	inlet air temperature
V	velocity

the regions of intense combustion were unchanged. On two occasions, these liquid-fuel investigations had to be stopped due to lengthening of the flame and this was corrected by cleaning the vaporiser tube.

Here we are concerned with the nature of the flow leaving a vaporiser, its dependence on the flow rates of air and kerosene fuel and of inlet air temperature and the possible consequences for the performance of a combustor fuelled by the vaporiser. Thus a phase-Doppler velocimeter has been used to examine the distribution of droplet diameters, the velocities of the droplets and the liquid fuel flux at the exit. The emphasis of the measurements is on the flow leaving the vaporiser but some measurements have been obtained to show the nature of the two-phase flow away from the vaporiser exit and in important regions within a combustor corresponding to a 1/6 annular sector of a reverse-flow arrangement. The distribution of droplets within the combustor was observed with a laser sheet and the nature of the combusting flow recorded photographically.

2. FLOW CONDITIONS AND INSTRUMENTATION

The combustor of Figure 1 was arranged within a plenum chamber and with air supplied by a 7.5 kW centrifugal fan at a flow rate of 41 g/s and measured by a calibrated orifice plate. Compressed air to the vaporiser was measured by a rotameter with mass flow rates shown in the following section and a value of 1.225 g/s ($\dot{m}_v$) in the combustor tests. The air to the vaporiser and combustor were passed through a 20 kW heater which raised the temperature up to 523°K (T_{air}). The kerosene fuel (Jet A) was pumped to the fuel injector at a range of flow rates, and for the combustor tests at values of 0.58 and 0.97 g/s ($\dot{m}_f$), corresponding to ground idle and take-off conditions with overall air-to-fuel ratios (A/F) of 70 and 42, respectively. The experimental condition was similar to that of Chow (1991) which was determined based on the pressure loss of engine operating condition. The properties of the kerosene fuel are provided in Table 1.

The combustor arrangement had two plenum chambers so that air entered through film-cooling slots, primary holes and dilution holes (Figure 2) in the proportions shown in Table 2 and the products of combustion, together with some remaining fuel and air, left the combustor and passed into the reverse flow duct. The details of the T-vaporiser and the two types of atomiser are indicated in Figure 2. The contraction of the annular chamber caused by turning the flow to a smaller radius was simulated by contracting the angled side walls of the model. In the primary and dilution regions, the flow could be observed through quartz windows which could be replaced by solid plates. The parallel side walls of earlier investigations were considered to have no effect on cross-flow velocities, as supported by the measurements of Toral and Whitelaw (1982), and the present trapezium cross-section is arranged to cause convergence of the flow as in an annular arrangement with the contraction of the reversed-flow duct. The flow in the primary zone is known to be in the form of a single vortex driven by the film-cooling flows and truncated, at least in part, by the primary jets. It gives rise to combustion in the primary region which is less intense than that of double-vortex arrangements with fuel burning between the planes of the primary and dilution jets. This view is supported by the photographs of Figure 3 which show an intense region of combustion between the two sets of jets and burning gases which increasingly extend into the reverse-flow nozzle as the inlet air temperature is increased. The results of Chow *et al.* (1989), obtained without the reverse-flow nozzle and with kerosene fuel, show that there was approximately 0.04% by mass of unburnt hydrocarbon in the exit plane of the combustor for the take-off condition at the highest inlet air temperature.

The phase-Doppler velocimeter of Figure 1 comprised a laser, transmitting optical components based on a rotating grating and an arrangement of lenses, a slit spatial filter and photomultipliers. A helium-neon laser with a power of 35 mW was used for measurements in ambient air and an argon-ion laser operating in the green line at power between 250 and 400 mW was used for measurements in the combustor. The optical system and related counter and software have been described in detail by Hardalupas

(1989). Light scattered by the fuel droplets was collected by the three photomultipliers arranged around the bisector plane of the incident light beams with elevation angles of 15 and 30 degrees to ensure that the refraction dominated the scattered light. The smaller collection angle was decided according to the geometric confinement of the combustor to allow light collection. The collected light was focused to the centre of a 50 μm slit and passed through a mask with three evenly spaced rectangular apertures. The three light paths were observed by the photomultipliers and the resulting electronic signals processed by the purpose-built counter and micro-computer (IBM-PC AT) to obtain velocity, and droplet-size distributions. Three configurations of optical arrangement were used as shown on Table 3 and allowed the measurement of droplet sizes up to 110, 347 and 270 μm.

The uncertainties of measurements of velocity and size have been considered in detail, for example by Liu, Hardalupas and Whitelaw (1992), and stem mainly from statistical uncertainties. Thus, the mean values of velocity, based on 7000 samples, can be expected to be precise within 2% and droplet diameter within 2 μm for droplets larger than 20 μm. The uncertainty of the flux measurements was around 30% and associated mainly with the evaluation of the effective area of the probe volume for each size range and the rejection of measurements due to the validation procedure of the instrument (Bachalo *et al.*, 1988; Hardalupas and Taylor, 1989).

3. RESULTS AND DISCUSSION

The results are presented in two sub-sections concerned respectively with the performance characteristics of the vaporiser and the behaviour of the combustor as influenced by the vaporiser. Figures 4 to 8 present the measurements of velocity and droplet-size distribution for three values of each of air inlet temperature, air and fuel flow rates. They were obtained with the vaporiser in free air, and the phase-Doppler velocimeter arrangement II of Table 3 measured the velocity component aligned to the axis of the exit tubes and 5 mm downstream of the exit plane, see Figure

4. Two atomisation devices were used in the entry tube of the vaporiser, one with axial injection and the other with radial injection through six 0.5 mm diameter holes; the arrangements of these atomisers are shown in Figure 2. The flow from each exit tube was measured in a preliminary experiment conducted in ambient air which confirmed that the centre-line velocities were within 5% with identical droplet distributions. The measuring volume was approximately 0.1 mm in diameter and 0.3 mm in length compared with the 5 mm exit diameter of the vaporiser.

The measurements with combustion were obtained with the vaporiser inside the combustor using optical arrangement III and the results of Figures 5 to 8 allow comparison with those obtained in free air. A few results were also obtained within the primary combustion zone using optical arrangement I, with which the velocity component of measurement was normal to the axis of the vaporiser exit tube, and they are presented in Figures 9 and 11.

3.1 Vaporiser Performance

Figure 4 presents droplet-size distributions and corresponding velocities measured with the vaporiser in free air, and with axial and radial atomisers. The size distributions are normalised and presented in terms of probability density functions (pdf) as in other cases. The air and fuel flow rates are the same as those with combustion and equivalent to the condition of an overall A/F of 70 and T_{air} of 523°K. The droplet size distributions are similar with Sauter mean diameters (SMDs) of 35 and 28 μm for the axial and radial atomisers, respectively, and with a slightly longer tail towards larger droplets for the former. The droplet velocities show a similar trend, decreasing slightly with droplet diameter and indicating larger variations as the number of droplets in the sample declines with increasing size. Those with the radial atomiser are around 10% higher than those with the axial atomiser since smaller droplets tends to evaporate faster to increase the bulk volume of the gas phase and the velocity.

The variation of velocity with fuel flow rate and inlet air temperature of the vaporiser air for the radial atomiser is quantified in Figure 5 by the mean velocity of the 15 μm droplets

which represent the gas phase. Figure 5a shows that the decrease in velocity with fuel flow rate is similar for each of three air flow rates and, as expected, the effect is smaller than that with air flow rate. The variations of Figure 5a can be attributed mainly to the variations in mass flow but those of Figure 5b with temperature are related to the volume of the gas.phase and with improved vapourisation so that the liquid fuel flux decreases with inlet air temperature. The velocities measured with combustion are highest because of the additional heat transfer to the vaporiser by the hot gas.

The Sauter-mean diameter (SMD) increases with fuel flow for both atomisers, Figure 6, and this explains the difference in velocities associated with the same mass flow rates of Figure 4, since the SMD is some 25% larger with the axial injector, and we can expect that the overall droplet population affects the velocities of particular droplet size ranges. The influence of inlet air temperature on the SMD clearly depends on the degree of atomisation and vapourisation so that droplets are evaporated preferentially in smaller sizes with consequent increase in SMD. It is evident that the radial atomiser is to be preferred.

Figure 7 presents a sample of droplet size distributions, corresponding to the SMD values of Figure 6b, with combusting flows represented by full lines. The results confirm the advantages of the radial atomiser and that combustion tends to cause the distributions to have increased proportions of larger droplets.

The droplet size distributions velocities and SMDs are important but should be viewed in the context of the amount of the total fuel which emerges from the vaporiser in the form of liquid droplets. Figure 8a shows the volume flux of droplets, considering all sizes, and normalised by the average value of flux corresponding to the amount of fuel supplied to the fuel injector. The normalised flux is never larger than 30%, can be as small as 0.2% and is reduced by smaller fuel flow rates and larger air flow rates, as expected from Figure 6; the radial atomiser is markedly better with low fuel flow rates but offers less advantage at the highest fuel flow rate. With combustion, however, the radial injector offers a distinct

advantage, as suggested by the size distribution shown in Figure 7, so that at flow and preheat conditions corresponding to take-off, i.e. T_{air} = 523°K and $\dot{m}_f$ = 0.97 g/s, the normalised flux is 0.6% in contrast to the 2% with the axial atomiser, and the difference is larger at smaller fuel flow for the ground-idle condition. The variation of liquid fuel flux with fuel flow rate is small for the axial fuel atomiser, Figure 8, but increased with the radial atomiser, with values of 0.6% and 0.1% for the high and low fuel flow rates at the highest inlet air temperature. The small sensitivity of the axial atomiser to liquid fuel flux without combustion may be attributed, in part, to the denser spray and reduced data rate.

Droplet distributions in the near field of the vaporiser, Figure 9, are associated with a different axial injector to that of Figure 4, but manufactured to the same design, and gave similar droplet size distributions. There are large droplets close to the edge of the vaporiser exit and nearby but with a small fraction of the total liquid fuel flux. Combustion causes the droplets away from the vaporiser to disappear and those at the edge of the tube to reduce in number.

3.2 Combustor Performance

The photographs of Figure 3.1 provide an impression of the flame at A/F of 70 and three inlet air temperatures with that at the lowest temperature closer to the ground-idle condition. They suggest the existence of combustion throughout the combustor with a particularly intense region between the primary and secondary jets. The luminosity of the flame is integrated across the combustor so that the flows in the planes of the jets, the spaces between the jets and of the vaporiser exits are not recognised, separately. However, observation by a laser sheet at various lateral planes in non-combusting flow, indicated by the sketch of Figure 10, suggested a cloud of droplets at a downstream region between the two vaporiser exits and confined to the primary zone, so that the region of intense combustion probably related to the burning of this cloud of droplets. The fuel jets impinged on the semi-circular dome of the combustor where liquid evaporated and burned to give a blue flame in a near

horseshoe-shape. This extended downstream and close to the wall, as indicated in the photographs, due to the effect of the counterclockwise-rotating flow in the primary zone.

The sizes of the non-combusting droplets in the cloud of Figure 10 were identified on the symmetry plane of the primary zone, Figures 11b and 11c, and confirmed Sauter-mean diameters between 14 to 17 μm at T_{air} = 523°K and A/F = 70 and 16 to 28 μm at T_{air} = 423°K, with no droplets larger than 60 μm. With A/F = 42 and T_{air} = 523°K, Figure 11a shows distributions similar to that of the lower fuel flow but with a larger number of droplets, and the consequence is indicated in Figure 3.2 by the larger combustion region and more luminous flame. The operating condition, A/F = 42 and T_{air} = 523°K, of Figure 3.2a is close to the take-off condition. A reduction of inlet air temperature by 100°K, Figure 3.2c, caused an increase of liquid fuel flux from 2% to 6%, Figure 8, and is related to the consequence of a change of the vaporiser performance. Those droplets not evaporated after impingement were transported downstream to the symmetry region by the primary vortex, partly due to the trapezium shape and resulting convergence of the flow. The droplets in the cloud were small, Figure 11, partly due to the impingement of the fuel jets on the head dome. However, it was observed that the cloud did not burn completely in the primary region, with some droplets transported downstream between the primary and dilution jets where intense combustion occurred.

With operation over a period of time and with overall equivalence ratios including that of take-off, the nature of the flame was observed to change so that it became longer. This observation coincided with a rise in surface temperature of the vaporiser tube over a short distance on either side of the centre of the T and it can be conjectured that build-up of carbon on the inner surface was reducing the heat transfer rate to the fuel-air mixture. The consequence was a reduction in atomisation and in vaporisation and, in the worst case, to have fuel dripping from the vaporiser tube and intermittent combustion. The deterioration of combustion in the primary zone led to combustion further downstream with adverse effects to the material of the reverse-

flow duct and the exhaust pattern factors. Cleaning of the atomiser tube caused the flame to return to its normal shape. The radial atomiser resulted in a bluer and shorter flame, consistent with the trend of less liquid fuel and longer vaporiser life.

4. CONCLUDING REMARKS

The characteristics of a vaporiser fuel injector have been quantified in terms of droplet velocity, size distribution and flux in combusting and non-combusting environments by phase-Doppler velocimetry, with inlet air velocity and temperature and fuel flow rate varied for a single axial-jet atomiser and for an arrangement with six radial jets.

The performance of the vaporiser was found to be better with the radial-hole atomiser and high inlet temperature, and combustion improved the performance further. The Sauter-mean diameter of the droplets emerging from the vaporiser was between 20 and 60 μm with the flux, when normalised by the area-averaged value of the supplied fuel, between 0.2% and 30% over the range of fuel and air flow rates corresponding to take-off and ground-idle without combustion. Increase of vaporiser air flow rate and temperature and decrease of fuel flow rate gave rise to smaller SMDs and less liquid fuel flux. Combustion resulted in increased SMD while the emerging liquid fuel flux from the vaporiser was reduced to a range between 0.1% and 8% due to heat transfer from combusting gases to the vaporiser tubes.

The performance of the combustor depended upon the liquid droplets discharged from the vaporiser, which were mostly transported to a central region downstream of the vaporiser by the vortex flow of the primary zone and had sizes less than 60 μm, with SMD of the droplets ranging from 14 to 17 μm at 523°K inlet air temperature and from 16 to 28 μm at 423°K. The length of the flame and the region of intense combustion in the downstream region increased with the amount of liquid fuel from the vaporiser. The performance of the vaporiser deteriorated with time, and more rapidly at high fuel flow, to give larger

proportions of large droplets and liquid fuel due to the formation of carbon at the fuel impingement point.

REFERENCES

Bachalo, W.D., Rudoff, R.C. and Brena de la Rosa, A. (1988) Mass flux measurements of a high number density spray system using the phase-Doppler particle analyzer. AIAA-paper-88-0236.

Bicen, A., Tse, D.G.N. and Whitelaw, J.H. (1987) Flow characteristics of a model annular combustor. AGARD-CP-422, paper 14.

Chow, S.K. (1991) Flow and combustion characteristics of a liquid-fuelled combustor. Ph.D. thesis, University of London.

Chow, S.K., Senda, M. and Whitelaw, J.H. (1989) Combustion Characteristics of a Liquid-Fuelled Model Annular Combustor. in Proc. 9th Int'l Symp. on Air Breathing Engines, Athens, Greece.

Chow, S.K. and Whitelaw, J.H. (1991) Scalar characteristics in a liquid-fuelled combustor with a curved exit nozzle. in Proc. Int'l Symp. on Aerothermodynamics in Combustion, June 3-5, Taipei, Taiwan, ROC.

Hardalupas, Y. (1989) Experiments with isothermal two-phase flow. Ph.D. Thesis, University of London.

Hardalupas, Y., Liu, C.H. and Whitelaw, J.H. (1992) Experiments with disk stabilised kerosene-fuelled flames. to appear in *Comb. Sci. and Tech.*

Hardalupas, Y. and Taylor, A.M.K.P. (1989) On the measurement of particle concentration near a stagnation point. *Exp. in Fluids*, **8**, 113.

Lefebvre, A.H. (1983) Gas Turbine Combustion. Hemisphere.

Sotheran, A. (1984) The Rolls-Royce annular vaporiser combustor. *J. Eng. for Gas Turbine and Power*, Trans. ASME, **106**, 88.

Toral, H. and Whitelaw, J.H. (1982) Velocity and scalar characteristics of the isothermal and combusting flow in a combustor sector rig. *Comb. and Flame*, **45**, 251.

TABLE 1 Properties of aviation kerosene (Jet A)*

Chemical Formula	$C_{12}H_{26}$
Relative density at 15 °C	0.8
Kinematic viscosity at 40 °C, mm/s	1.3
Lower specific energy, MJ/kg	42.8
Boiling point, °K	423-573
Freezing point, °K	223
Stoichiometric A/F ratio, in mass	14.8

* Lefebvre (1983)

TABLE 2 Gem combustion chamber data

Air Passages	Ref. No.	Air Flows, %
Outer Annulus		
1st cooling	1	10.6
2nd cooling	2	8.8
3rd cooling	3	6
Dilution holes	4	19.8
4th cooling	5	5.2
5th cooling	6	4.1
6th cooling	7	4
Vaporiser	9	3
Inner Annulus		
1st cooling	11	6
Primary holes	12	11.7
2nd cooling	14	5
Dilution holes	15	5 8
3rd cooling	16	10
TOTAL		100

TABLE 3 Characteristics of the phase-Doppler velocimeters

Optical Arrangements	I*	II†	III†	
Transmitting optics				
Laser	1W Ar-ion	35 mW He-Ne	1W Ar-ion	
operating power	400	35	250	mW
wavelength	514.8	632.8	514 8	nm
Beam intersection angle	4.85	3.156	2.565	deg.
Measurement volume length at $1/e^2$ intensity	1979	4680	4680	μm
Measurement volume diameter at $1/e^2$ intensity	84	128	104	μm
Fringe spacing	6.07	11.48	11.49	μm
Number of fringes	13	11	9	
Frequency shift	0-3	0-5	0-5	MHz
Receiving optics				
Focal length of collimating lens	600	500	500	mm
Angle of forward light collection w.r.t the bisector of the beams	30	30	15	deg.
Equivalent aperture at collimating lens:				
dimension of rectangular aperture	45 x 6	50 x 10	50 x 10	mm
separation between aperture 1 and 2	24	13.3	13.3	mm
separation between aperture 1 and 3	48	26.7	26.7	mm
Magnification	0.5	0.32	0.32	
Spatial filter slit width	100	50	50	μm
Effective length of measuring volume	200	312	604	μm
Phase angle-to-diameter conversion factor for channel 1 and 3	0.306	0.966	0.755	μm/deg.
Sizing range, up to	110	347	270	μm

* Velocity component of measurement normal to the axis of exit tube of the vaporiser

† Velocity component of measurement parallel to the axis of exit tube of the vaporiser

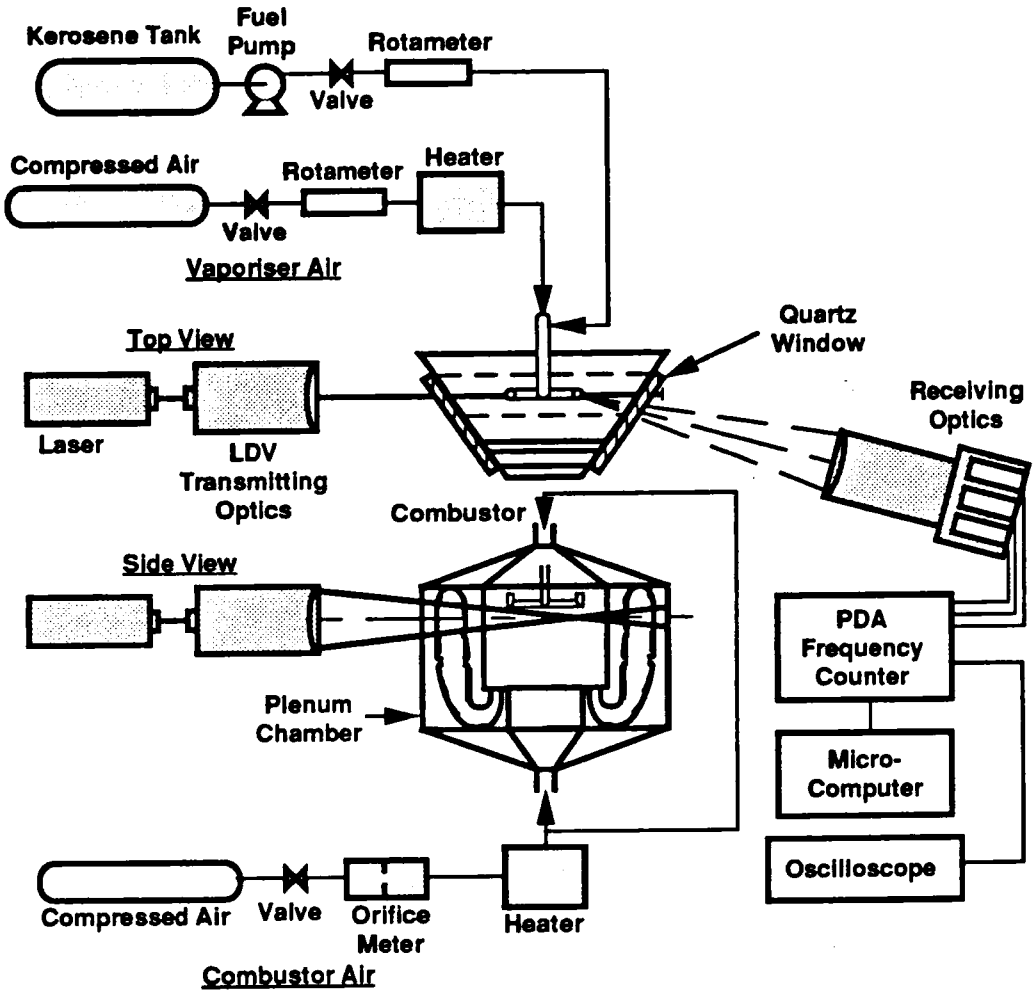


FIGURE 1 Flow configuration and instrumentation.

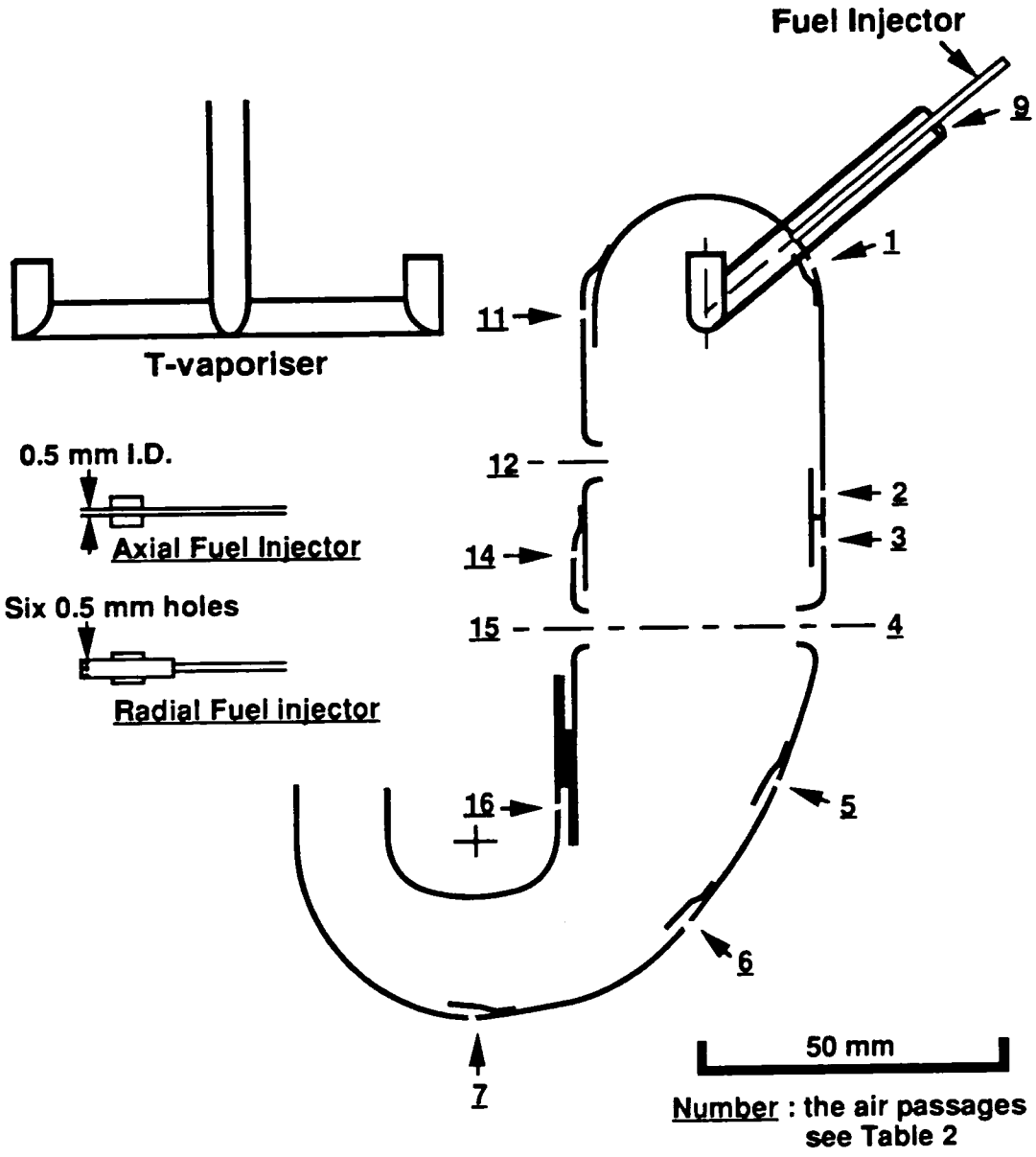


FIGURE 2 Dimensions and details of the combustor and fuel injectors.

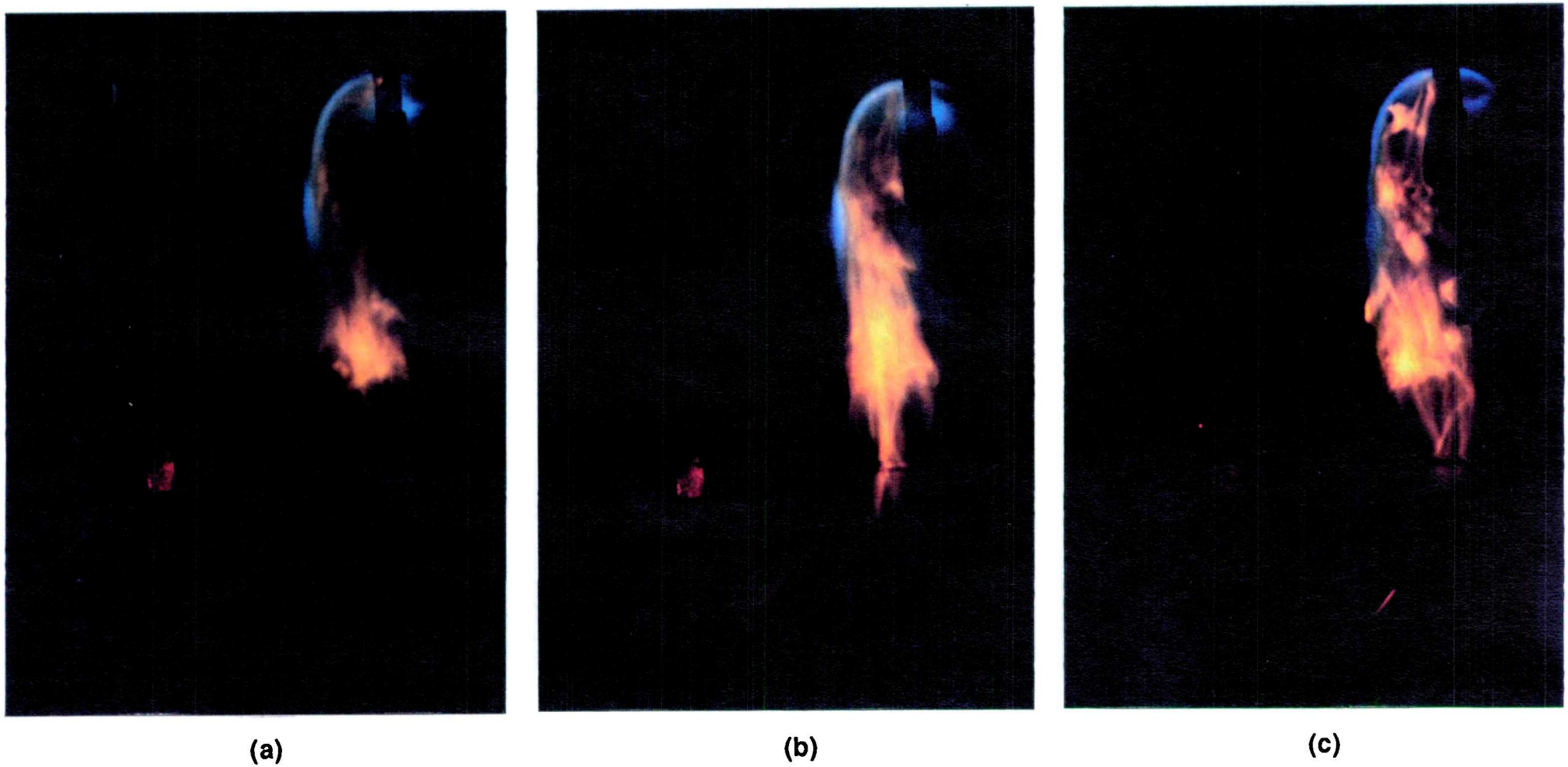


FIGURE 3.1 Photographs of combusting flow at A/F = 70.
(a) T_{air} = 523°K, (c) T_{air} = 473°K, (c) T_{air} = 423°K.

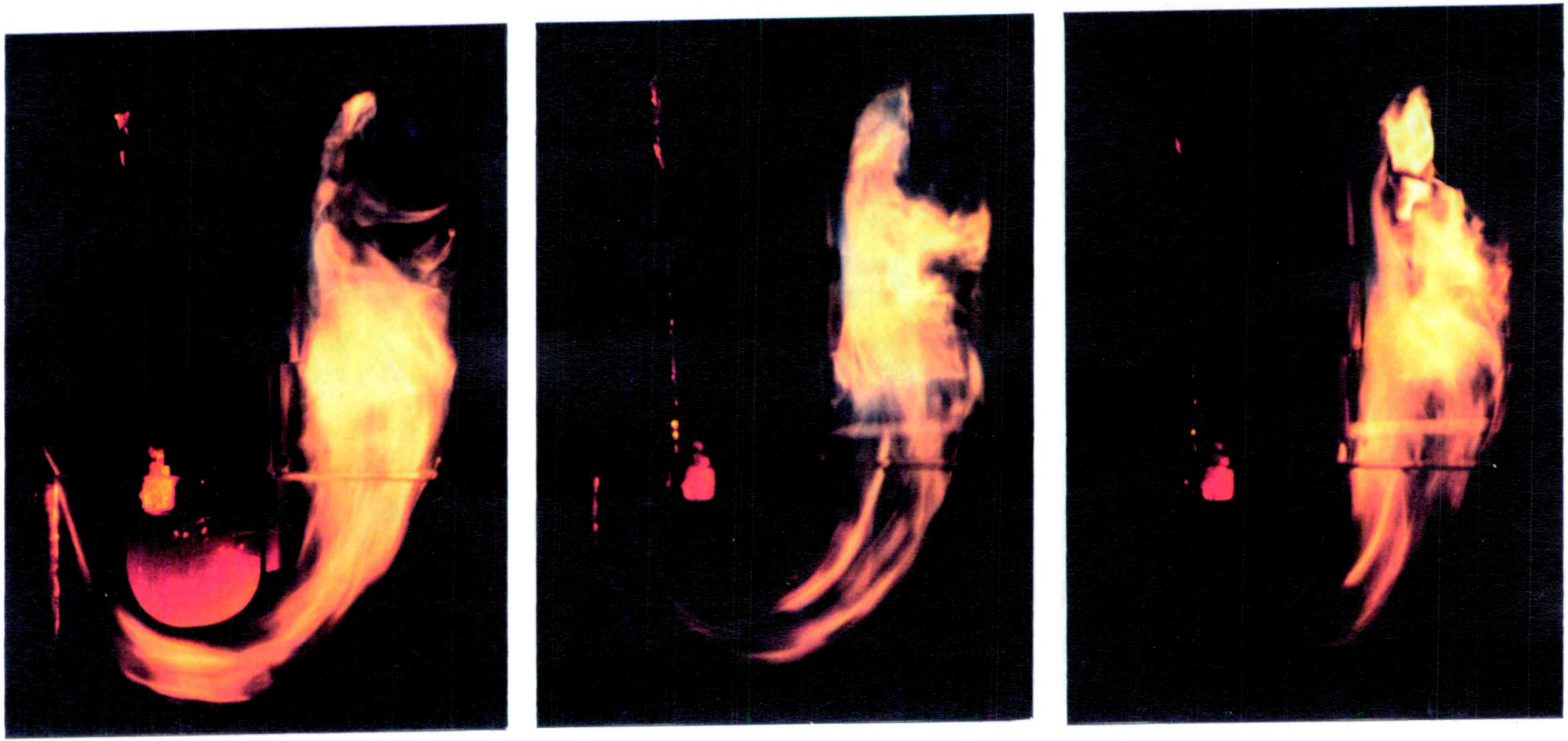


FIGURE 3.2 Photographs of combusting flow at A/F = 42.
(a) T_{air} = 523°K, (c) T_{air} = 473°K, (c) T_{air} = 423°K.

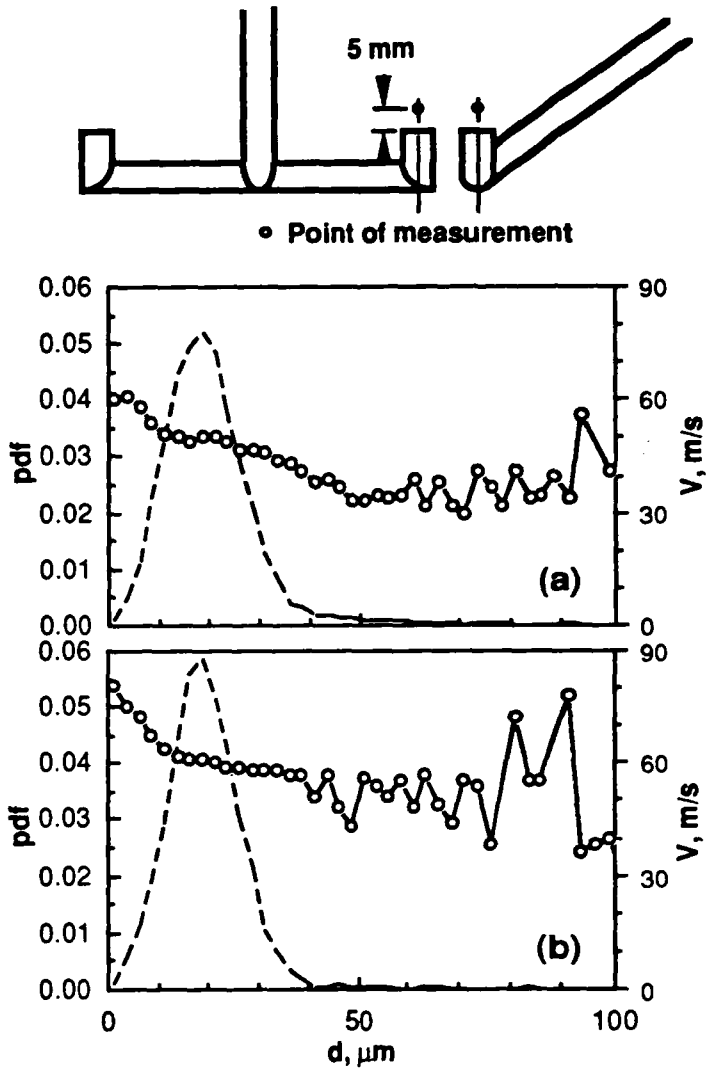


FIGURE 4 Velocity and droplet size at the exit of vaporiser.
Vaporiser in free air with $\dot{m}_v$ = 1.225 g/s, T_{air} = 523 °K, and $\dot{m}_f$ = 0.58 g/s.
(a) Axial atomiser; (b) Radial atomiser. (----- size pdf; —o— velocity)

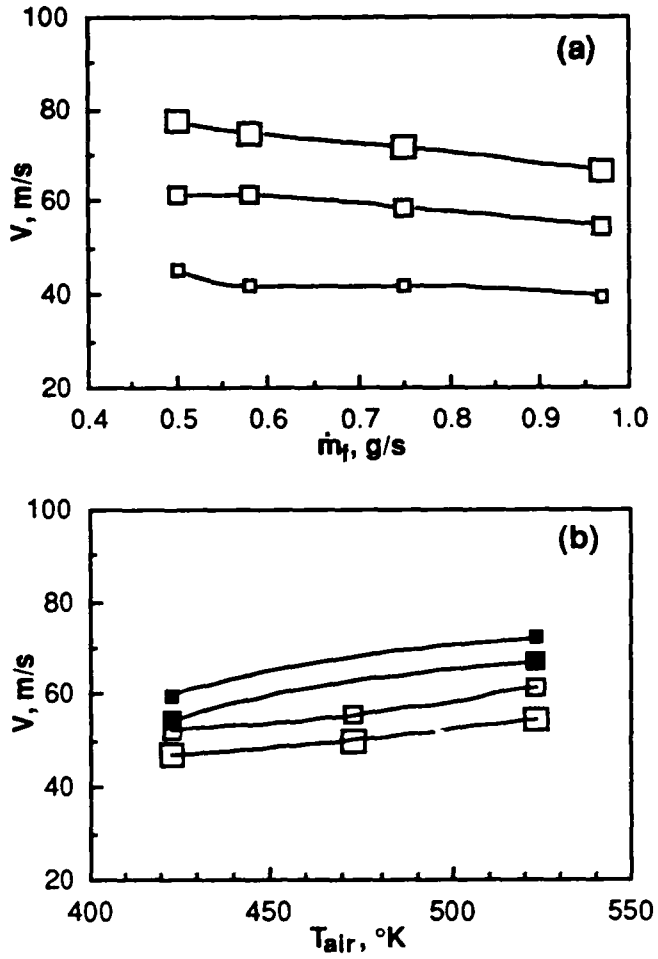


FIGURE 5 Mean velocity of 15 μm droplets at the exit of vaporiser with radial atomiser. (see Figure 4 for measurement locations)
(a) Vaporiser in free air with $\dot{m}_v$ = 1.02 (▫), 1.225 (□) and 1.429 g/s (□) and T_{air} = 523 °K.
(b) $\dot{m}_v$ = 1.225 g/s and $\dot{m}_f$ = 0.58 (□ , ■) and 0.97 g/s (□ , ■); open symbol: vaporiser in free air; block symbol: with combustion.

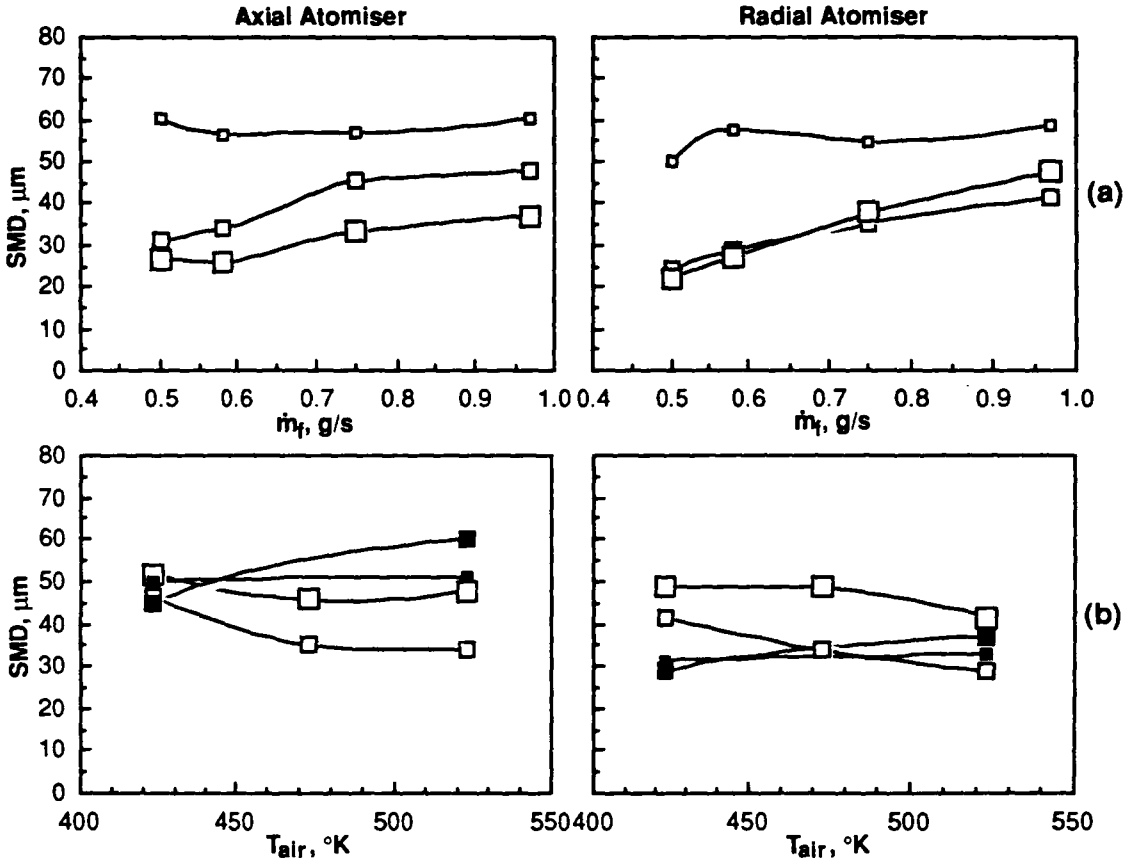


FIGURE 6 Sauter-mean diameter of droplets at the exit of vaporiser. (see Figure 4 for measurement locations; see Figure 5 for legend)

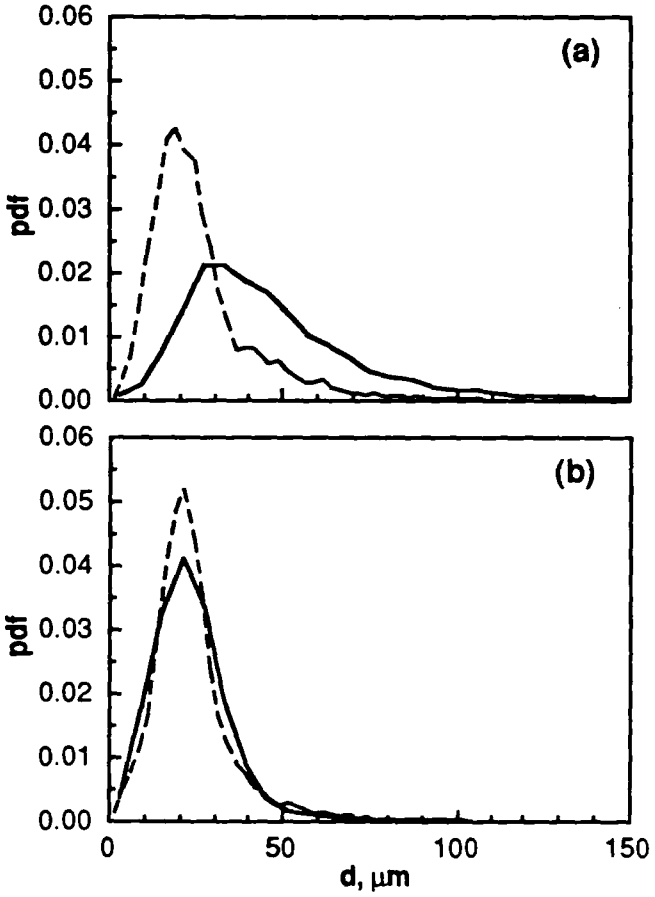


FIGURE 7 Size distributions of droplets at the exit of vaporiser, with $\dot{m}_v$ = 1.225 g/s, T_{air} = 523 °K, and $\dot{m}_f$ = 0.97 g/s. (- - - - - vaporiser in free air; ——— with combustion; see Figure 4 for measurement locations)
(a) Axial atomiser; (b) Radial atomiser

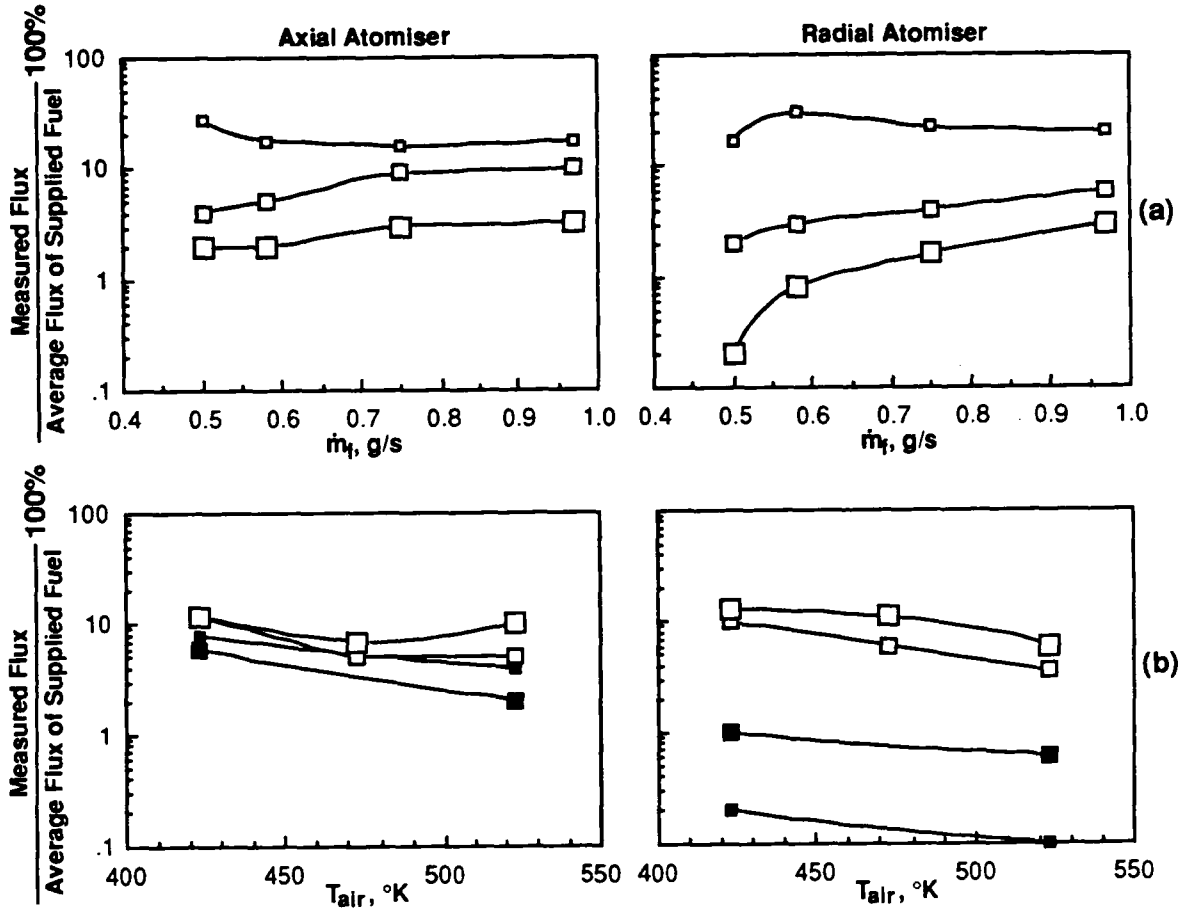


FIGURE 8 Normalised volume flux of droplets at the exit of vaporiser. (see Figure 4 for measurement locations; see Figure 5 for legend)

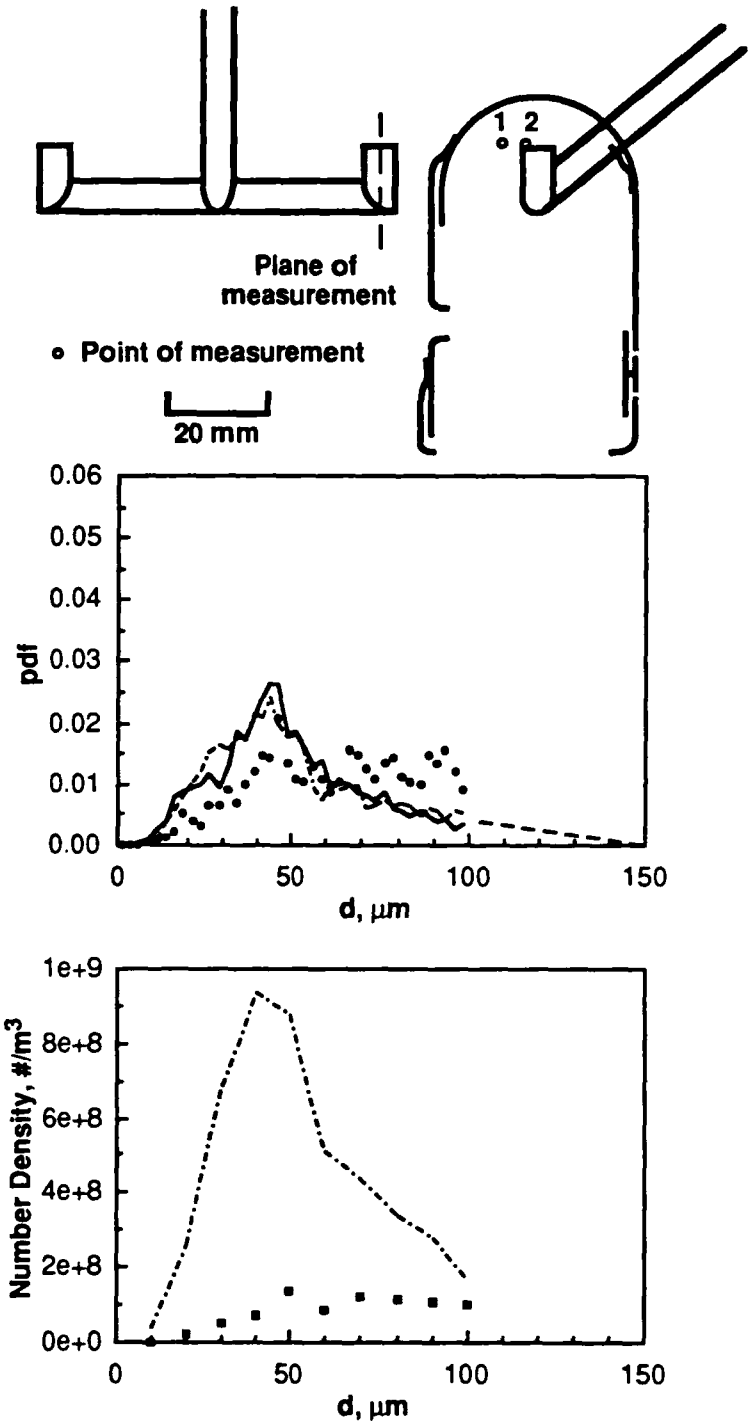


FIGURE 9 Size and number density distributions of droplets in the combustor near the vaporiser, with A/F = 42 and T_{air} =523 °K. (——— point 1 and ····· point 2 without combustion; • point 2 with combustion)

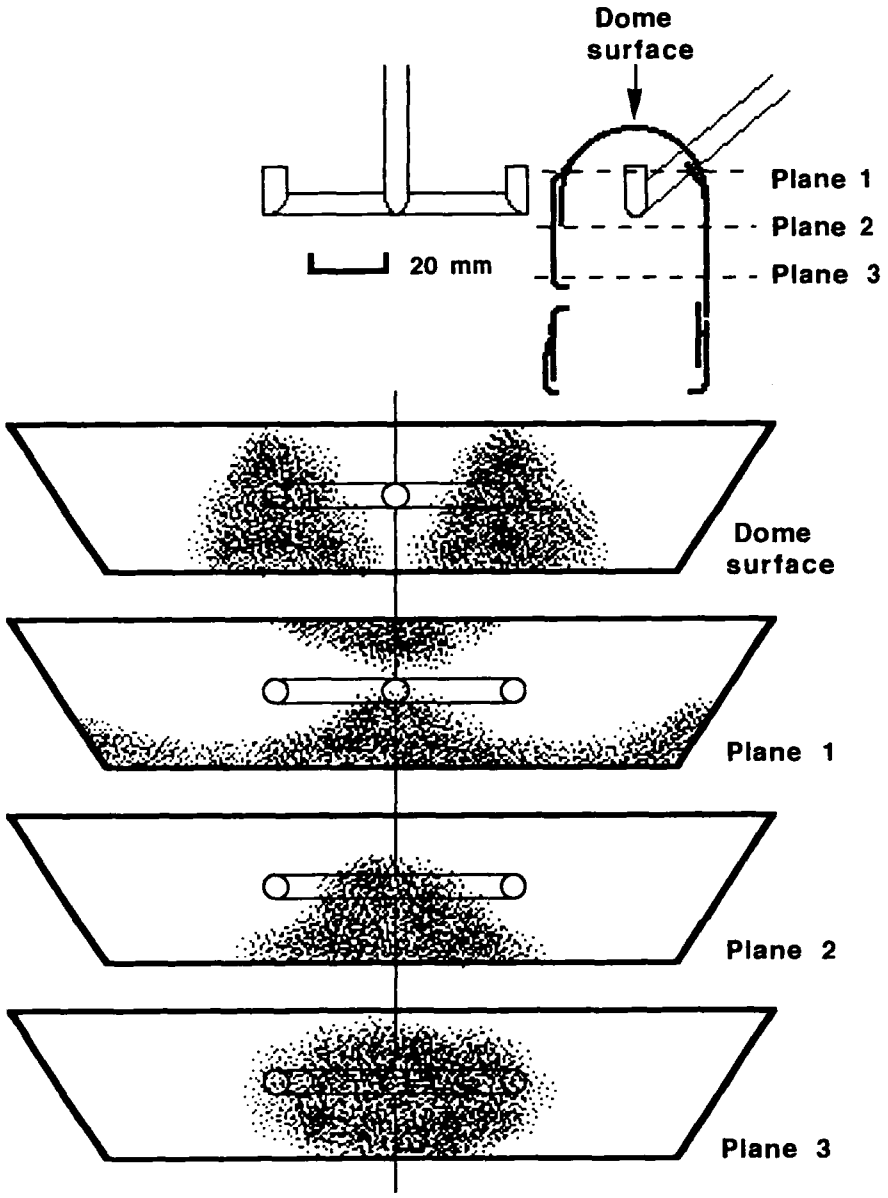


FIGURE 10 Droplet cloud in the combustor without combustion at A/F = 70 and T_{air} = 523 °K, observed by laser sheet.

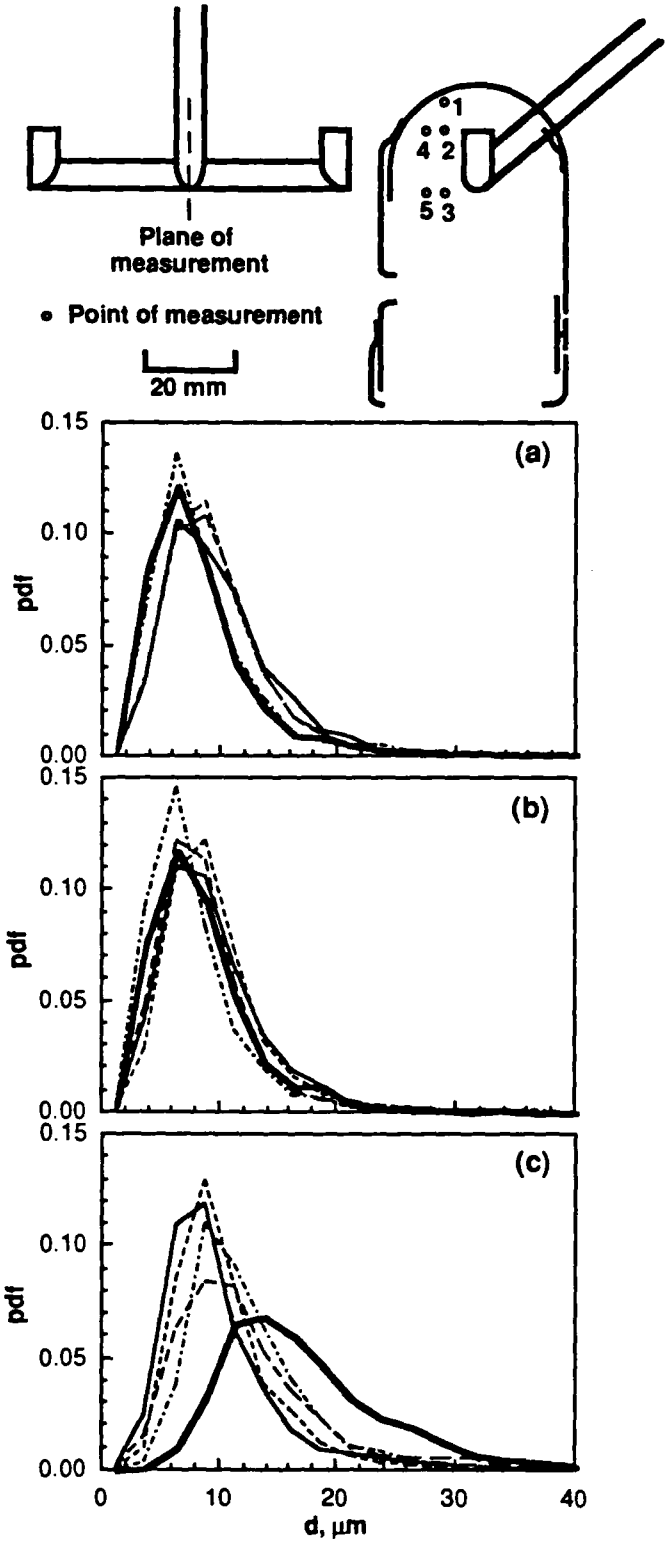


FIGURE 11 Size distributions of droplets in the primary zone in the combustor without combustion.
(a) T_{air} = 523 °K; A/F = 42; (b) T_{air} = 523 °K; A/F = 70;
(c) T_{air} = 423 °K; A/F = 70.
(Measurement point: - - - - - 1; ····· 2; ——— 3; ·-·-·-· 4; ——— 5)